TECHNISCHE UNIVERSITÄT MÜNCHEN

Physik-Department
Lehrstuhl für Funktionelle Materialien

Printed Organic Solar Cells

Kerstin Sabrina Wienhold, M. Sc.

Vollständiger Abdruck der von der Fakultät für Physik der Technischen Universität München zur Erlangung des akademischen Grades eines

Doktors der Naturwissenschaften (Dr. rer. nat.)

genehmigten Dissertation.

Vorsitzender:	Prof. Dr. Martin Zacharias
Prüfer der Dissertation:	1. Prof. Dr. Peter Müller-Buschbaum
	2. Prof. Dr. Aliaksandr Bandarenka

Die Dissertation wurde am 25.01.2021 bei der Technischen Universität München eingereicht und durch die Fakultät für Physik am 01.03.2021 angenommen.

"I am among those who think that science has great beauty.
A scientist in his laboratory is not a mere technician: he is also a child confronting natural phenomena which impress him as though they were fairy tales."

Marie Curie
(7.11.1867 - 4.7.1934)
Nobel Prize 1903 and 1911

Abstract

In this thesis, active layers based on conjugated donor polymers and nonfullerene small molecule acceptors are printed using a meniscus guided slot-die coating technique. The process of printing is followed *in situ* to gain insights into the structure formation and to enable an optimization of the printing parameters, inner morphology and solar cell performance. Towards further optimization of printed organic solar cells, the effect of solvent additive concentration on the morphology, optical properties and photovoltaic performance is studied. Furthermore, morphological changes, occuring under illumination of printed organic solar cells, are studied *in operando*, correlated to the degradation of device parameters and supported by a theoretical model. This thesis reveals the impact of inner morphology on the photovoltaic performance and is an important step towards realization of large-area organic solar cells with adequate long-term stability and high efficiency.

Zusammenfassung

In dieser Doktorarbeit werden aktive Schichten von konjugierten Donor-Polymeren und kleinen, Fulleren-freien Akzeptormolekülen mit einer meniskusgeführten Schlitzdrüsenbeschichtungstechnik gedruckt. Der Druckprozess wird *in situ* verfolgt, um Einblick in die Strukturbildung zu gewinnen und eine Optimierung der Druckparameter, der inneren Morphologie und der Leistung der Solarzelle zu ermöglichen. Zur weiteren Optimierung von gedruckten Solarzellen wird der Einfluss der Konzentration von Lösungsmitteladditiven auf die Morphologie, die optischen Eigenschaften und die Photovoltaik-Leistung untersucht. Darüber hinaus werden die morphologischen Änderungen unter Beleuchtung von gedruckten organischen Solarzellen *in operando* untersucht, mit der Abnahme der Leistungsparameter korreliert und durch ein theoretisches Model unterstützt. Diese Doktorarbeit zeigt den Einfluss der inneren Morphologie auf die Photovoltaik-Leistung und ist ein wichtiger Schritt zur Verwirklichung von großflächigen, organischen Solarzellen mit hinreichender Langzeitstabilität und hohem Wirkungsgrad.

Contents

List of abbreviations

AFM	atomic force microscopy
AM	air mass
AOI	angle of incidence
ASH	average step height
BHJ	bulk-heterojunction
BSE	backscattered electron
CB	chlorobenzene
DA	decoupling approximation
DESY	Deutsches Elektronen-Synchrotron
DIO	1,8-diiodooctane
DWBA	distorted wave Born approximation
EIA	effective interface approximation
EQE	external quantum efficiency
FF	fill factor
FWHM	full width at half maximum
GISAXS	grazing incidence small-angle X-ray scattering
GIWAXS	grazing incidence wide-angle X-ray scattering
HOMO	highest occupied molecular orbital
ITO	indium doped tin oxide

LED ..... light-emitting diode

LMA ..... local monodisperse approximation

LUMO ..... lowest unoccupied molecular orbital

MiNaXS ..... micro- and nanofocus small- and wide-angle X-ray scattering

MPP ..... maximum power point

PCE ..... power conversion efficiency

PETRA ..... Positron-Elektron-Tandem-Ring-Anlage

PL ..... photoluminescence

SDD ..... sample-detector distance

SE ..... secondary electron

SEM ..... scanning electron microscopy

SLD ..... scattering length density

UV/vis ..... ultraviolet/visible light

1 Introduction

In recent decades, awareness of climate change has increased and great effort has been made to reduce global warming as far as possible. However, at the same time, the global need for electrical power increased significantly due to remarkable technological progress and renewable energy technologies were considered to be a highly promising way to provide sufficient amount of power in an environmentally friendly way. [1–3] Within the last decades, the power generated from renewable energy sources rose significantly, whereas the contribution of non-renewable sources declined. Figure 1.1 illustrates the evolution of power generation in terawatt-hours [TWh] in Germany over the last 30 years. [4] Power from non-renewable sources, such as coal energy (black) and nuclear energy (gray), became less important. In contrast, the relevance of renewable energy sources (dark green), such as wind (blue), biomass (bright green) and solar radiation (yellow), increased significantly.

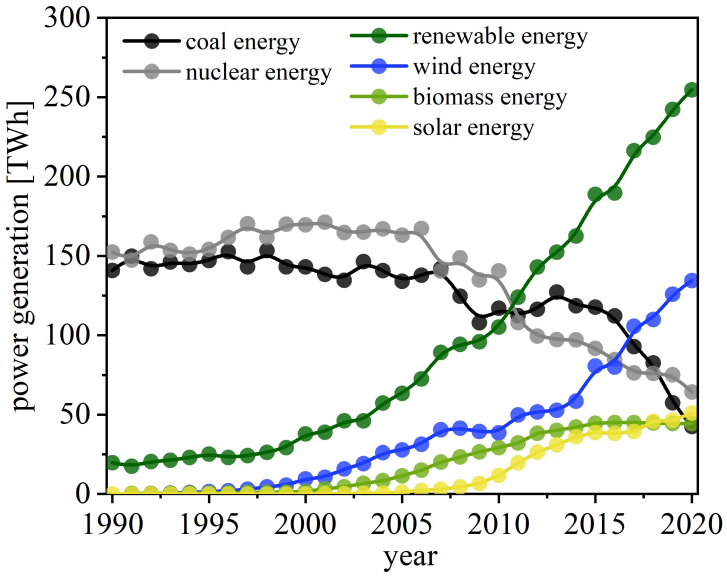

Figure 1.1: Power generation in terawatt-hours in Germany from 1990 to 2020. The evolution of coal energy (black), nuclear energy (gray), wind energy (blue), biomass energy (bright green) and solar energy (yellow) as well as the overall power generation from renewable energy sources (dark green) are given. Data are obtained from [4].

The main drawback of fossil fuels is their limitedness as well as their emission of CO_2, contributing to global warming. In contrast, nuclear power enables CO_2–neutral power

generation but suffers from severe drawbacks, such as the unresolved end-storage problem, enormous safety requirements and decreasing acceptance in broad segments of the population. [5, 6] Therefore, renewable energy technologies, which can provide power from naturally replenishing resources, such as solar, wind, marine, biomass and geothermal energy, are gaining interest. However, to manage the energy revolution towards climate-neutral power generation, several challenges have to be overcome. Examples are technical issues, such as resource availability and stability of supply, economic barriers, such as energy pricing and costs, and institutional requirements, such as administration and infrastructure. [7] In addition, socio-cultural factors, such as esthetics and general acceptance of new technologies, as well as environmental drawbacks, such as potential air and water pollution or consumption of resources, have to be considered.

Thus, new concepts of power supply such as net zero energy homes, whose annual energy consumption equals their annual energy generation from renewable sources, are applied. [8–11] Moreover, the idea of decentralized electrical power supply based on peer-to-peer networking has attracted considerable public interest as it allows overcoming supply shortage, the main drawback of emerging renewable energy technologies. [12, 13] Therefore, calculations and simulations have been performed as a first step towards realization of a decentralized, renewable power supply system, in which electrical power can be produced locally by private households as well as industry and can be traded with neighbors via a smart grid. [13, 14] Information on energy production and demand can be collected e.g. by a blockchain and an electricity tariff, depending on the present demand, is calculated. [15, 16] In periods of excess power generation, energy storage (e.g. in electrical vehicles) or consumption might be more attractive for the user, whereas in periods of higher demand and higher prices, energy saving will be rewarded. This environmentally friendly approach is given as one possible way to enable efficient, regional use of electrical power, better matching of demand and production as well as to achieve broader acceptance in the population as every user contributes to the network.

Furthermore, new technologies are continuously developed to enable power generation from renewable energy sources in private households. In particular, photovoltaics are considered to be a promising approach to meet future energy needs. [17, 18] To overcome the drawbacks of conventional silicon based solar cells, such as their high weight and inflexibility, new devices such as organic solar cells, consisting of a donor polymer and an acceptor molecule, being mixed to form a bulk-heterojunction (BHJ) structure, are developed. These devices offer potential advantages, such as being lightweight, mechanically flexible and semi-transparent, and have the ability to convert diffuse light into

electrical energy. [19–21] This enables new potential applications in architecture and daily life, which were not possible so far with silicon based devices. Examples are solar cell windows, roofs, trees, art and even clothing. [22–27] Therefore, organic photovoltaics have gained significant interest in industry and research during the last years. [28–34] Current research focuses on identifying new high-efficiency polymers in combination with suitable small molecule acceptors, which allow tuning the energy levels and exploiting the sun spectrum more efficiently. [35–39] To date, record power conversion efficiencies (PCEs) above 18% were reached for spin-coated organic solar cells, which is already above the threshold for commercialization. [40,41] However, for these devices, active areas were about a few square centimeters only. [42–44] To enable real-word use, up-scaling of the thin film deposition process as well as improving the long-term stability are necessary. [45–47] These parameters are illustrated in the triangle of marketability of organic solar cells (Figure 1.2).

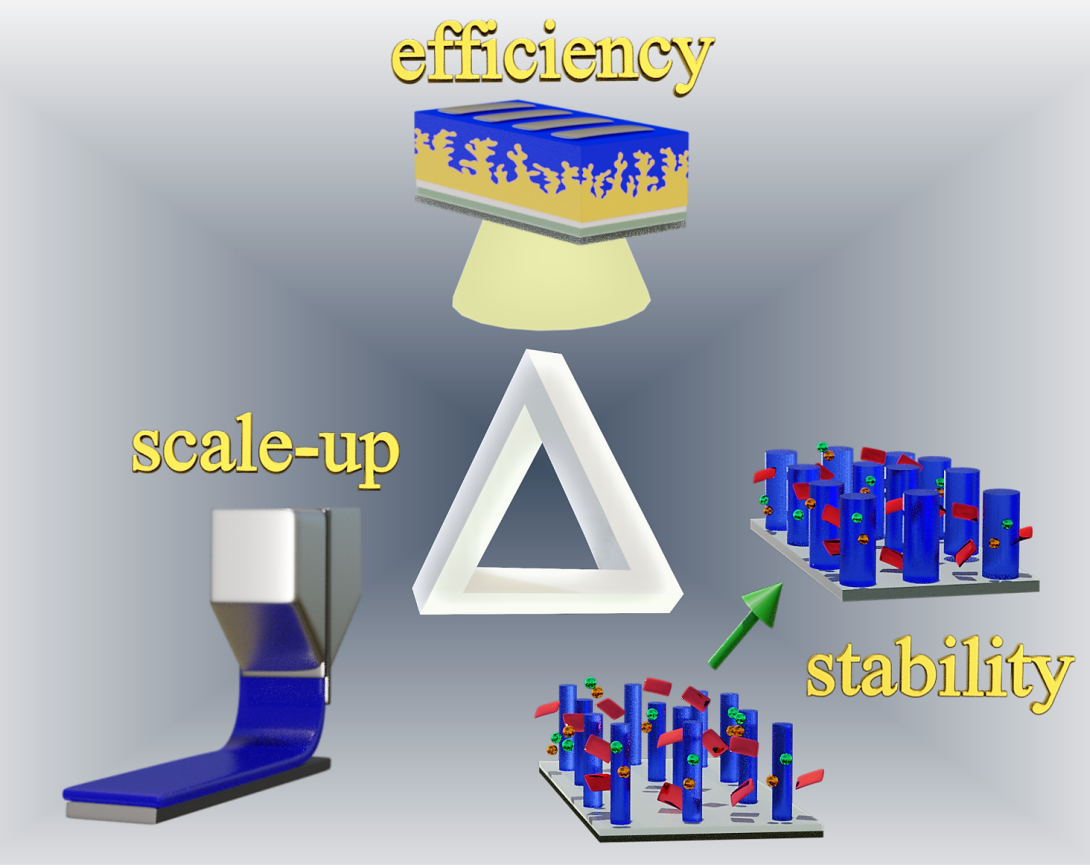

Figure 1.2.: The triangle of marketability describes the main factors which have to be fulfilled on the way to marketability of organic solar cells, namely high efficiency, long-term device stability and scale-up of the thin film deposition. This thesis focuses on studying and improving stability and scale-up.

To overcome the challenge of up-scaling of the thin film deposition, promising techniques, such as meniscus guided slot-die coating, inkjet printing and doctor blading have been developed. [48–54] These printing methods are compatible with roll-to-roll production and are assumed to be a possible way to realize fast and low-cost large-area thin film deposition of the solution-processible organic solar cell materials. [47,51,55] Compared to spin-coating, precursor solutions with lower concentrations are required for printing of active layers, facilitating the use of high-efficiency materials, which often suffer from poor solubility. Unfortunately, fundamentals of spin-coating and printing differ significantly and therefore, knowledge gained from one thin film deposition method, like spin-coating, cannot simply be transferred to the other method, like printing. [51,56] Thus, fundamental understanding of the processes, occuring during printing, is needed. Therefore, the structure evolution during printing and drying of thin films has to be studied and understood in detail in order to optimize the conditions of thin film deposition, influencing the inner morphology and device performance. [29, 57–59] Even though a few *in situ* studies have already been performed on different materials and printing techniques, the deposition process and film formation are not fully understood yet. [57, 60, 61] In addition, structure evolution is not only material-specific but also differs for different thin film deposition techniques. [61–63] Consequently, new high-efficiency polymers and small molecule acceptors have to be studied *in situ* for different processing conditions in order to achieve an optimum morphology and device performance. Furthermore, morphology control can be realized by addition of common solvent additives such as 1,8-diiodooctane (DIO). [35,64] Even though the stability of organic solar cells could be improved successfully by synthesis of new materials [65–67] or development of an inverted device structure [32, 68, 69], the poor long-term stability of most high-efficiency materials still hinders a commercial breakthrough. [70, 71] Thus, understanding the degradation mechanism of printed BHJ photovoltaics is essential to realize fabrication of large-area organic solar cells with outstanding PCE and excellent long-term stability. Chemical degradation of organic solar cells in presence of water or oxygen has been studied for many materials and can be avoided by encapsulation. [71, 72] However, physical degradation with morphological changes in the active layer occurs even in absence of reactive molecules. [73, 74]

In this thesis, the fluorinated low bandgap polymer poly[(2,6-(4,8-bis(5-(2-ethylhexylthio)-4-fluorothiophen-2-yl)-benzo[1,2-b:4,5-b']dithiophene))-*alt*-(5,5-(1',3'-di-2-thienyl- 5',7'-bis-(2-ethylhexyl)benzo[1',2'-c:4',5'-c']dithiophene-4,8-dione)], denoted PBDB-T-SF, and the chlorinated low bandgap polymer poly[(2,6-(4,8-bis(5-(2-ethylhexyl-3-chloro)thiophen-2-yl)-benzo[1,2-b:4,5-b']dithiophene))-*alt*-(5,5-(1',3'-di-2-thienyl-5',7'-bis(2-ethylhexyl)benzo-[1',2'-c:4',5'-c']dithiophene-4,8-dione))], denoted PBDB-T-2Cl, are used as electron donor

materials. In order to fabricate active layers, the respective high-efficiency polymer is mixed with the nonfullerene small molecule acceptor 3,9-bis(2-methylene-((3-(1,1-dicyanomethylene)-6,7-difluoro)-indanone))-5,5,11,11-tetrakis(4-hexylphenyl)-dithieno[2,3-d:2',3'-d']-s-in-daceno[1,2-b:5,6-b']dithiophene, denoted IT-4F, in a 1:1 weight ratio, and printed out of chlorobenzene (CB) using a meniscus guided slot-die coater. Organic solar cells based on PBDB-T-SF:IT-4F can achieve a PCE of 13%, whereas PBDB-T-2Cl:IT-4F based devices can achieve a PCE of 14%. [35, 75] In this thesis, the main challenges in the field of organic photovoltaics are addressed by providing an optimization of solar cell performance, giving insights into the process of meniscus guided slot-die coating and presenting the degradation mechanism of printed organic photovoltaics under illumination.

An overview of physical backgrounds is given in Chapter 2. Experimental methods and sample preparation are described in Chapter 3 and 4, respectively. In Chapter 5, the evolution of morphology and optical properties during *in situ* printing is detailed. The effect of solvent additives on the morphology and device performance is discussed in Chapter 6. In Chapter 7, the degradation mechanism of organic solar cells under illumination is described. A summarizing conclusion and outlook is given in Chapter 8.

2 Theoretical Background

The following chapter introduces the most relevant concepts needed for understanding the topics discussed in this thesis. In Section 2.1, a general description of organic solar cells is provided. Inner morphology and device geometry are described before introducing the working principle and possible loss mechanisms. Moreover, potential degradation pathways are discussed. In Section 2.2, the thin film deposition technique meniscus guided slot-die coating is introduced. Basic principles and parameters are given and wetting of a liquid on a solid surface is illustrated. The range of parameters, enabling a stable coating process, called coating window, is discussed. In Section 2.3, basic concepts of X-ray scattering as well as the advanced scattering techniques grazing incidence small-angle X-ray scattering (GISAXS) and grazing incidence wide-angle X-ray scattering (GIWAXS) are introduced.

2.1. Organic Solar Cells

2.1.1. Architecture

In organic solar cells, the active layer is based on organic semiconductors. [77–79] In order to generate power from sunlight, an electron donor and an electron acceptor are required. [80, 81] Usually, a donor polymer is combined with a small molecule acceptor, even though other approaches, such as all-polymer or ternary solar cells, are fabricated as well. [82–87] In the past, fullerene based acceptors derived from PCBM were predominantly used. [58, 88, 89] However, to date, nonfullerene small molecule acceptors such as IT-4F (Section 4.1) are prefered due to their advantages, such as tunable energy levels, improved stability and higher PCEs. [28,35,90] In order to achieve high efficiencies, these nonfullerene acceptor molecules are combined with low bandgap donor polymers, such as PBDB-T-SF or PBDB-T-2Cl (Section 4.1). The ideal bandgap was found to be about 1.5 eV. [91]

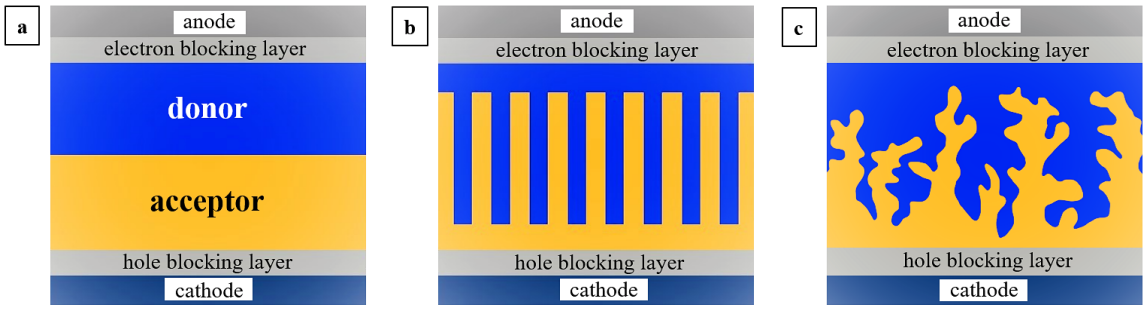

Figure 2.1.: Illustration of a cross section of an inverted organic solar cell with different active layer structures (Figure inspired by a graph from [76]). Electron blocking and hole blocking layers (bright gray) are introduced respectively between active layer and anode (dark gray) or cathode (dark blue) to achieve selective contacts. (a) In a bilayer based solar cell, a thin layer of donor material (blue) is located on top of a thin layer of acceptor (orange). (b) In an interdigitated heterojunction active layer, pillars or lamellae with dimensions comparable to the exciton diffusion length are present. (c) In a BHJ layer, a percolating network of donor and acceptor domains is formed.

The applied photoactive materials have high conjugation lengths (alternating single and double bonds), provoking delocalization of electrons. [76] Thus, electronic excitation of the polymer and generation of an exciton, a Coulomb bound electron-hole pair, is facilitated. The exciton moves to the donor:acceptor interface, where exciton splitting into free charge carriers occurs. The electron is transferred from the donor to the acceptor and electron and hole move towards the respective electrodes (Subsection 2.1.2). A cross section of an organic solar cell with inverted device geometry is shown in Figure 2.1. The active layer is sandwiched between the electrodes and the respective blocking layers, which are introduced to achieve selective contacts for charge extraction. [92] Different active layer morphologies, such as bilayer (Figure 2.1a), interdigitated heterojunction (Figure 2.1b) and BHJ (Figure 2.1 c), can be realized. [76] For a bilayer organic solar cell, a thin layer of donor is placed on top of a thin layer of acceptor material. In this approach, only a small interface area is formed. This is unfavorable for the device performance as a large donor:accepor interface is required to enable efficient exciton splitting. [93] In an interdigitated heterojunction active layer, small pillars or lamellae with a size that fits typical exciton diffusion lengths are created. This active layer morphology is considered to be ideal for organic solar cells as it enables efficient exciton splitting and charge transport. Unfortunately, this approach requires cost-intensive, technically challenging methods such as nano imprint lithography. [94, 95] The desired nanostructure is generated with one material and is then backfilled with the other to fabricate a two-component active layer. Thus, this approach is not suitable for large-scale, low-cost fabrication of organic solar

cells. A BHJ morphology is the most promising approach as a favorable inner structure can be realized by simply mixing the two components prior to thin film deposition. [75, 77] During drying of the thin film, a partial demixing occurs and a percolating, interdigitating network of donor and acceptor domains is formed. [96–98] A BHJ morphology enables efficient exciton generation and charge transport. However, a broad variation of different domain sizes is usually formed in the active layer. Thus, besides formation of favorable domain sizes, which fit typical exciton diffusion lengths, also unfavorable domain sizes evolve. Therefore, controlling the BHJ morphology is indispensable to optimize the device performance of organic solar cells.

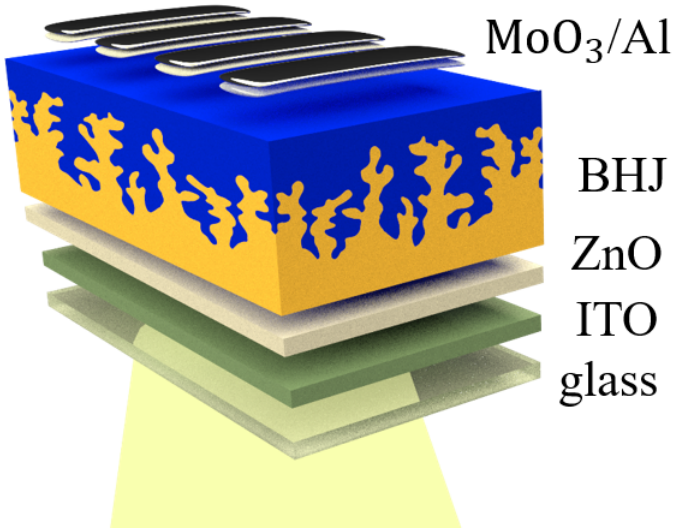

Figure 2.2: Illustration of a typical device stack of an inverted organic solar cell. The ITO coated glass substrate acts as cathode. ZnO is applied to act as hole blocking layer. The BHJ active layer is printed using a meniscus guided slot-die coater. Thin films of MoO_3 and Al are evaporated on top to act as electron blocking layer and anode, respectively.

The device stack of organic solar cells can be classified as conventional or inverted, depending on the orientation of the electrodes. [77] In the conventional geometry, a transparent conductive layer on a transparent substrate is used as anode. Typically, ITO coated glass substrates are used for this purpose. An electron blocking layer such as PEDOT:PSS is applied before coating the BHJ layer on top. A thin film of a material, acting as hole-blocking layer, such as LiF is applied to enable selective charge extraction. A metal such as aluminum is evaporated on top to act as cathode. In contrast, in an inverted device geometry, the ITO coated glass substrate acts as cathode, whereas the metal electrode acts as anode. [99] Thus, also the electron and hole blocking layers have to be inverted. Organic solar cells based on an inverted device geometry can obtain high PCEs and show a higher stability compared to standard geometry devices. [32, 100] Therefore, for all organic solar cells fabricated in the context of this thesis, an inverted geometry was applied. A typical device stack for an inverted organic solar cell is shown in Figure 2.2. A transparent substrate with high conductivity is used as cathode. Due

to the high transparency of the material, sunlight is transmitted through the electrode and can reach the active layer, where the photons are absorbed by the polymer. In this thesis, ITO coated glass substrates were used as cathode and substrate for printing due to their high transparency, good adhesiveness to polymer thin films and compatibility with solution-processing methods such as meniscus guided slot-die coating. However, for roll-to roll production of light-weight and mechanically flexible photovoltaics, transparent foils coated with a conductive layer are more suitable substrates. [19, 101, 102] In inverted organic solar cells, thin oxide films, such as ZnO or TiO_2, are applied as hole blocking layers to improve the electron extraction efficiency. [35, 103] In this thesis, ZnO was deposited via spin-coating. The active layer of an organic solar cell is based on a conjugated donor and a small molecule acceptor, forming a BHJ structure. The morphology can be further tuned by solvent additives as shown in this thesis (Chapter 6). In an ideal case, the thickness of the active layer should be about 100 nm to enable efficient absorption of sunlight on the one hand and a short distance to the electrodes on the other hand. [35] As active materials are solution-processible, the lab-scale method spin-coating as well as up-scalable thin film deposition methods, such as printing and spraying, can be applied. [104, 105] In this thesis, all active layers are slot-die coated and the process of film formation was studied in detail (Chapter 5). Thin films of MoO_3 are evaporated on top of the active layer to act as electron blocking layers and to allow selective charge extraction. In this thesis, thin films based on Al are evaporated on top to act as anode. In order to fabricate fully transparent organic solar cells, transparent top electrodes such as thin graphene single layers, can be applied. [106, 107]

2.1.2. Working Principle and Loss Mechanisms

Working Principle

In Figure 2.3, the energy conversion mechanism [76, 77, 108] in an organic solar cell is illustrated from a kinetic point of view (left) and as a simpified energy diagram (right). The process of energy conversion occurs in five steps. First, a photon is absorbed by the polymer donor, causing the generation of a strongly bound electron-hole pair, called exciton (Figure 2.3I). The generated exciton moves towards the donor:acceptor interface (Figure 2.3II), where exciton dissociation into free charge carriers occurs (Figure 2.3III). The electron is transferred from the donor to the acceptor, whereas the hole remains at the donor polymer. Electron and hole move towards the cathode or anode (Figure 2.3IV), respectively, where the photocurrent is extracted (Figure 2.3V). In the following, the five steps of energy conversion are described in more detail.

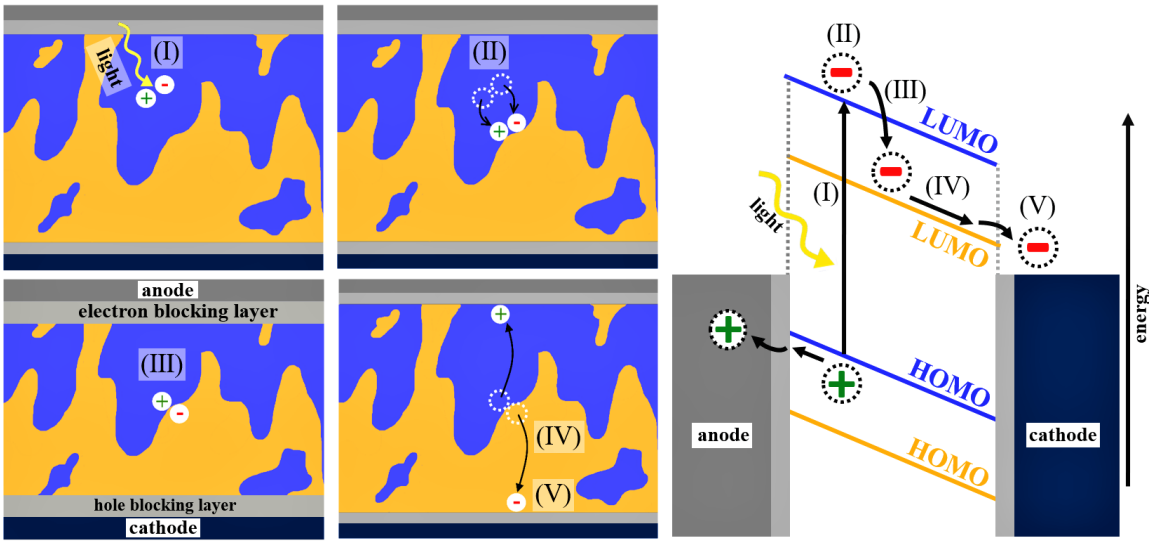

Figure 2.3.: Energy conversion mechanism in an organic solar cell shown from a kinetic point of view (left) and as simplified energy diagram (right): (I) photon absorption and generation of an exciton, (II) exciton diffusion towards the interface, (III) dissociation at the donor (blue):acceptor (orange) interface and separation of the electron–hole pair, (IV) charge carrier transport towards the corresponding electrodes, and (V) extraction of the generated photocurrent at the anode (gray) and the cathode (dark blue). Blocking layers (bright gray) are introduced between electrodes to achieve selective contacts for charge extraction. Reproduced from [K. S. Wienhold, X. Jiang, and P. Müller-Buschbaum, "Organic Solar Cells probed with Advanced Neutron Scattering Techniques," Appl. Phys. Lett., vol. 116, no. 12, p. 120504, **2020**.], with the permission of AIP Publishing.

I. Absorption of Photons and Exciton Generation

The energy conversion in an organic solar cell starts with absorption of a photon by the donor. In order to absorb the incoming light, the energy of the photon has to match or exceed the optical bandgap of the polymer. The optical bandgap is given by the energy gap between the highest occupied molecular orbital (HOMO) and the lowest unoccupied molecular orbital (LUMO). If a photon is absorbed, an electron can be excited from the HOMO to the LUMO and an electron-hole pair is generated in the donor polymer. With increasing conjugation length, the optical bandgap becomes smaller, which is favorable for application in organic solar cells as the sun spectrum can be exploited more efficiently. In addition, a broad absorbance spectrum of the donor as well as a high molar extinction coefficient are beneficial.

II. Diffusion towards the Donor:Acceptor Interface

After exciton generation in the donor polymer, the electron-hole pair diffuses to the donor:acceptor interface. The exciton has to reach the interface within the exciton lifetime before recombination of the electron-hole pair occurs. Therefore, the distance to the donor:acceptor interface has to be smaller than the exciton diffusion length. The exciton diffusion length is the distance, the electron-hole pair can diffuse within its lifetime, and is typically in the range of some tens of nanometers. [109, 110] Therefore, BHJ structures with polymer domain sizes in this range are favorable as exciton diffusion to the interface is facilitated.

III. Exciton Splitting at the Donor:Acceptor Interface

As typical exciton binding energies in organic solar cells are in the range of 0.3–1.0 eV, thermal energy is not sufficient to achieve exciton dissociation. [92, 111] Therefore, efficient exciton splitting can only occur at the donor:acceptor interface, where an electric field and material disorder facilitate exciton splitting. [112] Exciton dissociation has to occur within the exciton lifetime before recombination of electron and hole occurs. The offset between the LUMO levels of the donor and the acceptor will drive the formation of a charge transfer state, where the electron will be transferred to the acceptor molecule, whereas the hole remains at the polymer donor. [113] In the charge transfer state, electron and hole are located within neighboring molecules at the donor:acceptor interface and attract each other by Coulomb forces. With increasing distance, the Coulomb binding energy V of the exciton decreases as described by [114, 115]

$$V = \frac{e^2}{4\pi\varepsilon_\mathrm{o}\varepsilon_\mathrm{r} r}, \tag{2.1}$$

with r being the separation distance between electron and hole, e being the fundamental charge of the electron, ε_o being the permittivity of free space and ε_r being the dielectric constant of the polymer.

In organic solar cells, exciton splitting occurs at the donor:acceptor interface and depends critically on the interface area. [93] Therefore, BHJ structures with small domain sizes and high interface-to-volume ratio have a favorable effect on the device performance. If the distance between the positive and negative charge carriers becomes larger than the Coulomb capture radius, complete charge separation can take place, forming a charge-separated state with free charge carriers.

The Coublomb capture radius r_c is given by [113]

$$r_c = \frac{e^2}{4\pi\varepsilon_o\varepsilon_r k_B T}, \tag{2.2}$$

with k_B being the Boltzmann constant and T being the temperature, at which the Coulomb-binding energy between the electron and the hole equals the thermal energy.

IV. Charge Transport towards the Electrodes

After exciton splitting, the electron diffuses towards the cathode, whereas the hole diffuses towards the anode. To reduce recombination of charge carriers in proximity to the electrodes, blocking layers are introduced between the active layers and the electrodes. [92] An electron blocking layer hinders the electrons to reach the anode, whereas a hole blocking layer impedes hole transport towards the cathode.

V. Extraction of Photocurrent

The generated photocurrent is extracted at the anode and the cathode of the device.

Loss Mechanisms

In order to optimize the solar cell performance, potential loss mechanisms have to be inhibited as far as possible. [76, 92, 113] Loss mechanisms can occur at every step of energy conversion in the organic solar cell. Exciton recombination can occur directly after photon absorption if the distance to the donor:acceptor interface is larger than the exciton diffusion length. Moreover, recombination can also occur after exciton dissociation. In particular, the presence of defects, which usually have a lower charge carrier mobility than the surrounding molecules, can contribute to recombination by slowing down or hindering charge transport. In addition, charge trapping in islands can occur in the presence of very small domains, which often lack a connection to an electrode. Furthermore, when donor domains are connected to the cathode or acceptor domains are connected to the anode, charge carriers reach the wrong electrode and cannot contribute to the photocurrent. This loss mechanism can be avoided by introducing blocking layers, enabling a selective contact. Therefore, in order to improve the solar cell performance, an optimized morphology and a homogeneous active layer without defects has to be achieved. Therefore, the thin film deposition conditions have to be controlled. Thus, the choice of solvent or solvent additive matters as well as the donor:acceptor ratio and the processing temperature. [116–121]

2.1.3. Degradation Pathways

Degradation of organic solar cells can occur via chemical or physical pathways. [71] Chemical degradation takes place when reactive molecules, such as water or oxygen, undergo a chemical reaction with a component of the organic solar cell, such as the active layer or the electrodes. In contrast, an unfavorable change of the BHJ morphology under illumination, occuring in absence of chemical reactions, is referred to as physical degradation.

Chemical Degradation

Chemical degradation can occur in the active layer, the blocking layers and the electrodes of organic photovoltaics. Air humidity as well as oxygen can provoke degradation by undergoing chemical reactions with important components of organic solar cells. Illumination amplifies the degradation of device performance by several pathways. Oxygen and water can diffuse through the outer electrode and reach the active layer. [122, 123] In presence of organic molecules, oxygen can be activated by UV light and form superoxide anions or hydrogen peroxide, which can attack the active material. [71] The undergoing chemical reactions affect the degree of conjugation and therefore, the absorbance as well as the charge transport along the polymer backbone. [124] Moreover, decomposition of nonfullerene small molecule acceptors can be initiated by photocatalytic activity of ZnO under UV illumination. [125] In addition, photochemical formation of carbonyl and carboxylic groups, acting as electron traps, or reversible p-doping of the BHJ with oxygen, provoking the formation of immobilized superoxide anions, can reduce the electron mobility, hinder electron extraction and decrease the photocurrent. [126] Chemical reactions can shift the energy levels of the active materials and therefore, decrease the V_{OC}, which is determined by the energy difference between the donor HOMO and the acceptor LUMO. [127] Besides decomposition of the active layer, also chemical degradation of electrodes has to be considered. In a conventional device geometry, using PEDOT:PSS (Poly(3,4-ethylenedioxythiophene)-poly(styrenesulfonate)) as electron blocking layer, the acidic species PSS can induce etching of the ITO electrode. [128, 129] In addition, PEDOT:PSS is hygroscopic. As the PSS reacts with water, the interface area between the active layer and the electrode will be reduced, causing a reduction of J_{SC} and FF simultaneously. Furthermore, in both inverted and conventional solar cells, diffusion of water through pores of the aluminum electrode can cause metal oxide formation at the interface between active layer and electrode. [122,130] The insulating Al_2O_3 acts as charge blocking layer, hindering charge extraction and thus, decreases the device peformance. Chemical degradation pathways can be reduced significantly by encapsulation of the devices.

Physical Degradation

Illumination of organic solar cells provokes altering of the BHJ morphology and degradation of device performance. The degree of donor-acceptor intermixing has a strong impact on the charge transport and recombination of charge carriers. Thus, a lack of demixing of donor and acceptor provokes recombination losses and a decrease in FF. [76] Structure shrinkage can decrease the J_{SC} by charge trapping in islands. [31, 131, 132] In contrast, structure coarsening can cause a reduction of the interface-to-volume ratio. [74] Therefore, the exciton splitting probability and the extracted J_{SC} decrease. Increasing distances between donor domains provoke a reduction of the active area per unit cell area given by the polymer domain size and the interdomain distances, respectively. [70] Physical degradation, in particular by structure coarsening, increases with rising temperature. For temperatures above the glass transition temperature of the polymer, the clustering of active material and the reduction of J_{SC} can be described by a model based on Ostwald ripening. [121, 133] Ostwald ripening starts with formation of a nucleus, growing by attachment of surrounding molecules or small particles, diffusing towards the nucleus. The driving force for this phenomenon is the reduction of interface energy by formation of larger clusters. This process is accelerated at higher temperatures and is described by the Arrhenius equation [121, 134]:

$$k_{\mathrm{deg}} = A\exp\left(\frac{-E_{\mathrm{a}}}{k_{\mathrm{B}}T}\right), \tag{2.3}$$

with k_{deg} being the degradation constant, A being an experimental constant, E_{a} being the activation energy in [eV], which is usually about 300–350 meV, k_{B} being the Boltzmann constant ($8.62 \cdot 10^{-5}$ eV/K) and T being the temperature in [K].

As physical degradation can occur even in absence of reactive species, such as oxygen or air humidity, this degradation pathway cannot simply be prevented by encapsulation of the devices. In order to reduce unfavorable altering of the BHJ structure, the use of block-copolymers, forming a well-defined and more stable structure as well as cross-linking of the BHJ can be beneficial. [135–137] However, to overcome the drawback of photodegradation under operation, further research has to be carried out to understand the degradation mechanism of organic solar cells, which is also addressed in this thesis (Chapter 7).

2.2. Slot-Die Coating

2.2.1. Basic Principles and Parameters

On the way to commercialization of organic photovoltaics, up-scaling of the thin film deposition process has to be realized to enable an industrial large-scale production. Printing techniques, such as doctor blading, inkjet printing or meniscus guided slot-die coating, are promising techniques to overcome the up-scaling challenge and to allow a large-area, low-cost production of organic solar cells. [48–50] In this thesis, a meniscus guided slot-die coating technique [60], which is compatible with a roll-to-roll production process, is used to print active layers for application in organic solar cells. Basic components and adjustable parameters of a meniscus guided slot-die coater are illustrated in Figure 2.4.

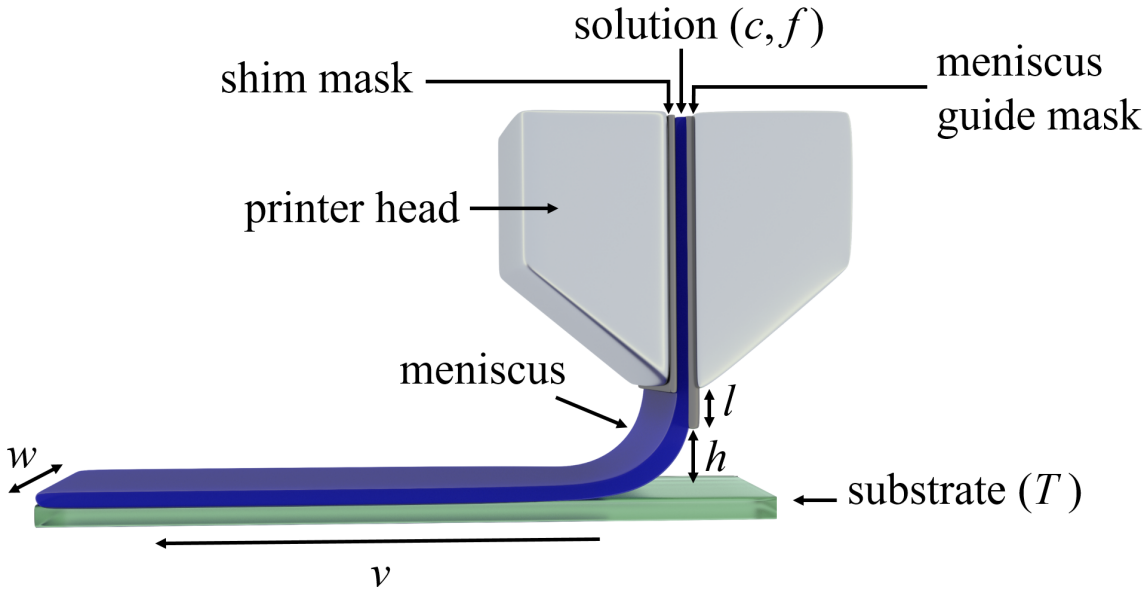

Figure 2.4.: Sketch of a meniscus guided slot-die coater in side view. A solution with concentration c is pumped with a constant flow rate f by a syringe pump and guided through a meniscus guide mask and a shim mask. The geometry of the masks defines coating width w and meniscus guide lenght l. The printer head is mounted at a certain height h above the substrate. The substrate is placed on a sample holder with built-in temperature control unit to enable printing at a defined temperature T. A motor moves the sample holder with a constant velocity v to enable thin film deposition of solution-processible materials.

The active materials are dissolved in an appropriate solvent prior to slot-die coating the active layer. During printing, the solution is pumped by a syringe pump and guided through a meniscus guide mask and a shim mask, which are mounted inside the printer head. The substrate is placed on a sample holder, moving with a constant velocity. To give

a homogeneous film without coating defects, such as ribbing, air entrainment or formation of breaklines, as well as to achieve a final dry film thickness favorable for application in organic solar cells, all parameters have to be optimized. [138, 139]

The adjustable parameters as illustrated in Figure 2.4 are

- c: concentration of the solution
- f: flow rate
- v: printing velocity
- h: height (distance between meniscus guide mask and substrate)
- w: coating width (width of masks)
- T: temperature of the substrate
- l: meniscus guide length.

The influence of the applied slot-die coating parameters on the final dry film thickness d_{dry} is given by [140]

$$d_{\mathrm{dry}} = k\frac{lfcv^{2/3}}{Tw\rho_{\mathrm{dry}}}, \tag{2.4}$$

with k being a proportionality constant, which has to be exerimentally determined for each system and ρ_{dry} being the density of the dry film.

2.2.2. Wetting Behavior and Coating Window

The homogeneity of the final dry film depends not only on the printing parameters but also on the wetting behavior of the solution on the substrate (Figure 2.5).

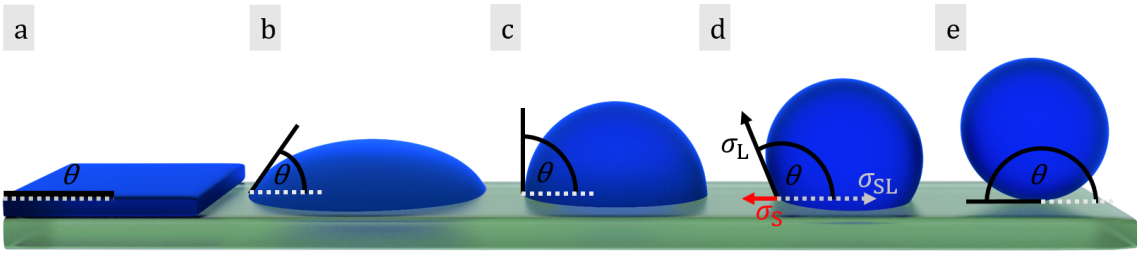

Figure 2.5.: Sketch of a sessile droplet on a solid surface. (a) spreading ($\Theta = 0°$), (b) wetting ($0° < \Theta < 90°$), (c) incomplete wetting ($\Theta = 90°$), (d) dewetting ($90° < \Theta < 180°$) as well as (e) complete dewetting ($\Theta = 180°$).

For defect-free printing of homogeneous thin films, attractive interactions between solution and substrate are favorable to prevent the formation of coating or drying defects. Wetting or dewetting of a solution on a substrate (Figure 2.5) is determined by the free surface energy and the interfacial free energies, which determine the inherent contact angle. The contact angle Θ of a sessile droplet on a solid surface is determined by the surface tension σ_S of the solid component, the surface tension σ_L of the liquid component and the interfacial tension σ_{SL} between the solid and the liquid (Figure 2.5) as described by Young's equation [141, 142]:

$$\cos\Theta = \frac{\sigma_S - \sigma_{SL}}{\sigma_L}. \tag{2.5}$$

For a contact angle of 0°, spreading occurs (Figure 2.5a). A contact angle of $< 90°$ implies wetting (Figure 2.5b). Above a contact angle of 90° (Figure 2.5c), dewetting occurs (Figure 2.5d), whereas for a contact angle of 180°, no wetting occurs (Figure 2.5e).

For meniscus guided slot-die coating, adhesive wetting of polymer solution on the substrate is required to ensure complete and homogeneous covering of the substrate. However, complete spreading of the solution on the substrate can provoke spilling the liquid over the edges of the substrate. The contact angle depends on the hydrophilicity or hydrophobicity of the substrate surface, which can be tuned by applying a suitable cleaning procedure. [143] In order to print homogeneous thin films, a stable coating process is necessary as adhesive, cohesive and surface tension forces have to oppose gravitation to stabilize the meniscus. Therefore, suitable parameters have to be applied.

The range of printing parameters, allowing defect-free printing, is called coating window. [144] For industrial applications, a high printing velocity is favorable as it allows fabricating large-area thin films in short time. Unfortunately, the film thickness is correlated to the printing velocity and cannot be chosen arbitrarily as inertial forces and elastic forces influence the coating process. Therefore, in order to achieve a specific film thickness and avoid wetting failure, the velocity has to be adjusted accordingly. To determine the operation limits of slot-die coating, which are important in order to optimize industrial thin film fabrication, dimensionless numbers have to be considered. To describe the process of slot-die coating, the Capillary number Ca, representing the ratio of viscous forces of the solution to surface tension forces, and the Reynolds number Re, representing the ratio of inertial forces of the coating solution, effusing from the slot, to viscous drag forces, are most important. [145]

The Capillary number is defined as

$$Ca \equiv \frac{\eta v}{\sigma}, \tag{2.6}$$

with η being the dynamic viscosity of the coating solution, v being the printing velocity and σ being the surface tension of the coating solution.

The Reynolds number is defined as

$$Re \equiv \frac{\rho v h}{\eta}, \tag{2.7}$$

with ρ being the density of the solution, v being the printing velocity, h being the height of the meniscus guide mask and η being the dynamic viscosity of the solution.

Depending on the Capillary or Reynolds number, which are proportional to the printing velocity, three different regions of minimum wet film thickness exist (Figure 2.6 a,b). [146] The dimensionless mininum wet film thickness d_{dl} is defined as

$$d_{\mathrm{dl}} \equiv \frac{d_{\mathrm{min,wet}}}{h}, \tag{2.8}$$

with $d_{\mathrm{min,wet}}$ being the minimum wet film thickness for stable coating and defect-free printing for a specific coating velocity.

In region I, the minimum wet film thickness increases with increasing Re or Ca. [144] In this region, surface tension forces are significant and the minimum wet film thickness increases with increasing printing velocity. In region II, the minimum wet film thickness is independent of Re or Ca as viscous forces dominate. Above a critical Reynolds number, which was found to be about 20 [144, 146], the minimum wet thickness decreases with increasing Re or Ca. In region III inertial forces dominate, which stabilize the coating bead. Therefore, the minimum wet film thickness decreases with increasing printing velocity. Printing parameters, which yield a film thickness above the minimum wet film thickness, enable a defect-free slot-die coating (Figure 2.6c, green area). In contrast, printing parameters, which would yield a wet film thickness smaller than the minimum wet film thickness, will provoke wetting failure and formation of defects (Figure 2.6c, red area). [144] In Figure 2.6d–f, the dependency of the minimum wet film thickness on the printing velocity and flow rate is shown for the surface tension, viscous and inertial region, respectively. In Figure 2.6g–i, the coating window, allowing defect-free printing, is illustrated for region I, II and III, respectively. The lower boundary of the coating window

(bright green line) gives the minimum wet film thickness or lower flow limit. The upper boundary (dark green line) corresponds to the maximum wet film thickness, allowing defect-free printing. However, for industrial application, the miminum wet film thickness or lower flow limit is much more important as it determines the productivity of the coating process. Above a critical printing velocity (red line), wetting failure occurs independently from the flow rate. In this thesis, the coating window was determined experimentally before thin film deposition. For all thin films printed in the context of this thesis, optimized parameters, enabling stable processing, were applied (Section 4.3).

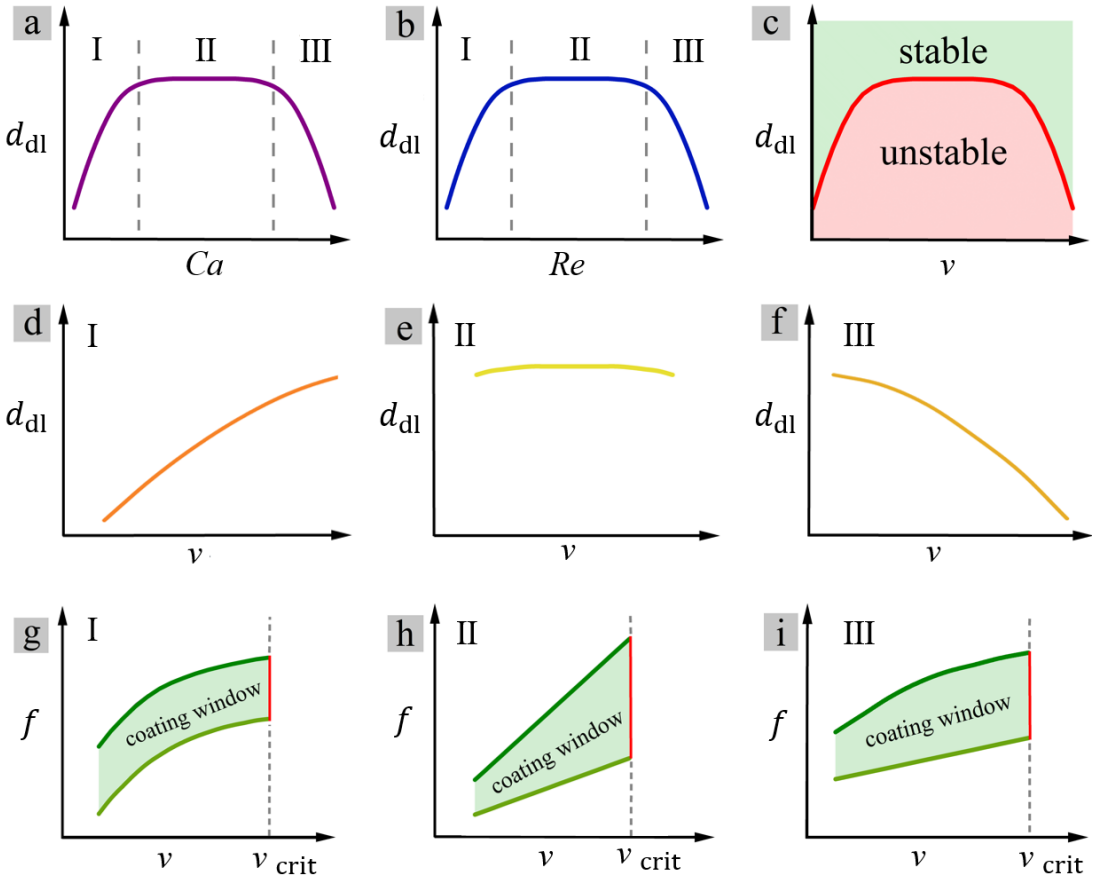

Figure 2.6.: Plots illustrating three regimes of minimum wet thickness and the coating windows for different dimensionless numbers and printing velocities (Image inspired by graphs from [144, 146]). Dimensionless minimum wet thickness versus (a) Capillary and (b) Reynolds number is given. Different regimes of minimum wet thickness are labeled with I–III. (c) The range of parameters, provoking stable (green area) or unstable processing (red area), is shown. Dimensionless minimum wet thickness versus printing velocity is shown for (d) regime I, (e) regime II and (f) regime III. The dependency of the coating window (green area) on the flow rate and printing velocity is shown for (g) regime I, (h) regime II and (i) regime III. Above a critical printing velocity (red line), stable processing is no longer possible.

2.3. X-ray Scattering

2.3.1. Basic Concepts

X-ray scattering techniques are based on the interaction of an electromagnetic wave with electrons in the sample under investigation. The electric field vector $\vec{E}(\vec{r})$ as a function of the position vector $\vec{r}$ with $r = (x, y, z)$ is given by [147]

$$\vec{E}(\vec{r}) = \vec{E}_0 \exp(\mathrm{i}\vec{k_\mathrm{i}} \cdot \vec{r}), \tag{2.9}$$

with $\vec{E}_0$ being the polarization dependent amplitude, $\vec{k_\mathrm{i}}$ being the wave vector and $k = \left|\vec{k_\mathrm{i}}\right| = \frac{2\pi}{\lambda}$ being the modulus.

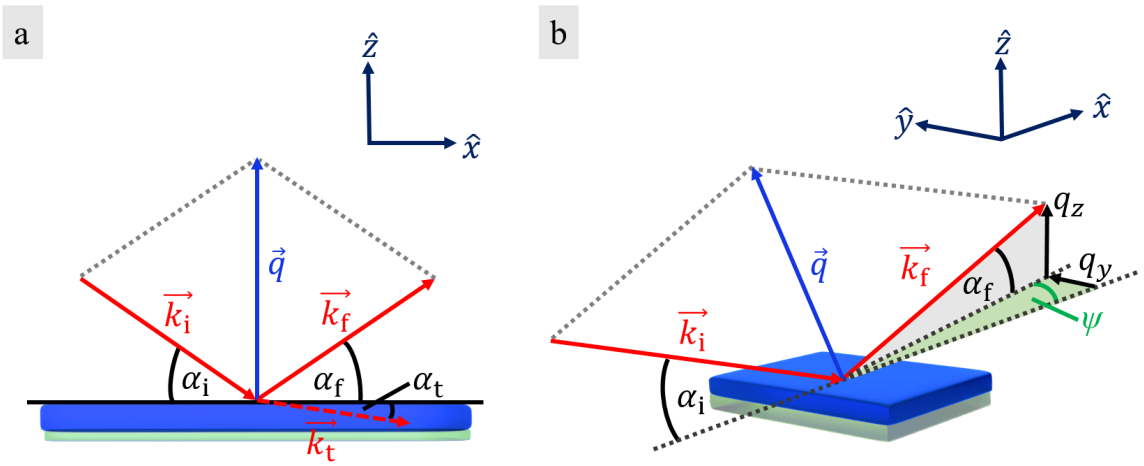

Figure 2.7.: Illustration of different scattering geometries. An incoming wave is reflected at the sample surface. (a) In case of specular in plane reflection, the final angle of the reflected wave in respect to the sample surface equals the incident angle, whereas for (b) diffuse out of plane scattering the final angle differs from the incident angle.

In Figure 2.7, basic scattering geometries are illustrated. The incoming beam with a wave vektor $\vec{k_\mathrm{i}}$ impinges onto the sample under an angle α_i. The beam enters the sample or is reflected on the surface. The final, reflected beam can be described by the wave vector $\vec{k_\mathrm{f}}$.

The exit angle is referred to as α_f. The scattering vector $\vec{q}$ gives the difference between the incident wave vector $\vec{k_\mathrm{i}}$ and the scattered wave vector $\vec{k_\mathrm{f}}$ as expressed by [148]

$$\vec{q} = \vec{k_\mathrm{f}} - \vec{k_\mathrm{i}}. \tag{2.10}$$

In case of specular reflection (Figure 2.7a), the scattering event occurs within a two-dimensional plane (xz-plane) and the incidence angle equals the exit angle ($\alpha_\mathrm{i} = \alpha_\mathrm{f}$). In contrast, for diffuse scattering (Figure 2.7b), scattering occurs out of plane with a non-neglegible momentum transfer in y direction under the angle Ψ. For diffuse scattering geometry, the final angle differs from the incidence angle ($\alpha_\mathrm{i} \neq \alpha_\mathrm{f}$). For elastic scattering, which is assumed for all scattering experiments performed in the context of this thesis, the energy is conserved during the scattering event and $\left|\vec{k_\mathrm{f}}\right| = \left|\vec{k_\mathrm{i}}\right| = k$.

The propagation of an electromagnetic wave through a medium is described by the Helmholtz equation [147]

$$\Delta\vec{E}(\vec{r}) + k^2\tilde{n}^2(\vec{r})\vec{E}(\vec{r}) = 0, \tag{2.11}$$

with $\tilde{n}^2(\vec{r})$ being the position dependent refractive index.

The complex refractive index can be described by a dispersion $\delta(\vec{r})$ and an absorption $\beta(\vec{r})$ component and is given by [147]

$$\tilde{n}(\vec{r}) = 1 - \delta(\vec{r}) + \mathrm{i}\beta(\vec{r}). \tag{2.12}$$

The dispersion $\delta(\vec{r})$ can be expressed by [147]

$$\delta(\vec{r}) = \frac{\lambda^2}{2\pi} r_\mathrm{e} \rho_e(\vec{r}) \sum_{j=1}^{N} \frac{f_j^0 + f_j'(E)}{Z}, \tag{2.13}$$

and the absorption component $\beta(\vec{r})$ is defined as [147]

$$\beta(\vec{r}) = \frac{\lambda^2}{2\pi} r_\mathrm{e} \rho_e(\vec{r}) \sum_{j=1}^{N} \frac{f_j''(E)}{Z}. \tag{2.14}$$

The classical electron radius

$$r_\mathrm{e} = \frac{e^2}{4\pi\epsilon_0 m_\mathrm{e} c_0^2} \tag{2.15}$$

is referred to as the Thompson scattering length with e being the elementary charge of an electron, ϵ_0 being the permittivity of free space, m_e being the mass of the electron and c_0 being the speed of light in vacuum. The term $\rho_\mathrm{e}(\vec{r})$ is referred to as the electron density as a function of spatial coordinates (x, y, z). Furthermore, the term $Z = \sum_{j=1}^{N} Z_j$ gives the total number of electrons with Z_j denoting the number of electrons per species j.

The atomic form factor f_j gives the forced oscillator strength of the electrons of the respective atom and is given by

$$f_j = f_j^0 + f_j'(E) + f_j''(E), \tag{2.16}$$

with $f_j'(E)$ and $f_j''(E)$ being dispersion and absorption corrections for the respective radiation energy E. [147]

For small incidence and exit angles, $\vec{q}$ is small and f_j^0 can be approximated to be $f_j^0 \approx Z_j$. For $f_j'(E) \ll f_j^0$, the dispersion $\delta(\vec{r})$ simplifies to [147, 149]

$$\delta(\vec{r}) = \frac{\lambda^2}{2\pi}\rho_\mathrm{e}(\vec{r}). \tag{2.17}$$

The absorption $\beta(\vec{r})$ can be expressed by

$$\beta(\vec{r}) = \frac{\lambda}{4\pi}\mu(\vec{r}), \tag{2.18}$$

with $\mu(\vec{r})$ being the material-specific, linear absorption coefficient.

Thus, in combination with the assumption of a homogeneous medium and absence of absorption edges, the complex refractive index $\tilde{n}$ can be expressed in a position independent form as given by [147, 149]

$$\tilde{n} = n + \mathrm{i}\beta = 1 - \frac{\lambda^2}{2\pi}r_\mathrm{e}\rho_\mathrm{e} + \mathrm{i}\frac{\lambda}{4\pi}\mu, \tag{2.19}$$

with n being the real part of the complex refractive index given by $n = \mathrm{Re}(\tilde{n}) = \frac{c_0}{c_\mathrm{M}}$ with c_M being the velocity of light in the medium and $\beta = \mathrm{Im}(\tilde{n})$ being the absorption coefficient and the imaginary part of the refractive index. Furthermore, ρ_e is the electron density and μ is the absorption coefficient.

If two materials can be distinguished by scattering techniques depends on the difference in refractive indices of the materials under investigation. The scattering contrast $\left|\Delta\right|^2$ can be expressed by [150]

$$\left|\Delta\right|^2 = \delta^2 + \beta^2. \tag{2.20}$$

For an uniform electron density, the scattering length density (SLD) is given by [151]

$$\mathrm{SLD} = \frac{n_\mathrm{e}\rho_\mathrm{e}N_\mathrm{A}r_\mathrm{e}}{M_\mathrm{w}}, \tag{2.21}$$

with n_e being the number of electrons in a molecule, ρ_M being the mass density, N_A the Avogadro constant and M_w the molar mass.

At incidence angles below the critical angle ($\alpha_\mathrm{i} < \alpha_\mathrm{c}$), total reflecion occurs and only surface related information is obtained. In order to investigate the inner structure, an incidence angle above the critical angle has to be applied. Yoneda discovered a significantly enhanced scattering intensity at the critical angle, originating from a maximum of the Fresnel coefficients. [151, 152] At the scattering intensity maxima, which is referred to as the Yoneda region, material sensitive information can be obtained as the critical angle is a material-specific property. For hard X-rays ($E > 5$ keV), the refractive index is smaller than unity and the X-ray beam is reflected at the interface between the medium of higher density (air) and the medium of lower density (investigated sample). For an incident angle which equals the critical angle of the medium ($\alpha_\mathrm{i} = \alpha_\mathrm{c}$), the transmitted wave propagates along the sample horizon ($\alpha_\mathrm{t} = 0$) and total external reflection is observed. The reflection is described by Snell's law given by [149]

$$\cos(\alpha_\mathrm{t}) = \frac{n_0}{n}\cos(\alpha_\mathrm{i}), \tag{2.22}$$

with α_i being measured in respect to the interface, n being the refrective index of the medium, n_0 being the refrective index of the surrounding atmosphere and α_t being the angle of the transmitted wave with respect to the interface.

For $\alpha_\mathrm{i} = \alpha_\mathrm{c}$, $\alpha_\mathrm{t} = 0$ and $n_0 = 1$ for air, the equation can be written as

$$\cos(\alpha_\mathrm{c}) = n = 1 - \frac{\lambda^2}{2\pi}r_\mathrm{e}\rho_\mathrm{e} = 1 - \frac{\lambda^2}{2\pi}\mathrm{SLD}. \tag{2.23}$$

Applying the small angle approximation according to the Taylor series ($\cos(\alpha_\mathrm{c}) = 1 - \frac{\alpha_\mathrm{c}^2}{2}$), the equation can be resolved to [147, 149]

$$\alpha_\mathrm{c} = \lambda\sqrt{\frac{\mathrm{SLD}}{\pi}}. \tag{2.24}$$

2.3.2. Grazing Incidence Small-Angle X-ray Scattering

Small angle X-ray scattering experiments are performed in grazing incidence geometry to investigate amorphous structures in the BHJ layer of organic solar cells. In this thesis, incidence angles above the critical angle of the material ($\alpha_\mathrm{i} > \alpha_\mathrm{c}$) are applied, which allows probing the full film thickness. Grazing incidence geometry ($\alpha_\mathrm{i} < 1°$) enables to investigate a larger film volume. According to Figure 2.7, the scattering vector $\vec{q} = \vec{k_\mathrm{f}} - \vec{k_\mathrm{i}}$ can be described as [151, 153]

$$\vec{q} = \frac{2\pi}{\lambda} \begin{pmatrix} \cos(\alpha_\mathrm{f})\cos(\Psi) - \cos(\alpha_\mathrm{i}) \\ \cos(\alpha_\mathrm{f})\sin(\Psi) \\ \sin(\alpha_\mathrm{i}) + \sin(\alpha_\mathrm{f}) \end{pmatrix}. \tag{2.25}$$

In scattering experiments in grazing incidence geometry, additional reflection events can occur at sample or substrate interfaces. To take these influences into account, the Born approximation is extended with first-order corrections. [151, 154] In the distorted wave Born approximation (DWBA), the incoming wave is approximated as a combination of a direct wave (Figure 2.8a) and a reflected one (Figure 2.8b). In addition, the outgoing wave is assumed to be a superposition of a directly scattered wave (Figure 2.8a) and a scattered wave, which is subsequently reflected at an interface (Figure 2.8c). Also a combination of these events with reflection at an interface, scattering at the object and another subsequent reflection is considered in the DWBA (Figure 2.8d). The probability for a scattering event to occur, and therefore, the differential cross section $\frac{\mathrm{d}\sigma}{\mathrm{d}\Omega}$ of diffuse scattering, is given by [148, 155]

$$\frac{\mathrm{d}\sigma}{\mathrm{d}\Omega} = \frac{A\pi^2}{\lambda^4}(1-n^2)^2 \left|T_\mathrm{i}\right|^2 \left|T_\mathrm{f}\right|^2 P(\vec{q}), \tag{2.26}$$

with σ being the cross section of all events, Ω being the solid angle and A being the illuminated area. T_i and T_f are the Fresnel transmission coefficients for the incident and final beam, respectively, and $P(\vec{q})$ is the scattering factor, containing information on the lateral film structure.

Therefore, scattering intensity depends strongly on the Fresnel transmitivity, which has its maximum at the critical angle of the material. High scattering intensity is observed when the beam exits under an angle, which equals the critical angle of the medium under investigation. As the size of real scattering objects varies around a mean value, several approximations are necessary. For polydispers domains, an effective average form factor has to be introduced by applying the local monodisperse approximation (LMA, Figure 2.9a) or the decoupling approximation (DA, Figure 2.9b). [156] In the LMA, monodisperse domains

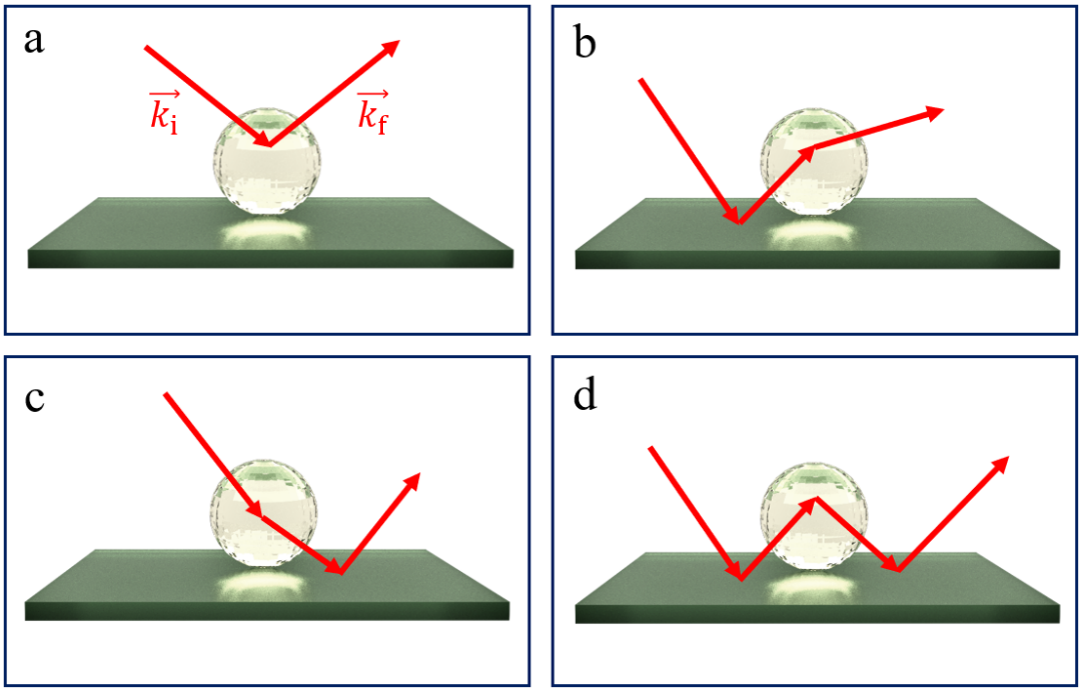

Figure 2.8.: Simplified graphical representation of scattering and reflection events taken into account in the DWBA, a first-order pertubation theory (Image inspired by a graph from [154]). The incoming beam is (a) scattered directly at the scattering object or (b) reflected at an interface before being scattered. (c) The outgoing beam can be scattered before being reflected. These scattering and reflection events can occur subsequently with (d) the beam being reflected, scattered and again reflected.

are assumed. Thus, kind and location of all scattering centers are strongly correlated. In contrast, size and position of scattering objects are not correlated in the DA. In this thesis, a model based on the LMA is applied to describe GISAXS data (Figure 2.9c). Structures are assumed to be standing cylinders with three different structure sizes, co-existing in the thin film. Furthermore, structures of a similar size form locally nearly monodisperse domains. However, on a mesoscopic scale, different structure sizes can be present, but it is assumed that objects with different form and structure factors do not interact with each other. The effective interface approximation (EIA) allows further simplification to model scattering data. [151] According to the EIA, scattering objects are assumed to have only one specific surface. Thus, only lateral interactions are considered and radius and height of the scattering objects can be decoupled. In polymer physics, GISAXS data are usually described with a model based on a combination of the DWBA, the LMA and the EIA. [31, 70, 97]

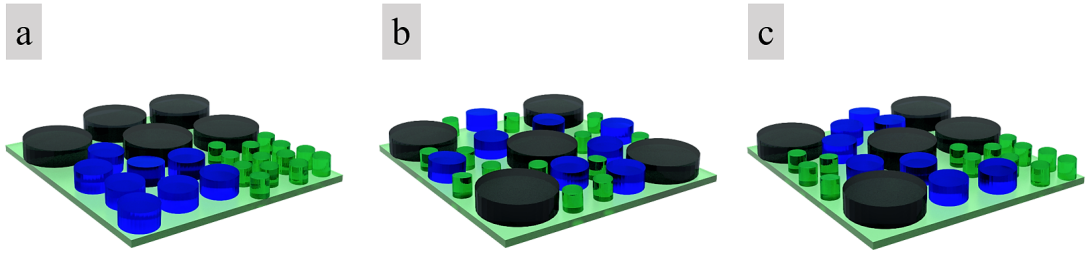

Figure 2.9.: Illustration of common approximation models for scattering factors. Scattering centers are represented by standing cylinders. Small (green), medium (blue) and large (black) structures are assumed to co-exist in the medium. (a) In the LMA, size and position of scattering objects are correlated and monodisperse domains are spatially separated. (b) In the DA, size and location of scattering objects are independent from each other. (c) In this thesis, a model based on the LMA with nearly locally monodisperse domains, which change on a mesoscopic scale, is assumed.

Data analysis can occur via modeling the complete GISAXS scattering pattern using specific software or by simply modeling a horizontal line cut performed at the critical angle of the material. [31, 157, 158] The full scattering function is represented by an incoherent superpositon of individual scattering events of different types of scattering objects j, which can be treated individually. The diffuse scattering factor $P(\vec{q})$ according to the DWBA and the LMA is approximated by [155]

$$P(\vec{q}) \propto NF(\vec{q})S(\vec{q}), \tag{2.27}$$

with N being the number density of scattering objects. The form factor $F(\vec{q})$ gives the Fourier transform of the electron density distribution. The structure factor $S(\vec{q})$ refers to the center-to-center distance of two neighboring structures of equal size. [159]

Scattering centers can be described with geometrical shapes, such as cylinders, spheres, ellipsoids or prisms. [158, 160] In this thesis, a cylindrical shape is assumed, which is a common approach in to model polymer thin films. [31, 70, 97] For a cylindrical scattering object with volume $V = \pi R^2 H$, with R being the radius and H being the height, the form factor can be expressed by [151, 155]

$$F_{\text{cylinder}}(q, R, H) = 2\pi R^2 H \frac{J_1(q_r R)}{q_r R} \sin\left(\frac{q_z H}{2}\right) \exp\left(\frac{-iq_z H}{2}\right), \tag{2.28}$$

with $q_r = \sqrt{q_x^2 + q_y^2}$ being the lateral component. $J_1(q_r R)$ is a Bessel function of first order, describing intensity modulations in q_y direction. [151] For well-defined object radii, these

modulations can be very pronounced. In contrast, for samples with high polydiversity, these modulations are smeared out.

According to the EIA, contributions from vertical scattering intensity can be neglected and the equation simplifies to

$$\left|F(q_y, q_z \approx 0)\right|^2 \approx \left(R\frac{J_1(q_y, R)}{q_y}\right)^2. \tag{2.29}$$

For a one-dimensional paracrystalline arrangement of scattering objects with Gaussian distributed average interdomain distance, the structure factor according to Hosemann is given by [156, 161, 162]

$$S(\vec{q}) = \frac{1-\Phi(\vec{q})^2}{1+\Phi(\vec{q})^2 - 2\Phi(\vec{q})\cos(\left|q\right| D)}, \tag{2.30}$$

with $\Phi(\vec{q}) = \exp(\pi\sigma^2\left|\vec{q}\right|^2)$. D refers to the average interdomain distance with standard deviation σ.

Assuming a cut at constant q_z, the equation simplifies to

$$S(q_y, q_z \approx 0) = \frac{1-\exp(\pi\sigma^2 q_y^2)^2}{1+\exp(\pi\sigma^2 q_y^2)^2 - 2\exp(\pi\sigma^2 q_y^2)\cos(q_y D)}. \tag{2.31}$$

2.3.3. Grazing Incidence Wide-Angle X-ray Scattering

In this thesis, grazing incidence wide-angle X-ray scattering (GIWAXS) experiments are performed to probe crystalline structures in the active layer. [127, 148] Information on the subnanometer scale is revealed and scattering is dominated by periodicity of the lattice. In crystals, single atoms, ions or molecules act as scattering centers and form a periodic structure, which can be probed with GIWAXS. The incoming wave with wave vector k_i impinges onto the sample under an angle $\theta = \alpha_\mathrm{i} = \alpha_\mathrm{f}$. For elastic in plane scattering, the wave vector k_f of the reflected wave is reflected under an angle, which is equal to the incident angle. The observed scattering intensity originates from constructive interference of scattered waves. In a crystal, waves are scattered from lattice planes separated by the distance d_{hkl} with hkl being the Miller indices. [163] In Figure 2.10, scattering in real space according to the Bragg condition is illustrated.

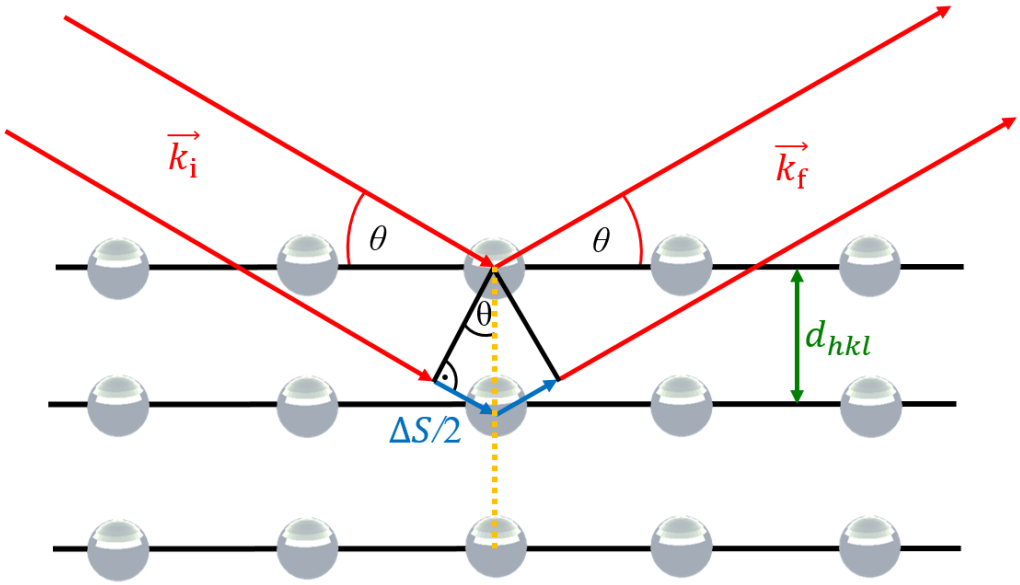

Figure 2.10.: Illustration of the Bragg condition. The incoming wave (red) is reflected at a scattering center (gray sphere). The reflected wave leaves the sample under an angle θ, which equals the incident angle. Constructive interference occurs when the difference of path length $\Delta S/2$ (bright blue) of two waves is equal to the distance d_{hkl} (green) between the lattice planes.

When scattered waves remain in phase, constructive interference occurs. Therefore, the difference in path lengths of two waves ΔS (Figure 2.10, blue) has to be equal to the wavelength or an integer multiple. ΔS can be calculated by the simple trigonometric function

$$\frac{\Delta S/2}{d_{hkl}} = \sin(\theta). \tag{2.32}$$

Constructive interference occurs when the Bragg condition is fulfilled. The Bragg equation is given by [163]

$$2d_{hkl}\sin(\theta) = n\lambda, \tag{2.33}$$

with n being an integer multiple and λ being the wavelength of the incoming X-ray beam.

The Bragg condition can be extended to the Laue condition in three dimensions. According to Laue, constructive interference occurs when the change of wave vector $\Delta\vec{k}$ is equal to a reciprocal lattice vector $\vec{Q}$ as given by [164]

$$\Delta\vec{k} = \vec{k}_f - \vec{k}_i = \vec{q} = \vec{Q}, \tag{2.34}$$

and

$$\vec{Q} = h\vec{a_1} + k\vec{a_2} + l\vec{a_3}, \tag{2.35}$$

with $\vec{a_1}$, $\vec{a_2}$ and $\vec{a_3}$ being the reciprocal lattice vectors and h, k, l being the Miller Indices. The reciprocal lattice is the Fourier transform of the real space crystal lattice and refers to the complete set of wave vectors that contribute to scattering. A scattering signal can be observed when the Laue condition is fulfilled. This can be illustrated by the Ewald construction (Figure 2.11), connecting real space and reciprocal space. [151, 165]

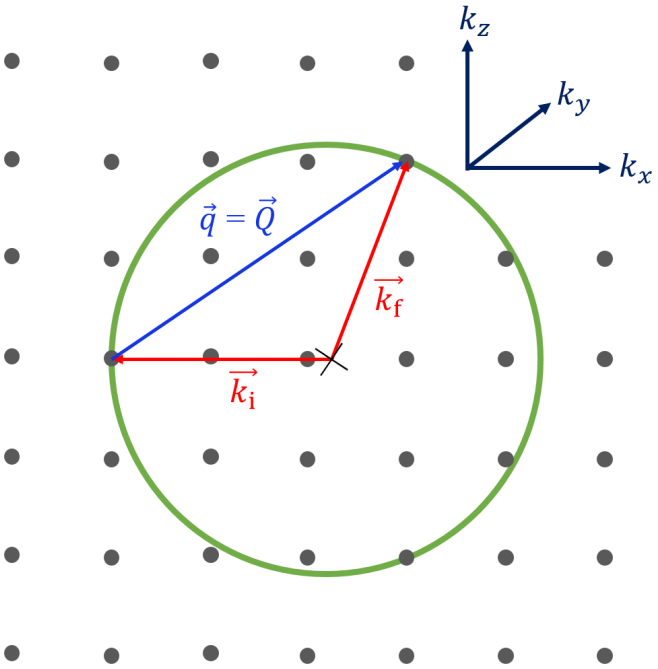

Figure 2.11: Illustration of the Ewald sphere. Constructive interference occurs when the difference between scattered wave vector and incident wave vector equals a reciprocal lattice vector (blue). The Laue condition is fulfilled when a reciprocal lattice point (gray circles) touches the Ewald sphere (green).

An incoming beam is reflected at a scattering center in real space (Figure 2.11, black cross), which refers to as the center of a sphere with radius $\left|k_i\right|$ (Figure 2.11 green circle). The entirety of every possible pair of $\vec{k_i}$ and $\vec{k_f}$ describes a sphere, the Ewald sphere. Diffraction peaks can be observed when a reciprocal lattice point (Figure 2.11 gray circles) touches the sphere. The Bragg peaks observed with GIWAXS allow estimating lattice spacing, crystal size, orientation as well as overall crystallinity, which is proportional to the scattering intensity.

The crystal orientation can be estimated by the shape and orientation of the scattering signal (Figure 2.12). [148, 153] In crystals, segments of polymer chains are folded together to align parallely (Figure 2.12 inset, polymer chains illustrated with blue color). However,

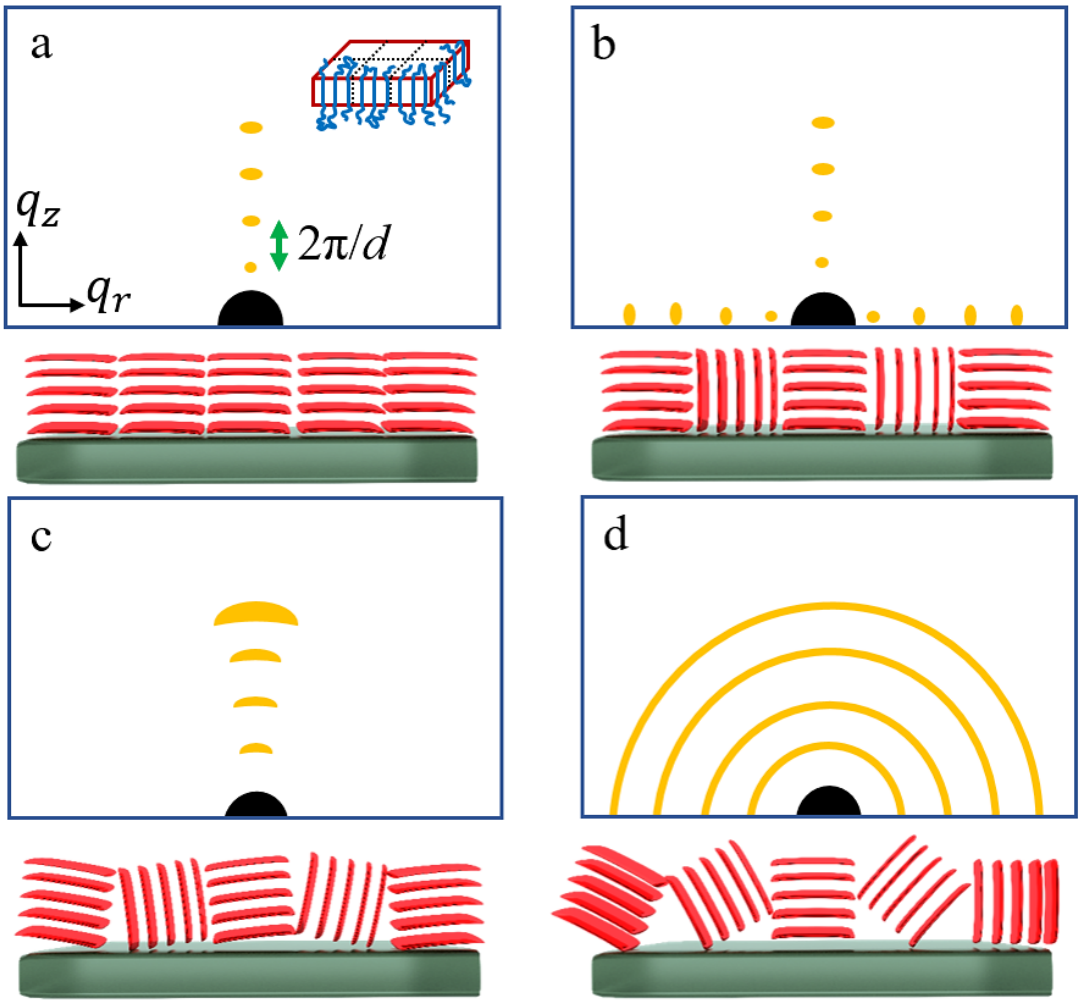

Figure 2.12.: Illustration of different lamellae orientations in a thin film and the corresponding GIWAXS scattering signal (Figure inspired by a graph from [148]). (a) For well ordered, vertically stacked lamellae, Bragg peaks along the q_z axis are observed. (b) For lamellae with vertical and horizontal orientation, Bragg peaks appear along the q_z and q_r axis. (c) For lamellae stacking with rotational disorder, broadening of Bragg peaks is observed. (d) For full rotational disorder, scattering rings are observed.

in semi-crystalline polymers, such as common donor materials for organic solar cells, the polymer does not fully crystallize. Thus, segments of polymer chains are not built into the crystal and remain amorphous. Crystals can arrange and form superior structures, such as lamellae (Figure 2.12 inset, red cuboid) or spherulites. [166] In Figure 2.12, different lamellae orientations and the corresponding GIWAXS scattering pattern are illustrated. For face-on orientation with lamellae being vertically stacked and well ordered without any rotational disorder, the observed Bragg peaks are nearly one-dimensional and appear along

the q_z axis (Figure 2.12a). If both face-on and edge-on orientated lamellae are present, the scattering signal will be observed along the q_z and the q_r axis (Figure 2.12b). Rotational disorder broadens the Bragg peaks (Figure 2.12c). In case of full rotational disorder, fully developed scattering rings are observed (Figure 2.12d). In face-on oriented lamellae (Figure 2.12a, red), the polymer backbone is oriented edge-on towards the substrate and thus, $\pi-\pi$ stacking occurs parallel to the substrate, whereas the side chains are oriented perpendicular to the substrate. In contrast, edge-on oriented stacking of lamellae refers to face-on stacking of polymer backbone. Therefore, the $\pi-\pi$ stacking occurs perpendicular to the substrate with the side chains being oriented parallel to the substrate. Due to anisotropic conductivity of the polymer, which is high along the backbone and in direction of $\pi-\pi$ stacking, face-on orientation of crystals is desired for application in organic solar cells as the charge transport towards the electrodes is facilitated. [148]

The lattice spacing can be estimated by re-writing the Bragg equation to

$$d_{hkl} = \frac{n\lambda}{2\sin(\theta)} = \frac{n2\pi}{q}. \tag{2.36}$$

A lower limit for the crystal size can be estimated by the Scherrer equation, which relates the crystal size D to the line broadening of a Bragg reflex at half the maximum intensity (FWHM), as expressed by [167, 168]

$$D = \frac{K\lambda}{\mathrm{FWHM}\cos(\theta)}. \tag{2.37}$$

K is the shape factor of the crystallite, which is often approximated by $K = 0.93$.

The FWHM is obtained by modeling the respective Bragg peaks in the azimuthal q integral of the GIWAXS data with Gaussian functions. Generally, Gaussian functions $f(x, \overline{x}, \sigma^2)$ are probability density functions of a normally distributed random variable x, which are expressed by [156]

$$f(x,\overline{x},\sigma^2) = \frac{1}{\sqrt{2\pi\sigma^2}}\exp\left(\frac{(x-\overline{x})^2}{2\sigma^2}\right), \tag{2.38}$$

with $\overline{x}$ being the center of the Gaussian function and the mean value. σ^2 is referred to as the variance and the FWHM is given by $\mathrm{FWHM} = 2\sqrt{2\ln 2}\sigma \approx 2.3548\sigma$.

3 Sample Characterization

The following chapter introduces characterization methods applied in the context of this thesis, to probe thin films. Basic principles of ultraviolet/visible light (UV/vis) spectroscopy, photoluminescence (PL) and external quantum efficiency (EQE) measurements are discussed in Section 3.1. In Section 3.2, all device performance parameters necessary for current-voltage (JV) characterization of organic solar cells are introduced. In Section 3.3, real space characterization methods, such as profilometry, optical microscopy, atomic force microscopy (AFM) and scanning electron microscopy (SEM), are detailed. In Section 3.4, structure investigation in reciprocal space is discussed. Thus, the advanced scattering techniques grazing incidence small-angle X-ray scattering (GISAXS) and grazing incidence wide-angle X-ray scattering (GIWAXS) are introduced.

3.1. Optical Characterization

UV/vis Spectroscopy

UV/vis spectroscopy is a characterization method, which allows probing the absorbance or reflectance of samples with photons of different wavelengths in the UV/vis region. In this thesis, all UV/vis spectroscopy measurements are performed in transmission geometry to probe the absorbance of active materials in thin films and solutions. Absorption can occur if the energy of the incoming photon is equal or larger than the energy of the optical bandgap of the material under investigation ($E_{\text{photon}} \geqq E_{\text{g}}$). For photons, which fulfill this condition, absorption occurs according to the Franck-Condon principle (Figure 3.1). [169–171] Initially, the respective molecule is in the electronic (Figure 3.1, S_0) and vibronic (Figure 3.1, $\nu = 0$) ground state. Upon absorption of a photon, the molecule undergoes a transition into an electronically (Figure 3.1, S_1) and vibrationally ($\nu > 0$) excited state. Both ground state and excited state are singlet states. As absorption processes occur within femtoseconds [172], the transition is assumed to occur vertically

without altering internuclear distances within the time span of the transition. [169] The probability of this process depends on the overlap of vibrational wavefunctions of initial and final state (Figure 3.1, red). [171]

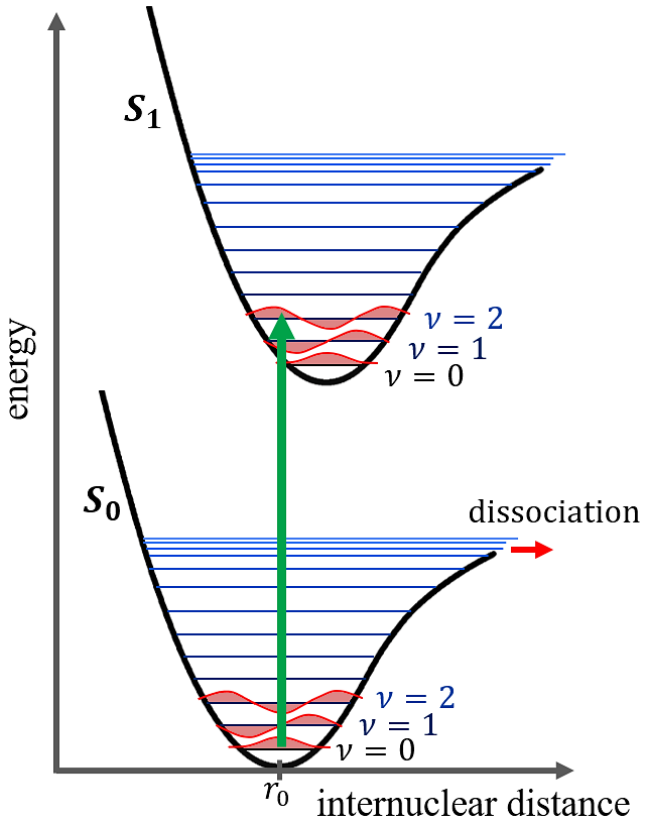

Figure 3.1: Simplified energy diagram visualizing the Franck-Condon principle. The Displacement from equilibrium (r_0) is illustrated with anharmonic oscillators. Initially, the molecule is in the electronic and vibronic ground state. Upon absorption of a photon, vertical transition into an electronically and vibrationally excited state occurs (green arrow). The probability for this transition depends on the overlap of vibrational wavefunctions (red) of initial and final state. At large internuclear distances, dissociation occurs as indicated by the red arrow.

In an UV/vis absorption spectroscopy experiment, the sample is illuminated with photons of different wavelengths (λ) and the transmitted light is detected. Absorbance $A(\lambda)$ and transmittance $T(\lambda)$ according to the Lambert-Beer law can be expressed by [173, 174]

$$A(\lambda) = \lg\left(\frac{I_0(\lambda)}{I(\lambda)}\right) = -\lg(T(\lambda)), \tag{3.1}$$

with $I_0(\lambda)$ and $I(\lambda)$ being the intensity of incoming and transmitted light, respectively.

Due to absorption processes, light intensity decays exponentially on its way through the medium and is given by [175, 176]

$$I(\lambda) = I_0(\lambda)\exp\left(-\mu(\lambda)d\right), \tag{3.2}$$

with $\mu(\lambda)$ being the material-specific, linear absorption coefficient and d being the path of light through the medium (thickness of thin film or cuvette).

Thus, the absorbance can be expressed by [175]

$$A(\lambda) = \lg\left(\frac{I_0(\lambda)}{I(\lambda)}\right) = \frac{1}{\ln(10)}\mu(\lambda)d. \tag{3.3}$$

Therefore, the material-specific absorption coefficient can be calculated by

$$\mu(\lambda) = \frac{A(\lambda)}{d}\ln(10). \tag{3.4}$$

For reflective samples, e.g. thin films, intensity losses due to total or partial reflection of light from interfaces with different refractive indices become significant and therefore, reflexion processes have to be taken into account. Thus, the absorbance $A(\lambda)$ can be expressed by [175]

$$A(\lambda) = -\lg\left(\frac{T(\lambda)}{I(\lambda) - R(\lambda)}\right), \tag{3.5}$$

with $R(\lambda)$ being the intensity of reflected light.

In this thesis, UV/vis spectroscopy is performed with thin films and in solution. In addition, *in situ* measurements allow following the film formation of slot-die coated active layers. A photograph of the *in situ* printing set-up is shown in Figure 3.2.

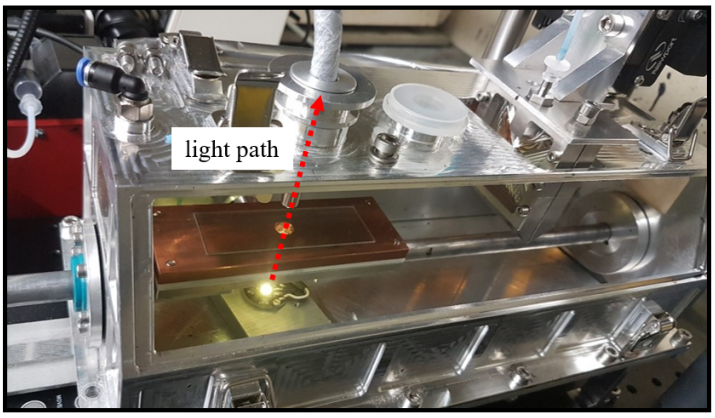

Figure 3.2: Photograph showing the set-up used to perform *in situ* UV/vis spectroscopy experiments. A light-emitting diode is installed at the bottom plate of the slot-die coater and below the sample holder to enable UV/vis spectroscopy in transmission geometry. The light path is marked with a dashed, red arrow. Reproduced with permission from Wiley [177].

In order to probe the absorbance of thin films *in situ* during film formation, a light source and glass fiber have to be implemented into the slot-die coater (Figure 3.2). Therefore, a MBB1D1 broadband light-emitting diode (LED) purchased from Thorlabs is installed below the sample holder. Due to broad emission (470–850 nm) of this LED, even low-bandgap materials with an absorption onset about 1.5 eV can be probed. A glass fiber is

applied to couple the transmitted light into a CAS 140 CT Instrument Systems Compact Array Spectrometer, which can detect a broad variety of wavelengths simultaneously with high time resolution (about 0.2 s per spectrum). For all static measurements performed in the context of this thesis, a Perkin Elmer Lamda 650 S or Perkin Elmer Lambda 35 UV/vis Spectrometer is used to measure the absorbance of thin films or solutions, respectively. The absorbance is normalized on the respective film thickness. For all UV/vis measurements performed in the context of this thesis, contributions originating from ambient light scattering or the substrate are substracted. For *in situ* UV/vis spectroscopy experiments (Subsections 5.1.2 and 5.2.3), no normalization is carried out as the thickness of the thin film changes during drying and is unknown for the wet state.

In order to determine the optical bandgap, a Tauc plot can be applied (Figure 3.3). The optical bandgap E_g can be determined by [176]

$$\mu(\lambda) = A(\lambda)(E - E_g)^{1/2}, \tag{3.6}$$

with $E = \frac{hc_0}{\lambda}$ being the energy of the photon, h being the Planck constant and c_0 being the speed of light in vacuum. The absorption coefficient $\mu(\lambda)$ can be calculated by Equation 3.4 with d being the thickness of the thin film and A being the absorbance obtained from the UV/vis spectrum. In the Tauc plot, $(\mu(\lambda)E)^{1/2}$ is plotted versus E (Figure 3.3). The optical bandgap is determined from the intercept at $\mu(\lambda) = 0$.

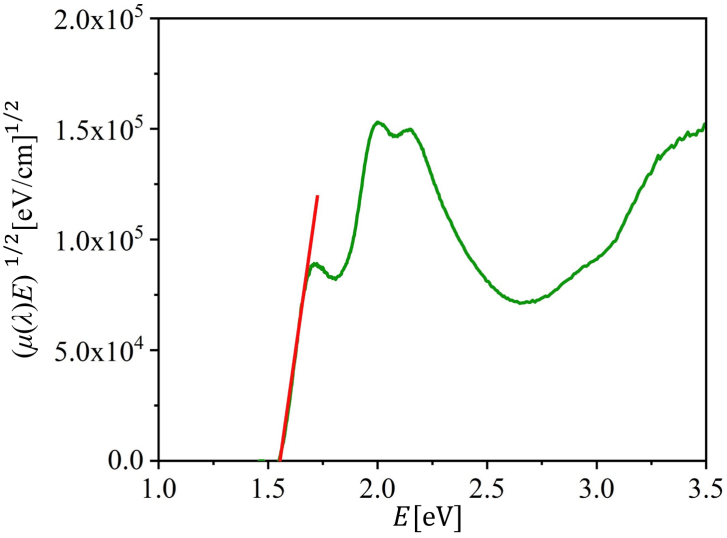

Figure 3.3: Tauc plot of a slot-die coated PBDB-T-SF:IT-4F thin film. The plot is extracted from the respective UV/vis spectrum. The optical bandgap is determined to be (1.55 ± 0.04) eV. The red line is a guide to the eye. Reproduced with permission from Wiley [177].

To determine the electronic transitions of a material, the UV/vis absorbance spectrum can be modeled with a set of Gaussian functions. [178] In Figure 3.4, the absorbance spectrum of PBDB-T-SF is shown for a dilute solution (Figure 3.4a) and a thin film

(Figure 3.4b). Electronic transitions are modeled with Gaussian functions (Figure 3.4, dark blue). All transitions are assumed to occur from the electronic and vibronic ground state (E_0, $\nu = 0$) into different vibration levels (ν) of the electronically excited state (Franck-Condon principle). Thus, a transition from the ground state to the vibration level $\nu = 0$ of the electronically excited state is denoted a (0-0) transition, whereas an excitation into the vibrational level $\nu = 1$ is denoted a (0-1) transition. This denotation is continued likewise for all transitions in the spectrum.

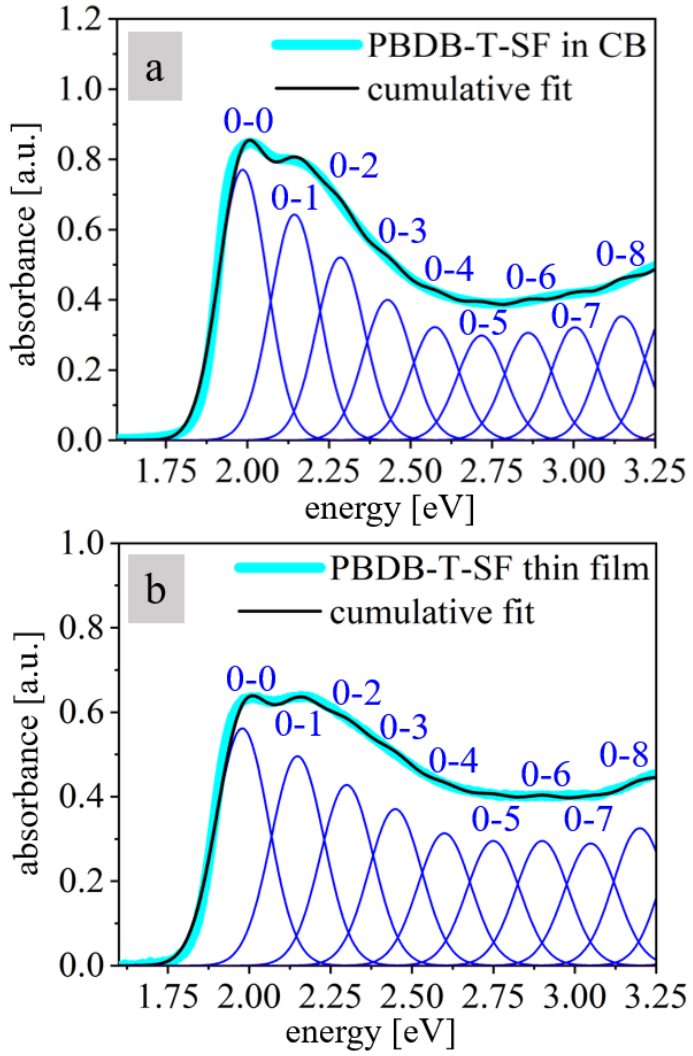

Figure 3.4: Electronic transitions are determined by modeling the absorbance spectra (bright blue) with sets of Gaussian functions of equal width (dark blue). Summing up all Gaussian functions gives the modeled absorbance spectra (black). The electronic transitions of the polymer PBDB-T-SF are shown for (a) a dilute CB solution and (b) a thin film. Reproduced and adapted with permission from Wiley [177].

For data modeling, several assumptions and approximations are applied. Each transition is presumed to occur at a specific energy or within a certain deviation around the center value, which can be described by a Gaussian distribution. [178] The height of the Gaussian functions corresponds to the probability of the respective transition, whereas the full width at half maximum (FWHM) is proportional to the state of order. For highly ordered systems, narrow Gaussian functions are observed, whereas broad functions indicate highly

disordered systems. For non-aggregated π-conjugated organic materials in solution, typical values for the FWHM of the respective Gaussian functions are in the range of 0.1 eV in solution at room temperature. [178] The FWHM of the (0-0) transition can be determined very exactly by the gradient at the absorption onset. The gradient of the experimental data has to be equal to that of the model function. Furthermore, all Gaussian functions of a set of Gaussian functions are supposed to have the same FWHM. In addition, it is assumed that the energy difference between two neighboring vibrational states is approximately constant. Thus, all Gaussian functions within a set have the same center-to-center distance towards their nearest neighbors. With these assumptions, the UV/vis spectrum can be modeled adequately. The sum of all Gaussian functions (Figure 3.4, black) fits the experimental UV/vis absorbance spectrum (Figure 3.4, bright blue).

Photoluminescence

PL measures the light emission of a sample after absorption of photons. [179,180] Thus, PL provides information on radiative relaxation processes, originating from exciton recombination, a possible loss mechanism in organic solar cells (Subsection 2.1.2). For excitation, a specific wavelength, which can be efficiently absorbed by the material under investigation, is chosen (e.g. at the absorbance maxima). After excitation with this wavelength, the emitted light is detected. As emission of photons occurs from different vibrational levels of the electronically excited state into different vibrational levels of the ground state, a broad emission spectrum (Figure 3.5) is observed, which can be described by a Gaussian function. [181,182].

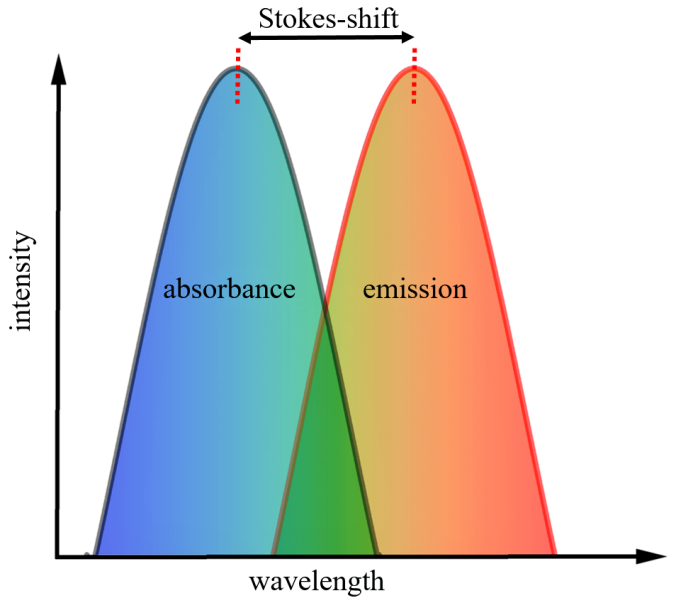

Figure 3.5: Illustration of typical absorbance (blue) and PL (red) spectra. Due to relaxation processes, the emission spectrum is red-shifted relative to the absorbance spectrum (Stokes-shift).

In addition, the emission spectrum is red-shifted compared to the absorbance. This shift towards lower energies is well-known as Stokes-shift. [180, 183] A Jablonski diagram illustrates processes, occuring upon absorption and emission of photons (Figure 3.6). [184]. Two mechanisms of radiative processes, namely fluorescence and phosphorescence, are distinguished. [179, 185]

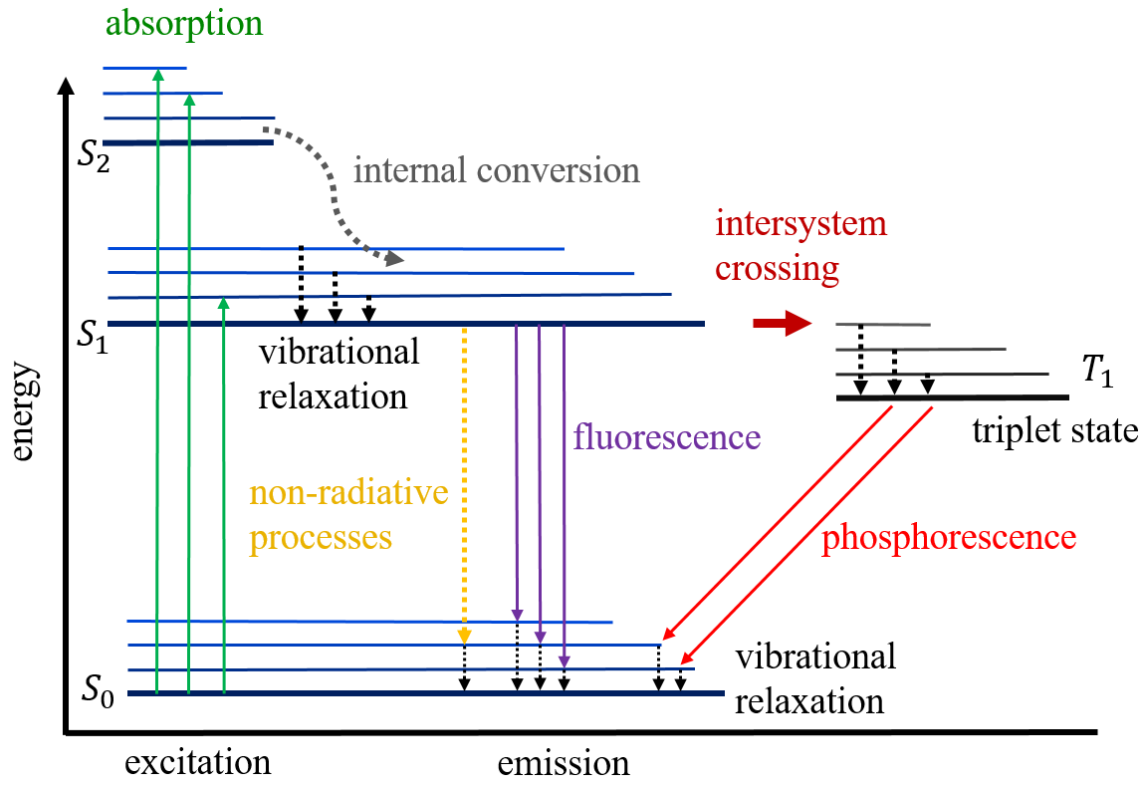

Figure 3.6.: Simplified schematic illustrating processes occuring upon absorption and subsequent emission of photons. Upon absorption of a photon, an electron is transferred into an electronically and vibrationally excited state (green arrows). In this state, internal conversion (gray arrow) and vibrational relaxation (black, dashed arrows) can provoke electronic and vibrational relaxation. A transition into the ground state can occur via non-radiative processes (yellow, dashed arrow) or via emission of photons (fluorescence, purple arrows). If intersystem crossing (red bold arrow) into a triplet state (T_1) occurs prior to emission of a photon, phosphorescence (red arrows) can take place. In the electronic ground state, vibrational relaxation processes occur (black dashed arrows).

Absorption of a photon and electronic excitation occurs according to the Franck-Condon principle (Figure 3.1). [182, 186] Thus, an electron is excited and transition from the electronic and vibrational ground state into an electronically and vibrationally excited

state occurs (Figure 3.6, green arrows). [182, 185] After transition from the ground singlet state into a higher energy singlet state, relaxation processes, such as internal conversion (Figure 3.6, gray dashed arrow) into a lower energy electronic state and vibrational relaxation (Figure 3.6, black, dashed arrows), can take place. [186, 187] Transition back to the electronic ground state can occur via non-radiative (Figure 3.6, yellow, dashed arrow) or radiative processes. A direct transition from the electronically excited to the electronic ground state via emission of a photon is called fluorescence (Figure 3.6, purple arrow). In contrast, intersystem crossing (Figure 3.6, red bold arrow) into a triplet state (T_1) and subsequent photon emission is called phosphorescence (Figure 3.6, red arrows). [184, 187] These relaxation processes provoke transition into vibrationally excited states of the electronic ground state, where subsequent vibrational relaxation occurs (Figure 3.6, black dashed arrows). In this thesis, all PL measurements are performed with a Perkin Elmer Fluorescence Spectrometer LS 55 using an excitation wavelength of 570 nm.

External Quantum Efficiency

External Quantum Efficiency (EQE) gives the ratio of the number of electrons, contributing to the photocurrent, to the number of photons of a given energy. [188] Thus, EQE estimates the probability that a photon of a certain wavelength, which is absorbed by the active layer, can contribute to the photocurrent.

The EQE can be calculated by [188]

$$\mathrm{EQE}(\lambda) = \frac{1}{P(\lambda)} \frac{J_{\mathrm{SC}}(\lambda)}{e} \frac{hc_0}{\lambda}, \tag{3.7}$$

with $P(\lambda)$ being the photon flux density of the applied light, e being the elementary charge, $J_{\mathrm{SC}}(\lambda)$ being the measured short-circuit current density at a certain wavelength, h being the Planck constant and c_0 being the speed of light in vacuum.

The J_{SC} of an organic solar cell can be obtained by integrating the current density versus all absorbed wavelengths (Figure 3.7, blue) as given by [189]

$$J_{\mathrm{SC}} = e \int P(\lambda)\mathrm{EQE}(\lambda) d\lambda. \tag{3.8}$$

In Figure 3.7, the EQE spectrum and the corresponding integrated J_{SC} is shown to illustrate the basic principle. Depending on the wavelengths, different loss mechanisms dominate. [190, 191] For wavelengths in the near UV region, exciton recombination occurs at the front surface of the solar cell, reducing the EQE significantly (Figure 3.7I). In the range of visible light, incoming photons can contribute efficiently to the photocurrent.

However, the EQE is reduced due to reflexion processes and limited exciton diffusion lengths (Figure 3.7II). At larger wavelengths, reduced absorption of photons and short exciton lifetimes reduce the EQE (Figure 3.7III). At wavelengths larger than the optical bandgap, no absorption occurs and the EQE is zero (Figure 3.7IV).

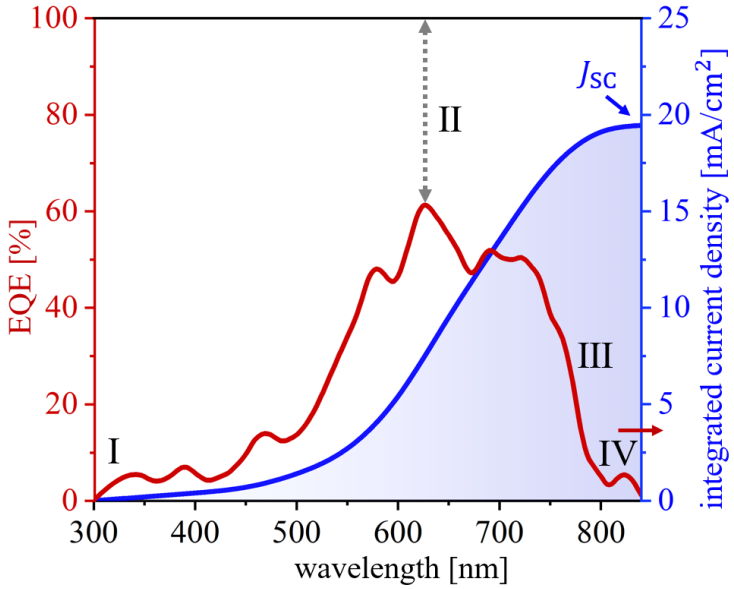

Figure 3.7: A typical EQE spectrum (red) and the corresponding integrated current density (blue) of an printed organic solar cell based on PBDB-T-SF:IT-4F with 0.25 vol % DIO are shown. Regions of different predominant loss mechanisms are indicated by numbers I–IV. The current density integrated versus all absorbed wavelengths gives the J_{SC} of the organic solar cell. Reproduced and adapted with permission from ACS publishing [192].

In this thesis, EQE spectra are measured using an Oriel QE-PV-SI Quantum Efficiency Measurement Kit provided from Newport. The photocurrent generated at different wavelengths is measured under illumination by a 6258 Xe OF lamp (Newport, 300 W), set with a reference and corrected for spectral error to fulfill standard test condition requirements (AM 1.5 illumination, 100 mW/cm^2). [189, 193] All solar cells are measured at ambient conditions without encapsulation.

3.2. Current-Voltage Characterization

The device performance of organic solar cells depends on environmental conditions, such as temperature and intensity of illumination. [194] Therefore, standard test conditions are set to enable a reproducible measurement procedure, which allows for comparison of different devices fabricated by different research groups. [193] Standard test conditions provide a realistic solar cell performance, representing the overall yearly average for mid-latitudes. As sunlight passes through the atmosphere, scattering and absorption processes occur before photons reach earth's surface. As these events depend on the path length through the atomosphere, the incident angle z, given with respect to the zenith (surface normal), has to be considered (Figure 3.8a). For larger z angles, the path through the atmosphere is longer

and more absorption and scattering events occur, altering the spectrum reaching earth's surface. [195] The path length of the sunlight through the atmosphere is referred to as air mass (AM, Figure 3.8a). [196] The sun spectrum AM0 (Figure 3.8b, orange) is defined as the sun spectrum outside the atmosphere, whereas the AM1.5 spectrum (Figure 3.8b, green), which is standard for photovoltaic performance measurements, corresponds to a pathlength of 1.5 times the thickness of the atmosphere and an angle of 48.2° with respect to the zenith. [195]

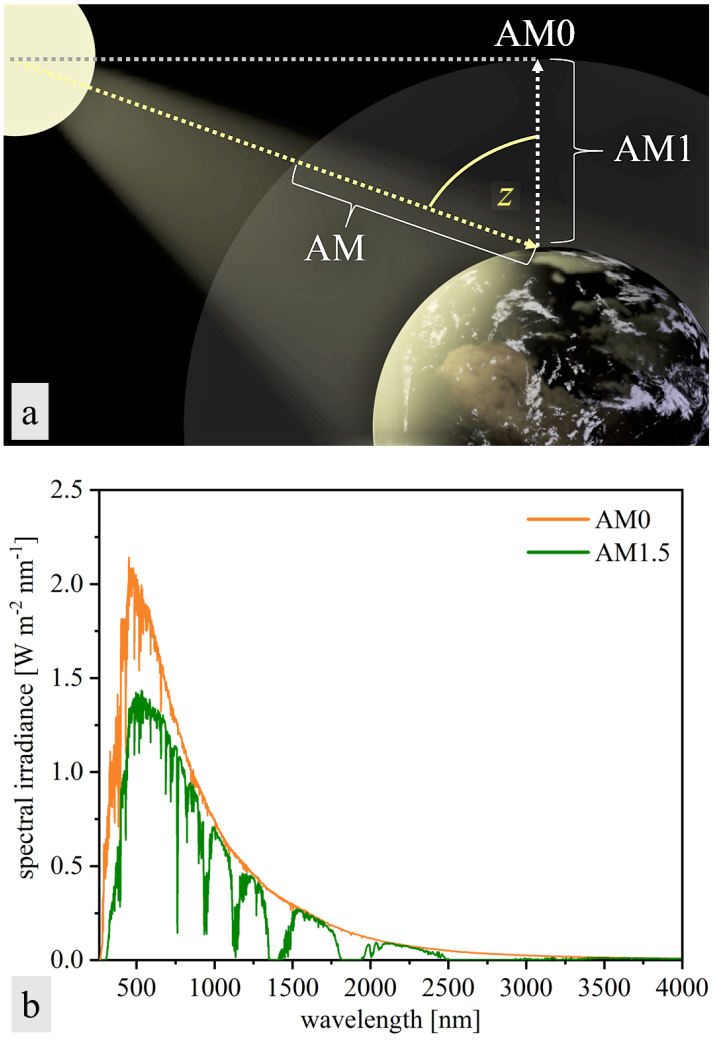

Figure 3.8: (a) Illustration of Air Mass (Image inspired by a graph from [195]). The path of sunlight (yellow, dashed arrow) through the atmosphere (gray) is referred to as Air Mass (AM, white curly bracket). At AM0, the sun emission spectrum equals the spectrum before entering the atmosphere. AM1 is given when the sun is in the zenith and the path length through the atmosphere equals its thickness. The incident angle towards the zenith (z) is indicated (yellow). Length scales are not true to scale. (b) The sun emission spectrum alters when it passes through the atmosphere as revealed by the sun emission spectrum AM0 (orange) and AM1.5 (green). Data are obtained from [197].

In this thesis, all organic solar cells are measured according to standard test conditions. Thus, all JV-curves are measured under AM1.5 illumination (100 mW/cm^2) with a SourceMeter Keithley 2400 at ambient conditions and without encapsulation. In Figure 3.9, a JV-curve for a printed organic solar cell based on a 1:1 ratio of PBDB-T-SF:IT-4F with 0.25 vol % DIO is given as an example. Key performance parameters are open-circuit voltage (V_{OC}), short-circuit current density (J_{SC}) and fill factor (FF).

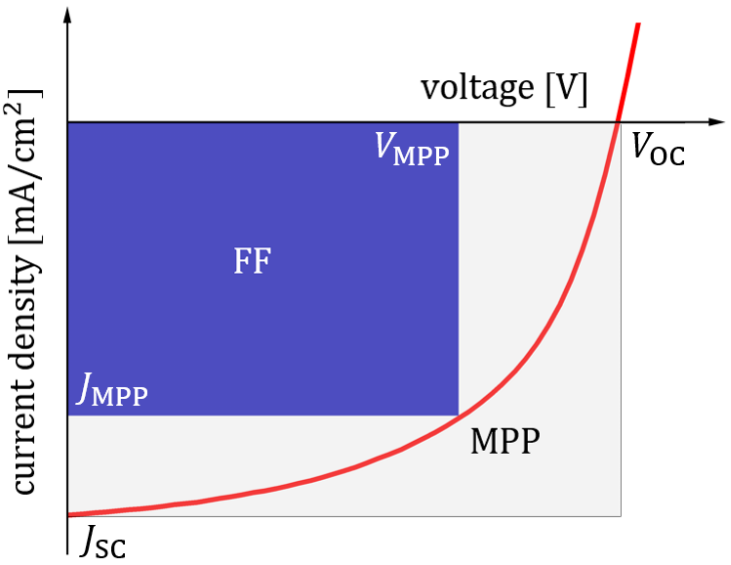

Figure 3.9: JV-curve of a printed organic solar cell is shown. Key performance parameters of an organic solar cells, namely V_{OC}, J_{SC} and FF are indicated. FF is given by the available power at the MPP of the real photovoltaic device divided by the theoretical maximum power. Reproduced and adapted with permission from ACS publishing [192].

V_{OC} is the electrical potential in a solar cell when it is disconnected from any circuit. At this point, the available voltage is at its maximum and the current is zero ($I = 0$). In contrast, J_{SC} is the current through the solar cell when the voltage across the solar cell is zero ($V = 0$). In both cases, no photocurrent is generated in the solar cell. V_{OC} of an organic solar cell is determined by [124, 198]

$$V_{OC} = \frac{E_g}{e} - \frac{k_B T}{e} \left(\frac{(1 - p_{diss}) \gamma N_c^2}{p_{diss} G} \right), \tag{3.9}$$

with e being the elementary charge, k_B being the Boltzmann constant, T being the temperature, p_{diss} being the exciton dissociation probability, γ being the Langevin recombination constant, N_c being the effective density of states and G the generation rate of bound electron–hole pairs.

J_{SC} depends on the EQE, which gives the probability that a photon of a specific wavelength contributes to the photocurrent. Integrated photocurrent density over all wavelengths gives J_{SC}.

FF gives the ratio of the available power at the maximum power point (MPP, Figure 3.9) divided by the maximum theoretical power output and is given by [71, 124]

$$FF = \frac{V_{MPP} J_{MPP}}{V_{OC} J_{SC}}, \tag{3.10}$$

with V_{MPP} and J_{MPP} being the extracted voltage and current at the MPP, respectively.

Power conversion efficiency (PCE) is defined as the maximum power produced by the solar cell divided by the power of incident light (P_{in}) and depends on the parameters V_{OC}, J_{SC} and FF of the device as expressed by [71, 124]

$$\text{PCE} = \frac{V_{\text{OC}} J_{\text{SC}} \text{FF}}{P_{\text{in}}}. \tag{3.11}$$

3.3. Structure Investigation in Real Space

Profilometry

Profilometry probes the height profile and roughness of thin films. [199, 200] In order to determine the film thickness, the films have to be scratched down to the substrate prior to the measurement. Then, the sample is placed on the stage inside the profilometer to scan perpendicularly over the scratch (Figure 3.10a). A diamant stylus is moved in vertical direction to contact the sample before scanning the surface laterally, whereas the vertical deflection is recorded and translated into a height profile (Figure 3.10b).

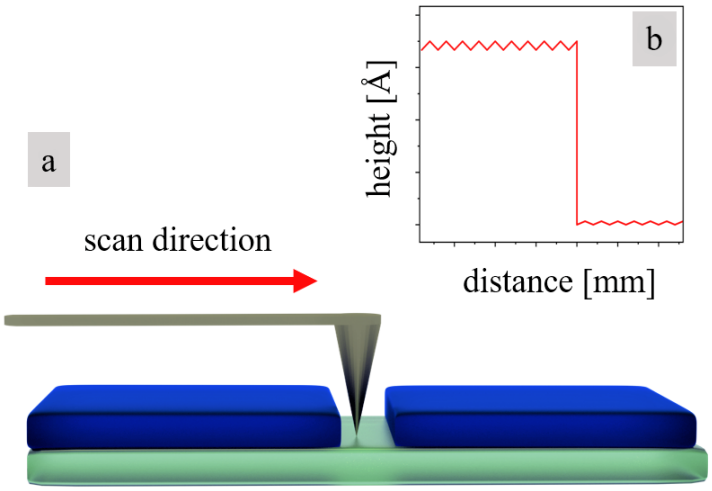

Figure 3.10: Profilometry is applied to determine the film thickness of an active layer (dark blue) on a glass substrate (bright blue). (a) A stylus (gray) moves perpendicularly over the scratch as indicated by a red arrow. (b) Average step height is determined by the difference between the average height at the surface and the average height inside the scratch.

In order to determine the film thickness, the average step height (ASH) is calculated by the difference between the mean height at the sample surface and the mean height inside the scratch, which is the mean height of the substrate. In this thesis, a BRUKER DektakXT Profilometer is used to determine the film thickness of slot-die coated active layers. Measurements are performed at different positions to obtain a statistically significant value for average film thickness and to exclude possible local differences. Data acquisition and analysis are performed using the included software Vision64 by Bruker.

Optical Microscopy

In an optical microscope, the sample is placed on a stage and illuminated with visible light. A system of lenses is applied to generate real space images of the sample surface with tunable magnification. [201] Thus, surface morphology as well as sample homogeneity can be probed. Optical microscopy is an easy applicable technique, which allows probing structures in the micrometer range. Due to diffraction, the resolution limit of a conventional visible light microscope depends on the wavelength λ of the light source and the numerical aperture (NA), a dimensionless number, determining the resolution power R of the microscope as expressed by the Rayleigh criterion [202]

$$R = \frac{1.22\lambda}{2\mathrm{NA}}. \tag{3.12}$$

NA is given by [201, 202]

$$\mathrm{NA} = nsin(\theta), \tag{3.13}$$

with n being the refractive index of the surrounding medium (for air: $n = 1$) and θ being half the angular aperture.

In this thesis, *in situ* optical microscopy is performed using a MINTRON 62V1P Video Microscope and a PHOTONIC Optics PL3000 lamp. The optical microscope is installed above the slot-die coater to enable a top view on the sample surface. The optics is focused on the center of the substrate before slot-die coating at room temperature and ambient conditions. The complete film formation process is recorded as a video and converted to individual images after the measurement with a time resolution of a second. For every region of drying, one characteristic image is shown. The scale bar is added using ImageJ. [203]

Atomic Force Microscopy

Atomic force microscopy (AFM) is a high-resolution technique, providing information on surface topology at nanometer scale. [204] In contrast to optical microscopy or scanning electron microscopy (SEM), the typical resolution limit of diffraction (Equation 3.12) does not apply and topographic information on surface roughness can be extracted quantitatively. [205] A very sharp tip is fixed at a cantilever spring to scan the sample surface (Figure 3.11). [204, 205] Spatial resolution depends critically on the diameter of the tip. Due to interaction between sample surface and tip, deformation of the cantilever

spring occurs. [206] This deformation can be measured precisely by a laser beam, which is focused on the backside of the cantilever. [205] Any oscillation of the cantilever causes a deflection of the laser beam, which is detected by a photodetector. Piezoelectric motors are applied to control the scanning direction on the sample surface as well as the height movement. Deformation of the cantilever provides information on surface morphology, such as height profile and surface roughness.

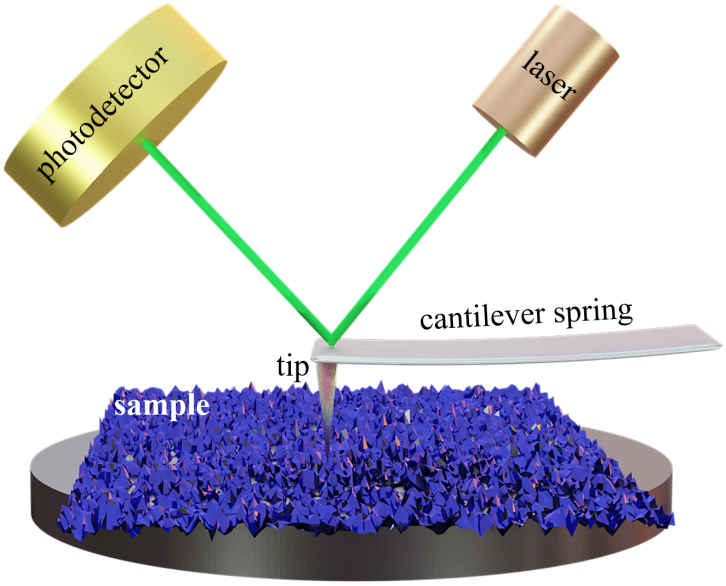

Figure 3.11: Illustration of the basic principle of AFM (image inspired by a graph from [207]). A very sharp tip (gray cone) fixed on a cantilever spring (gray plane) scans the sample surface (purple). Interaction between sample surface and tip causes deformation of the cantilever spring, which is measured by a laser beam (green) reflected at the cantilever and detected by a photodetector (golden).

The interaction between tip and sample can be described by the Lennard-Jones potential, giving the potential energy for different separation distances. [208] The Lennard-Jones potential is given by repulsive and attractive contributions. The repulsive term describes the Pauli repulsion at short ranges due to overlapping electron orbitals and is given by [209–211]

$$V = \frac{C_1}{r^n}, \tag{3.14}$$

with V being the potential energy, C_1 being a term, accounting for Pauli repulsion, and r being the separation distance between two particles or, in the case of an AFM measurement, the distance between tip and sample surface. The exponent is usually given by $n = 12$.

The attractive term of the Lennard-Jones potential is given by attractive interactions, originating from London dispersion forces, and is expressed by [212, 213]

$$V = -\frac{C_2}{r^6}, \tag{3.15}$$

with C_2 being a term, accounting for attractive dipole-dipole interactions.

Thus, the Lennard-Jones potential is expressed by [208, 214]

$$V = 4\epsilon \left[\left(\frac{\sigma}{r} \right)^{12} - \left(\frac{\sigma}{r} \right)^{6} \right], \tag{3.16}$$

with ϵ being the depth of the potential well and σ being the distance, at which the potential energy is zero.

In Figure 3.12, a normalized Lennard-Jones potential as well as the attractive term and the repulsive term are shown according to Equation 3.16.

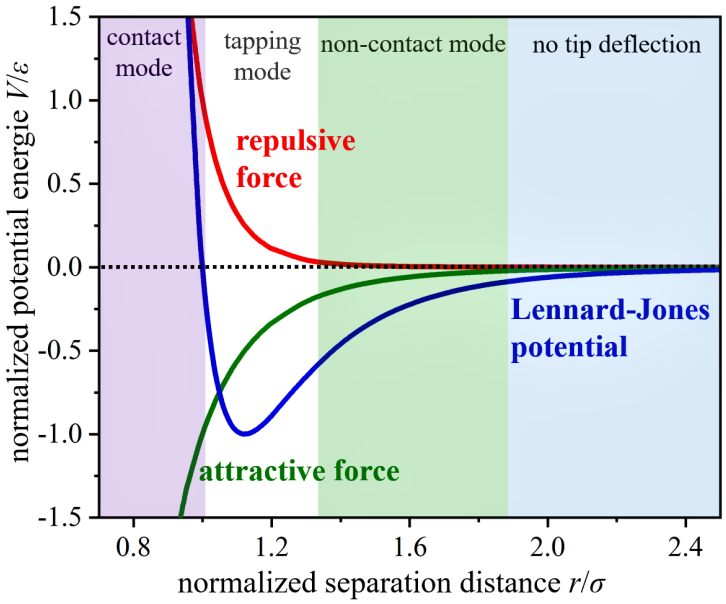

Figure 3.12: Illustration of potential energy between sample surface and AFM tip. The normalized Lennard-Jones potential (blue) is given by a repulsive (red) and an attractive (green) contribution. Depending on the separation distance, AFM is performed in contact mode (purple area), tapping mode (white area) or non-contact mode (green). At large separation distances, no interaction occurs (bright blue).

AFM measurements can be performed in contact mode (Figure 3.12, purple area), tapping mode (Figure 3.12, white area) or non-contact mode (Figure 3.12, green area). [205] In contact mode, the separation distance is very small and repulsive forces dominate. In tapping or non-contact mode, the sample-tip distance increases compared to the contact mode and attractive contributions become more dominant. In tapping mode, a piezoelectric element causes oscillation of the cantilever with a defined frequency. [206,215,216] Attractive as well as repulsive interactions between tip and sample surface alter the cantilever's oscillation. [205] Thus, phase, amplitude and frequency of driving oscillation and forced oscillation differ. The height of the tip is adjusted to keep the amplitude or frequency of oscillation constant. Topographic information is obtained by imaging the force applied during the intermittent contacts of the tip with the sample under investigation. In this thesis, AFM measurements are performed with an Asylum Research MFP-3D instrument in tapping mode (1.0 µm x 1.0 µm scan area, 75 kHz resonance frequency). Gywddion is used for data visualization and analysis. [217]

Scanning Electron Microscopy

Scanning electron microscopy (SEM) is a high-resolution technique, which can provide topographic as well as material sensitive information on conductive thin films on a sub-nanometer scale. [218, 219] Image resolution is limited by the wavelength of the beam used to investigate the sample surface. According to the particle-wave duality introduced by De Broglie, electrons have a shorter wavelength compared to photons at a given energy. [220, 221] Thus, the achieveable resolution of SEM outperformes that of classical optical microscopy by orders of magnitude. In addition, the resolution can be further enhanced by applying acceleration voltage. For a typical acceleration voltage of 5 keV, as used in this thesis, the relativistic De Broglie wavelength λ_e for an electron is given by [222, 223]

$$\lambda_\mathrm{e} = \frac{h}{p} = \frac{hc_0}{\sqrt{2m_\mathrm{e}c_0^2eV + (eV)^2}} \approx 17.3 \text{ pm}, \tag{3.17}$$

with h being Planck's constant, p being the electron momentum, c_0 being the speed of light in vacuum, V being the applied acceleration voltage, m_e being the rest mass of an electron and e being its elementary charge.

In Figure 3.13a, the basic working principle of SEM is illustrated. Thus, an electron beam is generated by an electron gun. [224] Electrons can be emitted thermally or by applying a field emission voltage. [219, 225] Also a combination of both processes, in a thermally assisted field emission gun (Schottky cathode), is possible. [224] To obtain high quality SEM images, the latter approach is usually applied as it provides a high electron flux, a well defined kinetic energy and enables the use of relatively low acceleration voltages (5 keV or less). [219, 226] Electrons are accelerated towards the anode by the applied acceleration voltage. [219] Electromagnetic lenses and apertures are applied to control beam size and focus, whereas scan coils position the beam on the sample. [224] A backscattered electron (BSE) detector, a secondary electron (SE) detector and a X-ray detector can be used to detect the respective signals, originating from interaction of the electron beam with the sample under investigation. BSEs originate from elastic scattering events (Figure 3.13b) and have a large escape depth due to their high energy. [219, 224] The detected signal provides material sensitive information such as phase composition. In contrast, SEs originate from inelastic scattering events (Figure 3.13c). Due to their low energy (10–50 eV), their escape depth is small and surface sensitive information is obtained. [219, 227] Protruding structures appear brighter due to reduced working distance. As brightness also depends on other factors such as the material under investigation, relative topographic information is obtained. Furthermore, X-rays can be emitted after a

core electron has been removed previously. Thus, an electron from a higher energy level can fall into the vacancy and provoke a release of energy by photon emission (Figure 3.13d) and energy-dispersive X-ray (EDX) spectroscopy can be performed. [218,219,224] Emitted X-ray photons provide information on the material composition. [218, 219] The escape depth is larger than that of SEs or BSEs.

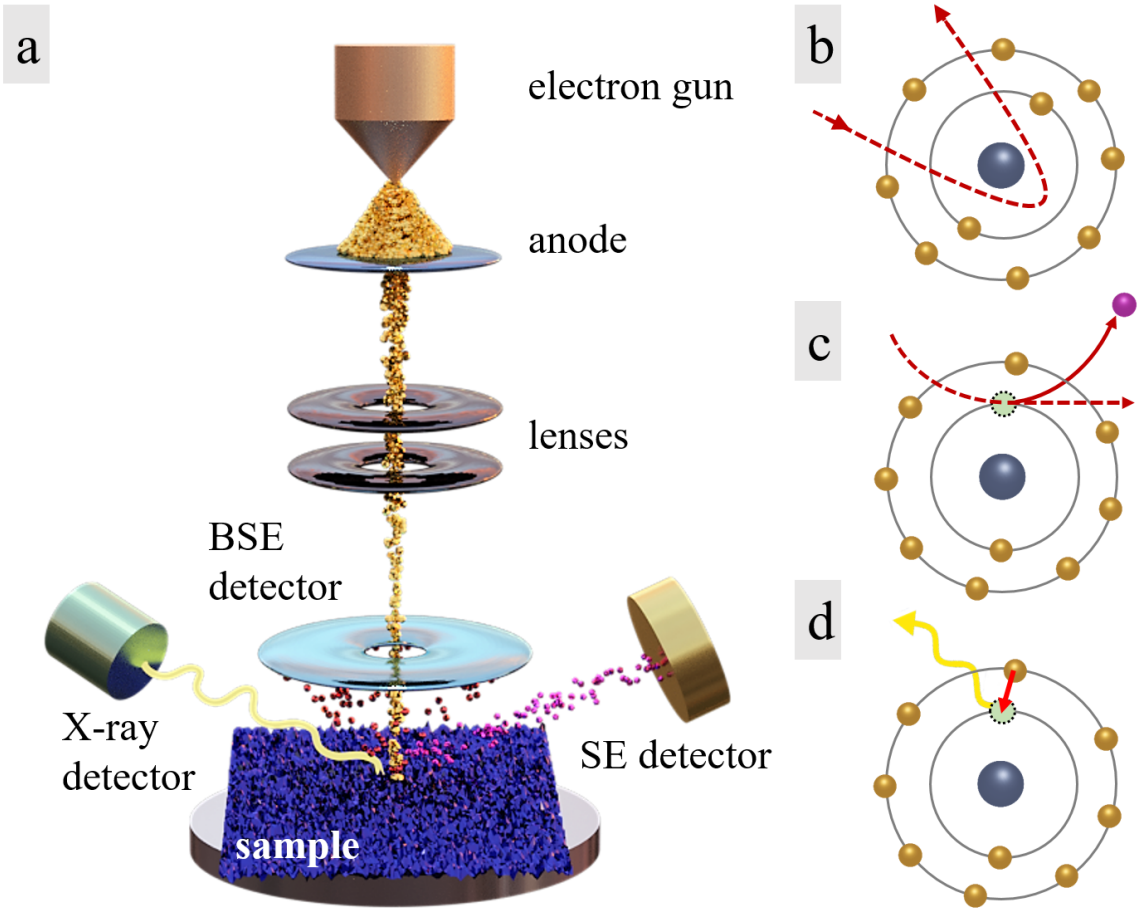

Figure 3.13.: Simplified illustration of (a) the SEM set-up and (b-d) occuring processes contributing to the signal (image inspired by graphs from [228]). (b) Secondary electrons, originating from inelastic scattering events, (c) backscattered electrons as well as (d) X-rays provide information on topography, phase contrast and material composition, respectively.

In this thesis, SEM measurements are performed under vacuum conditions with a Zeiss NVision 40 SEM located at the Zentrum für Nanotechnologie und Nanometerialien at the Technical University Munich. The instrument has a thermally assisted field emission gun and an in-lens detector to detect SEs. An acceleration voltage of 5 keV as well as a working distance of 4 mm are applied. All samples are cut to a size of 1.0 cm x 1.5 cm before the measurement. Images are contrast adjusted with ImageJ. [203]

3.4. Structure Investigation in Reciprocal Space

Grazing incidence X-ray scattering is an advanced scattering technique, which allows probing thin films with high quality and statistical significance in reciprocal space. [148,151] In this thesis, grazing incidence small-angle X-ray scattering (GISAXS) and grazing incidence wide-angle X-ray scattering (GIWAXS) are performed. A schematic of a typical GISAXS and GIWAXS set-up is illustrated in Figure 3.14.

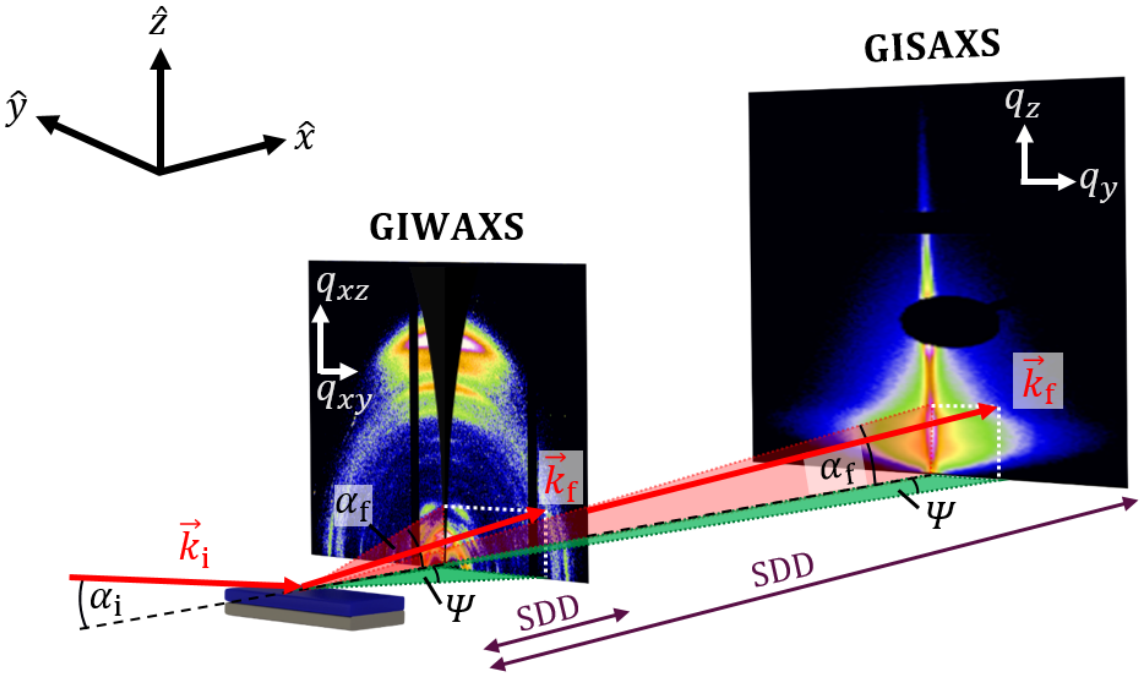

Figure 3.14.: Schematic of grazing incidence X-ray scattering (image inspired by a graph from [154]). The incoming beam (red) impinges onto the sample under a small angle. The diffusely scattered beam leaves the sample under an exit angle given by a component in vertical (red area) and lateral (green area) direction. The scattering signal is collected by a 2D detector mounted at different SDD. For GISAXS the SDD is usually in the range of meters, whereas GIWAXS is performed at a much shorter SDD in the range of some tens of centimeters.

The incoming X-ray beam (k_i, red) impinges onto the sample under a small incident angle (α_i) and is diffusely scattered under an lateral scattering angle Ψ (green) with respect to the yz-plane. [148, 151] Thereby, the vertical scattering angle α_f, given with respect to the sample surface, can differ from the incident angle. A 2D detector collects the scattering signal. Depending on the sample-detector distance (SDD), different morphological information is obtained. GISAXS is usually performed at a SDD of 1–5 m, which allows probing amorphous structures in the length scale of 1 nm to 1 µm. For GIWAXS, a shorter

SDD, which is typically in the range of some tens of centimeters, is applied to cover larger scattering angles and to probe crystalline structures. [148] Depending on the incident angle, surface as well as bulk sensitive information is obtained. For incidence angles smaller than the critical angle of the material under investigation, total reflection occurs and only surface sensitive information is obtained. For incident angles above the critical angle of the material, inner morphology is probed. Grazing incidence geometry allows obtaining a significant scattering signal even for thin films with thicknesses of 100 nm or less as well as probing a larger sample area in comparison to real space imaging methods, such as AFM or SEM (Section 3.3).

Grazing Incidence Small-Angle X-ray Scattering

A 2D GISAXS image of a printed sample based on a 1:1 ratio of PBDB-T-SF:IT-4F with 1.0 vol % DIO is given as an example for a typical scattering pattern (Figure 3.15a). For quantiative GISAXS data analyis, vertical (Figure 3.15a, green cuboid) and horizontal (Figure 3.15a, red cuboid) line cuts are performed. In the 2D GISAXS image, the scattering pattern is observed above the sample horizon. At the critical angle of the material under investigation, a significantly enhanced scattering signal (Figure 3.15b, Yoneda region) is observed. [152] At the specular reflection region, which equals the incident angle, the X-ray beam is directely reflected at the sample (Figure 3.15a). Due to very high scattering intensity at this position, a beamstop (Figure 3.15a,b) has to be applied to avoid oversaturation of the detector. [151]

For a given SDD and by applying the small angle approximation, the incident angle can be determined by applying the simple trigonometric function

$$\alpha_\mathrm{i} = \frac{1}{2}\arctan\left(\frac{(y_\mathrm{spec} - y_\mathrm{DB})p}{\mathrm{SDD}}\right), \tag{3.18}$$

with y_spec being the y-position of the specular reflection, y_DB being the y-position of the direct beam at the 2D detector and p being its pixel size.

Lateral (Ψ) and vertical (α_f) position of the scattered beam on the detector can be calculated by

$$\begin{pmatrix} \alpha_\mathrm{i} + \alpha_\mathrm{f} \\ \Psi \end{pmatrix} = \begin{pmatrix} \arctan(\frac{(y - y_\mathrm{DB})p}{\mathrm{SDD}}) \\ \arctan(\frac{(x - x_\mathrm{DB})p}{\mathrm{SDD}}) \end{pmatrix}. \tag{3.19}$$

For quantitative GISAXS data analysis, horizontal line cuts are performed at the critical angle of the polymer to obtain material sensitive morphological information (Figure 3.15c). Horizontal line cuts are fitted with a model based on the EIA of the DWBA and the LMA (Subsection 2.3.2). This approach allows extracting average structure sizes and interdomain distances in the thin film. Large structures in the q range below the resolution limit are not accessible with GISAXS (Figure 3.15c, red area). As the accessible length scales depend critically on the SDD, this parameter has to be chosen carefully to probe the desired q range and to obtain information on the desired structure sizes.

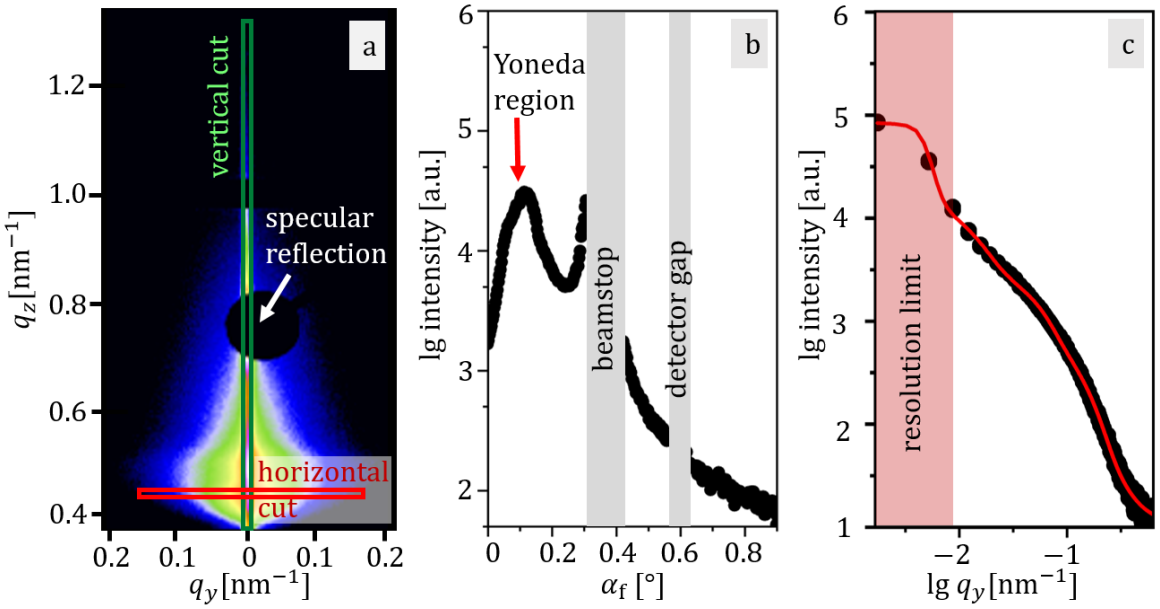

Figure 3.15.: 2D GISAXS data and its corresponding line cuts are shown. (a) In the 2D scattering image, the position of the specular reflection (white arrow), the vertical line cut (green cuboid) and the horizontal line cut (red cuboid) are marked. (b) In the vertial line cut, scattering is observed above the sample horizon. At the Yoneda region (marked with a red arrow), which is observed at the critical angle of the material under investigation, scattering intensity is significantly enhanced. Beamstop and detector gap are covered with gray bars. (c) A horizontal line cut is performed at the critical angle of the material under investigation and modeled with a model based on the EIA of the DWBA (red line). The resolution limit (red area) gives the q range, which is inaccessible with GISAXS. Reproduced and adapted with permission from ACS publishing [192].

Grazing Incidence Wide-Angle X-ray Scattering

In a GIWAXS experiment, a scattering signal is observed for all scattering events, fulfilling the Laue condition (Subsection 2.3.3). [229] Thus, the recorded GIWAXS scattering pattern (Figure 3.16a,b) represents a projection of allowed Bragg reflexes of the three-dimensional Ewald sphere onto a two-dimensional detector.

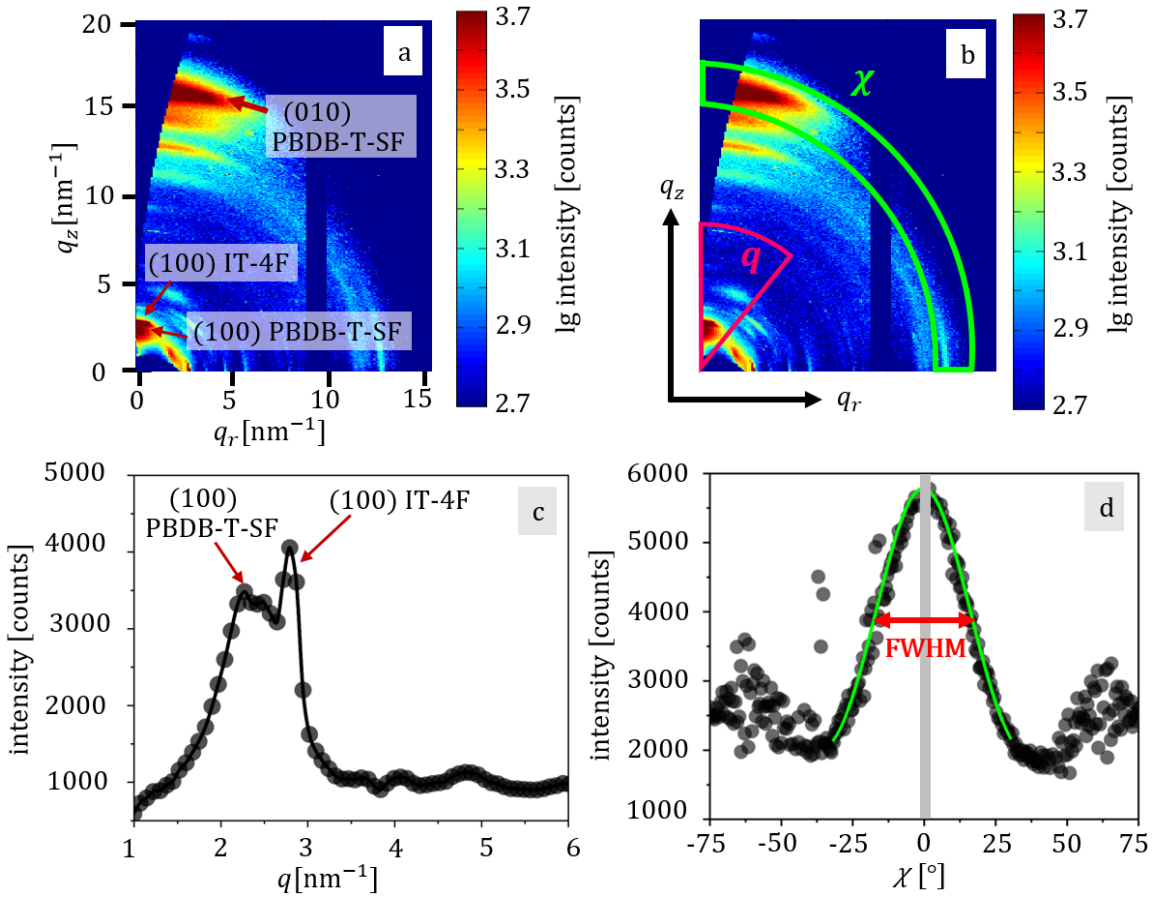

Figure 3.16.: 2D GIWAXS data and corresponding line cuts are shown. (a) In the 2D scattering image, the most prominent scattering signals are assigned to the (100) PBDB-T-SF, (100) IT-4F and (010) PBDB-T-SF Bragg peak (indicated by red arrows). The blue wedge-shaped area in the center covers the inaccessible area. (b) For data evaluation, a cake-shaped q integral (pink) as well as tube cuts in χ direction (bright green) are performed. (c) An azimuthal q integral is shown. The (100) PBDB-T-SF and IT-4F Bragg peaks are indicated by red arrows. (d) The tube cut performed at the (100) PBDB-T-SF Bragg peak position is shown. The FWHM (red) of the corresponding Gaussian function (bright green) to model the scattering data provides information on rotational disorder of crystallites. The inaccessible area is covered with a gray bar. Reproduced and adapted with permission from ACS publishing [192].

In a 2D GIWAXS pattern, the q_z and q_y components always contain a q_x component. For this reason, the coordinate system in Figure 3.14 is given by q_{xz} and q_{xy}. For quantitative data analysis, 2D GIWAXS detector images have to be corrected and reshaped, provoking a distortion of the detector image and a wedge-shaped inaccessible area around $q_r = 0$ (with $q_r = \sqrt{q_x^2 + q_y^2}$). [229] In Figure 3.16a, a 2D GIWAXS image of a printed sample based on a 1:1 ratio of PBDB-T-SF:IT-4F with 1.0 vol % DIO is given as an example for a typical scattering pattern. The (100) PBDB-T-SF, (100) IT-4F and (010) PBDB-T-SF Bragg peaks are indicated by red arrows. In order to compare scattering intensities of different Bragg peaks and to obtain information on the overall crystallinity, an azimuthal q integral (Figure 3.16b, pink) can be performed. The q value, where the Bragg peak is observed, is inversely proportional to the lattice spacing. [97, 230] Tube cuts are performed in χ direction (Figure 3.16b, bright green) to obtain information on rotational disorder of crystallites. [148, 231] In Figure 3.16c, an azimuthal q integral is given. The position of the (100) Bragg peaks of PBDB-T-SF and IT-4F are indicated by red arrows. A tube cut performed at the (100) PBDB-T-SF Bragg peak position and its corresponding Gaussian function to model scattering data are shown in Figure 3.16d. For PBDB-T-SF, most crystallites are orientated edge-on as a high scattering intensity is observed for χ values close to the inaccessible range (Figure 3.16d, $\chi = 0$). [148] However, also crystallites in other orientations and even in face-on orientation are present in the thin film as some scattering intensity is observed at all accessible χ angles. Scattering data are fitted with a Gaussian function (Figure 3.16, bright green). [230, 231] A broad FWHM implies high rotational disorder of crystallites, whereas a narrow FWHM occurs only for highly ordered crystallites. [148] The crystal size can be estimated by the line broadening of the respective Bragg peak as given by the Scherrer equation (Subsection 2.3.3).

Experimental Parameters for Grazing Incidence X-ray Scattering

All scattering measurements shown in this thesis are performed at the MiNaXS (micro- and nanofocus small- and wide-angle X-ray scattering) beamline P03 at the PETRA III (Positron-Elektron-Tandem-Ring-Anlage) synchrotron source at DESY (Deutsches Elektronen-Synchrotron), Hamburg (Sections 5.1, 5.2, 6.1: Figures 6.1, 6.3, 6.4) or with an in-house Ganesha SAXSLAB instrument (Section 6.1: Figure 6.5). [232] For all scattering experiments, a Dectris Pilatus 1M or a Dectris Pilatus 300k with a pixel size of 172 µm x 172 µm is used to collect the scattering signal. The numbers 1M and 300k denote the overall number of pixels of the respective detectors. The X-ray beam size is 10 µm x 27 µm for all experiments performed at the DESY and 100 µm x 200 µm for the measurement performed with the Ganesha instrument. Table 3.1 gives the SDD, the angle

of incidence (AOI) and the detector type for all GISAXS and GIWAXS measurements performed in the context of this thesis.

Table 3.1.: Parameters applied in the GISAXS and GIWAXS Experiments.

Section/ Figure	Sec. 5.1	Sec. 5.2	Sec. 6.1[1]	Fig. 6.5	Sec. 7.1
X-ray source / parameters	P03	P03	P03	Ganesha	P03
wavelength [nm]	0.09763	0.0965	0.09763	0.154	0.10642
AOI for GISAXS [°]	0.35	0.40	0.35	-	0.40
SDD for GISAXS [mm]	3176	4200	3176	-	5262
Pilatus Detector (GISAXS)	1M	300k	1M	-	1M
AOI for GIWAXS [°]	-	0.40	0.35	0.35	-
SDD for GIWAXS [mm]	-	195	179	95.67	-
Pilatus Detector (GIWAXS)	-	300k	300k	300k	-

[1] Scattering data in Figures 6.1 and 6.3, 6.4.

4 Sample Preparation

4.1. Materials

In the following chapter, the sample preparation, which was performed prior to all experiments performed in the context of this thesis, is introduced. Thus, the applied materials are given in Section 4.1. The substrate cleaning procedure is detailed in Section 4.2. The basic principle of the thin film deposition techniques spin-coating and meniscus guided slot-die coating is described in Section 4.3. The organic solar cell assembly is illustrated in Section 4.4.

PBDB-T-SF

The conjugated low bandgap polymer donor poly[(2,6-(4,8-bis(5-(2-ethylhexylthio)-4-fluorothiophen-2-yl)-benzo[1,2-b:4,5-b']dithiophene))-*alt*-(5,5-(1',3'-di-2-thienyl-5',7'-bis(2-ethylhexyl)benzo[1',2'-c:4',5'-c']dithiophene-4,8-dione))], denoted PBDB-T-SF, was purchased from Solarmer. The chemical structure is given in Figure 4.1a. The high-efficiency polymer PBDB-T-SF was designed for application as electron donor in organic solar cells. [35,233] The benzodithiophene (BDT) unit (Figure 4.1a, green) enhances the electron donating effect of the polymer, increases the hole mobility and contributes to a planar molecular structure, which facilitates π-π stacking and crystallization. [234] The benzo[1,2-b:4,5-c']dithiophene-4,8-dione (BDD) unit (Figure 4.1a, red) has an electron withdrawing effect and facilitates excitation of the polymer by UV/vis light. The thiophene units (Figure 4.1a, black) act as bridges, enlarging the conjugated π-system. In addition, the integration of thiophene units provokes broadening of the absorbance spectrum, lowers the optical bandgap and improves charge transport. In addition, the Coulomb potential between positive and negative charge carriers is reduced due to enlargement of separation distance between electron and hole. [114] Fluorination (Figure 4.1a, blue) of the polymer down-shifts energy levels and increases the device stability. Furthermore, fluorination

contributes to inter/intramolecular interactions with hydrogen atoms, provoking enhanced crystallinity and efficient charge transport. [35] Alkyl side chains (Figure 4.1a, gray) improve the solution-processibility by enhacing the solubility in common organic solvents.

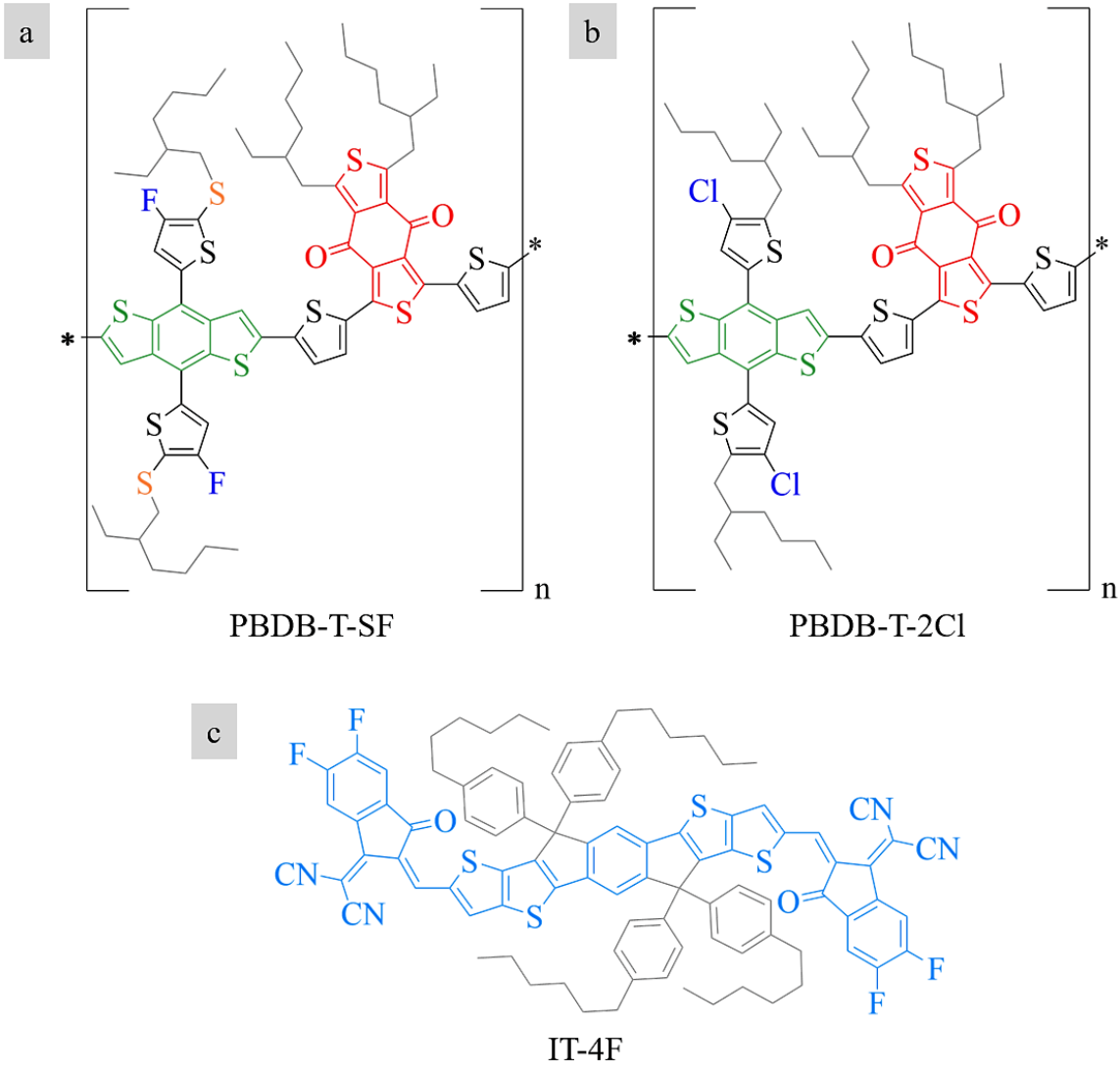

Figure 4.1.: Chemical structures of the conjugated polymers (a) PBDB-T-SF, (b) PBDB-T-2Cl and (c) the nonfullerene small molecule acceptor IT-4F. The conjugated polymers consist of a BDT (green) and a BDD (red) unit linked with thiophene groups (black). The halogen (F or Cl) is indicated in blue color, the sulfur atom (in PBDB-T-SF) in orange and the conjugated π-system of IT-4F in bright blue. For all materials shown, side chains are indicated in gray color.

PBDB-T-2Cl

The conjugated low bandgap polymer donor poly[(2,6-(4,8-bis(5-(2-ethylhexyl-3-chloro)-thiophen-2-yl)-benzo[1,2-b:4,5-b']dithiophene))-*alt*-(5,5-(1',3'-di-2-thienyl-5',7'-bis(2-ethylhexyl)-benzo[1',2'-c:4',5'-c']dithiophene-4,8-dione))], denoted PBDB-T-2Cl, was purchased from Ossila. The chemical structure of PBDB-T-2Cl (Figure 4.1b) resembles that of PBDB-T-SF (Figure 4.1a), therefore the polymers have similar chemical properties, such as broad absorbance and facilitated charge transport. [235] Chlorination (Figure 4.1b, blue) was found to down-shift the energy levels even more efficiently than fluorination, which is assumed to be due to its empty D orbit, which can help to accept π-electrons. [236]

IT-4F

The nonfullerene small molecule acceptor 3,9-bis(2-methylene-((3-(1,1-dicyanomethylene)-6,7-difluoro)-indanone))-5,5,11,11-tetrakis(4-hexylphenyl)-dithieno[2,3-d:2',3'-d']-s-indaceno[1,2-b:5,6-b']dithiophene, denoted IT-4F, was purchased from Solarmer. The chemical structure is given in Figure 4.1c. In contrast to fullerene based acceptors, the energy levels of nonfullerene small molecule acceptors can be fine-tuned by chemical modification of the molecular structure to match with the donor polymer. [237] The conjugated π-system (Figure 4.1c, bright blue) provokes a highly efficient electron transport, whereas alkyl chains ensure solution-processibility. Benzyl groups disrupt the planar molecular structure and weaken unfavorable aggregation of acceptor molecules. This contributes to a nanoscale bicontinuous phase separation and formation of a favorable BHJ structure. [238] Organic solar cells based on a 1:1 ratio of IT-4F and PBDB-T-SF can reach a PCE of 13%, whereas photovoltaics based on PBDB-T-2Cl:IT-4F can achieve a PCE of 14%. [35, 75, 233]

Chlorobenzene

Chlorobenzene (CB) is a common solvent capable of dissolving conjugated polymers and small molecule acceptors. CB (anhydrous, 99.8%) was purchased from Merck. The organic solvent has a density of 1.11 g/cm^3 and a boiling point of 132 °C.

1,8-Diiodooctane

1,8-Diiodooctane (DIO) is a well-established solvent additive used to improve the device performance of organic solar cells. Appropriate volumes of DIO are added to the solution prior to thin film deposition. DIO (anhydrous, 98%) was purchased from Merck. The solvent additive has a density of 1.84 g/cm^3 and a boiling point of 167–169 °C.

Zinc Acetate Dihydrate

Zinc acetate dihydrate was purchased from Merck and used for preparation of the ZnO precursor solution. The salt has a density of 1.74 g/cm^3, a melting point of 237 °C and a molar mass of 183.48 g/mol.

2-Methoxyethanol

2-Methoxyethanol (99.8%) was purchased from Merck and used for preparation of the ZnO precursor solution. The colorless liquid has a density of 0.97 g/cm^3 and a boiling point of 124 °C.

Monoethanolamine

Monoethanolamine (99.5%) was purchased from Merck and used for preparation of the ZnO precursor solution. The colorless, viscous liquid has a density of 1.01 g/cm^3 and a boiling point of 170 °C.

Aluminum pellets

Aluminum pellets (99.99%) were purchased from chemPUR and used as cathode material for inverted organic solar cells. The metal has a density of 2.70 g/cm^3, a melting point of 660 °C and a molar mass of 26.98 g/mol.

Molybdenum(IV) oxide

Molybdenum(IV) oxide (MoO_3, 99.98%) powder was purchased from Carl Roth and used as an electron blocking layer in printed organic solar cells. MoO_3 has a density of 4.69 g/cm^3, a melting point of 805 °C and a molar mass of 143.94 g/mol.

Zinc Powder

Zinc powder (particle size < 63 µm) was purchased from Carl Roth and used for etching of ITO coated glass substrates.

Deionized Water

For all substrate cleaning steps, which require purified water, deionized water produced by a PURELAB CHORUS 1 (VEOLIA) was used.

Alconox®

Alconox®, a laboratory cleaning detergent was purchased from Merck. The powder was dissolved in deionized water (16 g/l) and used for ultrasonic cleaning of ITO coated glass substrates and printer head components.

Acetone

Acetone (99.8%) was purchased from Merck and used for ultrasonic cleaning of ITO coated glass substrates and printer head components. The organic solvent has a density of 0.79 g/cm^3 and a boiling point of 56 °C.

Isopropanol

Isopropanol (99.8%) was purchased from Merck and used for ultrasonic cleaning of ITO coated glass substrates and printer head components. The organic solvent has a density of 0.79 g/cm^3 and a boiling point of 82 °C.

Hydrogen Peroxide

Hydrogen peroxide (H_2O_2, 30%) was purchased from Carl Roth. The oxidizing agent is used for acid cleaning of glass substrates. Hydrogen peroxide has a density of 1.11 g/cm^3 and a boiling point of 107 °C.

Sulfuric Acid

Sulfuric acid (H_2SO_4, 95–97%) was purchased from Carl Roth and used for acid cleaning of glass substrates. The inorganic acid has a density of 1.22 g/cm^3 and a boiling point of 335 °C.

Hydrochloric Acid

Hydrochloric acid (HCl, 37%) was purchased from Carl Roth. The inorganic acid is diluted with deionized water (1:1) and used for etching of ITO coated glass substrates. HCl has a density of 1.19 g/cm^3 and a boiling point of 45 °C.

Glass Substrates

Microscopic slides (7.5 cm x 7.5 cm) were purchased from Carl Roth. After acid cleaning (H_2O, H_2SO_4, H_2O_2, 80 °C, 15 minutes), the glass slides were used as substrates for printing. After thin film deposition, all slides were cut into pieces of 2.5 cm x 2.5 cm.

Indium Tin Oxide coated Glass Substrates

Indium tin oxide (ITO) coated glass slides (7.5 cm x 7.5 cm) with a sheet resistance of 12 ohms/sq were purchased from SOLEMS. All ITO coated glass substrates were ultrasonic cleaned with Alconox®, deionized water, acetone and isopropanol sequentially for 20 minutes before thin film deposition. After slot-die coating the active layer, the substrates were cut into pieces of 2.5 cm x 2.5 cm. The ITO coated glass slides were used as anode material in printed organic solar cells.

4.2. Substrate Cleaning

Acid Cleaning

To remove any impurities or organic traces at the substrate surface, the microscopic glass slides used in this thesis were cleaned in a hot acid bath [239] before slot-die coating the active layer. Therefore, a mixture of 50 ml deionized water, 180 ml H_2SO_4 and 80 ml H_2O_2 is filled in a beaker and placed in a water bath to safely heat the acidic solution to a temperature of 80 °C. The beaker, containing the acid bath, is covered with a watch glass to avoid evaporation. The glass substrates are positioned in a TEFLON™ holder and placed in the acid bath. After 15 minutes, the substrates are removed from the acidic solution and subsequently washed in three beakers filled with deionized water. Finally, each substrate is individually rinsed with deionized water and dried under continuous nitrogen (N_2) flow.

Ultrasonic Cleaning

ITO coated glass substrates are subsequentially ultrasonic cleaned with different solvents to preserve the conductive coating, which would be removed during acid cleaning. The ITO coated glass substrates are put in a TEFLON™ holder and rinsed with deionized water to remove dust particles. Then, the substrates are sequentially cleaned in Alconox®, deionized water, acetone and isopropanol. At each step, the sample holder is placed in a beaker

filled with the respective detergent or organic solvent and placed in an ultrasonic bath. After 20 minutes, the sample holder is removed and rinsed with the cleaning component used in the subsequent step. Finally, the substrates are removed from the sample holder and dried under continuous N_2 flow. Oxygen plasma cleaning is performed directly before thin film deposition.

Plasma Cleaning

Oxygen plasma cleaning is performed with a NANO PLASMA CLEANER (Diener Electronic). The substrates are placed in a vacuum chamber, which is flooded with oxygen. The plasma treatment is performed for 10 minutes (0.4 mbar, 40 Hz, 250 W). The oxygen plasma provokes decomposition of residual organic compounds at the substrate surface. In addition, the wettability of polar solvents such as the ZnO precursor solution is improved as the surface hydrophilicity increases. It should be noted that the subsequent thin film deposition has to be performed immediately after oxygen plasma cleaning as the favorable surface modification is only a temporary effect.

4.3. Thin Film Deposition

Spin-Coating of Hole Blocking Layers

Spin-coating is a well-established technique to prepare homogeneous thin films of solution-processible materials on a laboratory scale. During thin film deposition, centrifugal forces are applied to homogeneously distribute the precursor solution at the substrate surface. Therefore, the substrate is fixed at a plate inside the spin-coater by applying vacuum. Then, the precursor solution is pipetted on top of the substrate before rotating the plate at a well defined speed.

The final dry film thickness d_{dry} is proportional to the initial concentration c_{i} of the precursor solution and inversely proportional to the angular velocity ω as described by the Schubert's equation [240]:

$$d_{\mathrm{dry}} = C c_{\mathrm{i}} \omega^{-\frac{1}{2}} M_{\mathrm{W}}{}^{\frac{1}{4}}, \tag{4.1}$$

with M_{W} being the molar mass of the dissolved material and C being a system-specific parameter, which has to be determined experimentally.

In this thesis, thin ZnO layers are used as hole blocking layers in inverted organic solar cells. Electron transport layers are fabricated using a DELTA 6RT TT spin-coater (Süss MicroTec). To prepare the ZnO precursor solution for spin-coating, 1.000 g Zinc acetate dihydrate, 10.00 ml 2-Methoxyethanol and 284.0 µl Monoethanolamin are stirred at ambient conditions in air for 8 hours. [241] Then, 1500 µl of the precursor solution are pipetted on top of the ITO coated glass substrate before spin-coating at 5000 rotations per minute (rpm) for 60 s. Finally, all substrates are annealed at 200 °C for 60 minutes in air. After cooling down to room temperature, active layers are slot-die coated on top.

Meniscus Guided Slot-Die Coating of Active Layers

In this thesis, all active layers are printed with a custom-made meniscus guided slot-die coater constructed in the context of a Master's thesis [242] (Figure 4.2).

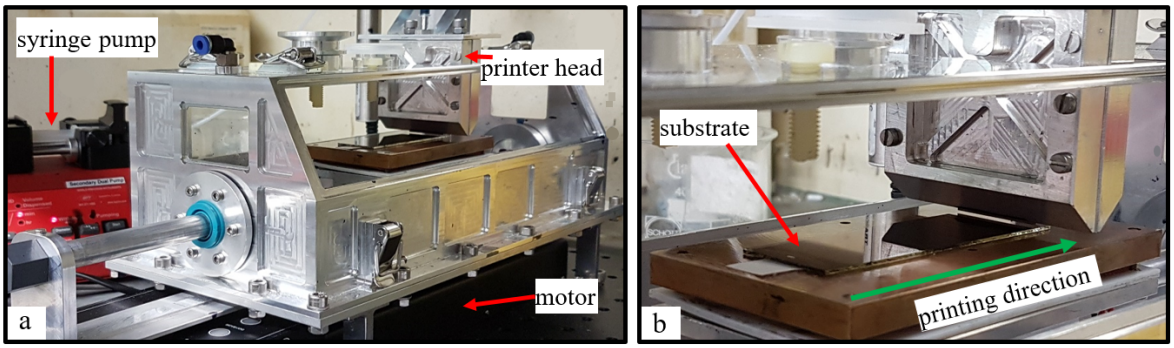

Figure 4.2.: Photographs of the set-up for meniscus guided slot-die coating. Selected components are labeled with red arrows.(a) A syringe pump provides a constant flow rate of solution, which is guided through masks inside the printer head. The substrate can be heated and is moved by a motor during printing. (b) The substrate is placed at the sample holder below the printer head. The printing direction is indicated by a green arrow. Reproduced and adapted with permission from ACS publishing [192].

A syringe pump provides a constant flow rate of the respective polymer:acceptor solution (Figure 4.2a). The solution is guided through a meniscuis guide mask and a shim mask, which are attached inside the printer head. A motor moves the sample holder, consisting of a copper plate with a built-in temperature control unit to enable printing at different temperatures. The substrate is placed on the copper holder (Figure 4.2b) prior to thin film deposition. The printing direction is indicated by a green arrow.

The homogeneity and thickness of the final dry film depend on the adjustable parameters, namely flow rate, printing velocity, height (distance between printer head and substrate), substrate temperature as well as polymer and acceptor concentration in the solution. A photograph of a representative slot-die coated active layer is given in Figure 4.3.

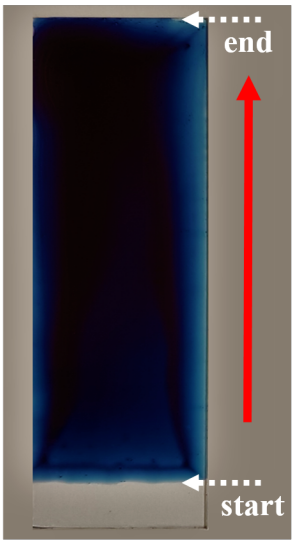

Figure 4.3: Photograph of a slot-die coated active layer based on PBDB-T-SF:IT-4F printed out of CB on a glass substrate (7.5 cm x 2.5 cm). The start and end position are labeled with white arrows. The printing direction is indicated by a red arrow. Reproduced and adapted with permission from ACS publishing [243].

In this thesis, solutions of the polymers PBDB-T-SF or PBDB-T-2Cl and the small molecule acceptor IT-4F are prepared in a N_2-filled glovebox. Compared to spin-coating, which is typically performed with solutions of high concentrations such as 20 mg/ml [35], much lower concentrations are needed for meniscus guided slot-die coating [192] to obtain a similar dry film thickness. Therefore, appropriate amounts of polymer and acceptor are weighted and dissolved in CB to give a 7 mg/ml solution. For PBDB-T-SF:IT-4F, the solution is stirred at 100 °C for 48 hours to dissolve the polymer. Due to high solubility of the chlorinated polymer, solutions containing PBDB-T-2Cl:IT-4F are stirred at room temperature for 4 hours only. Meniscus guided slot-die coating of active layers was performed using optimized printing parameters in order to obtain homogeneous thin films with a film thickness about 100 nm, which is reported to be ideal for application in organic solar cells. [35] In this work, all active layers are printed at ambient conditions with a flow rate of 10 µl/s, a printing velocity of 10 mm/s, a height of 1 mm and a concentration of 7 mg/ml to get a film thickness of (100 ±15) nm. The final dry film is transferred to a N_2-filled glovebox.

4.4. Organic Solar Cell Assembly

Inverted device geometry (glass/ITO/BHJ/MoO_3/Al) is applied for all organic solar cells fabricated in the context of this thesis. All active layers are printed using a custom-made meniscus guided slot-die coater (Section 4.3). ITO coated glass substrates (Section 4.1) are used as substrates and anode material. The conductive coating has to be partly removed. Therefore, the center part of the ITO layer is covered with Scotch tape and zinc powder is distributed over the spare area. Small stripes at the edges of the ITO coated glass substrate are etched away with a button bud tipped into diluted HCl. The remaining zinc powder is removed by rinsing the substrate with deionized water before all substrates are sequentially ultrasonic cleaned and plasma treated (Section 4.2). A photograph of a representative ITO coated glass substrate after etching and cleaning is given in Figure 4.4a. The ZnO precursor solution is spin-coated on top of the ITO coated glass substrate (Section 4.3) before annealing at 200 °C for 60 minutes in air. After cooling down to room temperature, a BHJ layer is printed on top using a CB solution, containing a conjugated donor polymer and a small molecule acceptor as well as appropriate volumes of solvent additive. For all printed organic solar cells, slot-die coating of the active layer was performed at ambient conditions in air. Optimized printing parameters (Section 4.3) are applied to give a film thickness about 100 nm. The final dry film is cut into pieces of 2.5 cm x 2.5 cm to fit into the masks used for physical vapor deposition of blocking layers and electrodes and transferred to a N_2-filled glovebox. Thin layers of MoO_3 (10 nm, 0.2 Å/s) and aluminum (100 nm, 2.0 Å/s) are applied on top of the printed active layer via physical vapor deposition under vacuum (10^{-5} mbar). A photograph of a representative printed organic solar cell based on PBDB-T-SF:IT-4F is shown in Figure 4.4b.

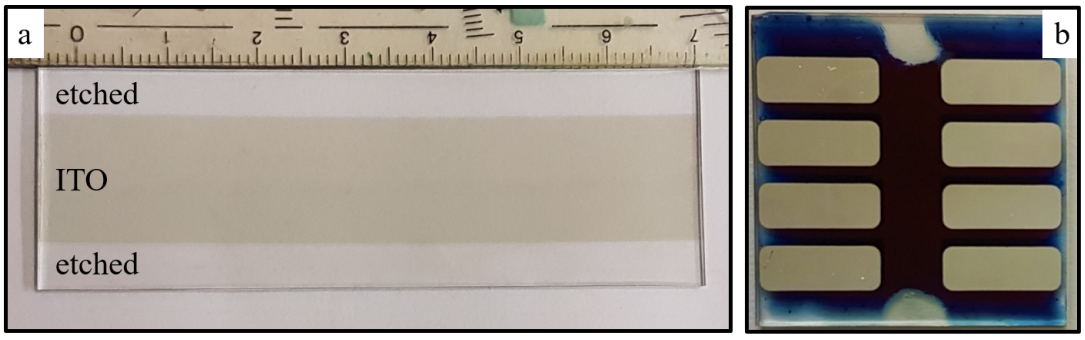

Figure 4.4.: Photographs of (a) an ITO coated glass substrate (7.5 cm x 2.5 cm) after etching and cleaning and (b) a representative slot-die coated organic solar cell based on PBDB-T-SF:IT-4F (2.5 cm x 2.5 cm, 0.12 cm^2 pixel size). Parts of the active layer were removed to enable contacting the anode. Reproduced and adapted with permission from Wiley [177].

5 *In Situ* Printing

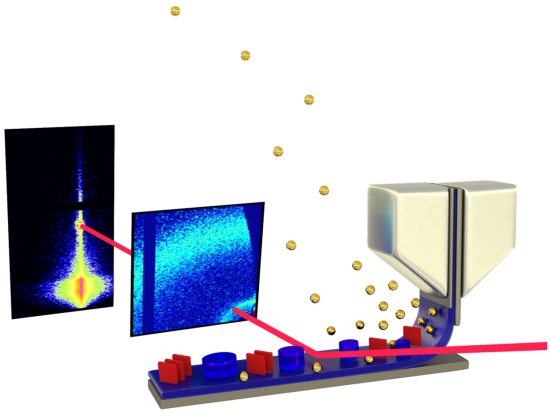

The following chapter is based on the published articles: "*In Situ* Printing: Insights into the Morphology Formation and Optical Property Evolution of Slot-Die Coated Active Layers Containing Low Bandgap Polymer Donor and Nonfullerene Small Molecule Acceptor" [177] (Kerstin S. Wienhold et al., *Sol. RRL*, vol. 4, no. 7, p. 2000086, **2020**, DOI: 10.1002/solr.202000086) and: "Following *In Situ* the Evolution of Morphology and Optical Properties during Printing of Thin Films for Application in Nonfullerene Acceptor based Organic Solar Cells" [243] (Kerstin S. Wienhold et al., *ACS Appl. Mater. Interfaces*, vol. 12, no. 36, p. 40381–40392, **2020**, DOI: 10.1021/acsami.0c12390). Content and images are reproduced with permission from Wiley and American Chemical Society, Copyright 2020.

Printing of active layers for high-efficiency organic solar cells with the slot-die coating technique can overcome the challenge of up-scaling, which will be needed for organic photovoltaics on the way to marketability. The morphology of a bulk-heterojunction (BHJ) organic solar cell has a very high impact on its power conversion efficiency (PCE). Therefore, it is of particular importance to understand the mechanisms of structure formation during

printing of active layers to enable further optimization of the solar cell performance and up-scaling of the production process. In Section 5.1, meniscus guided slot-die coating of the blend of the low bandgap conjugated polymer donor PBDB-T-SF and the nonfullerene small molecule acceptor IT-4F is studied *in situ* with optical microscopy, UV/vis spectroscopy, and grazing incidence small-angle X-ray scattering (GISAXS). Furthermore, a blend of the high-efficiency polymer donor PBDB-T-2Cl and the small molecule acceptor IT-4F is studied *in situ* with GISAXS, grazing incidence wide-angle X-ray scattering (GIWAXS) and UV/vis spectoscopy for different processing conditions (Section 5.2). For both systems investigated, the structure formation is followed from the liquid to the final dry film state. Thereby, five regimes of morphology formation are determined. The morphological evolution in the printed active layer is correlated to changing optical properties of the thin film. In the final dry film, polymer domains of several tens of nanometers are observed, which will be favorable for application in high-efficiency organic solar cells.

5.1. *In Situ* Characterization of PBDB-T-SF:IT-4F

The conjugated low bandgap high-efficiency polymer donor PBDB-T-SF and the non-fullerene small molecule acceptor IT-4F are printed out of chlorobenzene (CB) using a meniscus guided slot-die coating technique at ambient conditions. Morphological changes during film formation after slot-die coating the active layer are studied *in situ* with GISAXS, optical microscopy, and UV/vis spectroscopy. The structure formation is followed from the initial wet to the final dry film and results are correlated to changing optical properties. Five regimes of morphology formation are identified by combining results from *in situ* GISAXS, optical microscopy, and UV/vis spectroscopy.

5.1.1. Optical Microscopy

Active layers based on the conjugated donor polymer PBDB-T-SF and the nonfullerene small molecule acceptor IT-4F are printed out of CB at room temperature at ambient conditions. The slot-die coated thin film is analyzed *in situ* with optical microscopy to follow the phase transition from the liquid state to the final dry film (Figure 5.1). Optical changes at the surface of the printed active layer are observed and five regimes of film formation are suggested from the large-scale structure evolution. During slot-die coating, a solution of PBDB-T-SF and IT-4F, mixed in a 1:1 weight ratio in CB, is deposited on a microscopic glass slide. The initially deposited wet film exhibits a smooth surface without any distinct structure (Figure 5.1a). Within the first 140 s, no significant change occurs on the sample surface. Between 140 and 345 s after processing, slight waves evolve at the

film surface (Figure 5.1b). The curvature is enhanced significantly within the time period between 345 and 460 s (Figure 5.1c). The film reaches a maximum of waviness before the solution is drawn back between 460 and 500 s. Drying occurs from the edges to the center of the substrate (Figure 5.1d). After 500 s, the slot-die coated active layer appears completely dry and no optical changes occur anymore (Figure 5.1e). The final printed film is homogeneous on the length scales resolved with microscopy.

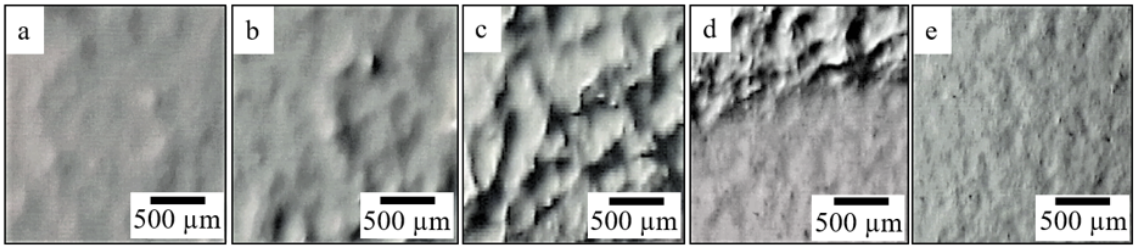

Figure 5.1.: *In situ* optical microscopy of a slot-die coated active layer based on PBDB-T-SF:IT-4F. Representative images are shown for different time periods after processing: a) 0–140 s; b) 140–345 s; c) 345–460 s; d) 460–500 s; e) 500–550 s. Reproduced with permission from Wiley.

The observation of surface waviness and the presence of different film formation regimes resemble findings from earlier *in situ* spin-coating studies of thin polymer films although spin-coating is the much faster process. [244] In an initial stage of spin-coating just as for slot-die coated thin films, a flat uniform surface was reported because a sufficient amount of solvent was present to completely dissolve the blend components. In the second regime, solvent evaporation provoked the formation of a heterogeneous solution and larger length scale structures about 100 µm, originating from Marangoni instabilities, were observed during spin-coating. After further solvent evaporation, a dry blend film resulted. Compared to spin-coated polymer films, on the mesoscopic scale, printed active layers show a similar drying behavior, even though five phases instead of three regimes can be distinguished and the time scales differ considerably.

5.1.2. UV/vis Spectroscopy

To further investigate the evolution of optical properties during printing of active layers based on PBDB-T-SF:IT-4F, *in situ* UV/vis spectroscopy is performed. A full absorbance spectrum is measured at different time steps to follow the transformation of the initial wet film (Figure 5.2a, black) to the final dry film (Figure 5.2a, green). During drying, absorbance of the thin film clearly increases in the wavelength range between 580 and 720 nm, whereas it decreases significantly between 450 and 579 nm. The absorption

onset of the active layer shifts continuously towards lower energies. The bandgap is determined with Tauc plot (Section 3.1) to be (1.63 $\pm$0.04) eV in the initial wet film and (1.52 $\pm$0.04) eV in the final dry film, which resembles values obtained for spin-coated thin films as well. [35]

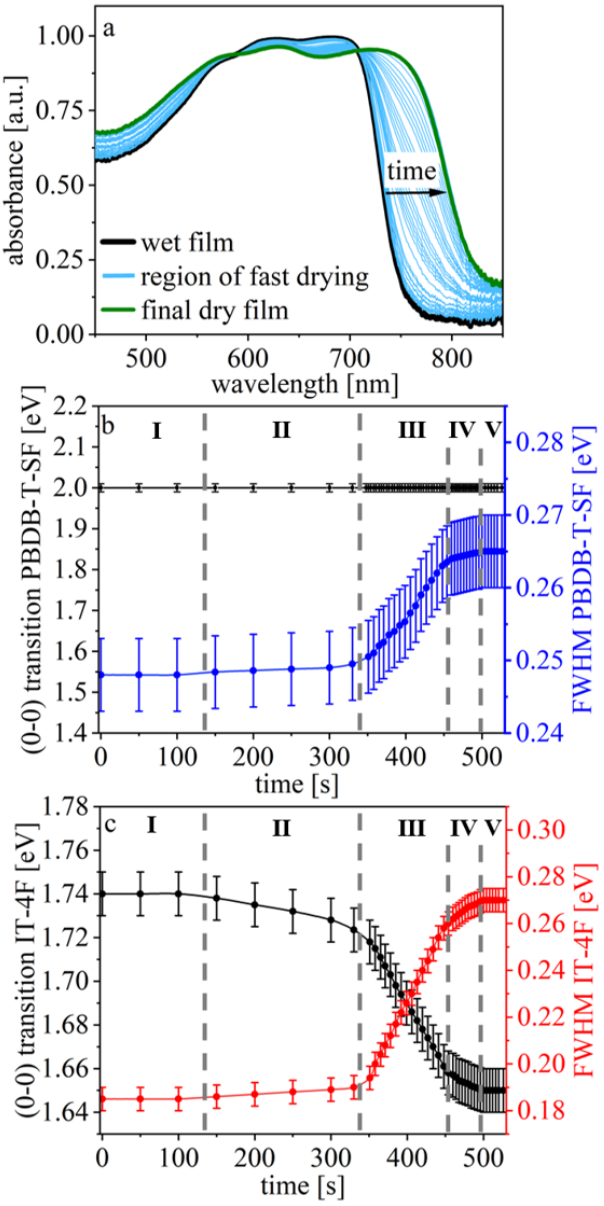

Figure 5.2: *In situ* UV/vis spectroscopy of a slot-die coated active layer. For each time step, the absorbance spectrum is fitted with a set of Gaussian functions of equal width. The broadening is applied equally to all Gaussian functions used in each new fit. a) A continuous change in absorbance (bright blue) is observed during phase transition from the wet film (black) to the final dry film (green). b) For PBDB-T-SF, the energy corresponding to the (0-0) transition (black) and the FWHM of the Gaussian function (dark blue) are shown for different time steps during the drying process. c) For IT-4F, the evolution of the (0-0) transition (black) and the FWHM of the Gaussian function (red) are given during drying of the thin film. Reproduced with permission from Wiley.

Within the first 345 s, only a slight change of absorbance can be observed in the UV/vis spectrum, whereas a pronounced change occurs between 345 and 460 s. Optical transitions are determined by modeling the absorbance data by fitting each UV/vis spectrum with a set of Gaussian functions (Section 3.1), which all have the same width. [178] For PBDB-T-SF and IT-4F, absorbance spectra of a thin film and a dilute CB solution are modeled with this approach to determine the electronic transitions of the polymer and

the small molecule acceptor. In a thin film based on a 1:1 ratio of PBDB-T-SF and IT-4F, electronic transitions of both materials overlap and add up to a broad absorbance spectrum. The UV/vis spectrum obtained for the final dry film has absorbance maxima at (630 $\pm$5) nm and (730 $\pm$5) nm (Figure 5.2a) and equals spectra obtained for spin-coated active layers. The evolution of the (0-0) transition and the broadening of the full width at half maximum (FWHM) of the corresponding set of Gaussian functions are given for PBDB-T-SF (Figure 5.2b) and IT-4F (Figure 5.2c) for different time steps during printing. For each time step, the absorbance spectrum is fitted with a set of Gaussian functions of equal width. Then, the next spectrum is fitted with a new set of Gaussian functions with different width. The width is adjusted for all the Gaussians simultaneously, i.e. the broadening is applied equally to all Gaussians used in each new fit.

In agreement with the results obtained from *in situ* optical microscopy (Figure 5.1), five regimes of film formation can be observed (Figure 5.2b,c). In the initial wet film, no optical changes can be observed within the first 140 s. Between 140 and 345 s, the FWHM of PBDB-T-SF (Figure 5.2b, dark blue) and IT-4F (Figure 5.2c, red) broadens and a slight energy shift occurs for the (0-0) transition of IT-4F (Figure 5.2c, black), whereas the (0-0) transition of PBDB-T-SF (Figure 5.2b, black) does not change significantly during drying of the thin film. A significant change in absorbance (Figure 5.2a, bright blue) is observed between 345 and 460 s. The absorbance of the thin film decreases in the wavelength range between 580 and 720 nm, whereas it increases significantly between 450 and 579 nm. Within the region of fast drying, a significant broadening of the FWHM is measured for both PBDB-T-SF (Figure 5.2b, dark blue) and IT-4F (Figure 5.2c, red) and an energy shift of the (0-0) transition of IT-4F (Figure 5.2c, black) is observed. Between 460 and 500 s, the FWHM of PBDB-T-SF and IT-4F as well as the (0-0) transition of IT-4F in the almost dry film shift slightly. After 500 s, optical properties of the thin film are stable and no further change can be observed.

Table 5.1 shows the electronic transitions for the conjugated polymer and the small molecule acceptor in a slot-die coated active layer for the initial wet film and the final dry film. The (0-0) transition of IT-4F is clearly red-shifted from (1.73 $\pm$0.01) eV to (1.67 $\pm$0.03) eV, an effect, which is well known for many small molecule acceptors. [245,246] The (0-1) transition does not shift significantly, whereas the (0-2) and (0-3) transitions are blue-shifted from (1.92 $\pm$0.01) to (2.03 $\pm$0.03) eV and from (2.01 $\pm$0.01) to (2.22 $\pm$0.02) eV. The width of the set of Gaussian functions increases from (0.185 $\pm$0.005) to (0.270 $\pm$0.005) eV during drying, implying an increase in disorder in the active layer. [178,247] We assume that this increase in disorder originates from formation of different domain sizes in the BHJ

Table 5.1.: Electronic Transitions of IT-4F and PBDB-T-SF in the Initial Wet Film and the Final Dry Film determined by Modeling the UV/vis Spectra with Sets of Gaussian Functions.

material	IT-4F	IT-4F	IT-4F	IT-4F
order of transition	0-0	0-1	0-2	0-3
transition in wet film [eV]	1.74 ± 0.01	1.83 ± 0.01	1.92 ± 0.01	2.01 ± 0.02
transition in dry film [eV]	1.65 ± 0.02	1.84 ± 0.02	2.03 ± 0.02	2.22 ± 0.02
material	PBDB-T-SF	PBDB-T-SF	PBDB-T-SF	PBDB-T-SF
order of transition	0-0	0-1	0-2	0-3
transition in wet film [eV]	2.00 ± 0.01	2.14 ± 0.01	2.28 ± 0.02	2.42 ± 0.02
transition in dry film [eV]	2.00 ± 0.01	2.15 ± 0.01	2.30 ± 0.02	2.45 ± 0.02

layer, different arrangement of polymer chains, depending on surrounding molecules, and a strong interaction between polymer and acceptor molecules. In contrast, in a solution, active materials mainly interact with solvent molecules. During drying of PBDB-T-SF, no significant shift of electronic transitions is observed. The absence of any pronounced bathochromic shift is due to a very effective aggregation of polymer chains in the precursor solution. [248–250] This effect results from fluorination of the polymer, provoking F-H and F-S interactions. [35, 248] Strong intermolecular π-π stacking in the dry film is expected to effectuate improved charge transport between polymer molecules but lowers the solubility of PBDB-T-SF. To minimize unfavorable solvent-polymer interactions, aggregates are formed in solution, facilitating nanophase separation and formation of a BHJ structure in the printed active layer. [251–253] Just as for the acceptor, the width of the set of Gaussian functions for the donor polymer is broadening during drying. The width changes from (0.250 ± 0.005) eV in the wet film to (0.265 ± 0.005) eV in the final dry film, indicating an increasing disorder in the polymer domains during drying of the thin film. [247] The energy shift of electronic transitions, together with an increase in the width of the set of Gaussian functions, provoke an overall broadening of the absorbance spectrum as well as a shift of the bandgap towards lower energies.

In contrast to the five regimes observed for slot-die coated PBDB-T-SF:IT-4F films in this study, only three phases of structure formation were reported for P3HT:PCBM thin films during wet chemical deposition. [62, 63] Wang et al. followed the evolution of the extinction coefficient of doctor bladed thin films with *in situ* ellipsometry. [62] Within the first phase, the absorbance spectra resembled the spectrum of a dilute solution, which

is in agreement with our findings. In the second drying phase, a significant red-shift of absorbance was observed and the extinction coefficient increased. In this study, for printed PBDB-T-SF:IT-4F, this regime is further subclassified as the observed optical changes in thin PBDB-T-SF:IT-4F films occur with different velocities. In the third phase described for P3HT:PCBM, the drying process slowed down until the thin film had fully solidified, whereas in this work, the last regime is defined to be the final dry film only. In addition to these studies, for spin-coated thin films based on P3HT:PCBM, the evolution of absorbance was followed with *in situ* UV/vis spectroscopy as well. [63] In the first stage, reduction of absorbance due to ejection of solution was reported. In the second stage, a steady state was reached. The solvent evaporation was ongoing but did not change the solution state of P3HT. In the third stage, the thin film was in a solid state and the absorbance increased until a plateau was reached. Even though the drying phases observed for doctor bladed or spin-coated P3HT:PCBM and slot-die coated PBDB-T-SF:IT-4F differ, all film formation processes show a red-shift and broadening of absorbance spectra. This is very favorable for application in organic solar cells as the solar spectrum can be exploited more efficiently.

5.1.3. Grazing Incidence Small-Angle X-ray Scattering

The kinetics of inner morphology formation of a slot-die coated active layer is probed via GISAXS. Horizontal line cuts of 2D GISAXS data are performed at the critical angle of PBDB-T-SF (Yoneda region) to trace the evolution during the *in situ* experiment (Figure 5.3). Average structure sizes and corresponding average distances between polymer domains can be obtained by modeling the horizontal line cuts with a model based on the DWBA and the LMA (Subsection 2.3.2). [151, 254, 255] In this model, polymer domains are described as cylindrical structures, which is a common approach in polymer physics to describe polymer thin films. [30, 31, 70]

Figure 5.3b shows data points obtained from the scattering experiments (black dots) as well as the modeling results (red line) from the beginning (bottom) to the end of the drying process (top). Structure parameters are obtained by modeling the horizontal line cuts with three substructures (Figure 5.4). For the photovoltaic performance, the medium structure size (Figure 5.4, blue), which is about (40 $\pm$1) nm for the final dry film, is most relevant as it fits typical exciton diffusion lengths. [108, 109] In the vertical line cuts of 2D GISAXS data, no characteristic scattering signal of correlated roughness [256–258] is observed (Figure A.5). Thus, along the surface normal, no enrichment layers are present.

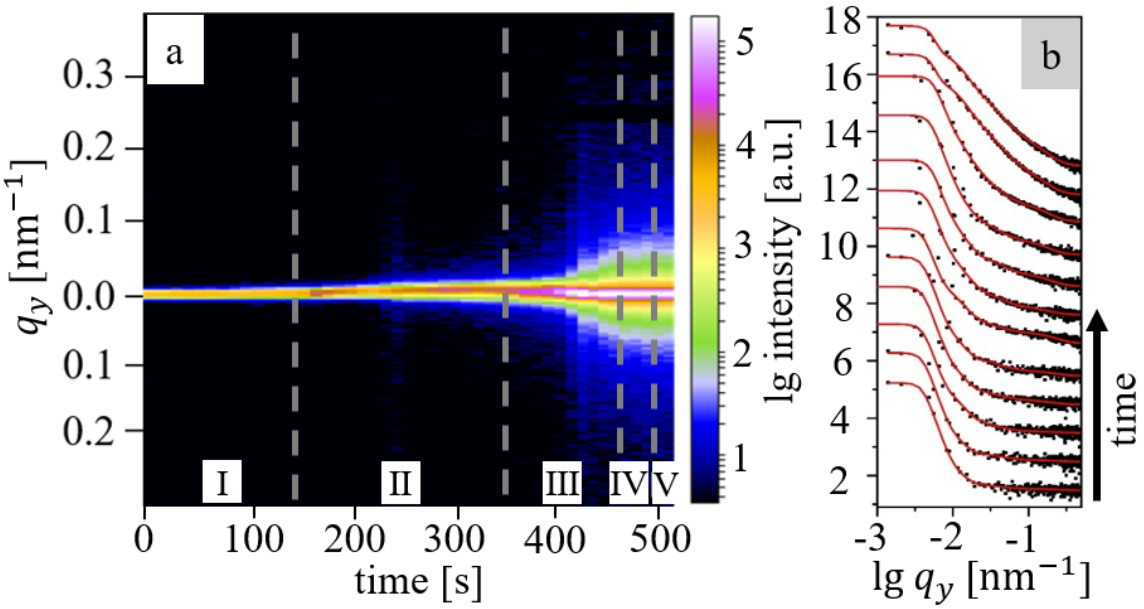

Figure 5.3.: *In situ* GISAXS follows the morphology change during drying of a slot-die coated thin film of PBDB-T-SF:IT-4F. a) Color mapping of horizontal line cuts performed at the critical angle of the polymer over time shows five regimes of film formation. b) Stacking of horizontal line cuts (black dots) and modeling results (red lines) from the initial wet film (bottom) to the final dry film (top) by applying a model based on the DWBA and the LMA. Data are shifted along the intensity axis for clarification. Reproduced with permission from Wiley.

In the *in situ* GISAXS experiment, five regimes of film formation, which are in agreement with the phases determined with *in situ* UV/vis spectroscopy, are distinguished (Figure 5.4 and 5.5). In the initial time period after processing, the wet film shows no significant morphological change within the first 140 s. However, some polymer agglomerates already exist in the very beginning (Figure 5.4a and 5.5, blue cylinders) and solvent molecules evaporate (Figure 5.5, golden spheres). Structure sizes are about (100 $\pm$2) nm for the largest (Figure 5.4a, black), (26 $\pm$1) nm for the medium (Figure 5.4a, blue) and (4 $\pm$1) nm for the smallest structure (Figure 5.4a, green). The corresponding distances are about (450 $\pm$10) nm, (130 $\pm$7.0) nm, and (80 $\pm$5.0) nm (Figure 5.4b). Between 140 and 345 s after thin film deposition, polymer chains in solution start to be integrated in the cylindrically shaped polymer domains (Figure 5.5, blue chains and cylinders). In this region, the three substructures grow slowly and reach average domain sizes of (105 $\pm$1) nm, (31 $\pm$1) nm, and (6 $\pm$1) nm, whereas the average distances do not change (Figure 5.4 and 5.5). In the third region, occuring between 345 and 460 s, distinct and fast growth of structures is visible, whereas the average distances do not change significantly (Figure 5.4 and 5.5). The average structure sizes grow to (107 $\pm$1) nm for the largest, (40 $\pm$1) nm

for the medium, and (7 ±1) nm for the smallest domain size. In the fourth region, occuring between 460 and 500 s, the thin film is almost dry and structures stop growing (Figure 5.4a and 5.5). Within this region of drying, residual solvent evaporates, provoking compaction [259,260] of the thin film and a reduction of average distances to (410 ±8) nm, (100 ±7) nm, and (57 ±5) nm for large, medium, and small structures (Figure 5.4b). In the final region, occuring after 500 s, the thin film is completely dry and average domain sizes and corresponding distances are stable (Figure 5.4 and 5.5). The dry film morphology of slot-die coated thin PBDB-T-SF:IT-4F films with structure sizes of some tens of nanometers is in agreement with structure sizes observed with AFM at the surface of spin-coated thin films, although the largest structure size is not reported in the earlier work. [35]

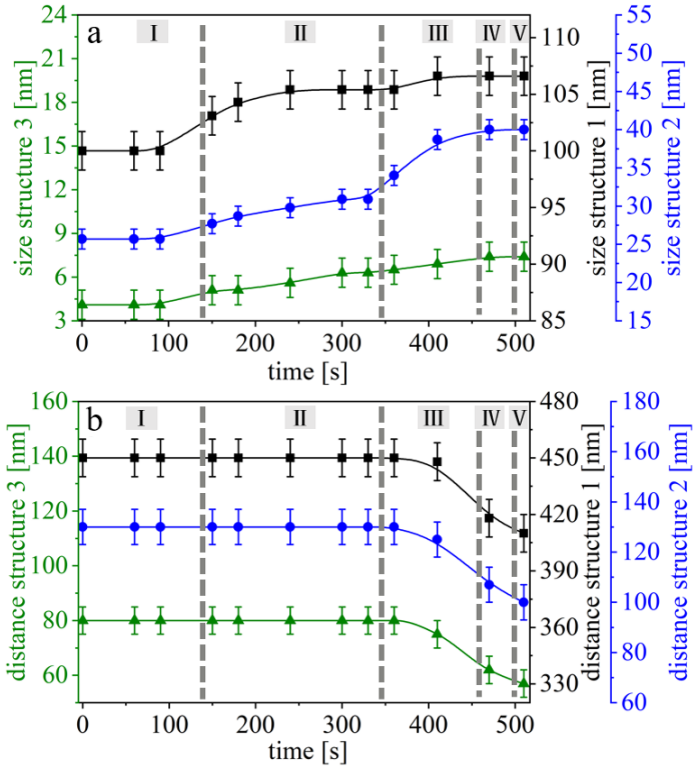

Figure 5.4: a) Average structure sizes and b) average distances obtained by modeling horizontal line cuts of the *in situ* GISAXS experiment. Structure evolution, occurring during the *in situ* GISAXS experiment, is shown for the largest (black squares), medium (blue circles), and smallest (green triangles) polymer substructure. Error bars give an estimate about the fit precision and give a range in which the fit still describes the data. Five regimes of film formation can be distinguished and are denoted I–V. Splines are guides to the eye. Reproduced with permission from Wiley.

In previous studies on printed thin films based on different materials, three or five phases of structure formation were reported from *in situ* GISAXS and grazing incidence X-ray diffraction (GIXD) experiments. For example, in case of active layers based on DPPBT:PCBM, only three regimes were distinguished. [54] In the first phase, the material was well dissolved. In the second phase, solvent evaporated quickly, provoking polymer aggregation. In the third phase, further aggregation, formation of fibrils, and quick crystallization occurred until the final morphology was reached. For doctor bladed thin

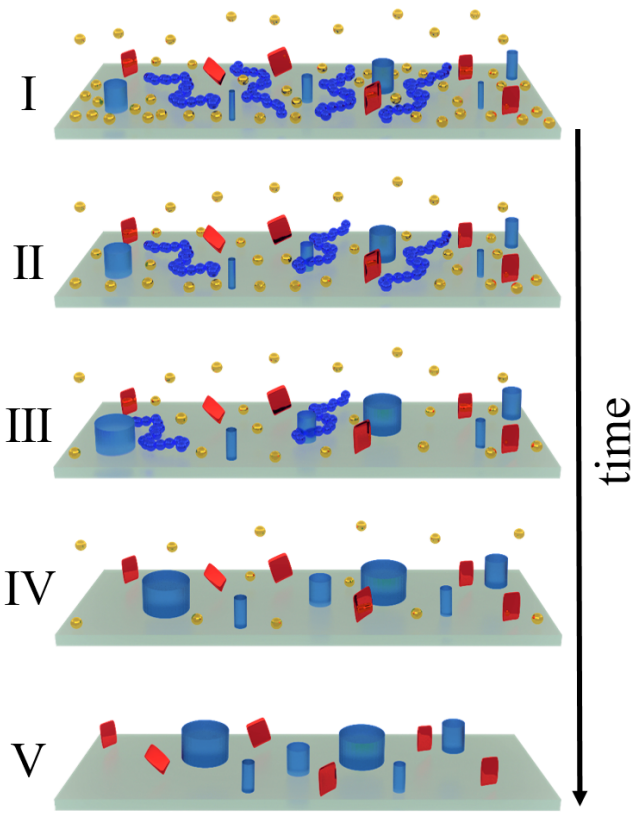

Figure 5.5: Schematic of structure evolution during drying of the printed active layer over time (from top to bottom), showing selected building blocks from the active layer morphology. Three sizes of polymer substructures (blue cylinders), polymer chains in solution (blue chains), the small molecule acceptor (red cuboids), and solvent molecules (golden spheres), evaporating during the drying process, are shown. Five stages of drying are illustrated. (I) Some polymer domains already exist in the beginning and solvent molecules evaporate. (II) Domains grow by incorporating polymer chains. (III) Distinct structure change and evaporation of solvent occurs. (IV) Polymer domains stop growing and average distances decrease. (V) The final dry film with stable morphology is observed. Reproduced with permission from Wiley.

films based on pBTT-C14:PCBM, five regimes were observed, differing from the five phases observed for slot-die coated PBDB-T-SF:IT-4F films. [61] In the first phase, the solvent evaporated quickly, whereas the solubility limit was increased by remaining solvent additive. In the second phase, interlamellar spacing decreased and crystallinity increased, whereas the distances observed in PBDB-T-SF:IT-4F were constant in this regime. In the third phase, solvent additive evaporated and further crystallization occurred, whereas for PBDB-T-SF:IT-4F rapid growth of amorphous domains was reported. In the fourth phase, backbone spacing decreased, resulting in a denser packing of the polymer, which resembled the observed decrease in distances in thin PBDB-T-SF:IT-4F based films. In the fifth phase, the film was dry and no further change of morphology occured. In addition, also for slot-die coated P3HT:PCBM, five regimes were distinguished with GISAXS, which again differ in the details from the five phases observed for pBTT-C14:PCBM or PBDB-T-SF:IT-4F. [97] The first phase was described as a well dissolved state. In the second phase, the domain radius increased slowly, whereas a fast decrease in distances was observed. In contrast, for PBDB-T-SF:IT-4F, distances did not change in this regime. In the third phase, a rapid structure growth and slight increase in distances occured, which is in contrast to the constant distances observed during printing of PBDB-T-SF:IT-4F and pBTT-C14:PCBM. In the fourth phase, a further structure growth was observed

and distances were constant, whereas no structure growth but a decrease in distances is observed for the other systems. In the last phase, the thin film was dry and stable. Therefore, the observed stages of structure formation differ significantly for different material systems, indicating that knowledge gained from one system cannot simply be transferred to another system.

5.1.4. Discussion

In *in situ* optical microscopy, UV/vis spectroscopy, and GISAXS, five regimes of film formation can be observed. Five stages were already reported for printing of P3HT:PCBM thin films. [97] In the initial time period after processing, the slot-die coated thin film is wet and no significant change of optical properties (Figure 5.1 and 5.2) or morphology (Figure 5.4) occurs within the first 140 s. Between 140 and 345 s, average structure sizes of polymer domains start to grow slowly (Figure 5.4a), absorbance of the thin film changes (Figure 5.2), and surface waviness (Figure 5.1b) increases simultaneously. In the third region of drying, occuring between 345 and 460 s, distinct and fast growth of nanostructures can be observed (Figure 5.4a), provoking a very pronounced change of optical properties in the active layer (Figure 5.2). The bandgap of the active layer clearly red-shifts from (1.63 $\pm$0.04) eV to (1.52 $\pm$0.04) eV and a shift of energy levels occurs. Data modeling with sets of Gaussian functions shows a broadening FWHM for the polymer and the acceptor (Figure 5.2b,c), indicating an increase in disorder in the active layer. In addition, distinct waves are visible at the sample surface (Figure 5.1c). Between 460 and 500 s, average distances between the polymer domains are reduced (Figure 5.4b) in the almost dry film and a withdrawal of solution from the edges to the center of the substrate is visible in optical microscopy (Figure 5.1d). A slight broadening of the FWHM can be observed for PBDB-T-SF and IT-4F as well as a shift of the (0-0) transition of IT-4F (Figure 5.2b,c). After 500 s, the slot-die coated active layer has solidified and the morphology and optical properties are stable. Thus, the structure formation of PBDB-T-SF:IT-4F films during slot-die coating differs from that reported in earlier studies performed on other material systems. Therefore, new and promising materials need to be studied individually to understand their structure formation process, which will be prerequisite for further optimization of the printing process and the device performance. In the following chapter, the evolution of morphology and optical properties is studied *in situ* for slot-die coated active layers based on the conjugated donor polymer PBDB-T-2Cl and the nonfullerene small molecule acceptor IT-4F (Section 5.2).

5.2. *In Situ* Characterization of PBDB-T-2Cl:IT-4F

Active layers based on the conjugated polymer donor PBDB-T-2Cl and the nonfullerene small molecule acceptor IT-4F are printed with a slot-die coating technique and probed *in situ* with GISAXS, GIWAXS and UV/vis spectroscopy. The morphology formation is followed from the liquid state to the final dry film for different printing conditions (at 25 °C and 35 °C), and five regimes of film formation are determined. Morphological changes are correlated to changing optical properties. During film formation, crystallization of the nonfullerene small molecule acceptor takes place, and polymer domains with sizes of some tens of nanometers emerge and a red-shift of the optical bandgap as well as a broadening of the absorbance spectrum occurs.

5.2.1. Grazing Incidence Small-Angle X-ray Scattering

In situ GISAXS follows the evolution of mesoscale structures during film formation of PBDB-T-2Cl:IT-4F based active layers printed with a meniscus guided slot-die coating technique. Horizontal line cuts of 2D GISAXS data are performed at the critical angle of PBDB-T-2Cl (Yoneda region) to obtain material sensitive information. The critical angle for PBDB-T-2Cl is calculated to be 0.10° for the applied X-ray energy of 12.85 keV. Below the critical angle of the polymer, total reflection occurs, whereas at higher incident angles, the X-ray beam penetrates the thin film.

Figure 5.6 shows the temporal evolution of the horizontal line cuts. Five regimes of film formation (I-V) are indicated for the active layer printed at a substrate temperature of 25 °C (Figure 5.6a,b) and 35 °C (Figure 5.6c,d). The overall drying time and extension of the regimes are reduced due to heating, a behavior which was already observed in a previous *in situ* study. [261] Horizontal line cuts are modeled with a well-established model based on the EIA of the DWBA (Subsection 2.3.2), a first order perturbation theory, taking into account that the X-ray beam can be reflected at an interface before or after being scattered at the scattering object or both. The model is combined with the LMA, assuming locally nearly monodisperse domains, which can change on a mesoscopic scale. Thus, average structure sizes and distances of polymer domains can be determined. [151, 254, 255] For PBDB-T-2Cl, three cylindrical substructures are used to model horizontal line cuts, which describes average inner film structures in a statistical way and is well-established in the analysis of printed polymer films. [30, 31, 70] Examples of these model fits are seen in Figure 5.6b,d (red lines).

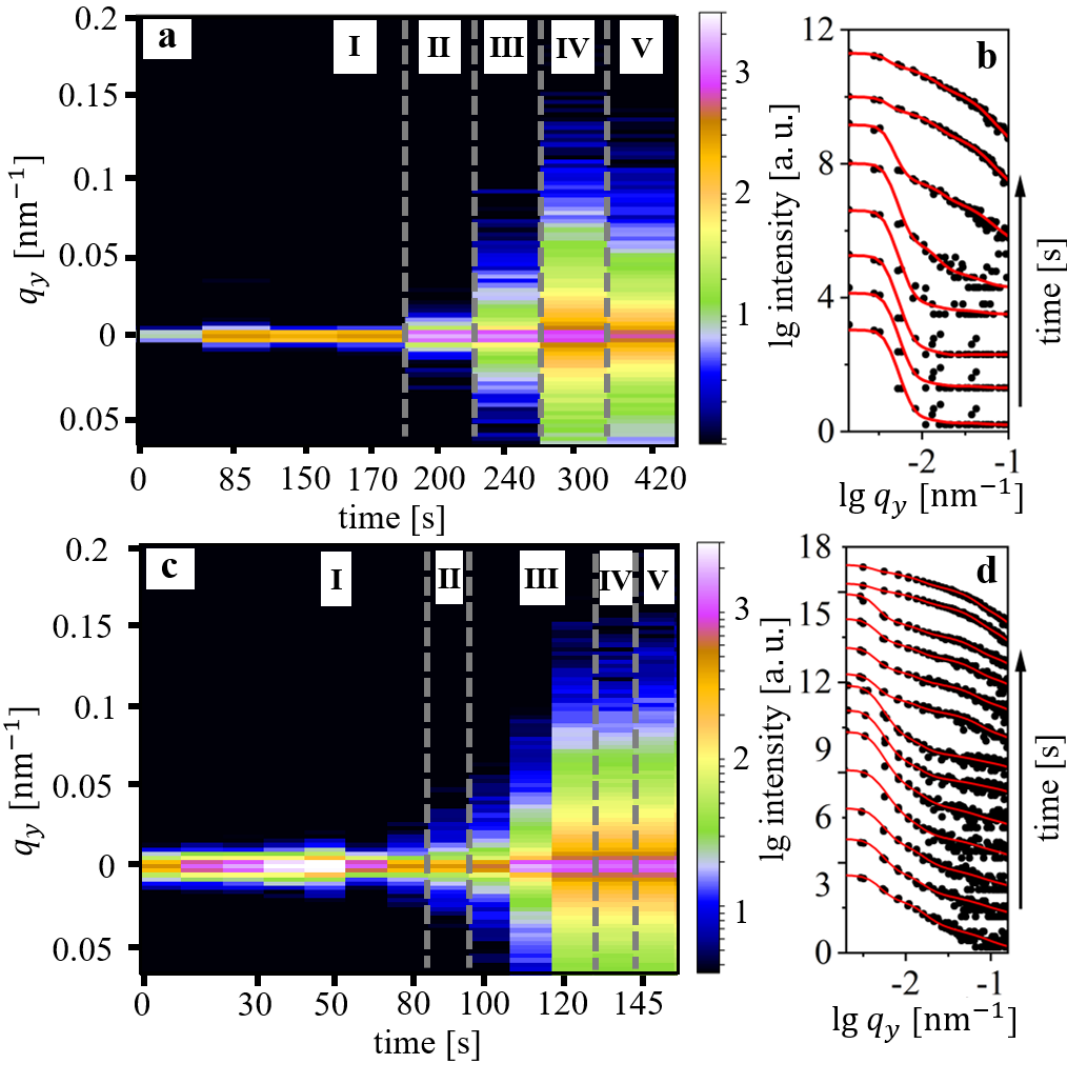

Figure 5.6.: *In situ* GISAXS probes the structure evolution during film formation of thin films printed at (a,b) 25 °C and (c,d) 35 °C. (a,c) In the 2D color mapping, five regimes of film formation (I–V) are separated by vertical dashed lines. (b,d) Horizontal line cuts (black dots) are shown together with best model fits (red lines) to follow the morphological evolution during printing (bottom, wet film; top, final dry film). The horizontal line cuts are shifted along the intensity axis for clarification. Reproduced with permission from ACS publishing.

In Figure 5.7, structure parameters extracted by modeling the horizontal line cuts are depicted. For the evolution of average structure sizes and distances, five regimes of film formation are again distinguished for the film printed at 25 °C (Figure 5.7a,b) and at 35 °C (Figure 5.7c,d). For both printing conditions, film formation undergoes the same mechanism but occurs significantly faster at higher temperatures.

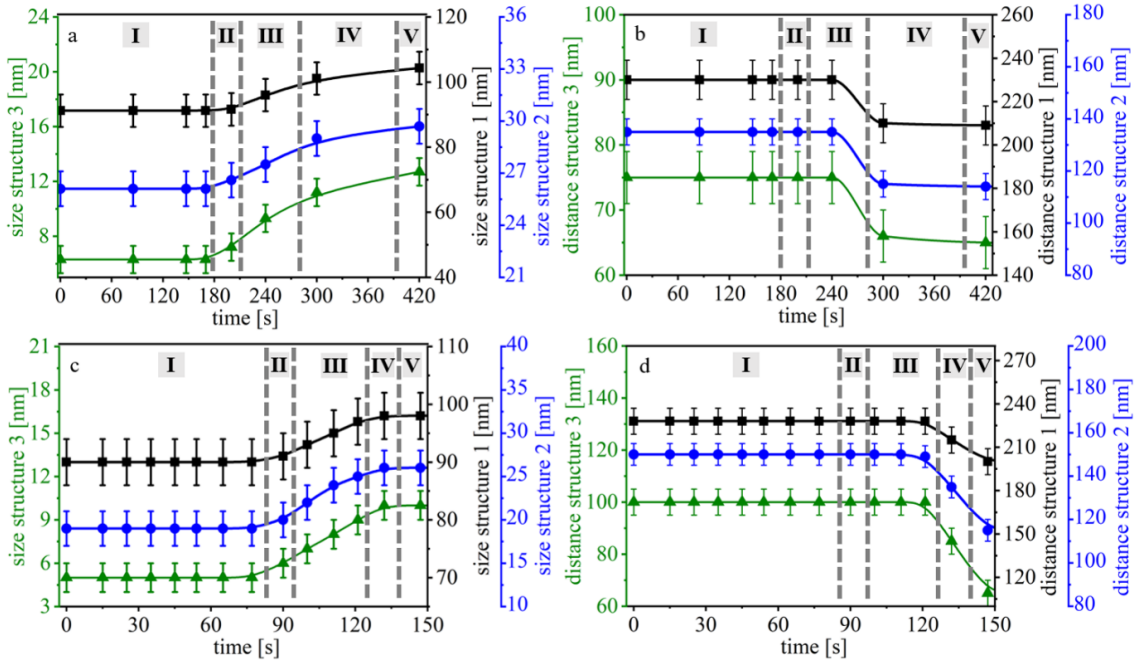

Figure 5.7.: Characteristic structure sizes obtained by modeling horizontal line cuts for thin films printed at (a) 25 °C and (c) 35 °C and corresponding distances for films printed at (b) 25 °C and (d) 35 °C. Morphological evolution during film formation can be followed for the smallest (green triangles), medium (blue circles), and largest (black squares) polymer substructure with error bars, estimating the fit error and giving a range in which the fit still describes the scattering data. Five phases of film formation are determined and denoted I–V. Solid lines are guides to the eye. Reproduced with permission from ACS publishing.

In the first phase, appearing within the first 180 s for 25 °C or 85 s for 35 °C, a wet film is observed. Some polymer agglomerates exist already in the solution, but significant morphological changes do not occur in this regime. For the sample printed at 25 °C, structure sizes are about (91 ±5) nm for the largest (Figure 5.7a, black), (26 ±1) nm for the medium (Figure 5.7a, blue), and (6 ±1) nm for the smallest structure (Figure 5.7a, green), whereas for the film processed at 35 °C, structure sizes of (90 ±5) nm for the largest (Figure 5.7c, black), (19 ±1) nm for the medium (Figure 5.7c, blue), and (5 ±1) nm for the smallest structure (Figure 5.7c, green) are observed in the initial state. Average distances are about (230 ±10), (135 ±5), and (75 ±5) nm for 25 °C (Figure 5.7b) and (230 ±10), (150 ±5), and (100 ±5) nm for 35 °C (Figure 5.7d). In the second regime, occuring until 220 s for 25 °C or 95 s for 35 °C, solvent molecules evaporate and polymer chains start to be integrated in the cylindrically shaped polymer domains, but average distances do not change. In this phase, polymer domains grow to average sizes of (92 ±5), (27 ±1), and (7 ±1) nm at a printing temperature of 25 °C and (91 ±5), (21 ±1), and

(6 ±1) nm for 35 °C, whereas average distances remain unchanged. In the third regime, a rapid structure growth of polymer domains by further integration of polymer chains is observed. For slot-die coating at room temperature, polymer structure sizes grow to (96 ±5), (28 ±1), and (9 ±1) nm between 220 and 280 s, whereas at a temperature of 35 °C, domains grow to average sizes of about (95 ±5), (24 ±1), and (8 ±1) nm in the regime between 95 and 125 s. For both printing conditions, average distances stay constant. In the fourth regime, occuring from 280 to 390 s at 25 °C or from 125 to 135 s at 35 °C, significant reduction of distances starts, whereas slight structure growth is still ongoing. At the end of the fourth phase, structure sizes for the film printed at room temperature are about (100 ±5), (29 ±1), and (11 ±1) nm with distances of (212 ±10), (117 ±5), and (67 ±5) nm. For the active layer slot-die coated at 35 °C, average structure sizes grow to (97 ±5), (25 ±1), and (9 ±1) nm, whereas distances are reduced to (215 ±10), (135 ±5), and (85 ±5) nm. In the last regime, the film is completely dry and the observed morphology is stable. For the film printed at 25 °C, average structure sizes of (105 ±5), (30 ±1), and (13 ±1) nm and distances of (210 ±10), (115 ±5), and (65 ±5) nm are observed in the final dry film. In the active layer slot-die coated at 35 °C, similar distances but smaller average structure sizes are present in the final dry film. Average domain sizes are determined to be about (98 ±5), (26 ±1), and (10 ±1) nm with corresponding distances of (200 ±10), (115 ±5), and (65 ±5) nm. For both printing conditions, the medium structure is assumed to be most relevant for solar cell performance as it fits typical exciton diffusion length scales. [108, 109] Generally, in this work, smaller domains and larger average distances are observed at higher processing temperatures. We assume the initial difference in size and distance of polymer agglomerates occurs due to preheating of the printing solution to the respective thin film deposition temperature. At higher temperatures, the kinetic energy of polymer chains in the solution is enhanced, reducing agglomeration of polymer chains. During drying, higher temperature accelerates solvent evaporation. Therefore, polymer chains have less time to rearrange and attach to growing polymer domains.

Besides lateral structure information obtained by modeling horizontal line cuts, vertical structure information is extracted from vertical line cuts of 2D GISAXS data. Since no characteristic scattering signal of correlated roughness is observed in the vertical line cuts for thin films processed at 25 °C or 35 °C, the printed films do not show enrichment layers irrespective of the printing temperature. [256–258] Thus, discussion of characteristic structures can be restricted to lateral direction. Structure sizes observed for slot-die coated active layers share some similarity with those reported from spin-coated PBDB-T-2Cl:IT-4F based thin films, for which a broad distribution of structure sizes,

ranging from a few nanometers to several hundreds of nanometers, was observed in previous studies. [236] Identification of different film formation regimes during printing was also reported for other systems, even though details of the film formation mechanism such as the temporal evolution of distances were different and are therefore rather material-specific. For example, for slot-die coated P3HT:PCBM, Pröller et al. reported a decrease in distances in the second regime, followed by an increase in interdomain distances in the subsequent regime. [97] In contrast, in the study of PBDB-T-2Cl:IT-4F, average distances do not change within the first three regimes and decrease in the fourth regime only. Concerning the evolution of average structure sizes, the film formation kinetics observed for P3HT:PCBM resembles that of PBDB-T-2Cl:IT-4F and also a similar impact of printing temperature was found in this system. In contrast, in a study performed on printed films based on DPPBT:PCBM, only three regimes of film formation were distinguished. [54]

With respect to the very similar system PBDB-T-SF:IT-4F, basically the same film formation regimes were observed as for PBDB-T-2Cl:IT-4F. [177] In both studies, the active material was slot-die coated out of CB. However, differences are found in the details of film formation. In particular, temporal evolution and duration of the five regimes differs. In comparison to the previous study, the duration of the regimes observed for active layers based on PBDB-T-2Cl:IT- 4F is shorter even for the experiment performed at room temperature. As final dry film thicknesses were very similar, we assume this originates from weaker intermolecular interactions between PBDB-T-2Cl and other polymer or acceptor molecules. Chlorination results in decreased intermolecular packing and overall lower crystallinity compared to the fluorinated counterpart because the size of a chlorine atom is bigger than that of a fluorine atom. [236] In contrast, PBDB-T-SF shows strong intermolecular interaction with other polymer molecules due to attractive F-H and F-S interactions. [35] Therefore, rearrangement of chlorinated polymer chains is facilitated compared to the fluorinated counterpart and a faster formation of the BHJ structure occurs. Experimentally, much higher solubility was observed for PBDB-T-2Cl, indicating enhanced interaction with solvent molecules. In addition, in the initial wet film, the size of the largest substructure was reduced for the chlorinated polymer, indicating weaker aggregation in solution. For the medium substructure, domain sizes were identical, whereas the smallest domain was found to be larger for PBDB-T- 2Cl. In the final dry film, smaller domains were observed for the largest and the medium substructure, whereas the smallest substructure was found to be larger. Therefore, the deviation of structure sizes is smaller for the chlorinated polymer. This is favorable for application in organic solar cells as both very small and very large structures decrease the photovoltaic performance as charge trapping or reduced exciton splitting probability due to decreased interface-to-volume ratio

will occur, respectively. [31, 262] However, the observation of very similar film formation kinetics on the mesoscale indicates that polymers with similar chemical structure can follow a very similar film formation mechanism. This implies that slight chemical modifications will not impact seriously on the film formation process, which facilitates the synthesis of advanced low bandgap polymers with favorable drying kinetics and improved solar cell performance.

5.2.2. Grazing Incidence Wide-Angle X-ray Scattering

To probe the evolution of crystalline structures during film formation of PBDB-T-2Cl:IT-4F based active layers, *in situ* GIWAXS is performed. In Figure 5.8, representative 2D GIWAXS data are shown for different time steps during film formation of thin films printed at 25 °C (Figure 5.8a–d) and 35 °C (Figure 5.8e–h).

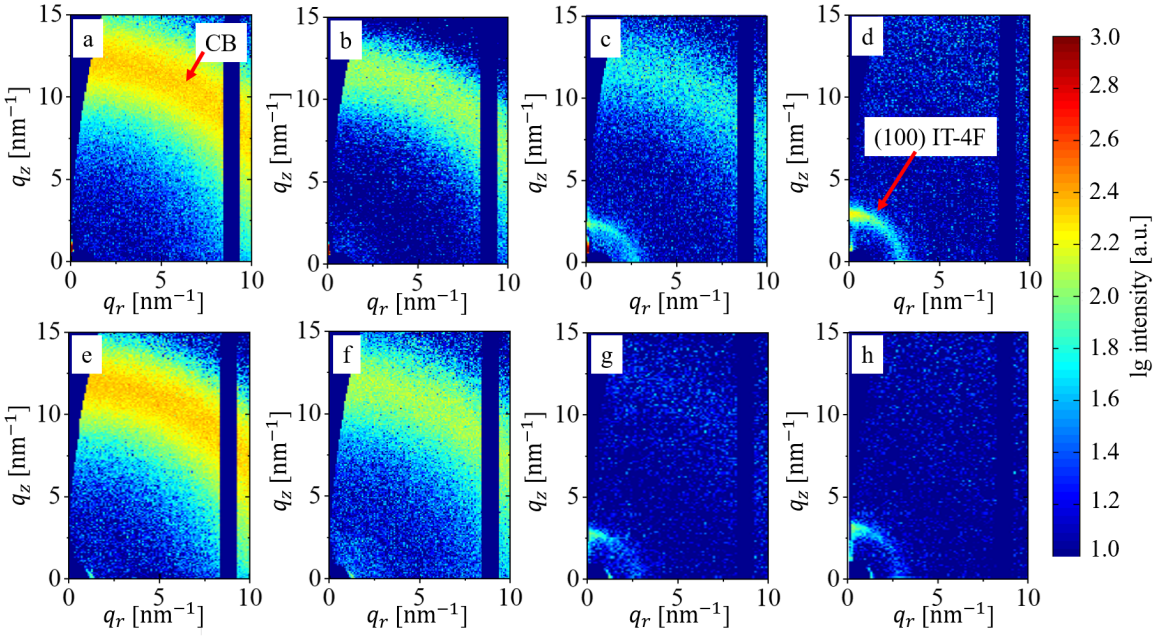

Figure 5.8.: 2D GIWAXS data for different time steps during film formation of active layers printed at (a–d) 25 °C after (a) 120 s, (b) 250 s, (c) 320 s, and (d) 420 s, and at (e–h) 35 °C after (e) 80 s, (f) 120 s, (g) 140 s, and (h) 150 s. The CB peak (marked in image a) vanishes during film formation, whereas the (100) IT-4F Bragg peak (marked in image d) develops. Reproduced with permission from ACS publishing.

After thin film deposition, a strong scattering signal attributed to CB is observed (Figure 5.8a,e), which decreases over time (Figure 5.8b,f). With further solvent evaporation, the (100) IT-4F Bragg peak is observed (Figure 5.8c,g). This peak broadens and increases

in intensity until the final active layer morphology is reached (Figure 5.8d,h). Azimuthal q integrals, covering a q_z range of 1.7–16.7 nm^{-1}, are shown for thin films printed at 25 °C (Figure 5.9a) and 35 °C (Figure 5.9c) to illustrate the decrease in CB content and increase in the (100) IT-4F Bragg peak during drying.

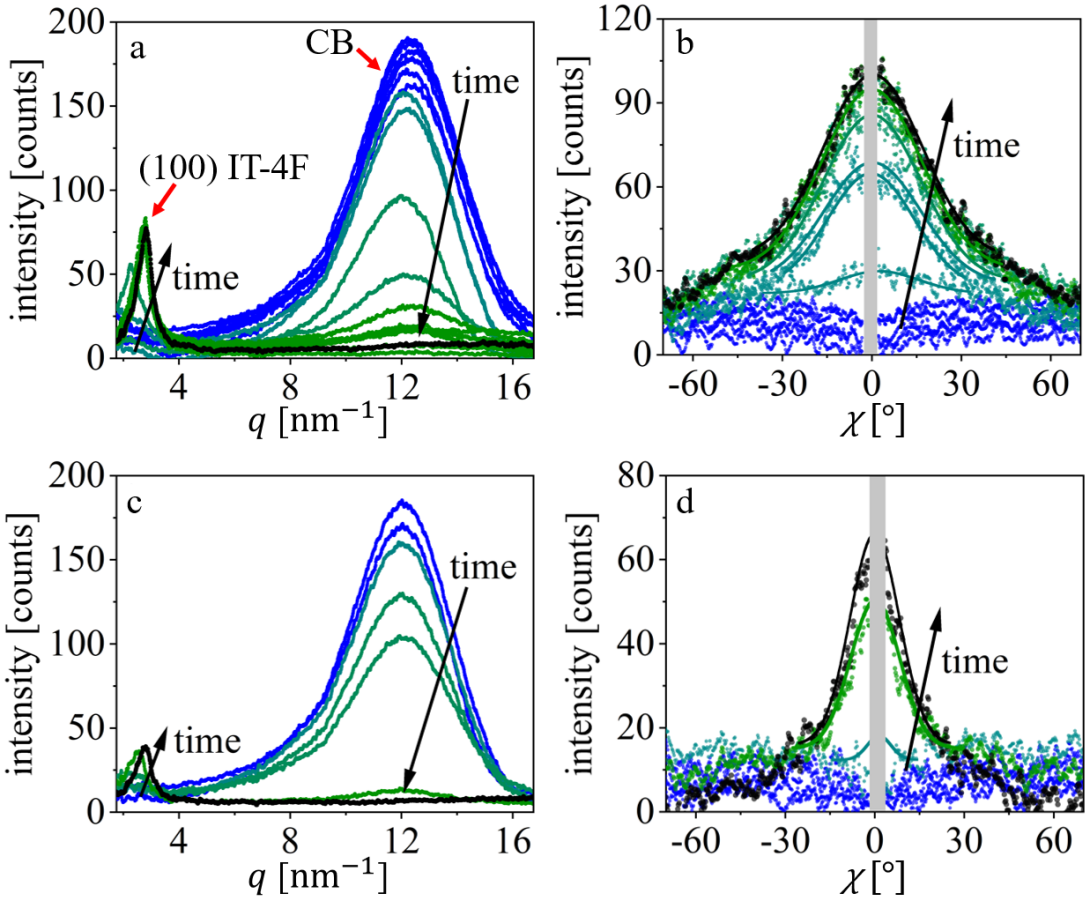

Figure 5.9.: Evolution of (a,c) azimuthal q integrals and (b,d) radial integrals performed at the (100) IT-4F Bragg peak position. The (100) IT-4F Bragg peak and the CB peak are labeled with red arrows (image a). In the azimuthal q integral for films printed at (a) 25 °C and (c) 35 °C, the intensity of the (100) IT-4F Bragg peak increases during film formation, whereas the solvent signal vanishes as indicated by arrows. Tube cuts (dots), performed for films printed at (b) 25 °C and (d) 35 °C, are analyzed by fitting of Gaussian functions (solid lines), increasing in intensity during film formation. The gray bar masks the inaccessible q range. Reproduced with permission from ACS publishing.

The intensity of the (100) Bragg peak in the final dry film is significantly higher for the thin film printed at 25 °C compared to that at 35 °C, indicating higher crystallinity at lower temperatures. At room temperature, it is assumed that the slower drying process provides sufficient time for IT-4F molecules to rearrange and to crystallize. In contrast,

solvent evaporates more rapidly at higher temperatures. As soon as the solvent is removed, molecules are immobilized and cannot crystallize further. For the active layer slot-die coated at 25 °C (Figure 5.9b) and 35 °C (Figure 5.9d), tube cuts (colored dots) are performed in the q range attributed to the (100) Bragg peak of the small molecule acceptor. In agreement with findings from previous studies, the q-position shifts during solvent evaporation. [97] Therefore, tube cuts are performed in a slightly different q range for different time steps during film formation. For the dry film, tube cuts are performed in the q range from 2.65 to 3.15 nm^{-1}, which has been determined to be the (100) IT-4F Bragg peak and can be assigned to edge-on orientation of crystallites. [192, 263] By fitting scattering data with Gaussian functions (solid lines), increase in intensity and broadening are observed during film formation. At room temperature, the FWHM of the Gaussian function increases continuously from (31.4 $\pm$2.8)° to (39.2 $\pm$0.5)° from the first observation of the (100) IT-4F Bragg peak to the final dry film, indicating an enhanced rotational disorder of crystallites in the active layer. For the thin film deposition at 35 °C, the FWHM increases from (9.4 $\pm$1.5)° to (19.8 $\pm$0.5)°. As a result, at lower temperatures, longer overall drying time not only increases degree of crystallinity but also rotational disorder of resulting crystals. [148] Due to edge-on orientation of resulting crystals, charge transport parallel to the electrodes will be facilitated, which would not have a positive effect on the device performance. [148, 264, 265]

In Figure 5.10, decrease in relative CB content (yellow dots) and increase in normalized IT-4F intensity (dark red dots), which is proportional to the number of crystalline domains, are given for different time steps for thin films printed at 25 °C (Figure 5.10a) and 35 °C (Figure 5.10c). Crystal sizes estimated by the Scherrer equation (bright red dots) and shift of the q-position of the (100) IT-4F Bragg peak (black dots), which is inversely proportional to the lattice spacing, are shown for active layers processed at 25 °C (Figure 5.10b) and 35 °C (Figure 5.10d). In agreement with findings from the *in situ* GISAXS experiment, five regimes of film formation are distinguished. In the first regime, occuring within the first 180 s at 25 °C or 85 s at 35 °C, a strong scattering signal originating from the solvent and no scattering contribution from the active materials are observed in the wet film (Figure 5.10a,c). IT-4F molecules are well dissolved in the CB solution. In the second phase, occuring until 220 s at 25 °C or 95 s at 35 °C, relative CB content decreases to (0.95 $\pm$0.17). Rapid solvent evaporation is observed in the third regime, occuring between 220 and 280 s at a printing temperature of 25 °C, and between 95 and 125 s at 35 °C, provoking a decrease in relative CB signal intensity to (0.35 $\pm$0.10) or (0.65 $\pm$0.17), respectively. In the fourth phase, residual solvent evaporates. This causes compaction of the thin film, reduction of lamellar spacing, and rapid crystallization of IT-4F. [259, 260]

For the sample printed at room temperature, the relative IT-4F intensity increases to (0.94 ±0.14), whereas the CB intensity vanishes in the time period between 280 and 390 s. Simultaneously, the q-position shifts from (2.27 ±0.05) to (2.76 ±0.05) nm^{-1} and crystals grow to a size of (9.5 ±1) nm.

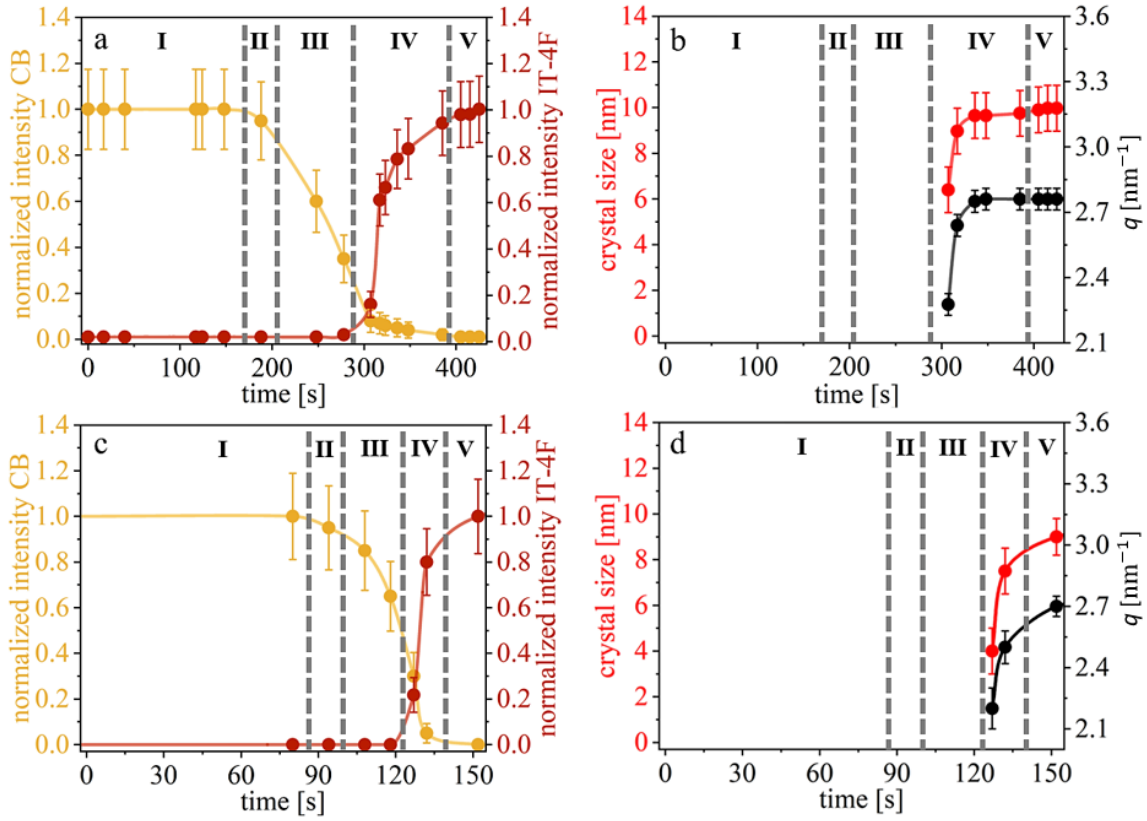

Figure 5.10.: Analysis of GIWAXS data. Intensities of CB (yellow) and IT-4F (red) signals are normalized to the maximum value for thin films printed at (a) 25 °C and (c) 35 °C. Minimum crystallite sizes are estimated by the Scherrer equation (red) and q-positions of the Bragg peaks (black) are shown for thin films processed at (b) 25 °C and (d) 35 °C. Five regimes of film formation (I–V) are separated by vertical dashed lines. Solid lines are guides to the eye. Reproduced with permission from ACS publishing.

For the thin film slot-die coated at 35 °C, the normalized IT-4F intensity increases to (0.80 ±0.16) and the solvent intensity vanishes, whereas crystals grow to a size of (7.5±1) nm and the q-position shifts from (2.20 ±0.05) to (2.70 ±0.05) nm^{-1} between 125 and 135 s. In contrast, amorphous polymer domains, which are observed with GISAXS, have already reached their final size, whereas average distances decrease in this regime. In the fifth region of film formation, the final morphology is present and IT-4F crystals stop growing. For the active layer printed at 25 °C, a crystal size of (10 ±1) nm and a

q-position of (2.76 $\pm$0.05) nm^{-1} are observed in the final dry film. For the sample slot-die coated at 35 °C, a crystal size of (9 $\pm$1) nm with a q-position of (2.7 $\pm$0.1) nm^{-1} is observed. Thus, for both printing temperatures studied, similar crystal sizes and similar lattice spacings are found, but overall crystallinity and rotational disorder are significantly higher for the thin film printed at lower temperature. For both printing conditions studied, crystallites are oriented predominantly edge-on. In agreement with results obtained from the *in situ* GISAXS experiments, details of the film formation mechanism are found to be material-specific and differ in several details from other polymer and acceptor molecules. In previous studies, the evolution of crystalline structures during film formation was studied with GIWAXS and grazing incidence X-ray diffraction (GIXD). For slot-die coated thin films based on DPPBT:PCBM, Liu et al. observed three phases of film formation. The first regime was described as a dissolved state. Rapid solvent evaporation and polymer aggregation occurred in the second phase. In the third regime, fibrils developed and rapid crystallization took place until the final film structure emerged. For P3HT:PCBM, Pröller et al. distinguished five regimes of film formation, differing from the film formation behavior found in this work for PBDB-T-2Cl:IT-4F, in particular concerning the temporal evolution. For the fullerene based active layer, first P3HT crystals were already observed in the second phase. Crystal size and (100) P3HT Bragg peak intensity increased in the third phase, whereas backbone spacing was reduced in the fourth phase. In contrast, for PBDB-T-2Cl:IT-4F, crystal structures were observed later and the rapid growth of crystalline structures occurred simultaneously to the reduction of backbone spacing. Thus, crystallization during film formation depends on chemical details of the used materials.

5.2.3. UV/vis Spectroscopy

The evolution of optical properties during thin film formation is followed *in situ* with UV/vis spectroscopy. At different time steps during film formation, a full absorbance spectrum is probed for active layers printed at 25 °C (Figure 5.11a) and 35 °C (Figure 5.11b). At both temperatures, a similar evolution of optical properties is observed. As expected, the evolution of optical properties occurs much faster at higher temperatures. During film formation, absorbance decreases in the wavelength range between 600 and 700 nm and increases for shorter wavelengths, whereas the absorption onset shifts continuously towards lower energies. For both printing conditions, the optical bandgap is determined with a Tauc plot to be (1.64 $\pm$0.04) eV for the wet film and (1.52 $\pm$0.04) eV for the dry film. Absorbance spectra of slot-die coated PBDB-T- 2Cl:IT-4F thin films have similar peak positions and a similar absorption onset compared to reported spin-coated layers.

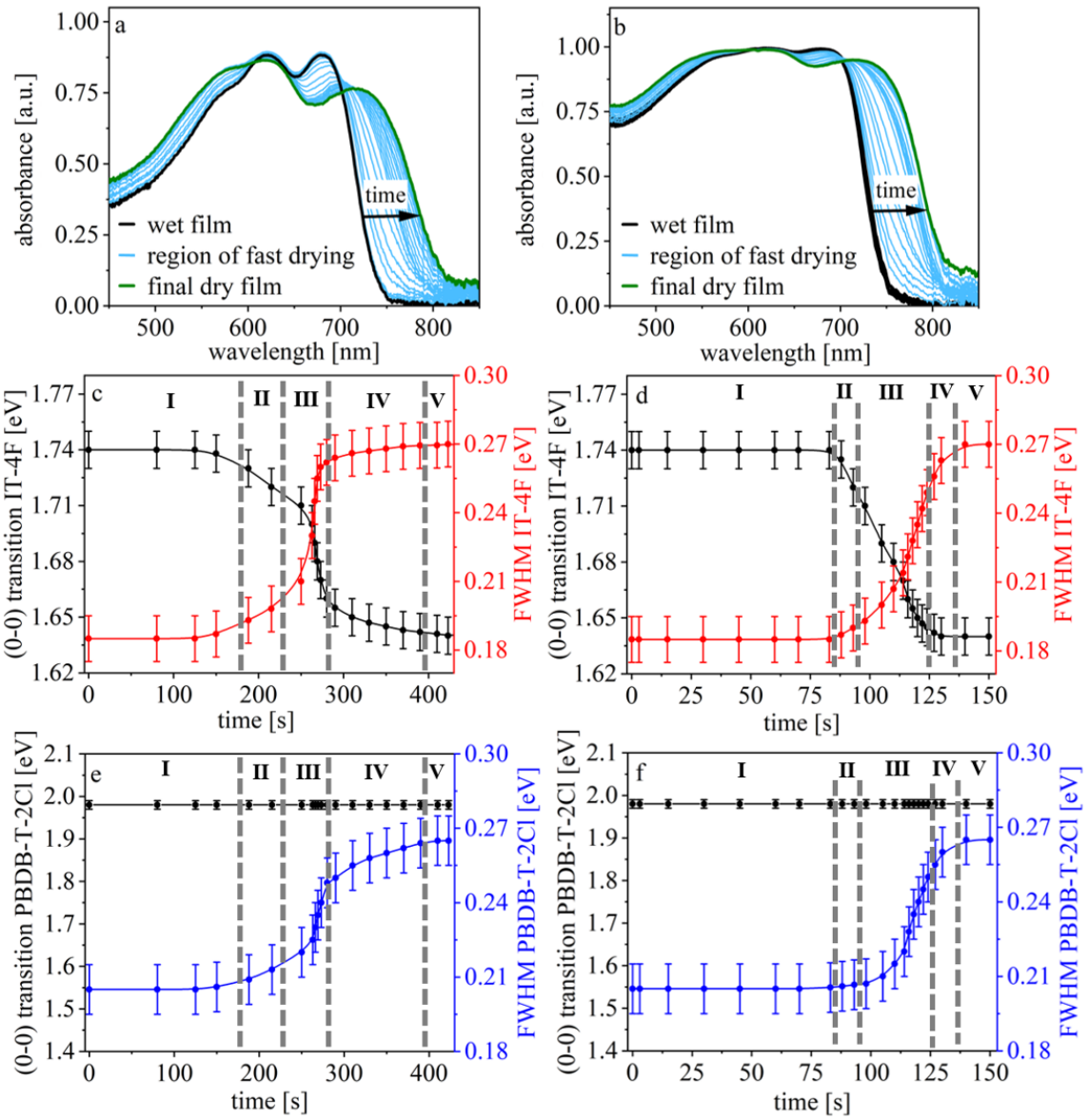

Figure 5.11.: Analysis of *in situ* UV/vis spectroscopy data. A continuous change in absorbance (bright blue) during transition from the wet (black) to the final dry film (green) is observed for thin films printed at (a) 25 °C and (b) 35 °C. The energy, corresponding to the (0-0) IT-4F transition (black), and the FWHM of the corresponding Gaussian function (red) are shown for films printed at (c) 25 °C and (d) 35 °C. For PBDB-T-2Cl, the evolution of the (0-0) transition (black) and the FWHM of the Gaussian function (blue) are shown for different time steps during the film formation process of a thin film processed at (e) 25 °C and (f) 35 °C. Reproduced with permission from ACS publishing.

However, relative intensities of peaks differ, which is assumed to be due to different thin film deposition methods, provoking slightly different inner morphologies. For slot-die coated active layers printed at different temperatures, absorbance spectra normalized on the film thickness show different peak intensities as well. Therefore, it is assumed that the relative peak intensities depend critically on the printing conditions. In comparison to the thin film printed at 35 °C, the active layer printed at 25 °C shows increased absorbance in the wavelength ranges from 550 to 650 nm and from 680 to 750 nm and decreased absorbance at shorter wavelengths. To gain insights into the film formation kinetics, optical transitions are determined by fitting absorbance spectra with sets of Gaussian functions. [178] To follow the evolution of energy levels of optical transitions, each UV/vis spectrum is fitted with a set of Gaussian functions of equal width and the next spectrum is fitted with a new set of Gaussian functions with different width for all of the functions simultaneously.

For both printing conditions, film formation occurred via the same mechanism but significantly faster at higher temperature. Electronic transitions of the acceptor and the polymer as well as the FWHM of the corresponding set of Gaussian functions showed no significant difference for the sample printed at 25 °C compared to that processed at 35 °C. For both printing conditions, the FWHM broadens from (0.185 $\pm$0.005) to (0.270 $\pm$0.005) eV for IT-4F and from (0.205 $\pm$0.005) to (0.265 $\pm$0.005) eV for PBDB-T-2Cl, indicating an increase in disorder in the BHJ layer. [178, 247] This increase in disorder during film formation is assumed to originate from formation of different structure sizes in the active layer, strong interactions between donor and acceptor molecules, and different arrangement of polymer chains due to interaction with surrounding molecules in the thin film. In contrast, in CB solution, polymer and acceptor molecules mainly interact with solvent molecules. In Table 5.2, the (0-0) transitions as well as higher order transitions are shown for the active materials in the wet film and the final dry film.

For the (0-0) IT-4F transition, a significant red-shift from (1.74 $\pm$0.01) to (1.64 $\pm$0.01) eV occurs during drying, which has previously been reported for small molecule acceptors. [75, 245] The (0-1) IT-4F transition does not shift, whereas higher order transitions are blue-shifted during solvent evaporation as the FWHM broadens. Similarly, for PBDB-T-2Cl, the (0-0) transition does not change, whereas higher order transitions are blue-shifted. The evolution of the (0-0) transition and the FWHM of the corresponding set of Gaussian functions are given for IT-4F (Figure 5.11c,d) and PBDB-T-2Cl (Figure 5.11e,f) for active layers printed at 25 °C (Figure 5.11c,e) and 35 °C (Figure 5.11d,f). In agreement with findings from the *in situ* X-ray scattering experiments, five regimes of

Table 5.2.: Electronic Transitions of the Small Molecule Acceptor IT-4F and the Conjugated Polymer PBDB-T-2Cl during Film Formation of Slot-Die Coated Thin Films.

material	IT-4F	IT-4F	IT-4F	IT-4F
order of transition	0-0	0-1	0-2	0-3
transition in wet film [eV]	1.74 ± 0.01	1.83 ± 0.01	1.92 ± 0.01	2.01 ± 0.01
transition in dry film [eV]	1.64 ± 0.01	1.83 ± 0.01	2.02 ± 0.02	2.21 ± 0.02
material	PBDB-T-2Cl	PBDB-T-2Cl	PBDB-T-2Cl	PBDB-T-2Cl
order of transition	0-0	0-1	0-2	0-3
transition in wet film [eV]	1.98 ± 0.01	2.08 ± 0.01	2.18 ± 0.02	2.28 ± 0.02
transition in dry film [eV]	1.98 ± 0.01	2.14 ± 0.01	2.30 ± 0.01	2.46 ± 0.02

film formation are distinguished. In the first phase, occuring within the first 180 or 85 s at a printing temperature of 25 °C or 35 °C, respectively, no change of optical properties occurs. In the initial phase, the (0-0) IT-4F transition occurs at (1.74 $\pm$0.01) eV and the FWHM of the corresponding set of Gaussian functions is (0.185 $\pm$0.005) eV. The (0-0) PBDB-T-2Cl transition occurs at (1.98 $\pm$0.01) eV and does not shift significantly during drying. In the wet film, the FWHM of the polymer is (0.205 $\pm$0.005) eV. In the second regime, occuring between 180 and 220 s at 25 °C or between 85 and 95 s at 35 °C, parameters extracted from fitting with a set of Gaussian functions start to change slightly. The (0-0) IT-4F transition shifts to (1.72 $\pm$0.01) eV, whereas the FWHM broadens to (0.20 $\pm$0.01) eV. For the conjugated polymer, the FWHM broadens to (0.21 $\pm$0.01) eV. In the third phase, occuring until 280 or 125 s for the active layers slot-die coated at 25 °C and 35 °C, respectively, a rapid change of optical properties occurs. The (0-0) IT-4F transition decreases to (1.65 $\pm$0.01) eV. The FWHM broadens to (0.26 $\pm$0.01) eV for IT-4F and (0.25 $\pm$0.01) eV for PBDB-T-2Cl. In the fourth regime, occuring until 390 s at 25 °C or 135 s at 35 °C, the film formation process is slowing but is still ongoing and all parameters reach their final value at the end of this phase. In the fifth regime, the film is dry and optical properties are stable. The (0-0) IT-4F transition occurs at (1.64 $\pm$0.01) eV, and the FWHM is (0.270 $\pm$0.005) eV for the acceptor and (0.265 $\pm$0.005) eV for the polymer.

In contrast to the five phases of film formation observed in this study, only three regimes were distinguished for P3HT:PCBM during film formation. [62,63] Wang et al. observed a significant red-shift of absorbance and an increased extinction coefficient in the second film formation phase with *in situ* ellipsometry. [62] For slot-die coated PBDB-T-2Cl:IT-4F, a

similar red-shift is observed, but this phase is further subclassified in our work, considering that optical changes occur with different velocities. In a previous work performed with PBDB-T-SF and IT-4F, we observed five regimes of film formation with *in situ* UV/vis spectroscopy as well. [177] For PBDB-T-SF and PBDB-T-2Cl, the film formation process occurs via the same mechanism if the polymer is mixed with IT-4F in a 1:1 ratio and printed out of CB. This indicates that materials with similar chemical structure can have a similar evolution of optical properties during film formation. Even though knowledge gained for different materials cannot always simply be transferred to other systems, all film formation processes share similarity, in particular concerning the significant red-shift and broadening of absorbance spectrum, which is assumed to be favorable for application in organic photovoltaics as the sun emission spectrum can be exploited with higher efficiency. [266, 267]

5.2.4. Discussion

The film formation processes of thin films based on PBDB-T-2Cl:IT-4F printed at 25 °C and 35 °C occur via the same mechanism, whereas five phases are tracked with *in situ* GISAXS, GIWAXS, and UV/vis spectroscopy (Figure 5.12).

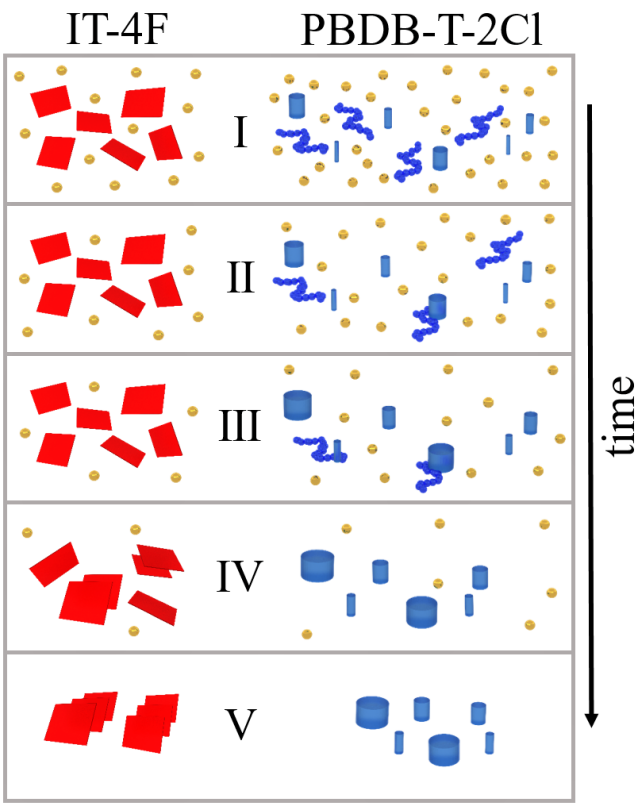

Figure 5.12: Schematic showing temporal evolution of IT-4F and PBDB-T-2Cl domains during film formation. (I) Initially, an excess of solvent (golden spheres) is present and the acceptor (red cuboids) is completely dissolved. Polymer chains (blue chains) and some agglomerates (blue cylinders) can already be observed. (II) Polymer domain growth occurs by attachment of chains. (III) Rapid growth of amorphous structures and solvent evaporation is observed. (IV) Residual solvent evaporates and average distances between polymer domains are reduced. Simultaneously, first IT-4F crystals are observed, which grow fast, whereas the backbone spacing is reduced. (V) The solvent is completely evaporated in the final dry film. Reproduced with permission from ACS publishing.

In the initial wet film, some agglomerates of PBDB-T-2Cl can already be probed with GISAXS, but most polymer chains are well dissolved in CB solution (Figure 5.12I). With GIWAXS, a strong scattering contribution from the solvent occurs, but no crystals are observed as IT-4F molecules are completely dissolved. We assume this is due to the very high solubility of the small molecule acceptor in CB, exceeding that of the conjugated polymer.

In the initial phase, the thin film absorbance is narrow compared to the final state. In the second regime, average polymer structures start to grow and the CB content in the thin film decreases slowly (Figure 5.12II). In this phase, optical properties start to change. The (0-0) IT-4F transition shifts towards lower energies, whereas the absorbance spectrum broadens slightly. In the third regime, rapid solvent evaporation and growth of polymer structures occur (Figure 5.12III). The (0-0) transition of the small molecule acceptor shifts significantly towards lower energies and rapid broadening of the absorbance spectrum occurs. In the fourth phase, the CB almost fully evaporated and the film formation process slows down (Figure 5.12IV). In this regime, polymer structures continue to grow slightly and interdomain distances decrease significantly. With GIWAXS, first IT-4F crystals are observed whose number and size increase rapidly, whereas the lamellar spacing is reduced simultaneously. We assume crystallization of the acceptor takes place at this late stage as high solubility of IT-4F in CB allows the molecule to stay completely dissolved even if only a small amount of solvent remains. Furthermore, a slight shift of the (0- 0) IT-4F transition towards lower energies is observed, whereas the absorbance spectrum continues to broaden slowly. In the fifth phase, the solvent is completely evaporated and the final BHJ morphology is formed (Figure 5.12V).

However, at 35 °C, enhanced temperature provokes faster film formation and formation of slightly different morphology in the final dry film. For the thin film slot-die coated at room temperature, the active materials have more time to rearrange. Therefore, larger amorphous PBDB-T-2Cl structures and higher crystallinity evolve and rotational disorder of IT-4F increases. Average distances between polymer domains observed with GISAXS and crystal size and lattice spacing of crystals observed with GIWAXS are very similar for both printing conditions. In the UV/vis spectra, the electronic transitions occur at the same energy and no bandgap shift is observed, but relative peak intensities differ for the films printed at 25 °C and 35 °C.

5.3. Conclusions

Slot-die coating of thin films based on PBDB-T-SF:IT-4F and PBDB-T-2Cl:IT-4F for application as active layers in high-efficiency organic solar cells is studied *in situ* to follow the evolution of morphology and optical properties from the initial wet film to the final dry film state. Combining results from GISAXS and UV/vis spectroscopy, morphological evolution of PBDB-T-SF:IT-4F is correlated to changing absorbance behavior. In addition, thin films based on PBDB-T-2Cl:IT-4F are studied *in situ* for different processing conditions with GISAXS, GIWAXS and UV/vis spectroscopy. For all systems investigated, we identify five regimes of film formation, which share similarity with earlier studies on printed active layers. However, details of the film formation are system-specific, in particular concerning the temporal evolution of interdomain distances, and the final dry film morphology depends on the printing conditions. For active layers printed at room temperature, higher crystallinity is observed, but due to edge-on orientation of crystals, no positive effect on device performance is expected. In comparison to PBDB-T-SF:IT- 4F based thin films, smaller structure sizes are observed in active layers based on PBDB-T-2Cl:IT-4F for the largest and medium substructure. The presence of smaller structures is favorable for application in organic solar cells as the exciton splitting probability is enhanced due to an increased interface-to-volume ratio. During film formation, edge-on oriented IT-4F crystals are formed. In active layers based on PBDB-T-SF:IT-4F and PBDB-T-2Cl:IT-4F, polymer domains with a size of some tens of nanometers are formed. As this structure size fits typical exciton diffusion lengths, a favorable effect on the solar cell performance is expected. Similar nanoscale structures were observed as well in the respective spin-coated thin films, demonstrating that with slot-die coating well-suited BHJ structures can be prepared as well after optimization of the printing parameters. Red-shift of the optical bandgap and overall broadening of absorbance spectra are observed during drying of slot-die coated active layers, which allows exploiting the sun emission spectrum more efficiently. The *in situ* experiments performed in this work provide insights into the evolution of the active layer morphology and optical properties, which have a high impact on the device performance, and are an important step towards further optimization and up-scaling of the organic solar cell production.

6 Effect of Solvent Additives

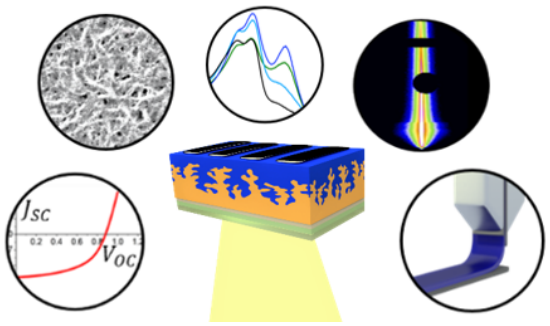

The following chapter is based on the published article: "Effect of Solvent Additives on the Morphology and Device Performance of Printed Nonfullerene Acceptor Based Organic Solar Cells" [192] (Kerstin S. Wienhold et al., *ACS Appl. Mater. Interfaces*, vol. 11, no. 45, pp. 42313-42321, **2019**, DOI: 10.1021/acsami.9b16784). Content and images are reproduced with permission from American Chemical Society, Copyright 2019.

The use of solvent additives is a common approach to control the active layer morphology and improve the performance of organic solar cells. Printing of active layers of high-efficiency organic solar cells and morphology control by processing with varying solvent additive concentrations are important to realize real-world use of bulk-heterojunction (BHJ) photovoltaics as it enables both up-scaling and optimization of device performance. In this chapter, active layers of the conjugated polymer PBDB-T-SF and the nonfullerene small molecule acceptor IT-4F are printed using meniscus guided slot-die coating. 1,8-Diiodooctane (DIO) is added to optimize the power conversion efficiency (PCE). The effect on the inner nanostructure and surface morphology of the material is studied for different solvent additive concentrations with grazing incidence small-angle X-ray scattering (GISAXS), grazing incidence wide-angle X-ray scattering (GIWAXS), scanning electron microscopy (SEM) and atomic force microscopy (AFM). Optical properties are studied with photoluminescence (PL), ultraviolet/visible light (UV/vis) absorption

spectroscopy and external quantum efficiency (EQE) measurements and correlated to the corresponding PCEs. Addition of 0.25 vol % DIO enhances the average PCE from 3.5 to 7.9%, whereas at higher concentrations the positive effect is less pronounced. A solar cell performance of 8.95% is obtained for the best printed device processed with an optimum solvent additive concentration. Thus, with the large-scale preparation method printing, similarly well working solar cells can be realized as with the spin-coating method.

6.1. Inner Structure and Surface Morphology

The donor polymer PBDB-T-SF is mixed with the small molecule acceptor IT-4F in a 1:1 ratio and printed out of chlorobenzene (CB) with different concentrations of DIO using a meniscus guided slot-die coater. The dry thin films have a thickness of around 100 nm, which is ideal for organic solar cells. [35] GISAXS and GIWAXS measurements are performed to analyze the inner nanostructure of the BHJ organic solar cells. [148] An incidence angle of 0.35° is chosen, which is above the critical angle of the polymer and the acceptor molecule. This allows probing the full film thickness and gaining insights into the inner structure. The application of grazing incidence geometry enables to measure thin films (e.g. 100 nm thickness) and to probe a larger sample area, thereby achieving a high statistical significance and quality. [155] In order to analyze 2D GISAXS data, horizontal line cuts (Figure 6.1a) are performed at the critical angle (Yoneda region) of PBDB-T-SF.

Average domain sizes and distances in the BHJ structure are obtained by modeling GISAXS data with a model based on the EIA of the DWBA (Subsection 2.3.2). [151, 254] According to the LMA, the overall scattering intensity can be described by incoherent superposition of scattering intensities of individual domains in the thin film. GISAXS data of printed active layers of PBDB-T-SF:IT-4F with different DIO concentrations are modeled with three substructures of cylindrical shape, which is a well-established approach to describe the polymer thin film morphology over a large range of length scales. [30, 70] Structure sizes (Figure 6.1b) and distances between domains (Figure 6.1c) in the BHJ structure are obtained by modeling the scattering data. [268] Results show decreasing average structure sizes and growing average distances with increasing DIO concentration. Active layers printed without solvent additive yield average structure sizes of (103 $\pm$1) nm, (39 $\pm$1) nm and (11 $\pm$1) nm, whereas the addition of only 0.25 vol % DIO decreases the average structure sizes to (83 $\pm$1) nm, (29 $\pm$1) nm and (10 $\pm$1) nm. This effect is favorable for the solar cell performance as charge transfer from the polymer to the small acceptor molecule is facilitated by gaining interface area. [93] At higher solvent additive concentrations, the morphology is further altered. Average domain sizes are reduced to (79 $\pm$1) nm,

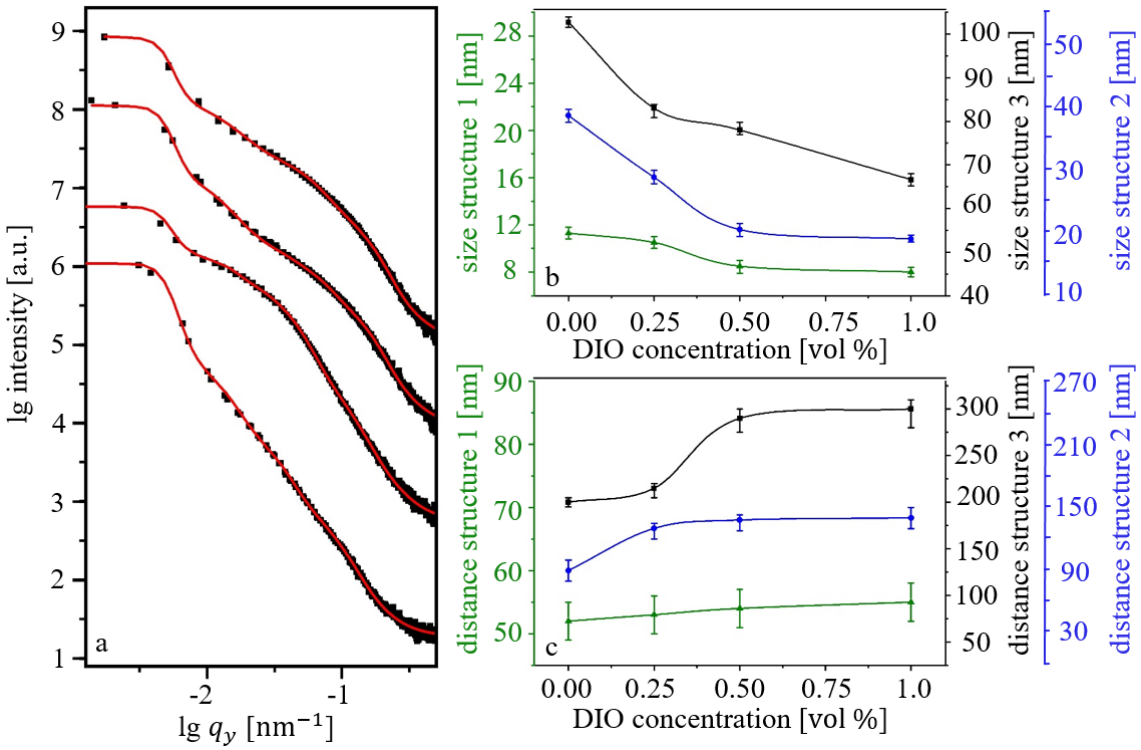

Figure 6.1.: (a) Horizontal line cuts of 2D GISAXS data (black dots) and modeling results (red lines) obtained for printed active layers with different DIO concentrations in CB solutions (0.00, 0.25, 0.5 and 1.0 vol % DIO from bottom to top); (b) average domain sizes for different DIO concentrations obtained by modeling; (c) average distances in the BHJ structure for different DIO concentrations. Splines (b and c) are guides to the eye. Reproduced with permission from ACS publishing.

(21 ±1) nm and (9 ±1) nm for 0.50 vol % and (67 ±1) nm, (19 ±1) nm and (8 ±1) nm for 1.0 vol % DIO. This reduction of average domain sizes can cause a decrease in the PCE due to a charge trapping assisted recombination mechanism. [113] Average distances between domains grow from (200 ±10) nm, (90 ±10) nm and (52 ±8) nm in the case of solvent additive free active layers to (215 ±10) nm, (130 ±10) nm and (53 ±8) nm for thin films processed with 0.25 vol % DIO. Enlargement of distances between donor and acceptor domains can provoke charge stabilization and lower the probability of recombination by reduction of Coulomb forces. [114, 238, 269] Higher DIO concentrations of 0.50 vol % and 1.0 vol % result in formation of average distances of (290 ±10) nm, (138 ±10) nm and (54 ±10) nm and respectively (300 ±10) nm, (140 ±10) nm and (55 ±8) nm. The significant increase in average domain distances with rising solvent additive concentrations obtained from the scattering experiment is supported by SEM and AFM.

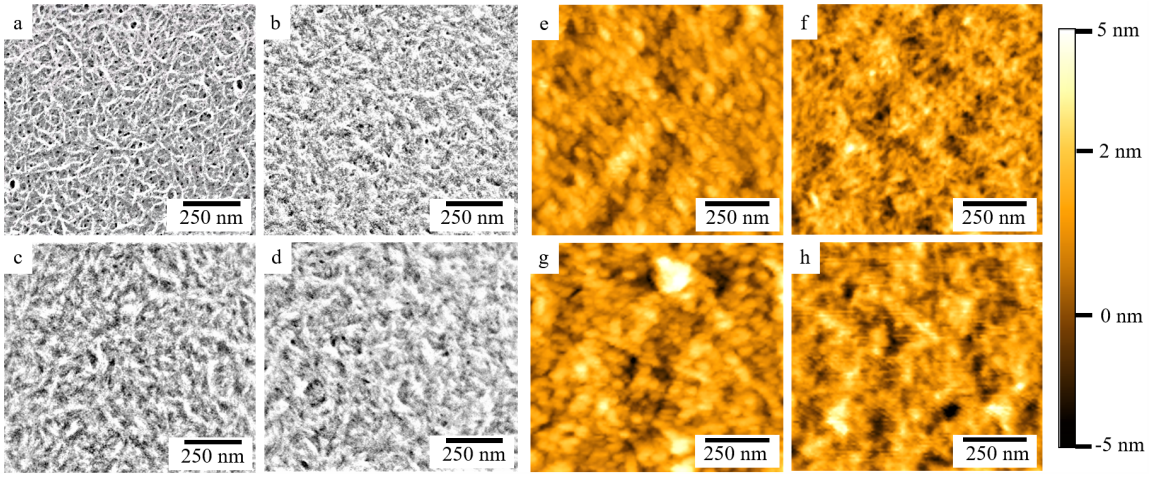

Figure 6.2.: SEM (a–d) and AFM (e–h) images show the surface morphology of active layers printed with different DIO concentrations in CB solutions: (a,e) 0.00 vol %, (b,f) 0.25 vol %, (c,g) 0.50 vol % and (d,h) 1.0 vol % DIO. Reproduced with permission from ACS publishing.

SEM and AFM measurements of printed thin films of PBDB-T-SF:IT-4F are performed to image the structure at the sample surface for different DIO concentrations (Figure 6.2). All active layers show a homogeneous film formation over the probed sample area. Active layers printed without solvent additive show a network of cylindrical structures, which are closely packed and even overlap (Figure 6.2a,e). The formation of large domains downsizes the interface area between donor and acceptor phase, which is unfavorable for organic solar cells due to reduced charge transfer. For samples printed with DIO, smaller average structure sizes are formed, which tend to form larger agglomerates, and domains occur less densely packed. In the AFM images, an increase in surface roughness is observed (Figure 6.2f–h). At a DIO concentration of 0.25 vol %, an interpenetrated network is formed, facilitating charge transfer from the electron donor polymer to the nonfullerene small molecule acceptor (Figure 6.2b,f). Slightly enhanced distances can provoke charge stabilization and minimize the undesirable effect of charge recombination at the interface. [114, 238] In active layers printed with DIO concentrations of 0.50 vol % (Figure 6.2c,g) or 1.0 vol % (Figure 6.2d,h), small structures are formed, which agglomerate strongly and provoke an increase in distances between domains. This morphology can elevate the risk of charge trapping in islands, hindering charge transport to the electrodes. [113] GIWAXS measurements are performed to analyze the crystalline part of the thin films as a function of DIO concentration. 2D GIWAXS data of printed thin film based on PBDB-T-SF:IT-4F (Figure 6.3) show an increase in intensity with rising DIO concentration for the (010) and (100) PBDB-T-SF Bragg peak signals and for the (100) IT-4F Bragg peak signal. [263] In addition, higher order Bragg peaks become visible in

the 2D GIWAXS data, indicating an overall increase in crystallinity with increasing DIO concentration. The increase in crystallinity originates from reduced intermolecular interactions, allowing the molecules to move freely, rearrange and form more crystalline structures.

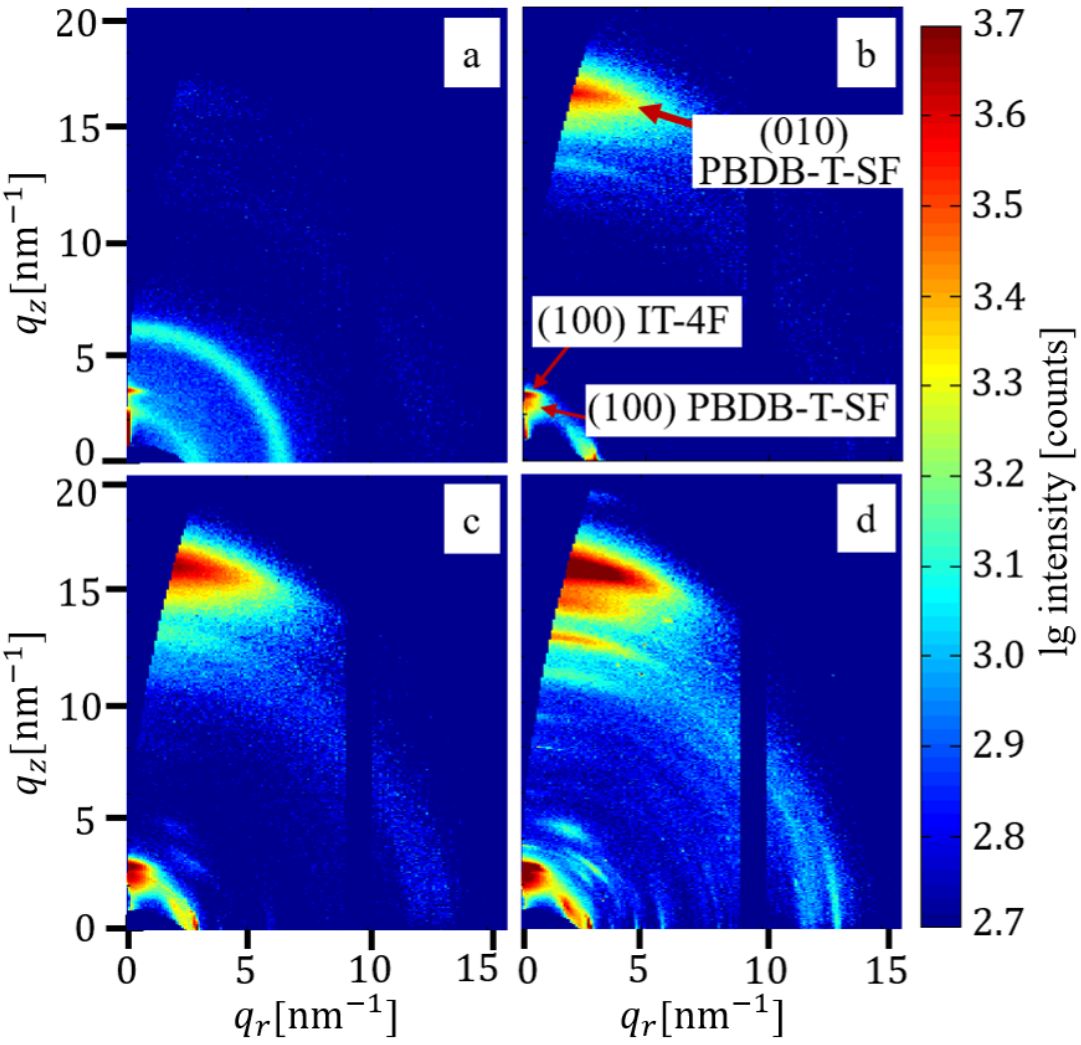

Figure 6.3.: 2D GIWAXS data of printed PBDB-T-SF:IT-4F films with different DIO concentrations: (a) 0.00 vol %, (b) 0.25 vol %, (c) 0.50 vol % and (d) 1.0 vol % DIO. Reproduced with permission from ACS publishing.

For a thin film printed with a 1:1 weight ratio of PBDB-T-SF and IT-4F with different DIO concentrations, the azimuthal q integral and tube cuts of the strongest (100) Bragg peaks from the 2D GIWAXS data are shown in Figure 6.4. The (100) PBDB-T-SF ($2.2 < q < 2.6$ nm^{-1}) and the (100) IT-4F ($2.65 < q < 2.9$ nm^{-1}) peak orientation distributions are analyzed by fitting of Gaussian functions (Figure 6.4b,c). For both the

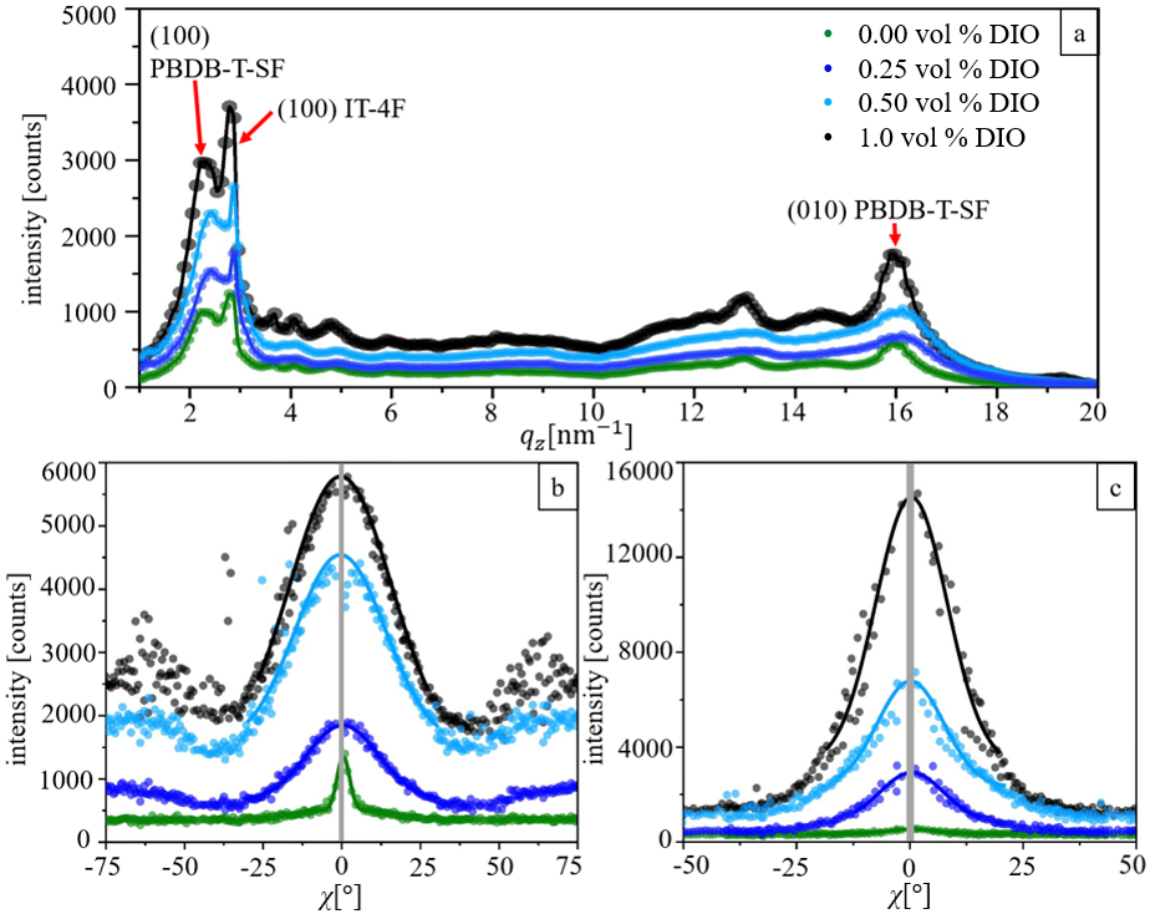

Figure 6.4.: GIWAXS data (dots) and modeling with Gaussian functions show an increase in crystallinity due to addition of DIO: (a) azimuthal q integral with marked (100) PBDB-T-SF and IT-4F, (010) PBDB-T-SF Bragg peaks and higher order Bragg peaks. The solid line is a guide to the eye. Tube cuts (dots) of the (b) (100) PBDB-T-SF Bragg peak and the (c) (100) IT-4F Bragg peak analyzed by fitting of Gaussian functions (solid lines). The gray bar masks the inaccessible q range. Reproduced with permission from ACS publishing.

polymer and the small molecule acceptor, the (100) signal can be assigned to edge-on orientation of crystallites. The FWHM of the Gaussian fits to the (100) PBDB-T-SF peak orientation distribution broadens from (4.7 $\pm$0.2)° for 0.00 vol % DIO to (27.2 $\pm$0.6)° for 0.25 vol %, (33.7 $\pm$2.5)° for 0.50 vol % and (38.1 $\pm$2.5)° for 1.0 vol % DIO. For the (100) IT-4F peak, the FWHM increases from (12.8 $\pm$0.9)° to (16.4 $\pm$2.2)° for 0.25 vol %, (17.3 $\pm$0.6)° for 0.5 vol % and (18.6 $\pm$1.3)° for 1.0 vol % DIO. Such broadening in the orientation distribution indicates enhanced rotational disorder of crystallites in the thin film with rising DIO concentration. As edge-on orientation facilitates the charge transport parallel to the substrate and respectively parallel to the electrodes, the present orientation

has an unfavorable effect on the solar cell performance. [148, 264, 265, 270] For comparison, 2D GIWAXS data (Figure 6.5) of printed pure IT-4F and pure PBDB-T-SF films with 0.25 vol % DIO are shown.

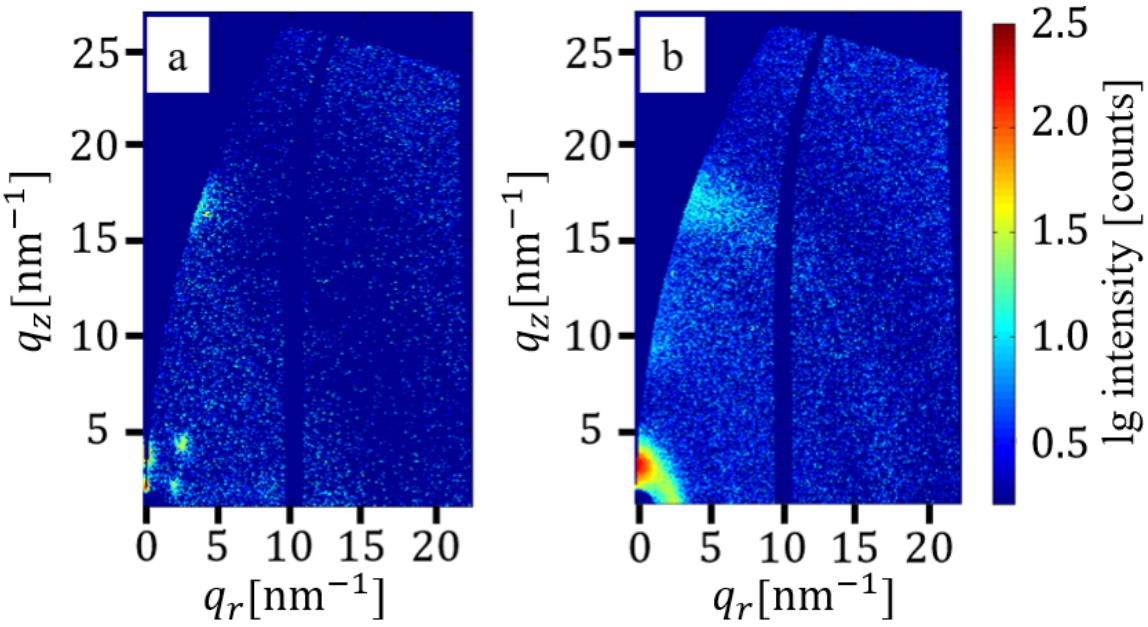

Figure 6.5.: 2D GIWAXS data of pure (a) IT-4F and (b) PBDB-T-SF printed out of CB with 0.25 vol % DIO. Reproduced with permission from ACS publishing.

We observe a similar crystallization behavior for the pure polymer in absence of an acceptor, whereas pure IT-4F film shows lower crystallinity but more ordered structures. Polymer-acceptor interactions seem to have a positive effect on the crystallization of IT-4F but enhance the rotational disorder of crystallites. Thus, the results from X-ray scattering experiments and SEM show the significant impact of DIO concentration on morphology and expected solar cell performance of printed active layers based on a 1:1 blend of PBDB-T-SF:IT-4F.

6.2. Optical Properties

PL is measured for thin films of pure electron polymer PBDB-T-SF, pure acceptor IT-4F, and a blend of 1:1 of donor and acceptor after excitation with a wavelength of 570 nm (Figure 6.6a). The pure materials show high PL intensity, whereas in a blend of PBDB-T-SF:IT-4F, the electron transfer from donor to acceptor provokes a significant reduction in intensity. As the low-bandgap polymer PBDB-T-SF shows absorbance in a broad wavelength range in the region of visible light (Figure 6.7), it can be efficiently

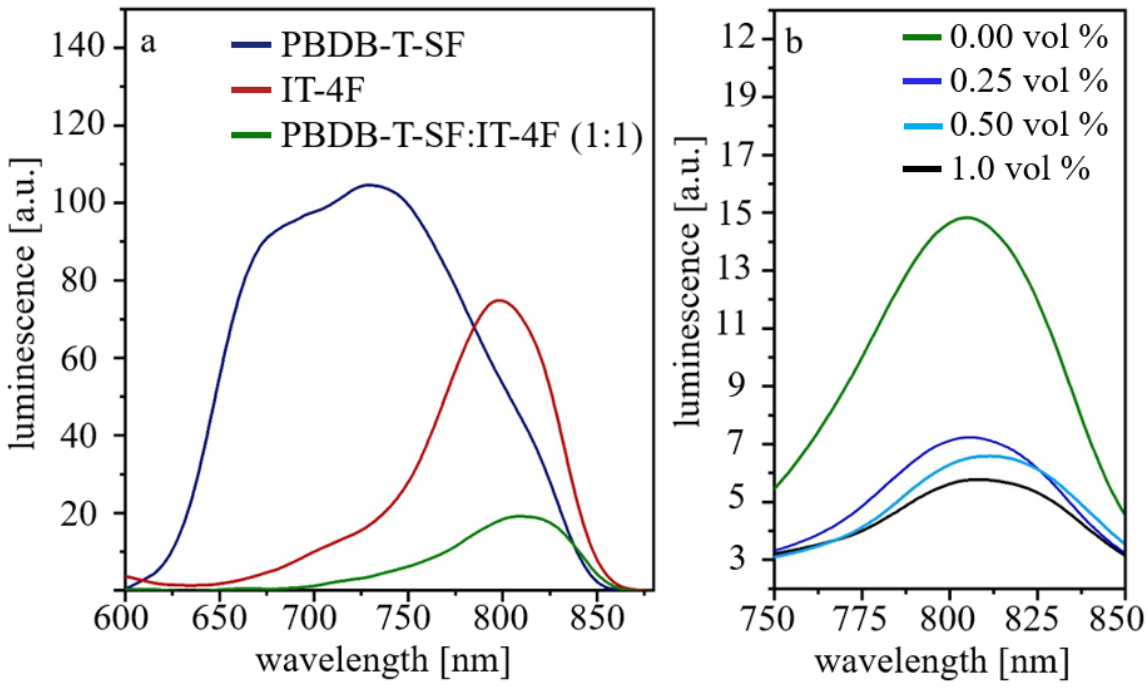

Figure 6.6.: (a) PL of pure donor polymer PBDB-T-SF, pure nonfullerene acceptor IT-4F and an active layer printed with a 1:1 ratio of donor and acceptor out of CB; (b) PL of active layers printed with varying DIO concentrations. Reproduced with permission from ACS publishing.

excited with the chosen wavelength. In a BHJ organic solar cell, the mechanism of energy conversion (Subsection 2.1.2) starts with excitation of the polymer by absorption of a photon and generation of an exciton. [108, 112] During the exciton lifetime, electron and hole, being attracted to each other by Coulomb forces, move towards the interface, where exciton splitting in a positive and a negative charge occurs. The electron is transferred to the electron acceptor (IT-4F), whereas the hole remains at the conjugated polymer (PBDB-T-SF). In a last step, electron and hole are transported towards the respective electrodes, where the current can be extracted. In absence of an acceptor, the polymer undergoes a transition back to the electronic ground state after the excited state lifetime under emission of a photon (PL). [271] Electron transfer from donor to acceptor provokes a reduction in PL intensity and allows us to draw conclusions about the efficiency of the charge transfer in an organic solar cell. [269, 272, 273] PL of printed active layers with different DIO concentrations is measured after excitation with a wavelength of 570 nm (Figure 6.6b). Increasing the DIO concentration causes a decrease in luminescence intensity. Due to decreasing domain sizes with increasing DIO concentration (Figure 6.1b), the interface area grows and charge transfer from the donor polymer to the acceptor molecule is facilitated. In addition, the exciton is generated closer to the interface and the distance,

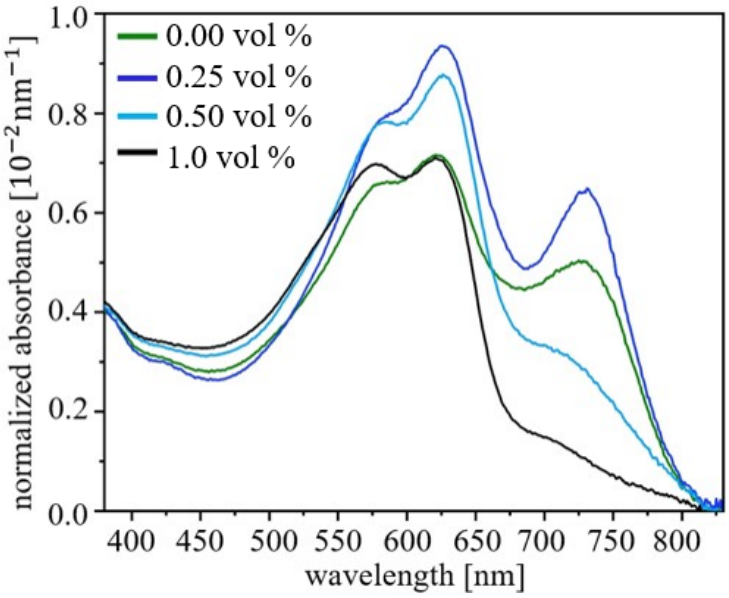

Figure 6.7: UV/vis absorbance spectra of active layers based on PBDB-T-SF:IT-4F printed out of CB with different DIO concentrations. All absorbance spectra were normalized on the dry film thickness. Reproduced with permission from ACS publishing.

which needs to be overcome by exciton diffusion, is reduced. This has a significant impact on the performance of BHJ organic solar cells as typical exciton diffusion lengths are about some tens of nanometers. [108, 109] The loss mechanism of charge recombination before reaching the interface becomes less probable. A moderate increase in distance between donor and acceptor can improve the solar cell performance by reduction of Coulomb forces and charge stabilization. [114, 238] In this case, exciton splitting is facilitated and the probability of charge recombination at the interface is reduced. These effects cause a decrease in PL intensity with rising DIO concentrations (Figure 6.6b). To conclude, addition of higher solvent additive concentrations and resulting small average domain sizes facilitate charge transfer from donor to acceptor by an enlargement of interface area but can provoke a decline in PCE by charge trapping. [113] To study the influence of DIO on absorption properties of printed BHJ organic solar cells, UV/vis spectroscopy is performed (Figure 6.7). The resulting absorbance spectra are normalized on the film thickness. The active layer based on a 1:1 blend of PBDB-T-SF:IT-4F shows absorbance in a broad wavelength range of visible light. The optical bandgap of the active material is determined with the Tauc plot method (Section 3.1) to be (1.55 $\pm$0.04) eV. Addition of DIO does not shift the bandgap itself but significantly influences the absorbance of photons with energies slightly above it due to increased crystallinity in the active layer. [274] An optimum DIO concentration of 0.25 vol % improves the absorbance in the wavelength range from 700 to 800 nm as compared to solvent additive free thin films. Active layers processed with higher concentrations of DIO (0.50 vol % and 1.0 vol %) show a distinct reduction of absorbance in this wavelength range with rising amounts of solvent additive due to an increased rotational disorder in the thin films. [275] By addition of low DIO

concentrations (0.25 and 0.50 vol %), active layers of PBDB-T-SF:IT-4F show an enhanced absorbance in the wavelength range from 570 to 700 nm. The best result is obtained for a DIO concentration of 0.25 vol % as the absorbance is significantly increased over a broad wavelength range (570–800 nm), which enables us to exploit the sun spectrum more efficiently.

The probability for generating photocurrent after absorption of a photon with a certain wavelength is studied with EQE. EQE spectra and integrated current density of printed organic solar cells with different DIO concentrations are shown in Figure 6.8.

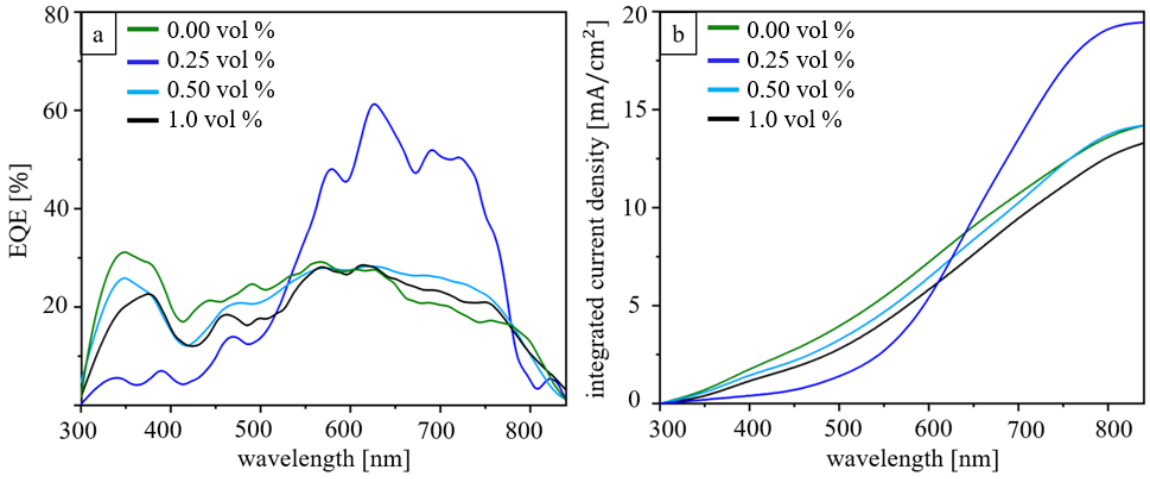

Figure 6.8.: (a) EQE spectra and (b) integrated photocurrent density of printed organic solar cells based on PBDB-T-SF:IT-4F with different DIO concentrations. Reproduced with permission from ACS publishing.

In the wavelength range from 300 to 520 nm, the device printed with a DIO concentration of 0.25 vol % shows a considerably lower EQE (Figure 6.8a) and absorbance (Figure 6.7) compared to devices with 0.00, 0.50 and 1.0 vol % DIO and a lower integrated current density can be observed between 300 and 610 nm (Figure 6.8b). Between 300 and 520 nm, addition of DIO seems to have a negative effect on the device performance as the solar cell printed without solvent additive shows a significantly higher EQE compared to devices with DIO (Figure 6.8a). However, in the wavelength range between 570 and 780 nm, a significantly enhanced EQE can be observed for a DIO concentration of 0.25 vol % (Figure 6.8a). This is in accordance with the distinct increase in absorbance in this wavelength range (Figure 6.7). In the wavelength range above 610 nm, the integrated photocurrent of the solar cell printed with a DIO concentration of 0.25 vol % clearly exceeds that of solar cells with other DIO concentrations. Addition of an optimum solvent

additive concentration of 0.25 vol % seems to provoke formation of a morphology favorable for absorption of low energy photons and subsequent photocurrent generation.

6.3. Organic Solar Cell Performance

Printed organic solar cells based on PBDB-T-SF:IT-4F are fabricated with different concentrations of DIO with a solar cell area about 6.25 cm^2 and a pixel size of 0.12 cm^2. For each DIO concentration, three times eight solar cells are tested. Resulting PCE values (colored dots) are shown in Figure 6.9. The red square gives the average PCE, whereas the error bar gives the standard deviation.

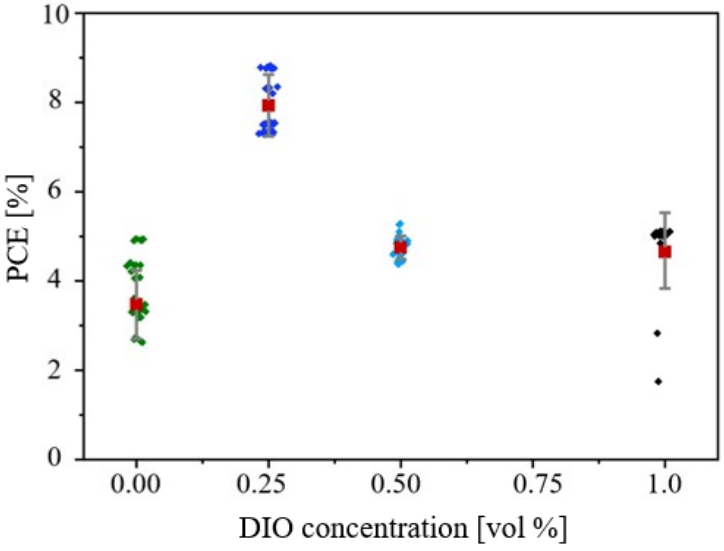

Figure 6.9: PCE of organic solar cells printed with different DIO concentrations. Efficiencies of measured pixels (small colored dots), average device performance (red square) and standard deviation (gray error bar) are given for different solvent additive concentrations. Reproduced with permission from ACS publishing.

Slot-die coated organic solar cells without DIO reach an average PCE of (3.5 $\pm$0.8)%. Addition of 0.25 vol % DIO to the precursor solution improved the average PCE to (7.9 $\pm$0.7)% with a top device performance of 8.95%. The corresponding short-circuit density (J_{SC}) of 19.46 mA/cm^2 and the open-circuit voltage (V_{OC}) of 0.87 V are close to literature values for spin-coated small area devices with 0.5 vol % DIO (J_{SC} = 20.88 mA/cm^2 and V_{OC} = 0.88 V for an aperture area of 0.037 cm^2 or J_{SC} = 18.93 mA/cm^2 and V_{OC} = 0.86 V for an aperture area of 1.00 cm^2) [35]. The deviation in optimum DIO concentration in printed devices compared to spin-coated devices originates from different polymer and acceptor concentrations used for printing (7 mg/mL for printing vs. 20 mg/mL for spin-coating) giving a different DIO to active material ratio. By further increasing the DIO concentration, average PCE values of (4.6 $\pm$0.3)% for 0.50 vol % and (4.6 $\pm$0.9)% for 1.0 vol % of DIO are obtained.

In Table 6.1 the best PCE achieved for different DIO concentrations, the corresponding J_{SC}, V_{OC} and FF as well as the average PCE are given.

Table 6.1.: Best PCE Values for Slot-Die Coated Organic Solar Cells with Different DIO Concentrations and the Responsive Short-Circuit Current Density, Open-Circuit Voltage and Fill Factor (FF)[1]

DIO conc. [vol %]	best PCE [%]	J_{SC} [mA/cm^2]	V_{OC} [V]	FF [-]	avg. PCE [%]
0.00	4.80	14.18	0.86	0.39	3.5 ± 0.8
0.25	8.95	19.46	0.87	0.52	7.9 ± 0.7
0.50	5.17	14.19	0.82	0.44	4.6 ± 0.3
1.00	4.98	13.32	0.85	0.44	4.6 ± 0.9

[1] For all solvent additive concentrations, average PCE values are given.

At an optimum DIO concentration of 0.25 vol %, the J_{SC} of the slot-die coated organic solar cells is significantly enhanced as smaller structures are formed. The interface area between donor and acceptor increases and exciton splitting is facilitated. At higher DIO concentrations, a smaller J_{SC} is observed due to charge trapping provoked by very small structures in combination with large distances. In addition, DIO enhances the crystallinity of IT-4F and PBDB-T-SF and influences the V_{OC}. At an optimum solvent additive concentration of 0.25 vol %, the V_{OC} is slightly enhanced due to higher crystallinity. Due to edge-on orientation of crystallites, charge transport occurs parallel to the electrodes, which is not favorable for the device performance. For a DIO concentration of 0.50 and 1.0 vol %, this effect is further enhanced and a lower V_{OC} is observed. Current-voltage (JV) curves for best photovoltaic devices processed with varying DIO concentrations are shown in (Figure 6.10).

Organic solar cells processed with 0.25 vol % DIO exhibit the best performance as the solvent additive simultaneously has positive and negative effects on the morphology and optical properties. For a small DIO concentration of 0.25 vol %, positive effects, such as an increased crystallinity and gain of interface area by decreasing average structure sizes, dominate, whereas at higher DIO concentrations, negative effects, such as an increased rotational disorder of crystallites and loss mechanisms due to large distances between domains, dominate. The average PCE improved significantly by addition of an optimum DIO concentration of 0.25 vol % compared to solvent additive free devices, whereas at higher concentrations the positive effect on the solar cell performance is less pronounced.

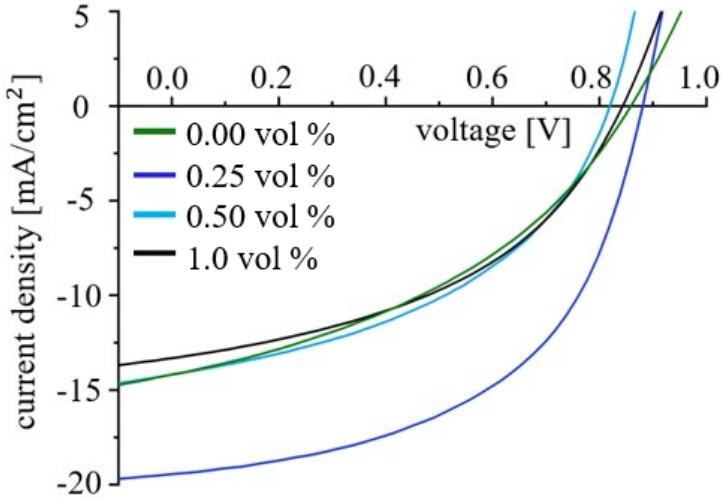

Figure 6.10: Current-voltage curves for the best photovoltaic devices printed out of CB with different DIO concentrations. Reproduced with permission from ACS publishing.

These findings are fully consistent with the morphology and optical properties obtained from GISAXS, GIWAXS, SEM, AFM, PL, UV/vis spectroscopy and EQE and demonstrate the significant influence of DIO concentration on the structure and performance of printed high-efficiency organic solar cells.

6.4. Conclusions

We have investigated the effect of DIO on the morphology, optical properties and PCE of printed BHJ organic solar cells based on the conjugated polymer PBDB-T-SF and the small molecule acceptor IT-4F. A meniscus guided slot-die coater has been used for the thin film deposition of the active material. Scattering experiments in grazing incidence geometry as well as SEM and AFM reveal shrinking average structure sizes and growing distances between domains with rising DIO concentration. Moreover, crystallinity is enhanced by addition of DIO, which appears beneficial as higher crystallinity typically causes better device performance. However, due to edge-on orientation of crystallites, charge transport parallel to the electrodes is facilitated, which is less favorable for the solar cell performance. A decrease in PL intensity with rising DIO concentration shows an improved charge transfer from polymer donor to small molecule acceptor due to reduced average domain sizes and an enlargement of interface area. UV/vis spectroscopy and EQE show an improved absorbance and facilitated generation of photocurrent for a DIO concentration of 0.25 vol % in a broad wavelength range. An optimum DIO concentration of 0.25 vol % yields the best photovoltaic performance. Thus, a different amount of DIO (0.25 vol %) is giving optimal devices as compared to spin-coating (0.50 vol %). The average PCE of these printed devices improves from 3.5 to 7.9% compared to devices processed without solvent additive and efficiencies up to 8.95% are obtained. At higher

DIO concentrations, the PCE cannot be further improved due to formation of small average structure sizes, provoking charge trapping. Thus, similarly as for spin-coated active layers, also in case of printed active layers, the morphology optimization is important for achieving best performing solar cells and parameters optimized for spin-coating cannot be simply transferred to printing. The results obtained in the context of this work are an important step towards further up-scaling of high-efficiency organic solar cells.

7 *In Operando* Degradation

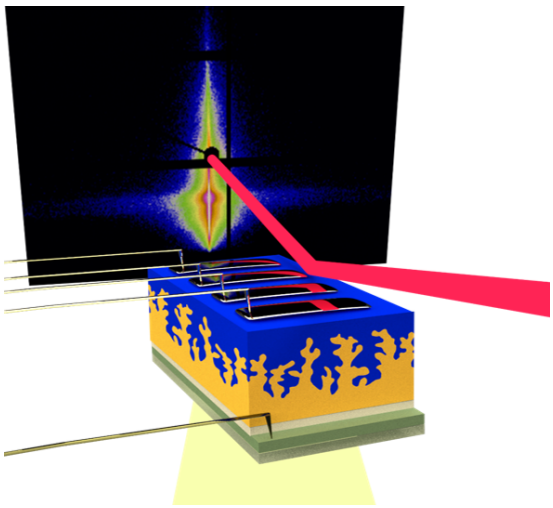

The following chapter is based on the published article: "Following *In Operando* the Structure Evolution-Induced Degradation in Printed Organic Solar Cells with Nonfullerene Small Molecule Acceptor" [262] (Kerstin S. Wienhold et al., *Sol. RRL*, vol. 4, no. 9, p. 2000251, **2020**, DOI: 10.1002/solr.202000251). Content and images are reproduced with permission from Wiley, Copyright 2020.

Understanding the degradation mechanisms of printed bulk-heterojunction (BHJ) organic solar cells during operation is essential to achieve long-term stability and realize real-world applications of organic photovoltaics. Herein, degradation of printed organic solar cells based on the conjugated polymer PBDB-T-SF and the nonfullerene small molecule acceptor IT-4F with 0.25 vol % 1,8-diiodooctane (DIO) solvent additive is studied *in operando* for two different donor:acceptor ratios. The inner nanostructure is analyzed with grazing incidence small-angle X-ray scattering (GISAXS) and current-voltage (JV) characteristics are probed simultaneously. Irrespective of the mixing ratio, degradation occurs by the same degradation mechanism. A decrease in short-circuit current density (J_{SC}) is identified to be

the determining factor for the decline in power conversion efficiency (PCE). The decrease in J_{SC} is induced by a reduction of relative interface area between the conjugated polymer and the small molecule acceptor in the BHJ structure, resembling the morphological degradation of the active layer.

7.1. Physical Degradation of Organic Solar Cells

Morphology degradation of PBDB-T-SF:IT-4F based organic solar cells printed with two different donor:acceptor ratios is studied *in operando* under illumination by a solar simulator. To exclude chemical degradation pathways within this study, experiments are performed under moderate vacuum conditions (10^{-2} mbar). Therefore, we avoid possible reactions between the active layer materials and oxygen, such as irreversible photochemical formation of carbonyl and carboxylic groups, acting as electron traps, or reversible p-doping of the active layer with oxygen, provoking the formation of immobilized superoxide anions. [126] In addition, possible degradation of the aluminum electrodes or the active layer by air humidity [122, 123, 130, 276] is ruled out under these conditions. Potential decomposition of the nonfullerene small molecule acceptor by photocatalytic activity of ZnO under illumination with UV light [125] is ruled out, as the light of the solar simulator passes through a glass substrate, which is not transparent to this wavelength range. As *JV* characteristics depend on the light intensity [198, 277], this parameter is kept stable during the measurement (AM 1.5 illumination, 100 mW/cm^2). Moreover, the chamber is cooled to 15 °C to avoid temperature-induced changes of morphology or solar cell performance. [133, 134, 278] As proved in earlier studies, [31, 70, 74] morphology degradation can be adequately studied *in operando* with a simultaneous measurement of GISAXS and *JV* characteristics.

To obtain statistical information, four organic solar cells are connected in parallel to measure average *JV* characteristics. In addition, in the GISAXS experiment the X-ray beam is aligned to impinge onto the sample as a small line, providing morphological information on the four organic solar cells simultaneously. For GISAXS we select an incidence angle of 0.4° well above the critical angles of the involved materials, such as PBDB-T-SF and IT-4F, to probe information from the full thickness and analyze the inner nanostructure of the active layer. [148, 155] Grazing incidence geometry allows analyzing a larger sample area with high statistical significance and to measure thin films with a layer thickness about 100 nm, which is assumed to be the ideal thickness regime for organic solar cells. [35]

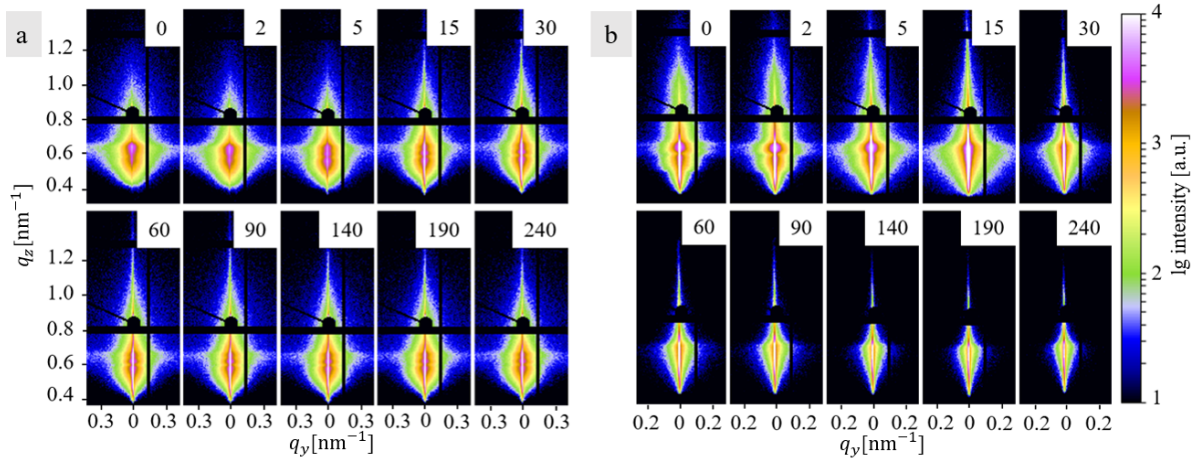

Figure 7.1.: 2D GISAXS data of printed organic solar cells based on a (a) 1:1 and (b) 1:2 donor:acceptor ratio of PBDB-T-SF:IT-4F, measured during operation at dedicated time steps as indicated in minutes (insets). Reproduced with permission from Wiley.

2D GISAXS data of printed organic solar cells with a 1:1 and 1:2 donor:acceptor ratio show the significant change of morphology during operation (Figure 7.1). Within the first 30 minutes, a fast and distinct structure evolution is observed. At longer illumination times, the change of morphology decelerates and almost stabilizes but does not fully stop within the time span of the *in operando* experiment. For 2D GISAXS data analysis, horizontal line cuts are performed at the strongest scattering contribution, the critical angle (Yoneda region) of PBDB-T-SF, which is calculated to be 0.12° for the applied X-ray energy of 11.65 keV. To obtain average polymer domain sizes in the active layer, these horizontal line cuts are modeled. The used model is based on the EIA of the DWBA (Subsection 2.3.2). [151, 254] To consider the LMA, the overall scattering intensity is defined as an incoherent superposition of scattering intensities, originating from individual polymer domains in the thin film. The GISAXS data are modeled with three cylindrical substructures, which is a well-established approach to characterize the morphology of thin polymer films. [29, 30, 268] The respective cylinders are assumed to be pure polymer domains. [70]

In Figure 7.2a,e, horizontal line cuts of 2D GISAXS data (black dots) for printed organic solar cells based on a 1:1 and 1:2 donor:acceptor ratio and corresponding modeling results (red lines) are shown for different operation times (from bottom to top). For organic solar cells based on a 1:1 donor:acceptor ratio, average structure sizes of polymer domains increase under operation (Figure 7.2b–d). The largest structure (Figure 7.2b) grows from (80 $\pm$2) nm to (98 $\pm$2) nm, whereas the medium structure (Figure 7.2c)

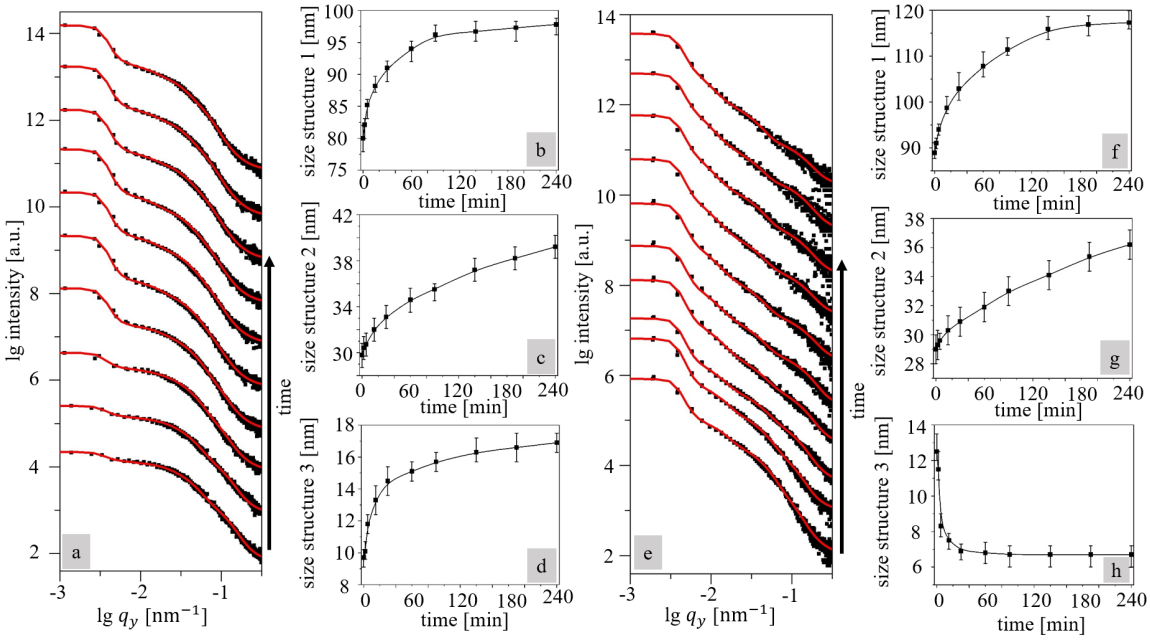

Figure 7.2.: Temporal evolution of the morphology of printed organic solar cells based on a (a–d) 1:1 PBDB-T-SF:IT-4F ratio and (e–h) 1:2 ratio. (a,e) Horizontal line cuts of 2D GISAXS data (black dots) and modeling results (red lines) by applying a model based on the DWBA and the LMA are shown for different time steps of operation (0, 2, 5, 15, 30, 60, 90, 140, 190, and 240 minutes, from bottom to top). Parameters determined from GISAXS modeling are the average domain sizes of the (b,f) largest, (c,g) medium, and (d,h) smallest polymer domains. Error bars give a range in which the fit still describes the scattering data. The solid black lines in (b–d) and (f–h) are guides to the eye. Reproduced with permission from Wiley.

grows from (30 ±1) nm to (39 ±1) nm and the smallest structure (Figure 7.2d) from (10 ±0.5) nm to (17 ±0.5) nm. The corresponding distances are (200 ±10) nm, (130 ±10) nm, and (50 ±5) nm and do not change significantly within the time span of the experiment. For organic solar cells based on a 1:2 donor:acceptor ratio, the largest domain structure (Figure 7.2f) grows from (90 ±2) nm to (117 ±2) nm. The medium structure size (Figure 7.2g) is about (29 ±1) nm at the start of operation and grows to (36 ±1) nm during operation, which is similar to findings obtained for the device based on a 1:1 donor:acceptor ratio. In contrast, the size of the smallest polymer domains (Figure 7.2h) is reduced from (12.5 ±1.0) nm to (6.5 ±1.0) nm, which is a trend opposite to what is found in the 1:1 donor:acceptor ratio device. The corresponding distances are (200 ±10) nm, (100 ±10) nm, and (40 ±5) nm and do not alter during operation. The observed structural growth under operation of a printed organic solar cell based on a 1:1 ratio of PBDB-T-SF:IT-4F shares a limited similarity to findings from previous studies performed on spin-coated P3HT:PCBM devices with a 1:1 donor:acceptor

ratio. [70] However, for such fullerene based organic solar cells, the domain sizes and also the average distance between medium-sized domains increased significantly under illumination. In active layers prepared with solvent additive, so far domain shrinkage was reported as the morphology degradation mechanism instead of domain coarsening. [31] Therefore, for the PBDB-T-SF:IT-4F solar cells of this study being manufactured with 0.25 vol % DIO as solvent additive [192], the observed domain coarsening is unexpected. The observed morphological degradation in PBDB-T-SF:IT-4F solar cells based on a 1:2 ratio shares no similarity with previous studies performed on organic solar cells with an excess of acceptor. Schaffer et al. observed a decrease in the medium and smallest domain sizes under illumination of a spin-coated PCPDTBT:PCBM based organic solar cell with a 1:2.7 donor:acceptor ratio prepared with solvent additive. [74] For a spin-coated PTB7-Th:PCBM based device with a donor:acceptor ratio of 1:1.5, Yang et al. observed decreasing average structure sizes for devices processed with solvent additive. [31] In both systems, the FF and not the J_{SC} were detrimental to device failure. The amount of residual solvent additive was determined by the relative scattering intensity at the critical angle of the respective compound. [31, 74] Loss in solvent additive was found responsible for domain shrinkage in previous works, which is not observed in this study (Figure 7.3).

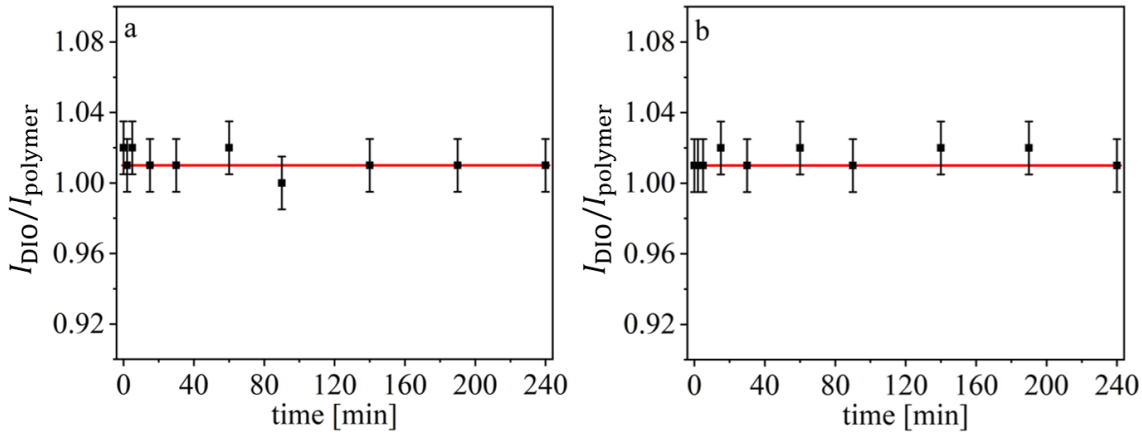

Figure 7.3.: Temporal evolution of DIO content determined by the scattering intensity at the critical angle of DIO normalized on the scattering intensity at the critical angle of the polymer to rule out fluctuations of the X-ray beam. The $I_{\mathrm{DIO}}/I_{\mathrm{polymer}}$ ratio for organic solar cells based on a (a) 1:1 and (b) 1:2 donor:acceptor ratio is given for different time steps. The red line is a guide to the eye. Reproduced with permission from Wiley.

This is favorable, as DIO was found to enhance the device performance of printed PBDB-T-SF:IT-4F based organic solar cells by provoking the formation of small polymer domains in the BHJ layer. [192] In contrast to previous studies, structure coarsening without altering the average distances between polymer domains is found to be the crucial

factor for device failure in our work. We assume this is due to different chemical structures of the active materials, provoking different interactions of donor and acceptor molecules with surrounding molecules. During device degradation, rearrangement of polymer can occur, provoking microstructure evolution and charge trapping. However, aggregation of nonfullerene small molecule acceptor is diffusion-limited and therefore, has a stabilizing effect on the BHJ morphology. [279] In addition, the correlated roughness determined by vertical line cuts of 2D GISAXS data is only poorly developed and changes only slightly or even decreases under illumination (Figure 7.4) which differs from previous studies, which observed a significant increase in correlated roughness for solar cells processed with DIO. [31] Thus, the different degradation mechanism found for PBDB-T-SF:IT-4F solar cells as compared to other systems is attributed to different mobility and interactions of the involved donor and acceptor materials.

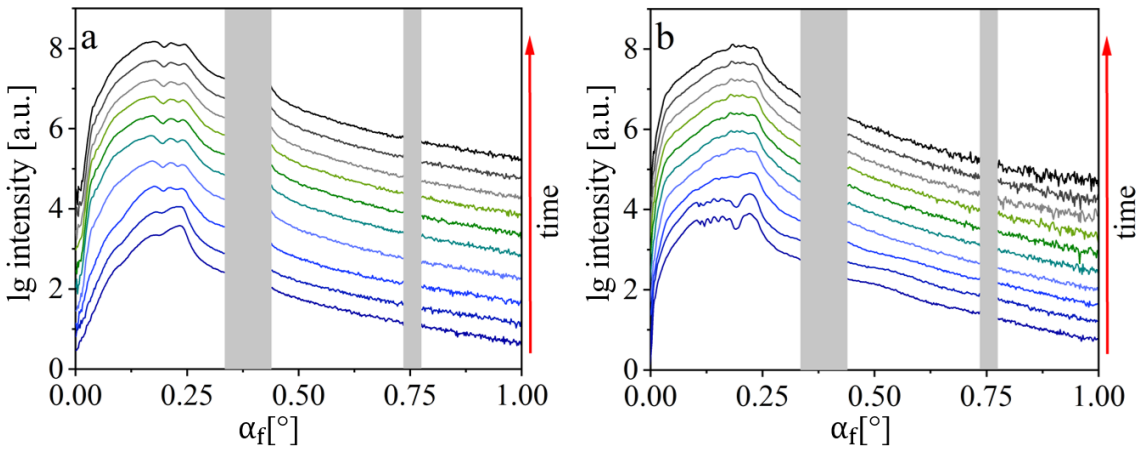

Figure 7.4.: Vertical line cuts of 2D GISAXS data for a (a) 1:1 and (b) 1:2 donor:acceptor ratio are shown for different time steps of operation (0, 2, 5, 15, 30, 60, 90, 140, 190 and 240 minutes, from bottom to top as indicated by the red arrow). The position of beamstop and detector gaps are indicated by the gray area. Reproduced with permission from Wiley.

7.2. Modeling the Short-Circuit Current Density

From the three different characteristic structure sizes determined in the GISAXS data analysis, the size of the medium substructure, which is about some tens of nanometers, is expected to be the crucial factor, as it is close to the scale of typical exciton diffusion lengths determined for several organic solar cell materials. [57, 108–110, 112] For slot-die coated active layers based on PBDB-T-SF:IT-4F, the size of the medium substructure is about 30 nm. The morphology observed with atomic force microscopy (AFM) for spin-coated

active layers is similar to the morphology observed for slot-die coated PBDB-T-SF:IT-4F films, even though the largest structure was not reported in the previous study. [35] To correlate morphological changes obtained from the scattering experiment with the solar cell performance, JV-curves are measured simultaneously, and characteristic device parameters are extracted. Figure 7.5a,c shows the temporal evolution of normalized device parameters, namely PCE, J_{SC}, V_{OC}, and FF of printed organic solar cells based on a 1:1 and a 1:2 donor:acceptor ratio within the first 4 hours of illumination.

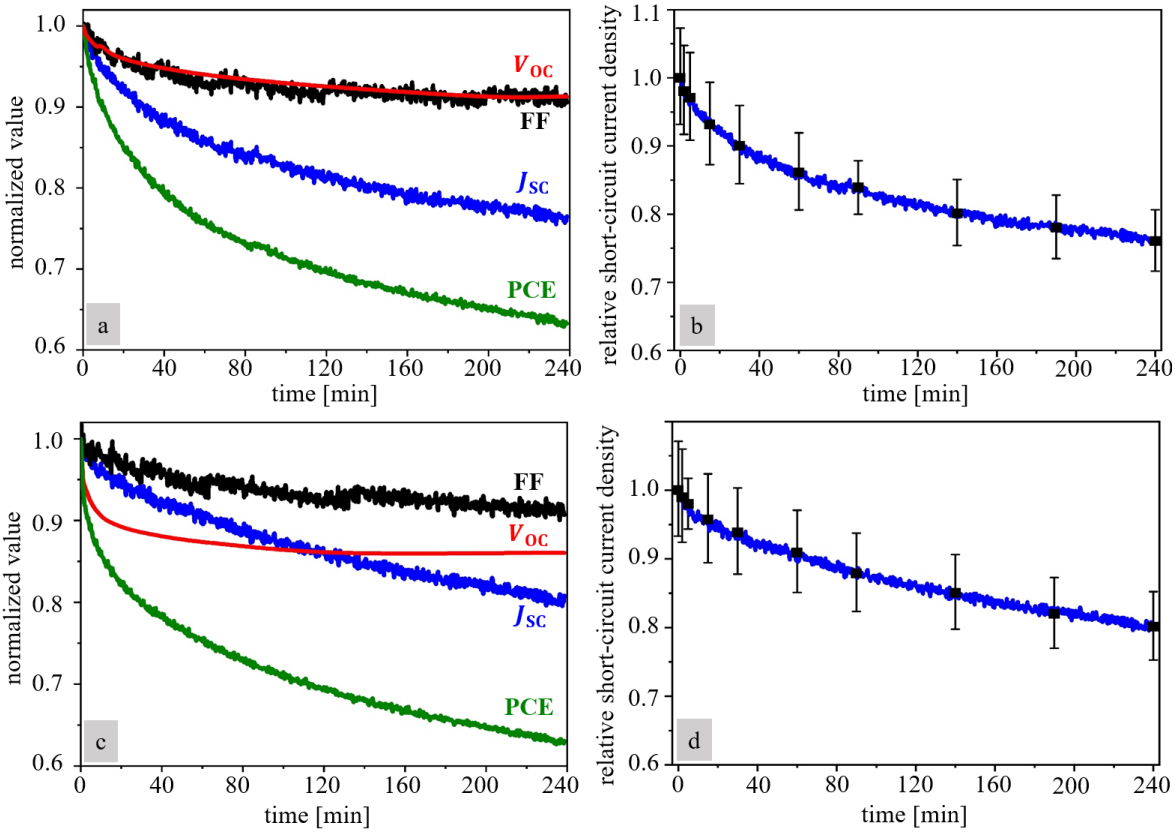

Figure 7.5.: Degradation of normalized device parameters during operation for a printed organic solar cell based on a (a,b) 1:1 and (c,d) 1:2 donor:acceptor ratio of PBDB-T-SF:IT-4F in terms of (a,c) PCE (green), J_{SC} (blue), V_{OC} (red), and FF (black). (b,d) Comparison of measured (blue) and theoretically predicted J_{SC} (black dots) using a model as explained in the text. Error bars arise from the GISAXS modeling error. Reproduced with permission from Wiley.

The degradation of J_{SC} is identified to be the determining factor for the decay of solar cell performance, as the device parameters V_{OC} and FF stabilize after 30 minutes and the relative values do not drop below 0.91 for V_{OC} and 0.86 for FF within the timescale of the experiment. Figure 7.5b,d shows the evolution of normalized J_{SC} extracted from the JV-curves (blue) in comparison to the theoretically predicated value, applying the model

from Equation 7.1 (black dots). Error bars are estimated by calculating the theoretically predicted J_{SC} (Equation 7.1) for the upper and lower domain size limit as determined in the GISAXS data modeling (Figure 7.2c,g). Based on knowledge from earlier studies of P3HT:PCBM solar cells, the significant reduction of normalized J_{SC} to 0.76 for a 1:1 and 0.80 for a 1:2 donor:acceptor ratio is expected to result from structure coarsening and related reduction of interface-to-volume ratio between donor and acceptor. As exciton splitting takes place at the interface, the probability of exciton dissociation into free charge carriers depends critically on the interface between donor and acceptor. [93, 280] Figure 7.6 shows the structure coarsening and reduction of interface-to-volume ratio in the BHJ during operation. In our model approach, in agreement with the model described by Schaffer et al. [70], it is assumed that only the medium-sized domains significantly contribute to the solar cell performance, as typical exciton diffusion lengths are in a similar range. In accordance with the model applied to describe the scattering data, polymer domains are described as cylinders (Figure 7.6a,c).

In the model, a photon is absorbed by a polymer molecule within a cylindrically shaped domain, and an exciton is generated, moving to the donor:acceptor interface, where dissociation into free charge carriers occurs. [113, 281] The probability for this process depends on the relative interface area between polymer and acceptor, which is defined as the interface-to-volume ratio of the polymer cylinder. Excitons, moving along the length of the cylinder, will undergo recombination before reaching the interface and do not contribute to the J_{SC}. Therefore, the photocurrent is independent of the length of the cylinder, and a consideration of the cylinder cross section is sufficient to explain the evolution of relative J_{SC}. The probability of exciton dissociation and generation of photocurrent depends on the relative interface area and respectively on the circumference of the cylinder (Figure 7.6b,d).

Equation 7.1 is based on a model developed by Schaffer et al. to predict the degradation of normalized J_{SC} in a P3HT:PCBM based spin-coated organic solar cell during operation. [70] Schaffer et al. described the degradation of short-circuit current density in P3HT:PCBM based photovoltaics to originate from a reduction of active area per unit cell area. Therefore, the geometrical factor to describe the evolution of morphology is given by the cylinder size and the average interdomain distances. The crucial factor for device failure of P3HT:PCBM based solar cells was the significant increase in average domain distances, which provoked an increase in the unit cell area, and therefore, reduced the ratio of active area per unit cell area, even though the average polymer domain sizes increased moderately. However, for PBDB-T-SF:IT-4F based organic solar cells, average distances and thus, the unit cell area

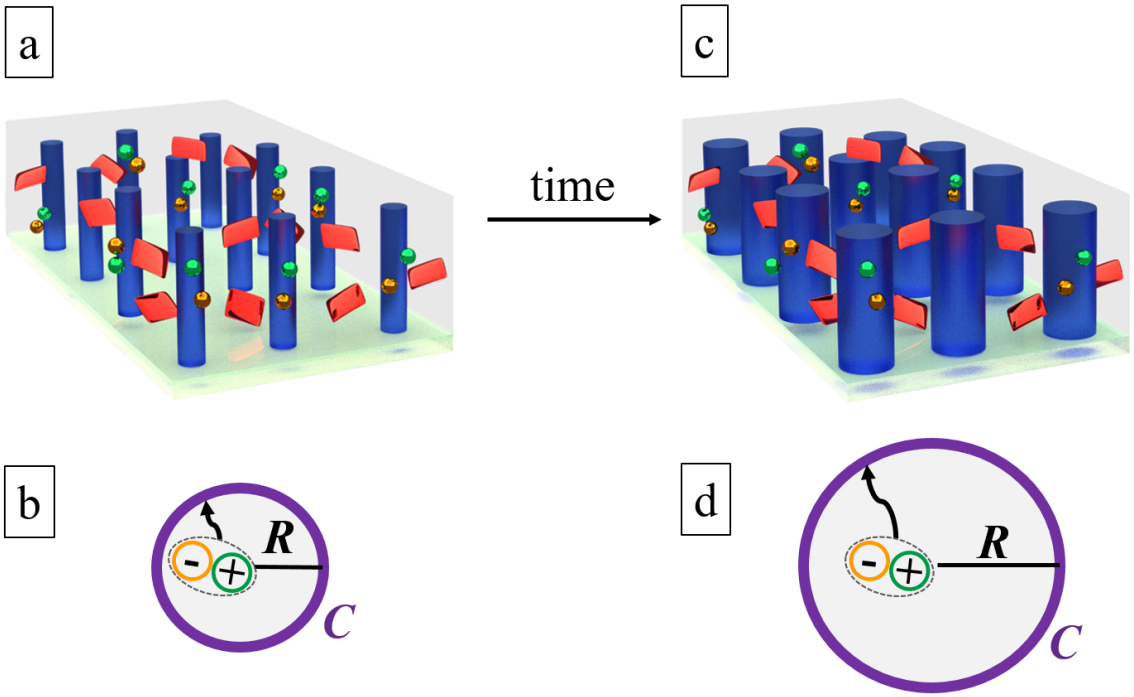

Figure 7.6.: Schematic of the morphology evolution in the active layer during operation as assumed in the model with only a small fraction of acceptor molecules shown for clarity of presentation. (a) At the start of operation, a BHJ structure with small polymer domains (blue cylinders) and small molecule acceptor domains (red cuboids) is observed. (b) A cross section of a polymer cylinder with a small radius is shown. A high interface-to-volume ratio facilitates exciton dissociation into free charge carriers at the donor-acceptor interface. Electron (orange) and hole (green) move towards the electrodes and a high J_{SC} is measured experimentally. The relative interface area is given by the circumference (purple) of the cylinder per cross-sectional area. (c) Under illumination, growth of polymer domains occurs. (d) In the cross section, a reduction of relative interface (purple) between donor and acceptor is observed, provoking a reduction of exciton dissociation probability. In a polymer cylinder with large radius, the interface-to-volume ratio is reduced, provoking a reduction of exciton dissociation probability and J_{SC}. Reproduced with permission from Wiley.

are stable during the experiment. As a consequence, we develop a new model to describe the degradation of PBDB-T-SF:IT-4F based solar cells, which describes the relationship between normalized J_{SC} and relative circumference C (defined as the circumference of the cylinder normalized on the cross-sectional area). I refers to the light intensity, e is the elementary charge, and p is the probability that a photon absorbed in the polymer domain contributes to the photocurrent. The light intensity I is stable during the *in operando* measurement. As chemical degradation pathways are ruled out by the measurement conditions, chemical properties of the active layer do not alter during the experiment for

which reason p is assumed to be constant. In this model approach, structure parameters R (medium cylinder radii) are extracted from GISAXS data modeling (Figure 7.2c,g). Thus, the evolution of the J_{SC} under illumination can be described by

$$J_{SC}^{norm}(t) = \frac{J_{SC}(t)}{J_{SC}(0)} = \frac{peIC(t)}{peIC(0)} = \frac{\frac{2\pi R(t)}{R(t)^2\pi}}{\frac{2\pi R(0)}{R(0)^2\pi}} = \frac{R(0)}{R(t)}. \tag{7.1}$$

In this work, model and experiment are shown to be in excellent agreement. Therefore, the decrease in interface-to-volume ratio is identified to be the determining factor for the significant degradation of J_{SC} during operation. The reduction of relative J_{SC} to 0.76 for a 1:1 or 0.80 for a 1:2 donor:acceptor ratio provokes a decline in normalized PCE to 0.63.

7.3. Conclusions

In the *in operando* study, we compare printed organic solar cells based on donor:acceptor ratios of 1:1 and 1:2. Irrespective of the mixing ratio, degradation occurs by the same degradation mechanism, and a decrease in J_{SC} is identified to be the determining factor for the decline in PCE. With GISAXS, a growth of polymer domains is observed, whereas domain distances remain unchanged, causing a reduction of interface-to-volume ratio in the BHJ. Thereby the probability of exciton dissociation is lowered. The observed decline in J_{SC} correlates very well with the calculated current based on the changed nanoscale BHJ structure. Thus, morphology degradation is leading to device failure. The degradation mechanism observed for printed PBDB-T-SF:IT-4F based devices differs from previous studies on spin-coated fullerene based organic solar cells. Therefore, new materials should be studied *in operando*, as knowledge gained from one material system might not simply be transferred to other materials or processing conditions. This work gives insights into the degradation of meniscus guided slot-die coated organic solar cells and is a first step towards development of long-term stable organic photovoltaics.

8 Conclusion & Outlook

Towards marketability of organic solar cells, optimization of the factors given in the triangle of marketability, namely efficiency, long-term stability as well as scale-up of the thin film deposition, is necessary. In this thesis, focus is put on studying and optimizing the process of meniscus guided slot-die coating, a printing technique, which is compatible to roll-to-roll production. The evolution of inner morphology and optical properties of printed thin films was studied *in situ* to gain insights into the film formation and to enable optimization and up-scaling of the thin film deposition. In order to improve the PCE of printed photovoltaics, the effect of solvent additives on morphology, optical properties and device performance was investigated, as knowledge gained from spin-coating cannot simply be transferred to printing. To gain insights into the physical degradation of slot-die coated organic photovoltaics under illumination, morphological changes, occuring in the active layer, were studied *in operando* and correlated to a theoretical model, which can predict the evolution of J_{SC}.

The first result chapter (Chapter 5) aims on understanding the process of meniscus guided slot-die coating, an up-scalable printing technique. Therefore, the film formation of printed active layers was probed *in situ* to follow the evolution of inner morphology and to correlate these findings to changing optical properties. As a model system, the conjugated polymers PBDB-T-SF or PBDB-T-2Cl and the small molecule acceptor IT-4F were printed out of CB at ambient conditions. Five stages of film formation were identified. In the first phase, the film was completely wet and no morphological or optical changes were observed. In the second phase, polymer domains started to grow slowly, whereas absorbance of the thin film changed simultaneously. In the third phase, fast growth of inner nanostructures occurred, provoking a very pronounced change of optical properties in the thin film. Data modeling with Gaussian functions showed a shift of energy levels as well as a broadening of the FWHM for the polymer and the acceptor, indicating an increase in disorder in the active layer. The optical bandgap red-shifted significantly. In the fourth phase, reduction

of average distances between polymer domains and a slight change of absorbance were observed. In addition, fast crystallization of IT-4F was observed in this phase. In the fifth phase, the printed active layer was completely dry and no further changes occurred. Understanding the structure evolution during slot-die coating is prerequisite to further optimize the printing process, enable large-scale deposition and to improve the device performance of organic solar cells.

Beyond optimization of the thin film deposition technique, solvent additives are a common approach to improve the BHJ and solar cell performance. In the second result chapter (Chapter 6), the effect of DIO on the nanostructure, optical properties and device performance of slot-die coated active layers is discussed. The best photovoltaic performance was achieved for an optimum DIO concentration of 0.25 vol % DIO. GISAXS, AFM and SEM revealed the formation of smaller domains and larger distances with rising solvent additive concentrations. Thus, the interface area increased and exciton spliting was facilitated. However, the risk of charge trapping increased as well. For rising solvent additive concentrations, increased crystallinity of polymer and acceptor domains was observed with GIWAXS. The crystallites were found to be oriented edge-on, which facilitated the charge transport parallel to the electrodes, and did not have a favorable effect on the device performance. For rising DIO concentrations, a decrease in PL was observed, indicating improved charge transfer from polymer donor to small molecule acceptor due to reduced average domain sizes and enlargement of interface area. For a DIO concentration of 0.25 vol %, an improved absorbance and facilitated generation of photocurrent were observed with UV/vis spectroscopy and EQE. For an optimum DIO concentration of 0.25 vol %, the average PCE improved from 3.5 to 7.9% and efficiencies up to 8.95% were obtained. Understanding the effect of solvent additives on the device performance of slot-die coated organic solar cells is an important step towards optimization and up-scaling of printed photovoltaics.

However, towards real-world use, the poor long-term stability of organic solar cells has to be improved. Therefore, the mechanism of device degradation under illumination has to be understood. In the last result chapter (Chapter 7), morphological changes, occuring in the BHJ layer, were followed *in operando* with GISAXS and correlated to the degradation of device parameters. A model was introduced to predict the decline of J_{SC} under illumination. Organic solar cells with a donor:acceptor ratio of 1:1 and 1:2 were studied. For both systems, degradation of solar cell performance occurred due to coarsening of structures, provoking a decrease in interface area and decline of exciton splitting probability. These findings show the significant impact of active layer morphology on device parameters and

give insights into the degradation of printed organic solar cells, which is prerequisite for the development of printed organic photovoltaics with high efficiency and long-term stability.

This work addresses the factors efficiency, stability and up-scaling of the thin film deposition, stated in the triangle of marketabilty of organic solar cells. Furthermore, it shall give guidance for further investigations, which are necessary to enable real-world use of organic photovoltaics. Towards marketability, the high efficiencies, which could be achieved for printed organic solar cells, are assumed to be sufficient for most applications, but the development of a continuous thin film deposition process as well as further optimization of device stability are indispensable. Therefore, roll-to-roll production has to be realized to enable cost-effective, large-scale production of organic photovoltaics. Encapsulation of solar cells will be necessary to avoid chemical degradation by water and oxygen but cannot prevent physical degradation by morphological changes in the BHJ layer. Therefore, further studies have to be performed to overcome this drawback. Possible ways to stabilize the BHJ morphology might be the synthesis of new materials with well-defined morphology such as block-copolymers, cross-linking of the polymer donor or the use of new additives, which enhance the long-term stability. Furthermore, post-treatment of freshly processed active layers with alcohol or the use of co-solvents might increase the stability as well, even though so far these procedures were mainly used to enhance the efficiency of spin-coated devices.

Finally, real-world application of long-term stable organic solar cells will be possible when the pathways of degradation are fully understood and can be inhibited. In addition, a cost-effective, large-scale production process has to be developed. Then, manifold applications of organic solar cells in art and architecture as well as solar trees, clothes and windows can be realized and decentralized power generation becomes feasible. Organic solar cells are expected to be of great importance in the energy revolution towards climate-neutral power generation and reduction of global warming.

A

Appendix: *In Situ* Printing

The following chapter is based on the published articles: "*In Situ* Printing: Insights into the Morphology Formation and Optical Property Evolution of Slot-Die Coated Active Layers Containing Low Bandgap Polymer Donor and Nonfullerene Small Molecule Acceptor" [177] (Kerstin S. Wienhold et al., *Sol. RRL*, vol. 4, no. 7, p. 2000086, **2020**, DOI: 10.1002/solr.202000086) and: "Following *In Situ* the Evolution of Morphology and Optical Properties during Printing of Thin Films for Application in Nonfullerene Acceptor based Organic Solar Cells" [243] (Kerstin S. Wienhold et al., *ACS Appl. Mater. Interfaces*, vol. 12, no. 36, p. 40381–40392, **2020**, DOI: 10.1021/acsami.0c12390). Content and images of the following chapter can be found in the supporting information of the respective articles and are reproduced with permission from Wiley and ACS publishing, Copyright 2020.

A1. *In Situ* Printing Set-Up

A meniscus guided slot-die coater (Figure A.1) was used to study the film formation *in situ* at the MiNaXS beamline P03, DESY, Hamburg. The set-up for meniscus guided slot-die coating mainly consists of a syringe pump, a sample holder, which was moved by a motor and a printer head. A meniscus guide mask and a shim mask, mounted inside the printer head, guided the solution to provide a stable meniscus during printing, whereas a motor moved the sample holder with a constant velocity. The small, light-weight set-up was mounted on a beamline at the synchrotron source in order to perform *in situ* X-ray scattering experiments with high brilliance and time resolution to follow the fast process of film formation. The printer was installed perpendicular to the X-ray beam to enable *in situ* GISAXS (Figure A.1a) or GIWAXS (Figure A.1b).

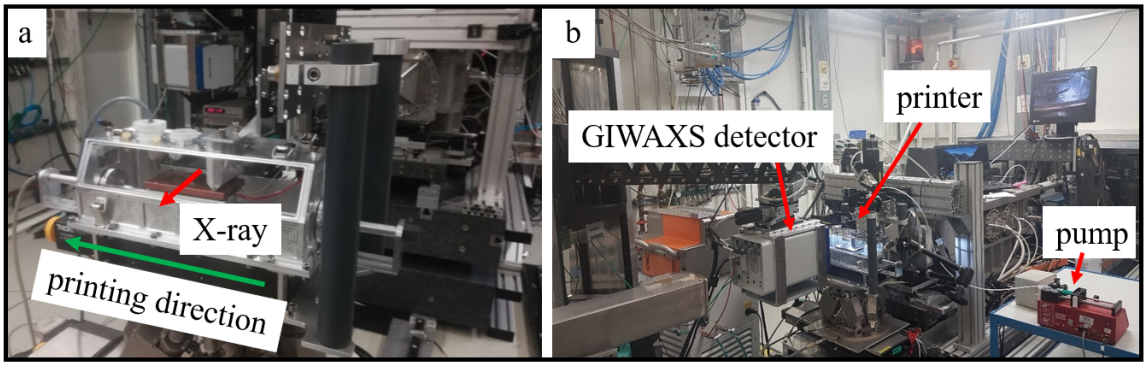

Figure A.1.: The small, light-weight set-up is installed at the synchrotron source to carry out *in situ* (a) GISAXS and (b) GIWAXS experiments. The X-ray beam (red arrow), printing direction (green arrow) as well as selected components (GIWAXS detector, printer, syringe pump) are marked. Reproduced with permission from ACS publishing and Wiley.

A2. *In Situ* Printing of PBDB-T-SF:IT-4F

A.2.1. Tauc Plot for PBDB-T-SF:IT-4F

The optical bandgap of the active material was determined with a Tauc plot. The absorption coefficient α was obtained from the respective UV/vis spectrum. The bandgap E_g is determined to red-shift from (1.63 $\pm$0.04) eV to (1.52 $\pm$0.04) eV during film formation (Figure A.2).

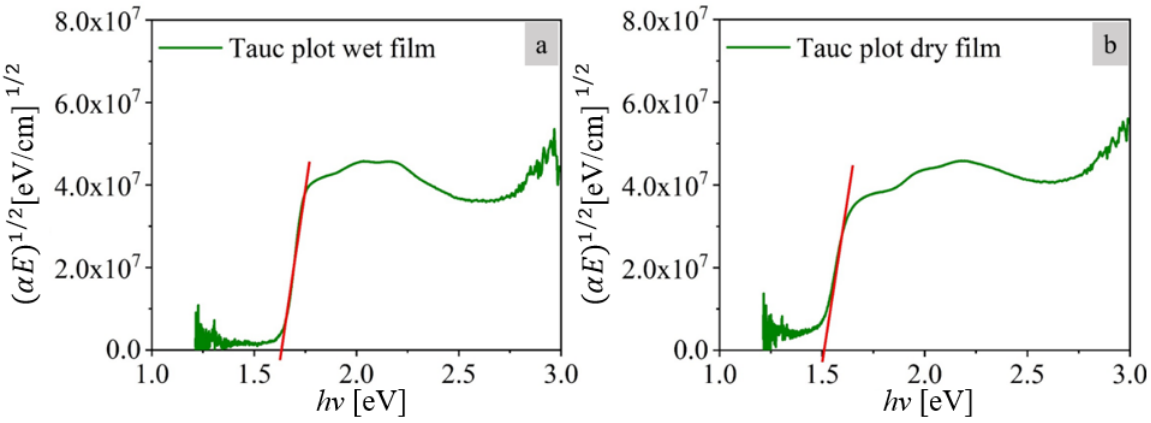

Figure A.2.: The bandgap of a printed active layer based on PBDB-T-SF:IT-4F is determined with a Tauc plot to be (a) (1.63 $\pm$0.04) eV for the wet film and (b) (1.52 $\pm$0.04) eV for the final dry film. Reproduced with permission from Wiley.

A.2.2. Modeling UV/vis Spectra of IT-4F

Electronic transitions were determined by modeling UV/vis absorbance spectra (Figure A.3, green) with sets of Gaussian functions, which all have the same width. The UV/vis spectrum for IT-4F in solution (Figure A.3a) and as a thin film (Figure A.3b) is modeled with a set of Gaussian functions of equal width (red). Summing up all Gaussian functions gives the modeled absorbance (black).

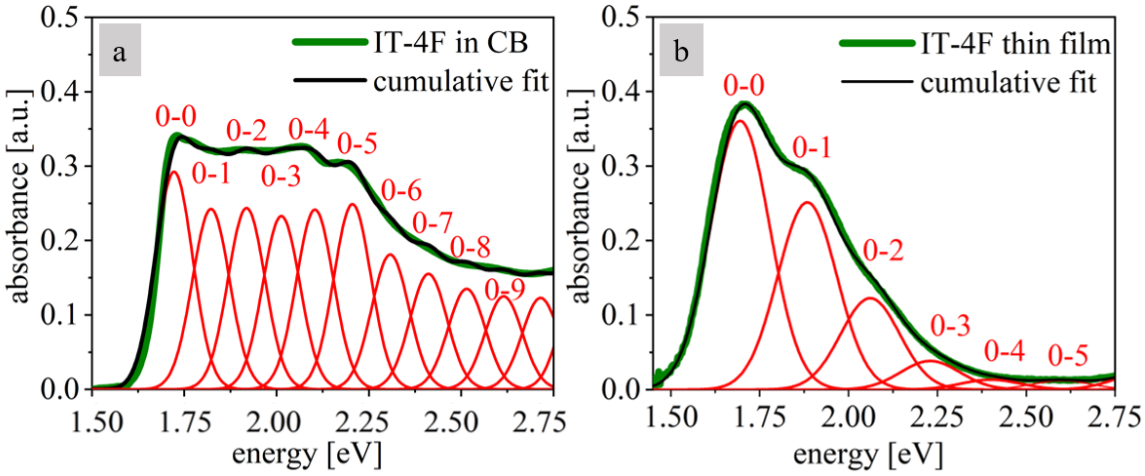

Figure A.3.: Electronic transitions of the small molecule acceptor IT-4F are determined with sets of Gaussian functions (red) of equal width. Electronic transitions of IT-4F are shown for (a) a dilute CB solution and (b) a dry film. Reproduced and adapted with permission from Wiley.

A.2.3. Modeling UV/vis Spectra of PBDB-T-SF:IT-4F

The absorbance of a slot-die coated active layer is shown for the initial wet film (Figure A.4a, green) and the final dry film (Figure A.4b, green). As contributions of PBDB-T-SF and IT-4F overlap in the absorbance spectra, center positions and width of the set of Gaussian functions were adopted from modeling pure PBDB-T-SF (Figure 3.4) and IT-4F (Figure A.3) in solution and as thin films. Summing up all Gaussian functions gives the modeled absorbance (Figure A.4, black).

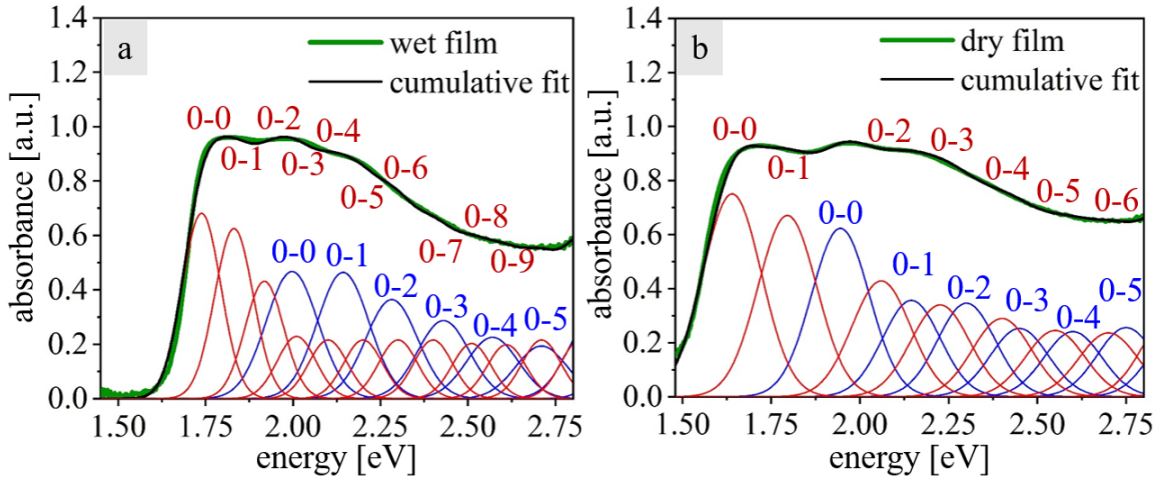

Figure A.4.: In a slot-die coated thin film based on PBDB-T-SF:IT-4F, electronic transitions of polymer (blue) and acceptor (red) overlap. Sets of Gaussian functions are applied to determine the electronic transitions of (a) the initial wet film and (b) the final dry film. Reproduced with permission from Wiley.

A.2.4. GISAXS Radiation Damage Test for PBDB-T-SF:IT-4F

Radiation damage has to be excluded in all *in situ* studies performed at high brilliance synchrotron sources such as the DESY to rule out morphology changes caused by the X-ray radiation. Radiation damage is excluded after the *in situ* experiment by comparing the *in situ* position with several *ex situ* positions, which have not been illuminated with the X-ray beam before. Therefore, GISAXS was measured at 20 *ex situ* positions. *Ex situ* (Figure A.5, green) and *in situ* (Figure A.5, red) measurements show excellent agreement in the horizontal (Figure A.5a) and vertical (Figure A.5b) line cut. Error bars are defined by the Poisson distribution of the beam profile and the standard deviation of the sample homogeneity. Therefore, radiation damage is excluded in this *in situ* study.

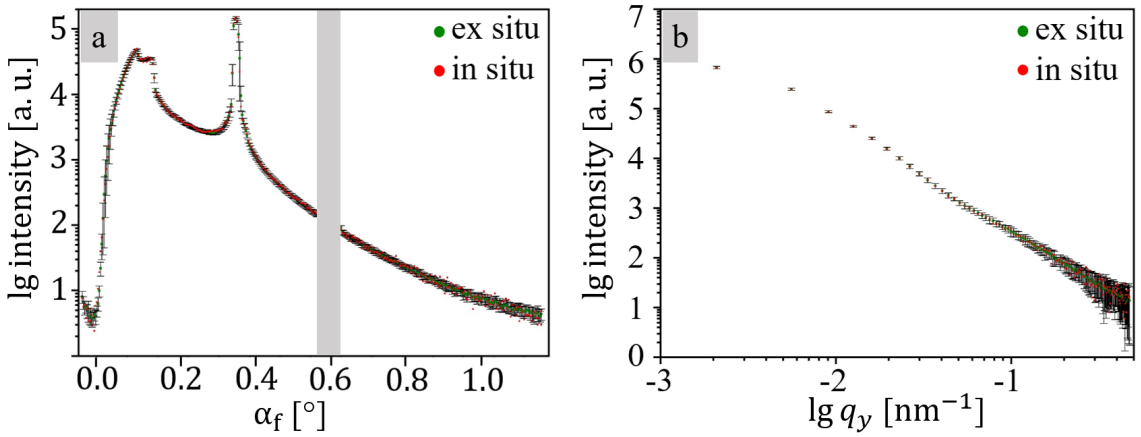

Figure A.5.: Comparison of (a) horizontal and (b) vertical line cuts of GISAXS measurements performed at the *in situ* and several *ex situ* positions. Radiation damage is ruled out in this *in situ* study due to excellent agreement of *in situ* and *ex situ* measurements. The Detector gap is marked with a gray bar. Reproduced with permission from Wiley.

A3. *In Situ* Printing of PBDB-T-2Cl:IT-4F

A3.1. Tauc Plot for PBDB-T-2Cl:IT-4F

The optical bandgap of PBDB-T-2Cl:IT-4F is determined with Tauc plot to red-shift from (1.64 ±0.04) eV to (1.52 ±0.04) eV for active layers processed at 25 °C (Figure A.6a,b) and 35 °C (Figure A.6c,d).

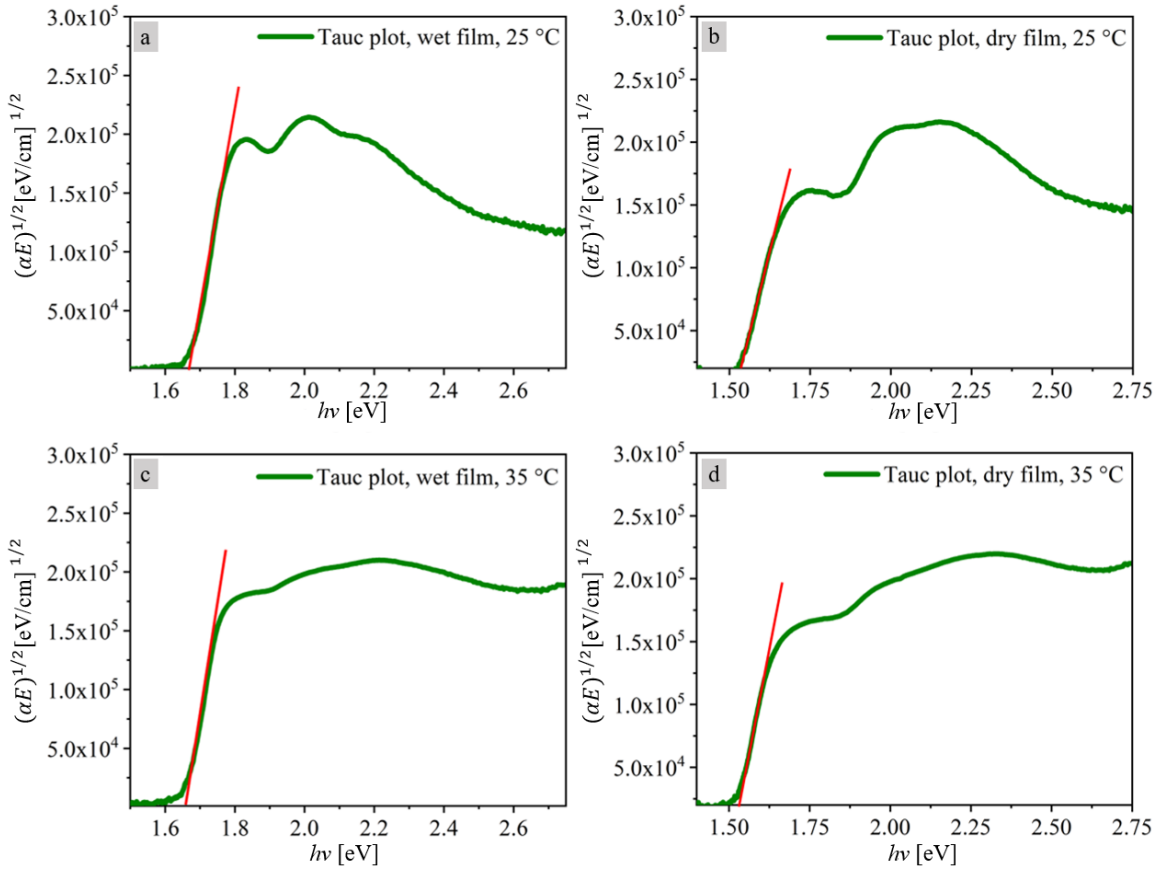

Figure A.6.: Tauc plots of (a) the wet film printed at 25 °C, (b) the dry film printed at 25 °C, (c) the wet film printed at 35 °C and (d) the dry film printed at 35 °C. Reproduced with permission from ACS publishing.

A3.2. Modeling UV/vis Spectra of PBDB-T-2Cl

To determine the electronic transitions of PBDB-T-2Cl, UV/vis absorbance spectra were measured for a printed wet film (Figure A.7a, green) and the final dry thin film (Figure A.7b, green).

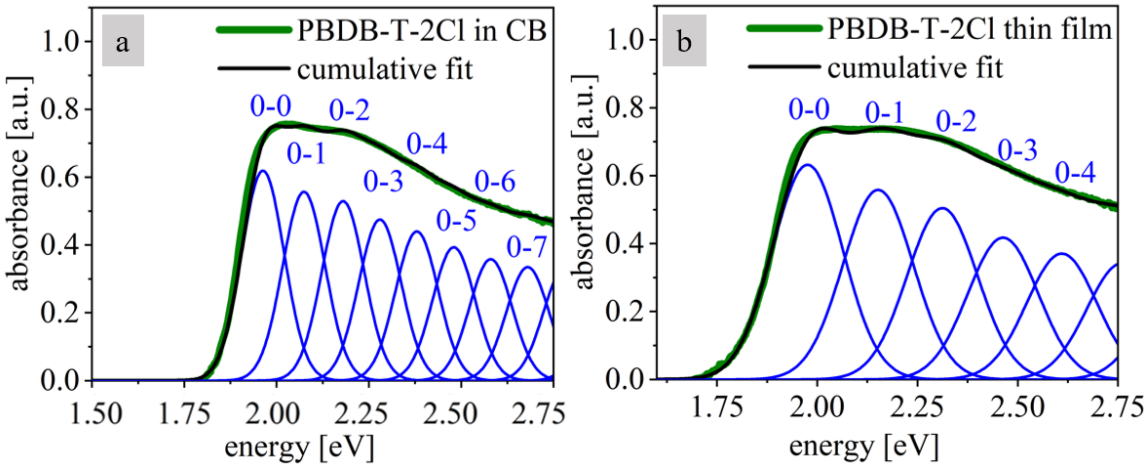

Figure A.7.: Electronic transitions of PBDB-T-2Cl are determined by modeling with sets of Gaussian functions (blue). Absorbance spectra (green) and modeling results (black) are given for (a) a dilute CB solution and (b) a dry film. Reproduced with permission from ACS publishing.

A3.3. Modeling UV/vis Spectra of PBDB-T-2Cl:IT-4F

UV/vis spectra of printed active layers based on PBDB-T-2Cl:IT-4F and the corresponding sets of Gaussian functions to model the absorbance are illustrated in Figure A.8. The absorbance of the thin films is shown for dilute solutions (Figure A.8a,c) and dry films (Figure A.8b,d) for a processing temperature of 25 °C (Figure A.8a,b) and 35 °C (Figure A.8b,d).

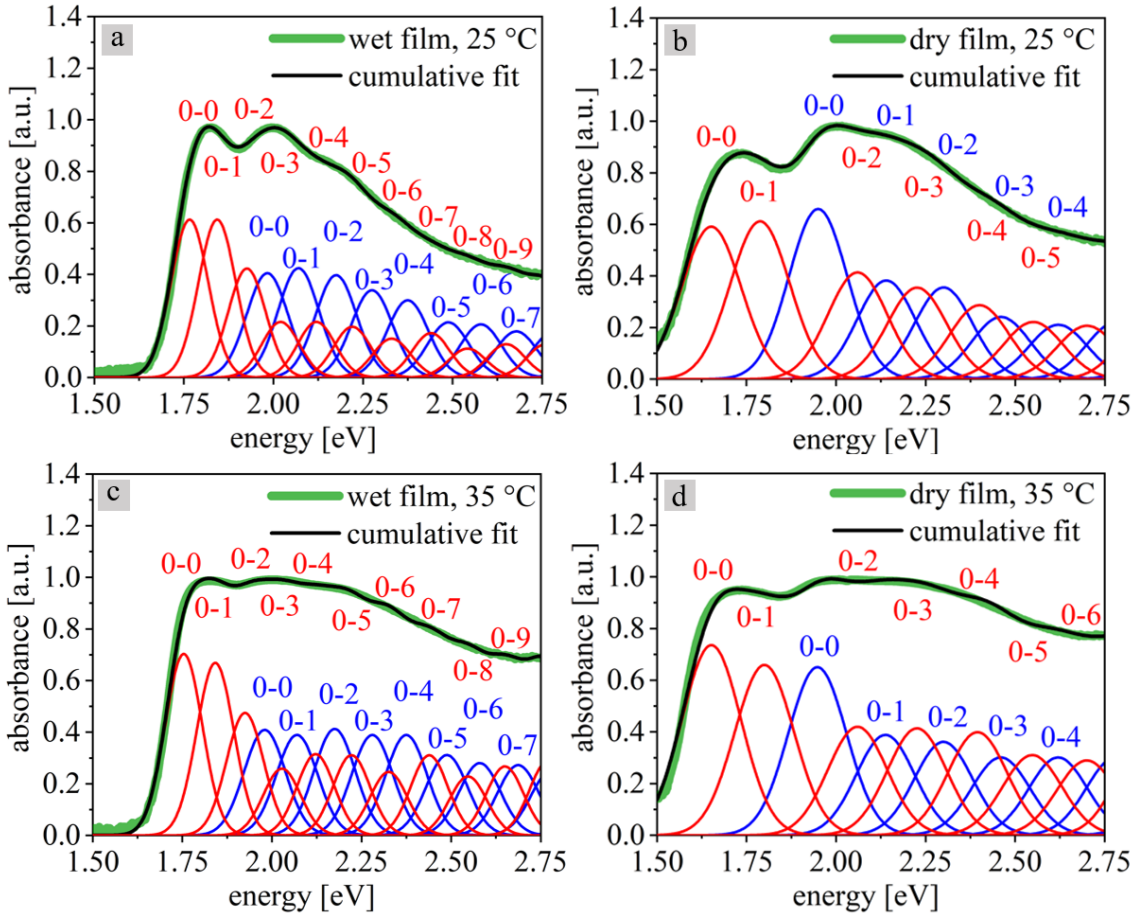

Figure A.8.: In printed active layer, contribution of PBDB-T-2Cl (blue) and IT-4F (red) overlap. Electronic transitions in thin films slot-die coated at (a,b,) 25 °C and (c,d) 35°C are determined by modeling with sets of Gaussian functions. Absorbance spectra (green) and modeling results (black) are given for (a,c) a wet film and (b,d) a dry film. Reproduced with permission from ACS publishing.

A3.4. GISAXS Radiation Damage Test for PBDB-T-2Cl:IT-4F

In this experiment, exposure to X-ray radiation was minimized by a measurement script, enabling a measurement time of 0.05 s in combination with a fast shutter operation, and by moving of the measurement position (for printing at 35 °C). For the sample printed at 25 °C (Figure A.9a,b) as well as for the film printed at 35 °C (Figure A.9c,d), radiation damage is ruled out due to excellent agreement of *in situ* (red) and *ex situ* (green) measurements.

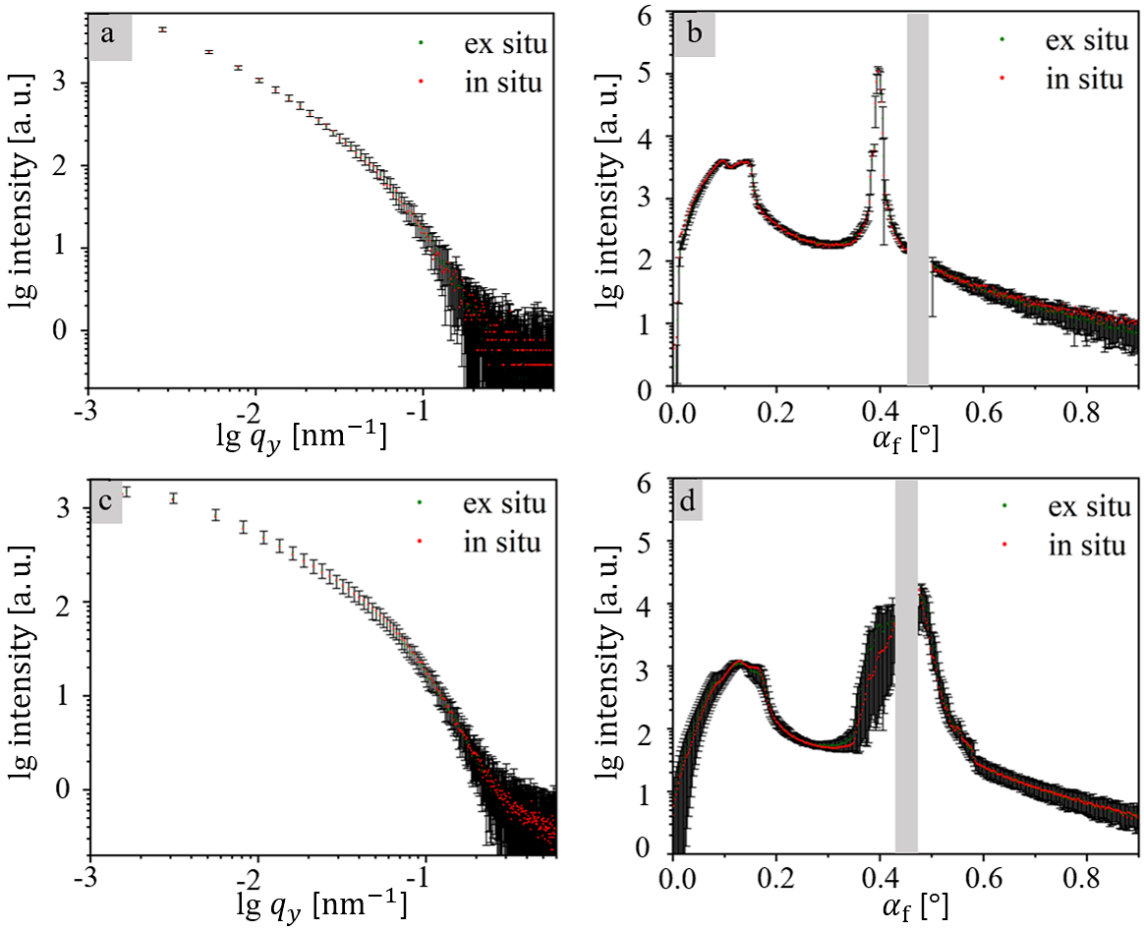

Figure A.9.: Comparison of (a,c) horizontal and (b,d) vertical line cuts of 2D GISAXS data performed at *in situ* (red) and *ex situ* (green) positions for thin films printed at (a,b) 25 °C and (c,d) 35 °C. Error bars are estimated by the Poisson distribution of the X-ray beam and the sample homogeneity. Due to excellent agreement of *in situ* and *ex situ* measurements, radiation damage is ruled out in this experiments. Detector gaps are marked with gray bars. Reproduced with permission from ACS publishing.

A3.5. GIWAXS Radiation Damage Test for PBDB-T-2Cl:IT-4F

To rule out radiation damage in the GIWAXS experiment, tube cuts were performed at the (100) IT-4F Bragg peak position. Tube cuts and azimuthal q integrals of measurements performed at *in situ* (red) and *ex situ* (green) positions are shown in Figure A.10. For the sample printed at 25 °C (Figure A.10a,b) as well as for the film printed at 35 °C (Figure A.10c,d), radiation damage is ruled out due to excellent agreement of *in situ* and *ex situ* measurements.

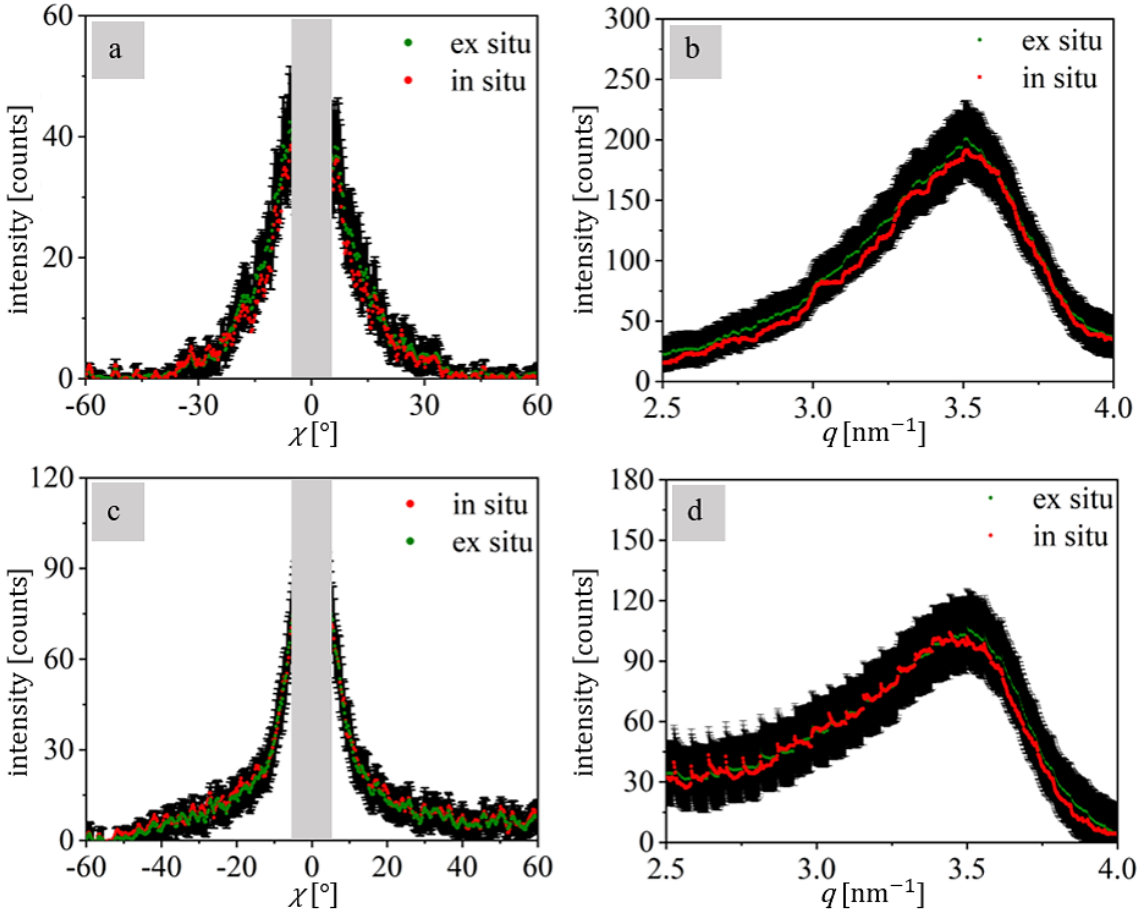

Figure A.10.: Comparison of tube cuts and azimuthal q integrals for samples printed at (a,b) 25 °C and (c,d) 35 °C at *in situ* (red) and *ex situ* (green) positions. Radiation damage is excluded in these experiments due to excellent agreement of *in situ* and *ex situ* positions. The inaccessible q range is marked with gray bars. The error bars are estimated by the Poisson distribution of the X-ray beam and the sample homogeneity. Reproduced with permission from ACS publishing.

B Appendix: *In Operando* Degradation

The following chapter is based on the published article: "Following *In Operando* the Structure Evolution-Induced Degradation in Printed Organic Solar Cells with Nonfullerene Small Molecule Acceptor" [262] (Kerstin S. Wienhold et al., *Sol. RRL*, vol. 4, no. 9, p. 2000251, **2020**, DOI: 10.1002/solr.202000251). Content and images of the following chapter can be found in the supporting information of the respective articles and are reproduced with permission from Wiley, Copyright 2020.

In Operando Set-up

Photographs of the *in operando* set-up in front (Figure B.1a) and top view (Figure B.1b) installed at the MiNaXS beamline P03, DESY, Hamburg are shown. Vacuum conditions (10^{-2} mbar) and water cooling (15 °C) were applied to ensure a stable temperature and to rule out chemical degradation by oxygen or air humidity. *JV* characteristics were probed with a SourceMeter Keithley® 2400. The X-ray beam entered the chamber through Kapton® windows. The light of the sun simulator was reflected at a mirror to enter the chamber.

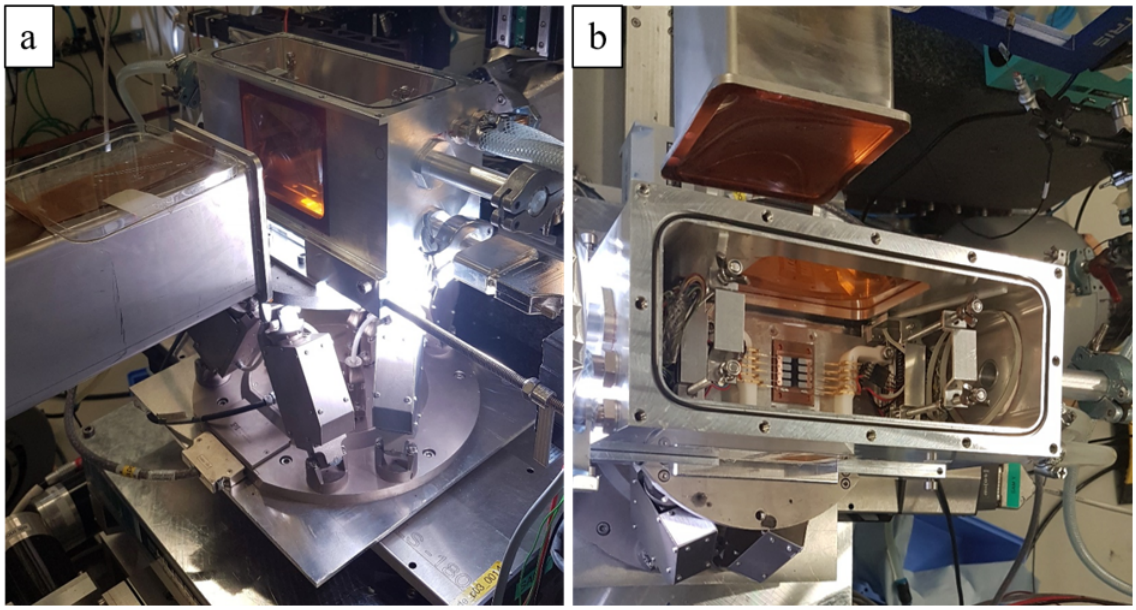

Figure B.1.: Photographs of the *in operando* set-up in (a) front and (b) top view. Reproduced with permission from Wiley.

Radiation Damage Test

Figure B.2 shows the radiation damage test for printed organic solar cells based on a 1:1 and 1:2 ratio of PBDB-T-SF:IT-4F. 100 GISAXS measurements with an exposure time of 0.3 s per frame were continuously performed at one fixed spot. No morphological change is observed in the horizontal (Figure B.2a,c) or vertical (Figure B.2b,d) line cuts for exposure times up to 30 s. In this work, the overall exposure time is kept far below the threshold for radiation damage as only 10 frames were performed for each sample. Therefore, radiation damage is excluded for all *in operando* studies performed in the context of this thesis.

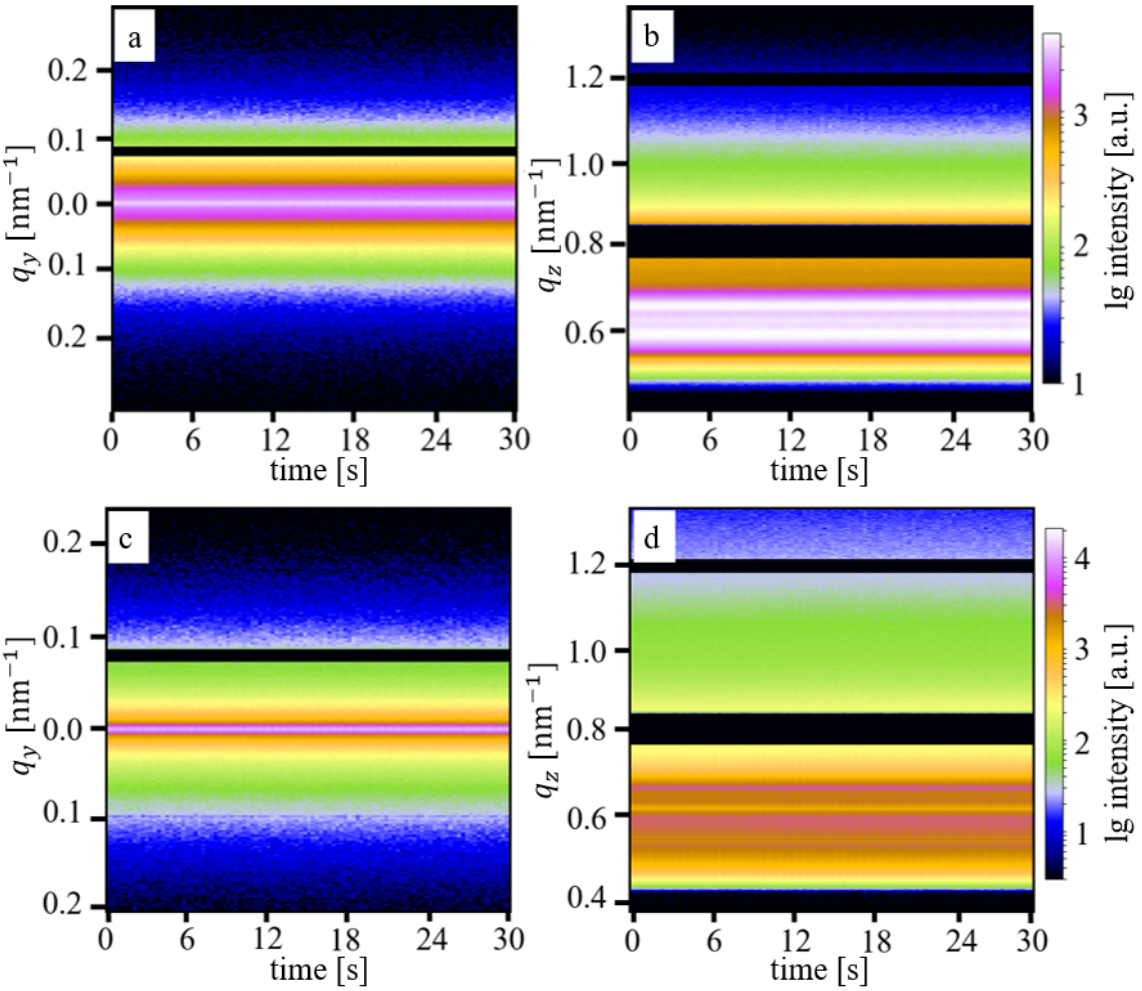

Figure B.2.: Radiation damage tests performed at active layers of printed organic solar cells based on a (a,b) 1:1 and (c,d) 1:2 donor:acceptor ratio under vacuum conditions. The (a,c) horizontal and (b,d) vertical line cuts are stable for 30 s of continuous GISAXS measurements at one fixed spot. Reproduced with permission from Wiley.

Solar Cell Performance

Table B.1 gives the average device parameters of the investigated organic solar cells at the beginning of operation. Four pixels close to the GISAXS measurement position were connected in parallel to record average JV characteristics. It should be noted that the achieved device performance is lower as compared to values commonly achieved in our laboratory and reported in literature, due to the need for transporting the devices to the synchrotron radiation source DESY in Hamburg.

Table B.1.: Average Device Parameters at the Beginning of Illumination for the Solar Cells investigated. For each Device, four Pixels close to the GISAXS Measurement Position were Connected in Parallel.

donor:acceptor ratio	PCE [%]	J_{SC} [mA/cm^2]	V_{OC} [V]	FF [-]
1:1	2.3	7.43	0.74	0.42
1:2	4.5	17.78	0.61	0.41

Bibliography

[1] O. Ellabban, H. Abu-Rub, and F. Blaabjerg, "Renewable Energy Resources: Current Status, Future Prospects and their enabling Technology", *Renew. Sust. Energ. Rev.*, vol. 39, pp. 748–764, **2014**.

[2] I. Dincer, "Renewable Energy and Sustainable Development: A Crucial Review", *ACS Appl. Mater. Interfaces*, vol. 4, pp. 157–175, **2000**.

[3] G. K. Singh, "Solar Power Generation by PV (Photovoltaic) Technology: A Review", *Energy*, vol. 53, pp. 1–13, **2013**.

[4] www.ag-energiebilanzen.de, visited on 02.01.2021.

[5] M. Dittmar, "Nuclear Energy: Status and Future Limitations", *Energy*, vol. 37, no. 1, pp. 35–40, **2012**.

[6] M. Asif, and T. Muneer, "Energy Supply, its Demand and Security Issues for Developed and Emerging Economies", *Renew. Sust. Energ. Rev.*, vol. 11, no. 7, pp. 1388–1413, **2007**.

[7] M. Yaqoot, P. Diwan, and T. C. Kandpal, "Review of Barriers to the Dissemination of Decentralized Renewable Energy Systems", *Renew. Sust. Energ. Rev.*, vol. 58, pp. 477–490, **2016**.

[8] M. T. Iqbal, "A Feasibility Study of a Zero Energy Home in Newfoundland", *Renew. Energy*, vol. 29, no. 2, pp. 277–289, **2004**.

[9] M. A. F. Alrashed, "Analysis of Critical Climate related Factors for the Application of Zero-Energy Homes in Saudi Arabia", *Renew. Sust. Energ. Rev.*, vol. 41, pp. 1395–1403, **2015**.

[10] F. AlFaris, A. Juaidi, and F. Manzano-Agugliaro, "Intelligent Homes' Technologies to optimize the Energy Performance for the Net Zero Energy Home", *Energy Build.*, vol. 153, pp. 262–274, **2017**.

[11] J. Kneifel, W. Healy, J. Filliben, and M. Boyd, "Energy Performance Sensitivity of a Net-Zero Energy Home to Design and Use Specifications", *J. Build. Perform. Simul.*, vol. 9, no. 1, pp. 70–83, **2016**.

[12] J. Wu, and N. Tran, "Application of Blockchain Technology in Sustainable Energy Systems: An Overview", *Sustainability*, vol. 10, no. 9, p. 3067, **2018**.

[13] A. Ahl, M. Yarime, K. Tanaka, and D. Sagawa, "Review of Blockchain-Based Distributed Energy: Implications for Institutional Development", *Renew. Sust. Energ. Rev.*, vol. 107, pp. 200–211, **2019**.

[14] A. Q. Huang, M. L. Crow, G. T. Heydt, J. P. Zheng, and S. J. Dale, "The Future Renewable Electric Energy Delivery and Management (FREEDM) System: The Energy Internet", *Proc. IEEE*, vol. 99, no. 1, pp. 133–148, **2011**.

[15] C. Pop, T. Cioara, A. Tudor, M. Antal, I. Anghel, I. Salomie, and M. Bertoncini, "Blockchain Based Decentralized Management of Demand Response Programs in Smart Energy Grids", *Sensors*, vol. 18, no. 1, p. 162, **2019**.

[16] E. Mengelkamp, B. Notheisen, C. Beer, D. Dauer, and C. Weinhardt, "A Blockchain-Based Smart Grid: Towards Sustainable Local Energy Markets", *Comput. Sci. Res. Dev.*, vol. 33, pp. 207–214, **2018**.

[17] T. J. M. Oliver, "The Market for Solar Photovoltaics", *Energy Policy*, vol. 27, no. 7, pp. 371–385, **1999**.

[18] V. Devabhaktuni, M. Alam, S. Shekara Sreenadh Reddy Depuru, R. C. Green, D. Nims, and C. Near, "Solar Energy: Trends and enabling Technologies", *Renew. Sust. Energ. Rev.*, vol. 19, pp. 555–564, **2013**.

[19] M. Kaltenbrunner, M. S. White, E. D. Głowacki, T. Sekitani, T. Someya, N. S. Sariciftci, and S. Bauer, "Ultrathin and Lightweight Organic Solar Cells with high Flexibility", *Nat. Commun.*, vol. 3, no. 770, pp. 1–7, **2012**.

[20] C.-C. Chueh, S.-C. Chien, H.-L. Yip, J. F. Salinas, C.-Z. Li, K.-S. Chen, F.-C. Chen, W.-C. Chen, and A. K.-Y. Jen, "Toward High-Performance Semi-Transparent Polymer Solar Cells: Optimization of Ultra-Thin Light Absorbing Layer and Transparent Cathode Architecture", *Adv. Energy Mater.*, vol. 3, no. 4, pp. 417–423, **2013**.

[21] J. Kettle, N. Bristow, T. K. N. Sweet, N. Jenkins, G. A. dos Reis Benatto, M. Jørgensen, and F. C. Krebs, "Three Dimensional Corrugated Organic Photovoltaics for Building Integration; Improving the Efficiency, Oblique Angle and Diffuse Performance of Solar Cells", *Energy Environ. Sci.*, vol. 8, pp. 3266–3273, **2015**.

[22] S. Berny, N. Blouin, A. Distler, H.-J. Egelhaaf, M. Krompiec, A. Lohr, O. R. Lozman, G. E. Morse, L. Nanson, A. Pron, T. Sauermann, N. Seidler, S. Tierney, P. Tiwana, M. Wagner, and H. Wilson, "Solar Trees: First Large-Scale Demonstration of Fully Solution Coated, Semitransparent, Flexible Organic Photovoltaic Modules", *Adv. Sci.*, vol. 3, no. 5, p. 1500342, **2016**.

[23] T. Sano, S. Inaba, and V. Vohra, "Ternary Active Layers for Neutral Color Semi-transparent Organic Solar Cells with PCEs over 4%", *ACS Appl. Energy Mater.*, vol. 2, no. 4, pp. 2534–2540, **2019**.

[24] V. Shrotriya, "Polymer Power", *Nat. Photonics*, vol. 3, pp. 447–449, **2009**.

[25] P. Gangwar, N. M. Kumar, A. K. Singh, A. Jayakumar, and M. Mathew, "Solar Photovoltaic Tree and its End-of-Life Management using Thermal and Chemical Treatments for Material Recovery", *Case Stud. Therm. Eng.*, vol. 14, p. 100474, **2019**.

[26] M. B. Schubert, and J. H. Werner , "Flexible Solar Cells for Clothing", *Mater. Today*, vol. 9, no. 6, pp. 42–50, **2006**.

[27] Z. Zhang, Z. Yang, J. Deng, Y. Zhang, G. Guan, and H. Peng, "Stretchable Polymer Solar Cell Fibers", *Small*, vol. 11, no. 6, pp. 675–680, **2015**.

[28] P. Cheng, G. Li, X. Zhan, and Y. Yang, "Next-Generation Organic Photovoltaics based on Non-Fullerene Acceptors", *Nat. Photonics*, vol. 12, p. 1458–1463, **2018**.

[29] S. Guo, W. Wang, E. M. Herzig, A. Naumann, G. Tainter, J. Perlich, and P. Müller-Buschbaum, "Solvent-Morphology-Property Relationship of PTB7:PC71BM Polymer Solar Cells", *ACS Appl. Mater. Interfaces*, vol. 9, no. 4, pp. 3740–3748, **2017**.

[30] C. J. Schaffer, J. Schlipf, E. D. Indari, B. Su, S. Bernstorff, and P. Müller-Buschbaum, "Effect of Blend Composition and Additives on the Morphology of PCPDTBT:PC71BM Thin Films for Organic Photovoltaics", *ACS Appl. Mater. Interfaces*, vol. 7, no. 38, pp. 21347–21355, **2015**.

[31] D. Yang, F. C. Löhrer, V. Körstgens, A. Schreiber, S. Bernstorff, J. M. Buriak, and P. Müller-Buschbaum, "In-Operando Study of the Effects of Solvent Additives on the Stability of Organic Solar Cells Based on PTB7-Th:PC71BM", *ACS Energy Lett.*, vol. 4, no. 2, pp. 464–470, **2019**.

[32] W. Wang, C. J. Schaffer, L. Song, V. Körstgens, S. Pröller, E. D. Indari, T. Wang, A. Abdelsamie, S. Bernstorff, and P. Müller-Buschbaum, "In Operando Morphology Investigation of Inverted Bulk Heterojunction Organic Solar Cells by GISAXS", *J. Mater. Chem. A*, vol. 3, pp. 8324–8331, **2015**.

[33] X. Shi, J. Chen, K. Gao, L. Zuo, Z. Yao, F. Liu, J. Tang, and A. K. Y. Jen, "Terthieno[3,2-b]Thiophene (6T) Based Low Bandgap Fused-Ring Electron Acceptor for Highly Efficient Solar Cells with a High Short-Circuit Current Density and Low Open-Circuit Voltage Loss", *Adv. Energy Mater.*, vol. 8, no. 12, p. 1702831, **2018**.

[34] D. Baran, R. S. Ashraf, D. A. Hanifi, M. Abdelsamie, N. Gasparini, J. A. Röhr, S. Holliday, A. Wadsworth, S. Lockett, M. Neophytou, C. J. M. Emmott, J. Nelson, C. J. Brabec, A. Amassian, A. Salleo, T. Kirchartz, J. R. Durrant, and I. McCulloch,

"Reducing the Efficiency-Stability-Cost Gap of Organic Photovoltaics with Highly Efficient and Stable Small Molecule Acceptor Ternary Solar Cells", *Nat. Mater.*, vol. 16, pp. 363–369, **2017**.

[35] W. Zhao, S. Li, H. Yao, S. Zhang, Y. Zhang, B. Yang, and J. Hou, "Molecular Optimization Enables over 13% Efficiency in Organic Solar Cells", *J. Am. Chem. Soc.*, vol. 139, no. 21, pp. 7148–7151, **2017**.

[36] F. Liu, T. Hou, X. Xu, L. Sun, J. Zhou, X. Zhao, and S. Zhang, "Recent Advances in Nonfullerene Acceptors for Organic Solar Cells", *Macromol. Rapid Commun.*, vol. 39, no. 3, p. 1700555, **2018**.

[37] D. Mühlbacher, M. Scharber, M. Morana, Z. Zhu, D. Waller, R. Gaudiana, and C. Brabec, "High Photovoltaic Performance of a Low-Bandgap Polymer", *Adv. Mater.*, vol. 18, no. 21, pp. 2884–2889, **2006**.

[38] H. Yao, Y. Chen, Y. Qin, R. Yu, Y. Cui, B. Yang, S. Li, K. Zhang, and J. Hou, "Design and Synthesis of a Low Bandgap Small Molecule Acceptor for Efficient Polymer Solar Cells", *Adv. Mater.*, vol. 28, no. 37, pp. 8283–8287, **2016**.

[39] J. Zhou, Y. Zuo, X. Wan, G. Long, Q. Zhang, W. Ni, Y. Liu, Z. Li, G. He, C. Li, B. Kan, M. Li, and Y. Chen, "Solution-Processed and High-Performance Organic Solar Cells using Small Molecules with a Benzodithiophene Unit", *J. Am. Chem. Soc.*, vol. 135, no. 23, pp. 8484–8487, **2013**.

[40] Y. Lin, Y. Firdaus, F. H. Isikgor, M. I. Nugraha, E. Yengel, G. T. Harrison, R. Hallani, A. El-Labban, H. Faber, C. Ma, X. Zheng, A. Subbiah, C. T. Howells, O. M. Bakr, I. McCulloch, S. De Wolf, L. Tsetseris, and T. D. Anthopoulos, "Self-Assembled Monolayer Enables Hole Transport Layer-Free Organic Solar Cells with 18% Efficiency and Improved Operational Stability", *ACS Energy Lett.*, vol. 5, no. 9, pp. 2935–2944, **2020**.

[41] Q. Liu, Y. Jiang, K. Jin, J. Qin, J. Xu, W. Li, J. Xiong, J. Liu, Z. Xiao, K. Sun, S. Yang, X. Zhang, L. Ding, "18% Efficiency Organic Solar Cells", *Sci. Bull.*, vol. 65, no. 4, pp. 272–275, **2020**.

[42] M. H. Hoang, G. E. Park, S. Choi, C. G. Park, S. H. Park, T. van Nguyen, S. Kim, K. Kwak, M. J. Cho, and D. H. Choi, "High-Efficiency Non-Fullerene Polymer Solar Cell fabricated by a Simple Process using new Conjugated Terpolymers", *J. Mater. Chem. C*, vol. 7, pp. 111–118, **2019**.

[43] L. Dou, J. Gao, E. Richard, J. You, C.-C. Chen, K. C. Cha, Y. He, G. Li, and Y. Yang, "Systematic Investigation of Benzodithiophene- and Diketopyrrolopyrrole-based Low-Bandgap Polymers designed for Single Junction and Tandem Polymer Solar Cells", *J. Am. Chem. Soc.*, vol. 134, no. 24, pp. 10071–10079, **2012**.

[44] O. K. Kwon, J.-H. Park, D. W. Kim, S. K. Park, and S. Y. Park, "An All-Small-Molecule Organic Solar Cell with High Efficiency Nonfullerene Acceptor", *Adv. Mater.*, vol. 27, no. 11, pp. 1951–1956, **2015**.

[45] F. C. Krebs, J. Fyenbo, and M. Jørgensen, "Product Integration of Compact Roll-To-Roll processed Polymer Solar Cell Modules: Methods and Manufacture using Flexographic Printing, Slot-Die Coating and Rotary Screen Printing", *J. Mater. Chem.*, vol. 20, pp. 8994–9001, **2010**.

[46] S. Jung, A. Sou, K. Banger, D.-H. Ko, P. C. Y. Chow, C. R. McNeill, and H. Sirringhaus, "All-Inkjet-Printed, All-Air-Processed Solar Cells", *Adv. Energy Mater.*, vol. 4, no. 14, p. 1400432, **2014**.

[47] M. Helgesen, J. E. Carlé, and F. C. Krebs, "Slot-Die Coating of a High Performance Copolymer in a Readily Scalable Roll Process for Polymer Solar Cells", *Adv. Energy Mater.*, vol. 3, no. 12, pp. 1664–1669, **2013**.

[48] C. N. Hoth, S. A. Choulis, P. Schilinsky, and C. J. Brabec, "High Photovoltaic Performance of Inkjet Printed Polymer:Fullerene Blends", *Adv. Mater.*, vol. 19, no. 22, pp. 3973–3978, **2007**.

[49] C. N. Hoth, P. Schilinsky, S. A. Choulis, and C. J. Brabec, "Printing Highly Efficient Organic Solar Cells", *Nano Lett.*, vol. 8, no. 9, pp. 2806–2813, **2008**.

[50] F. C. Krebs, "All Solution Roll-To-Roll Processed Polymer Solar Cells Free from Indium-Tin-Oxide and Vacuum Coating Steps", *Org. Electron.*, vol. 10, no. 5, pp. 761–768, **2009**.

[51] P. Schilinsky, C. Waldauf, and C. J. Brabec, "Performance Analysis of Printed Bulk Heterojunction Solar Cells", *Adv. Funct. Mater.*, vol. 16, no. 13, pp. 1669–1672, **2006**.

[52] T. M. Eggenhuisen, Y. Galagan, A. F. K. V. Biezemans, T. M. W. L. Slaats, W. P. Voorthuijzen, S. Kommeren, S. Shanmugam, J. P. Teunissen, A. Hadipour, W. J. H. Verhees, S. C. Veenstra, M. J. J. Coenen, J. Gilot, R. Andriessen, and W. A. Groen, "High Efficiency, Fully Inkjet Printed Organic Solar Cells with Freedom of Design", *J. Mater. Chem. A*, vol. 3, pp. 7255–7262, **2015**.

[53] J. Chang, C. Chi, J. Zhang, and J. Wu, "Controlled Growth of Large-Area High-Performance Small-Molecule Organic Single-Crystalline Transistors by Slot-Die Coating using a Mixed Solvent System", *Adv. Mater.*, vol. 25, no. 44, pp. 6442–6447, **2013**.

[54] F. Liu, S. Ferdous, E. Schaible, A. Hexemer, M. Church, X. Ding, C. Wang, and T. P. Russell, "Fast Printing and In Situ Morphology Observation of Organic Photovoltaics using Slot-Die Coating", *Adv. Mater.*, vol. 27, no. 5, pp. 886–891, **2015**.

[55] N. Espinosa, R. García-Valverde, A. Urbina, and F. C. Krebs, "A Life Cycle Analysis of Polymer Solar Cell Modules prepared using Roll-to-Roll Methods under Ambient Conditions", *Sol. Energy Mater. Sol. Cells*, vol. 95, no. 5, pp. 1293–1302, **2011**.

[56] C. J. Brabec, J. A. Hauch, P. Schilinsky, and C. Waldauf, "Production Aspects of Organic Photovoltaics and their Impact on the Commercialization of Devices", *MRS Bull.*, vol. 30, no. 1, pp. 50–52, **2005**.

[57] F. Liu, W. Zhao, J. R. Tumbleston, C. Wang, Y. Gu, D. Wang, A. L. Briseno, H. Ade, and T. P. Russell, "Understanding the Morphology of PTB7:PCBM Blends in Organic Photovoltaics", *Adv. Energy Mater.*, vol. 4, no. 5, p. 1301377, **2014**.

[58] C. J. Brabec, S. Gowrisanker, J. J. M. Halls, D. Laird, S. Jia, and S. P. Williams, "Polymer-Fullerene Bulk-Heterojunction Solar Cells", *Adv. Mater.*, vol. 22, no. 34, pp. 3839–3856, **2010**.

[59] M. Kim, J.-H. Kim, H. H. Choi, J. H. Park, S. B. Jo, M. Sim, J. S. Kim, H. Jinnai, Y. D. Park, and K. Cho, "Electrical Performance of Organic Solar Cells with Additive-Assisted Vertical Phase Separation in the Photoactive Layer", *Adv. Energy Mater.*, vol. 4, no. 2, p. 1300612, **2014**.

[60] S. Pröller, D. Moseguí González, C. Zhu, E. Schaible, C. Wang, P. Müller-Buschbaum, A. Hexemer, and E. M. Herzig, "Note: Setup for Chemical Atmospheric Control during In Situ Grazing Incidence X-ray Scattering of Printed Thin Films", *Rev. Sci. Instrum.*, vol. 88, p. 066101, **2017**.

[61] T. Kassar, M. Berlinghof, N. S. Güldal, T. Schmutzler, F. Zontone, M. Brandl, E. Metwalli, J. Will, N. Li, T. Ameri, C. J. Brabec, and T. Unruh, "Real-Time Study on Structure Formation and the Intercalation Process of Polymer: Fullerene Bulk Heterojunction Thin Films", *Sol. RRL*, vol. 4, no. 3, p. 1900508, **2020**.

[62] T. Wang, A. D. F. Dunbar, P. A. Staniec, A. J. Pearson, P. E. Hopkinson, J. E. MacDonald, S. Lilliu, C. Pizzey, N. J. Terrill, A. M. Donald, A. J. Ryan, R. A. L. Jones, and D. G. Lidzey, "The Development of Nanoscale Morphology in Polymer:Fullerene Photovoltaic Blends during Solvent Casting", *Soft Matter*, vol. 6, no. 17, pp. 4128–4134, **2010**.

[63] M. Abdelsamie, K. Zhao, M. R. Niazi, K. W. Chou, and A. Amassian, "In Situ UV-Visible Absorption during Spin-Coating of Organic Semiconductors: A new Probe for Organic Electronics and Photovoltaics", *J. Mater. Chem. C*, vol. 2, no. 17, p. 3373, **2014**.

[64] C. McDowell, M. Abdelsamie, K. Zhao, D.-M. Smilgies, G. C. Bazan, and A. Amassian, "Synergistic Impact of Solvent and Polymer Additives on the Film Formation

of Small Molecule Blend Films for Bulk Heterojunction Solar Cells", *Adv. Energy Mater.*, vol. 5, no. 18, p. 1501121, **2015**.

[65] S. M. McAfee, S. V. Dayneko, P. Josse, P. Blanchard, C. Cabanetos, and G. C. Welch, "Simply Complex: The Efficient Synthesis of an Intricate Molecular Acceptor for High-Performance Air-Processed and Air-Tested Fullerene-Free Organic Solar Cells", *Chem. Mater.*, vol. 29, no. 3, pp. 1309–1314, **2017**.

[66] S. Holliday, R. S. Ashraf, A. Wadsworth, D. Baran, S. A. Yousaf, C. B. Nielsen, C.-H. Tan, S. D. Dimitrov, Z. Shang, N. Gasparini, M. Alamoudi, F. Laquai, C. J. Brabec, A. Salleo, J. R. Durrant, and I. McCulloch, "High-Efficiency and Air-Stable P3HT-based Polymer Solar Cells with a new Non-Fullerene Acceptor", *Nat. Commun.*, vol. 7, no. 11585, pp. 1–11, **2016**.

[67] H. J. Son, W. Wang, T. Xu, Y. Liang, Y. Wu, G. Li, and L. Yu, "Synthesis of Fluorinated Polythienothiophene-Co-Benzodithiophenes and Effect of Fluorination on the Photovoltaic Properties", *J. Am. Chem. Soc.*, vol. 133, no. 6, pp. 1885–1894, **2011**.

[68] B. Zimmermann, U. Würfel, and M. Niggemann, "Longterm Stability of Efficient Inverted P3HT:PCBM Solar Cells", *Sol. Energy Mater. Sol. Cells*, vol. 93, no. 4, pp. 491–496, **2009**.

[69] Q. L. Song, M. L. Wang, E. G. Obbard, X. Y. Sun, X. M. Ding, X. Y. Hou, and C. M. Li, "Degradation of Small-Molecule Organic Solar Cells", *Appl. Phys. Lett.*, vol. 89, no. 25, p. 2511181, **2006**.

[70] C. J. Schaffer, Christoph C. M. Palumbiny, M. A. Niedermeier, C. Jendrzejewski, G. Santoro, S. V. Roth, and P. Müller-Buschbaum, "A Direct Evidence of Morphological Degradation on a Nanometer Scale in Polymer Solar Cells", *Adv. Mater.*, vol. 25, no. 46, pp. 6760–6764, **2013**.

[71] M. Jørgensen, K. Norrman, and F. C. Krebs, "Stability/Degradation of Polymer Solar Cells", *Sol. Energy Mater. Sol. Cells*, vol. 92, no. 7, pp. 686–714, **2008**.

[72] G. Dennler, C. Lungenschmied, H. Neugebauer, N. S. Sariciftci, M. Latrèche, G. Czeremuszkin, and M. R. Wertheimer, "A new Encapsulation Solution for Flexible Organic Solar Cells", *Thin Solid Films*, vol. 511-512, pp. 349–353, **2006**.

[73] D. Yang, Q. Yang, L. Yang, Q. Luo, Y. Chen, Y. Zhu, Y. Huang, Z. Lu, and S. Zhao, "A Low Bandgap Asymmetrical Squaraine for High-Performance Solution-Processed Small Molecule Organic Solar Cells", *Chem. Commun.*, vol. 50, pp. 9346–9348, **2014**.

[74] C. J. Schaffer, C. M. Palumbiny, M. A. Niedermeier, C. Burger, G. Santoro, S. V. Roth, and P. Müller-Buschbaum, "Morphological Degradation in Low Bandgap

Polymer Solar Cells - an In Operando Study", *Adv. Energy Mater.*, vol. 6, no. 19, p. 1600712, **2016**.

[75] S. Zhang, Y. Qin, J. Zhu, and J. Hou, "Over 14% Efficiency in Polymer Solar Cells Enabled by a Chlorinated Polymer Donor", *Adv. Mater.*, vol. 30, no. 20, p. 1800868, **2018**.

[76] W. Tress, *Organic Solar Cells: Theory, Experiment, and Device Simulation*. Cham: Springer International Publishing AG, vol. 208, **2014**.

[77] S. Holliday, Y. Li, and C. K. Luscombe, "Recent Advances in High Performance Donor-Acceptor Polymers for Organic Photovoltaics", *Prog. Polym. Sci.*, vol. 70, pp. 34–51, **2017**.

[78] B. P. Rand, J. Genoe, P. Heremans, and J. Poortmans, "Solar Cells utilizing Small Molecular Weight Organic Semiconductors", *Prog. Photovolt: Res. Appl.*, vol. 15, no. 8, pp. 659–676, **2007**.

[79] R. S. Kularatne, H. D. Magurudeniya, P. Sista, M. C. Biewer, and M. C. Stefan, "Donor–Acceptor Semiconducting Polymers for Organic Solar Cells", *J. Polym. Sci. A*, vol. 51, no. 4, pp. 743–768, **2013**.

[80] N. Marinova, S. Valero, and J. L. Delgado, "Organic and Perovskite Solar Cells: Working Principles, Materials and Interfaces", *J. Colloid Interface Sci.*, vol. 488, pp. 373–389, **2017**.

[81] Y. Lin, F. Zhao, S. K. K. Prasad, J.-D. Chen, W. Cai, Q. Zhang, K. Chen, Y. Wu, W. Ma, F. Gao, J.-X. Tang, C. Wang, W. You, and J. M. Hodgkiss, "Balanced Partnership between Donor and Acceptor Components in Nonfullerene Organic Solar Cells with 12% Efficiency", *Adv. Mater.*, vol. 30, no. 16, p. 1706363, **2018**.

[82] H. Sun, Y. Tang, C. W. Koh, S. Ling, R. Wang, K. Yang, J. Yu, Y. Shi, Y. Wang, H. Y. Woo, and X. Guo, "High-Performance All-Polymer Solar Cells Enabled by an N-Type Polymer Based on a Fluorinated Imide-Functionalized Arene", *Adv. Mater*, vol. 31, no. 15, p. 1807220, **2019**.

[83] Y. Zhou, T. Kurosawa, W. Ma, Y. Guo, L. Fang, K. Vandewal, Y. Diao, C. Wang, Q. Yan, J. Reinspach, J. Mai, A. L. Apppleton, G. I. Koleilat, Y. Gao, S. C. B. Mannsfeld, A. Salleo, H. Ade, D. Zhao, and Z. Bao, "High Performance All-Polymer Solar Cell via Polymer Side-Chain Engineering", *Adv. Mater.*, vol. 26, no. 22, pp. 3767–3772, **2014**.

[84] S. Shi, J. Yuan, G. Ding, M. Ford, K. Lu, G. Shi, J. Sun, X. Ling, Y. Li, and W. Ma, "Improved All-Polymer Solar Cell Performance by Using Matched Polymer Acceptor", *Adv. Funct. Mater.*, vol. 26, no. 31, p. 5669–5678, **2016**.

[85] T. Ameri, P. Khoram, J. Min, and C. J. Brabec, "Organic Ternary Solar Cells: A Review", *Adv. Mater.*, vol. 25, no. 31, p. 4245–4266, **2013**.

[86] Q. An, F. Zhang, Q. Sun, M. Zhang, J. Zhang, W. Tang, Y. Yin, and Z. Deng, "Efficient Organic Ternary Solar Cells with the Third Component as Energy Acceptor", *Nano Energy*, vol. 26, p. 180–191, **2016**.

[87] Z.-Q. Jiang, T.-T. Wang, F.-P. Wu, J.-D. Lin, and L.-S. Liao, "Recent Advances in Electron Acceptors with Ladder-Type Backbone for Organic Solar Cells", *J. Mater. Chem. A*, vol. 6, no. 36, pp. 17256–17287, **2018**.

[88] S. S. van Bavel, M. Bärenklau, G. de With, H. Hoppe, and J. Loos, "P3HT/PCBM Bulk Heterojunction Solar Cells: Impact of Blend Composition and 3D Morphology on Device Performance", *Adv. Funct. Mater.*, vol. 20, no. 9, pp. 1458–1463, **2010**.

[89] J. A. Hauch, P. Schilinsky, S. A. Choulis, R. Childers, M. Biele, and C. J. Brabec, "Flexible Organic P3HT:PCBM Bulk-Heterojunction Modules with more than 1 Year Outdoor Lifetime", *Sol. Energy Mater. Sol. Cells*, vol. 92, no. 7, pp. 727–731, **2008**.

[90] J. Hou, O. Inganäs, Olle, R. H. Friend, and F. Gao, "Organic Solar cells based on Non-Fullerene Acceptors", *Nat. Mater.*, vol. 17, no. 2, pp. 119–128, **2018**.

[91] B. Minnaert, and M. Burgelman, "Efficiency Potential of Organic Bulk Heterojunction Solar Cells", *Prog. Photovolt: Res. Appl.*, vol. 15, no. 8, pp. 741–748, **2007**.

[92] J. D. Servaites, M. A. Ratner, and T. J. Marks, "Organic Solar Cells: A new Look at Traditional Models", *Energy Environ. Sci.*, vol. 4, pp. 4410–4422, **2011**.

[93] B. A. Collins, Z. Li, J. R. Tumbleston, E. Gann, C. R. McNeill, and H. Ade, "Absolute Measurement of Domain Composition and Nanoscale Size Distribution explains Performance in PTB7:PC71BM Solar Cells", *Adv. Energy Mater.*, vol. 3, no. 1, pp. 65–74, **2013**.

[94] W. Zeng, K. S. L. Chong, H. Y. Low, E. L. Williams, T. L. Tam, and A. Sellinger, "The use of Nanoimprint Lithography to improve Efficiencies of Bilayer Organic Solar Cells based on P3HT and a Small Molecule Acceptor", *Thin Solid Films*, vol. 517, no. 24, pp. 6833–6836, **2009**.

[95] J. Y. Park, N. R. Hendricks, and K. R. Carter, "Solvent-Assisted Soft Nanoimprint Lithography for Structured Bilayer Heterojunction Organic Solar Cells", *Langmuir*, vol. 27, no. 17, p. 11251–11258, **2011**.

[96] C. McDowell, and G. C. Bazan, "Organic Solar Cells processed from Green Solvents", *Curr. Opin. Green Sustain. Chem.*, vol. 5, pp. 49–54, **2017**.

[97] S. Pröller, F. Liu, C. Zhu, C. Wang, T. P. Russell, A. Hexemer, P. Müller-Buschbaum, and E. M. Herzig, "Following the Morphology Formation In Situ in Printed Active Layers for Organic Solar Cells", *Adv. Energy Mater.*, vol. 6, no. 1, p. 1501580, **2016**.

[98] M. Sanyal, B. Schmidt-Hansberg, M. F. G. Klein, C. Munuera, A. Vorobiev, A. Colsmann, P. Scharfer, U. Lemmer, W. Schabel, H. Dosch, and E. Barrena, "Effect of Photovoltaic Polymer/Fullerene Blend Composition Ratio on Microstructure Evolution during Film Solidification Investigated in Real Time by X-ray Diffraction", *Macromolecules*, vol. 44, no. 10, pp. 3795–3800, **2011**.

[99] D. W. Zhao, S. T. Tan, L. Ke, P. Liu, A. K. K. Kyaw, X. W. Sun, and D. L. Kwong, "Optimization of an Inverted Organic Solar Cell", *Sol. Energy Mater. Sol. Cells*, vol. 94, no. 6, p. 985–991, **2010**.

[100] X. Tong, B. E. Lassiter, and S. R. Forrest, "Inverted Organic Photovoltaic Cells with High Open-Circuit Voltage", *Org. Electron.*, vol. 11, no. 4, p. 705–709, **2010**.

[101] R. R. Søndergaard, M. Hösel, D. Angmo, T. T. Larsen-Olsen, and F. C. Krebs, "Roll-to-Roll Fabrication of Polymer Solar Cells", *Mater. Today*, vol. 15, no. 1-2, pp. 36–49, **2012**.

[102] P. Kopola, T. Aernouts, R. Sliz, S. Guillerez, M. Ylikunnari, D. Cheyns, M. Välimäki, M. Tuomikoski, J. Hast, G. Jabbour, R. Myllylä, and A. Maaninen, "Gravure Printed Flexible Organic Photovoltaic Modules", *Sol. Energy Mater. Sol. Cells*, vol. 95, no. 5, pp. 1344–1347, **2011**.

[103] H. Sun, J. Weickert, H. C. Hesse, and L. Schmidt-Mende, "UV Light Protection through TiO_2 Blocking Layers for Inverted Organic Solar Cells", *Sol. Energy Mater. Sol. Cells*, vol. 95, no. 12, pp. 3450–3454, **2011**.

[104] D. Vak, S.-S. Kim, J. Jo, S.-H. Oh, S.-I. Na, J. Kim, and D.-Y. Kim, "Fabrication of Organic Bulk Heterojunction Solar Cells by a Spray Deposition Method for Low-Cost Power Generation", *Appl. Phys. Lett.*, vol. 91, no. 8, p. 081102, **2007**.

[105] C. J. Brabec, and J. R. Durrant, "Solution-Processed Organic Solar Cells", *MRS Bull.*, vol. 33, no. 7, pp. 670–675, **2008**.

[106] Y. Song, S. Chang, S. Gradecak, and J. Kong, "Visibly-Transparent Organic Solar Cells on Flexible Substrates with All-Graphene Electrodes", *Adv. Energy Mater.*, vol. 6, no. 20, p. 1600847, **2016**.

[107] Z. Liu, J. Li, Z.-H. Sun, G. Tai, S. Lau, and F. Yan, "The Application of Highly Doped Single-Layer Graphene as the Top Electrodes of Semitransparent Organic Solar Cells", *ACS Nano*, vol. 6, no. 1, p. 810–818, **2012**.

[108] A. J. Heeger, "25th Anniversary Article: Bulk Heterojunction Solar Cells: Understanding the Mechanism of Operation", *Adv. Mater.*, vol. 26, no. 1, pp. 10–28, **2014**.

[109] H. Hoppe, and N. S. Sariciftci, "Morphology of Polymer/Fullerene Bulk Heterojunction Solar Cells", *J. Mater. Chem.*, vol. 16, pp. 45–61, **2006**.

[110] N. Kaur, M. Singh, D. Pathak, T. Wagner, and J. M. Nunzi, "Organic Materials for Photovoltaic Applications: Review and Mechanism", *Synth. Met.*, vol. 190, pp. 20–26, **2014**.

[111] M. Knupfer, "Exciton Binding Energies in Organic Semiconductors", *Appl. Phys. A*, vol. 77, no. 5, pp. 623–626, **2003**.

[112] P. W. M. Blom, V. D. Mihailetchi, L. J. A. Koster, and D. E. Markov, "Device Physics of Polymer:Fullerene Bulk Heterojunction Solar Cells", *Adv. Mater.*, vol. 19, no. 12, pp. 1551–1566, **2007**.

[113] C. M. Proctor, M. Kuik, and T.-Q. Nguyen, "Charge Carrier Recombination in Organic Solar Cells", *Prog. Polym. Sci.*, vol. 38, no. 12, pp. 1941–1960, **2013**.

[114] B. Carsten, J. M. Szarko, L. Lu, H. J. Son, F. He, Y. Y. Botros, L. X. Chen, and L. Yu, "Mediating Solar Cell Performance by Controlling the Internal Dipole Change in Organic Photovoltaic Polymers", *Macromolecules*, vol. 45, no. 16, pp. 6390–6395, **2012**.

[115] S. N. Hood, and I. Kassal, "Entropy and Disorder Enable Charge Separation in Organic Solar Cells", *J. Phys. Chem. Lett.*, vol. 7, no. 22, pp. 4495–4500, **2016**.

[116] K. Kawano, J. Sakai, M. Yahiro, and C. Adachi, "Effect of Solvent on Fabrication of Active Layers in Organic Solar Cells based on Poly(3-hexylthiophene) and Fullerene Derivatives", *Sol. Energy Mater. Sol. Cells*, vol. 93, no. 4, pp. 514–518, **2009**.

[117] S. Hong, M. Yi, H. Kang, J. Kong, W. Lee, J.-R. Kim, and K. Lee, "Effect of Solvent on Large-Area Polymer–Fullerene Solar Cells fabricated by a Slot-Die Coating Method", *Sol. Energy Mater. Sol. Cells*, vol. 126, pp. 107–112, **2014**.

[118] K. Schmidt, C. J. Tassone, J. R. Niskala, A. T. Yiu, O. P. Lee, T. M. Weiss, C. Wang, J. M. J. Fréchet, P. M: Beaujuge, and M. F. Toney, "A Mechanistic Understanding of Processing Additive-Induced Efficiency Enhancement in Bulk Heterojunction Organic Solar Cells", *Adv. Mater.*, vol. 26, no. 2, pp. 300–305, **2014**.

[119] H.-C. Liao, C.-C. Ho, C.-Y. Chang, M.-H. Jao, S. B. Darling, and W.-F. Su, "Additives for Morphology Control in High-Efficiency Organic Solar Cells", *Mater. Today*, vol. 16, no. 9, pp. 326–336, **2013**.

[120] S. Sutty, G. Williams, and H. Aziz, "Role of the Donor Material and the Donor–Acceptor Mixing Ratio in increasing the Efficiency of Schottky Junction Organic Solar Cells", *Org. Electron.*, vol. 14, no. 10, pp. 2392–2400, **2013**.

[121] B. Ray, P. R. Nair, and M. A. Alam, "Annealing dependent Performance of Organic Bulk-Heterojunction Solar Cells: A Theoretical Perspective", *Sol. Energy Mater. Sol. Cells*, vol. 95, no. 12, p. 3287–3294, **2011**.

[122] M. Hermenau, M. Riede, K. Leo, S. A. Gevorgyan, F. C. Krebs, and K. Norrman, "Water and Oxygen Induced Degradation of Small Molecule Organic Solar Cells", *Sol. Energy Mater. Sol. Cells*, vol. 95, no. 5, pp. 1268–1277, **2011**.

[123] K. Norrman, S. A. Gevorgyan, and F. C. Krebs, "Water-Induced Degradation of Polymer Solar Cells studied by $H_2{}^{18}O$ Labeling", *ACS Appl. Mater. Interfaces*, vol. 1, no. 1, pp. 102–112, **2009**.

[124] N. Grossiord, J. M. Kroon, R. Andriessen, and P. W. M. Blom, "Degradation Mechanisms in Organic Photovoltaic Devices", *Org. Electron.*, vol. 13, no. 3, pp. 432–456, **2012**.

[125] Y. Jiang, L. Sun, F. Jiang, C. Xie, L. Hu, X. Dong, F. Qin, T. Liu, L. Hu, X. Jiang, and Y. Zhou , "Photocatalytic Effect of ZnO on the Stability of Nonfullerene Acceptors and its Mitigation by SnO_2 for Nonfullerene Organic Solar Cells", *Mater. Horiz.*, vol. 6, no. 7, pp. 1438–1443, **2019**.

[126] A. Seemann, T. Sauermann, C. Lungenschmied, O. Armbruster, S. Bauer, H.-J. Egelhaaf, and J. Hauch, "Reversible and Irreversible Degradation of Organic Solar Cell Performance by Oxygen", *Sol. Energy*, vol. 85, no. 6, pp. 1238–1249, **2011**.

[127] D. M. González, C. J. Schaffer, S. Pröller, J. Schlipf, L. Song, S. Bernstorff, E. M. Herzig, and P. Müller-Buschbaum, "Codependence between Crystalline and Photovoltage Evolutions in P3HT:PCBM Solar Cells Probed with In-Operando GIWAXS", *ACS Appl. Mater. Interfaces*, vol. 9, no. 4, pp. 3282–3287, **2017**.

[128] E. Andreoli, K.-S. Liao, A. Haldar, N. J. Alley, and S. A. Curran, "PPy:PSS as Alternative to PEDOT:PSS in Organic Photovoltaics", *Synth. Met.*, vol. 185-186, no. 1, pp. 71–78, **2013**.

[129] S. D. Yambem, K.-S. Liao, N. J. Alley, and S. A. Curran, "Stable Organic Photovoltaics using Ag Thin Film Anodes", *J. Mater. Chem.*, vol. 22, no. 14, pp. 6894–6898, **2012**.

[130] M. Wang, F. Xie, J. Du, Q. Tang, S. Zheng, Q. Miao, J. Chen, N. Zhao, and J. B. Xu, "Degradation Mechanism of Organic Solar Cells with Aluminum Cathode", *Sol. Energy Mater. Sol. Cells*, vol. 95, no. 12, pp. 3303–3310, **2011**.

[131] J. T. Rogers, K. Schmidt, M. F. Toney, G. C. Bazan, and E. J. Kramer, "Time-Resolved Structural Evolution of Additive-Processed Bulk Heterojunction Solar Cells", *J. Am. Chem. Soc.*, vol. 134, no. 6, pp. 2884–2887, **2012**.

[132] E. Pérez-Gutiérrez, J. Lozano, J. Gaspar-Tánori, J.-L. Maldonado, B. Gómez, L. López, L.-F. Amores-Tapia, O. Barbosa-García, and M.-J. Percino, "Organic Solar Cells all made by Blade and Slot–Die Coating Techniques", *Sol. Energy*, vol. 146, pp. 79–84, **2017**.

[133] B. Conings, S. Bertho, K. Vandewal, A. Senes, J. D'Haen, J. Manca, and R. A. J. Janssen, "Modeling the Temperature Induced Degradation Kinetics of the Short Circuit Current in Organic Bulk Heterojunction Solar Cells", *Appl. Phys. Lett.*, vol. 96, no. 16, p. 163301, **2010**.

[134] S. Schuller, P. Schilinsky, J. Hauch, and C. J. Brabec, "Determination of the Degradation Constant of Bulk Heterojunction Solar Cells by Accelerated Lifetime Measurements", *Appl. Phys. A*, vol. 79, no. 1, pp. 37–40, **2004**.

[135] F. Li, K. G. Yager, N. M. Dawson, J. Yang, K. J. Malloy, and Y. Qin, "Complementary Hydrogen Bonding and Block Copolymer Self-Assembly in Cooperation toward Stable Organic Solar Cells with Tunable Morphologies", *Macromolecules*, vol. 46, no. 22, pp. 9021–9031, **2013**.

[136] G. Griffini, J. D. Douglas, C. Piliego, T. W. Holcombe, S. Turri, J. M. J. Fréchet, and J. L. Mynar, "Long-Term Thermal Stability of High-Efficiency Polymer Solar Cells based on Photocrosslinkable Donor-Acceptor Conjugated Polymers", *Adv. Mater.*, vol. 23, no. 14, pp. 1660–1664, **2011**.

[137] E. F. Palermo, S. B. Darling, and A. J. McNeil, "π-Conjugated Gradient Copolymers suppress Phase Separation and Improve Stability in Bulk Heterojunction Solar Cells", *J. Mater. Chem. C*, vol. 2, no. 17, pp. 3401–3406, **2014**.

[138] Y.-T. Lin, W.-B. Chu, and T.-J. Liu, "Slot Die Coating of Dilute Suspensions", *Asia-Pac. J. Chem. Eng.*, vol. 4, no. 2, pp. 42313–42321, **2009**.

[139] K. L. Bhamidipati, S. Didari, P. Bedell, and T. A. L. Harris., "Wetting Phenomena during Processing of High-Viscosity Shear-Thinning Fluid", *J. Non-Newtonian Fluid Mech.*, vol. 166, no. 12-13, p. 723–733, **2011**.

[140] S. Hong, J. Lee, H. Kang, and L. Kwanghee, "Slot-Die Coating Parameters of the Low-Viscosity Bulk-Heterojunction Materials used for Polymer Solar Cells", *Sol. Energy Mater. Sol. Cells*, vol. 112, pp. 27–35, **2013**.

[141] T. S. Chow, "Wetting of Rough Surfaces", *J. Phys.: Condens. Matter*, vol. 10, pp. 445–451, **1998**.

[142] T. Young, "An Essay on the Cohesion of Fluids", *Philos. Trans. Royal Soc.*, vol. 95, pp. 42313–42321, **1805**.

[143] P. Müller-Buschbaum, "Influence of Surface Cleaning on Dewetting of Thin Polystyrene Films", *Eur. Phys. J. E*, vol. 12, no. 3, pp. 443–448, **2003**.

[144] X. Ding, J. Liu, Jianhua, and T. A. L. Harris, "A Review of the Operating Limits in Slot Die Coating Processes", *AIChE J.*, vol. 62, no. 7, pp. 2508–2524, **2016**.

[145] M. S. Carvalho, "Low–Flow Limit in Slot Coating: Theory and Experiments", *AlChE*, vol. 46, no. 10, pp. 1907–1917, **2000**.

[146] Y.-R. Chang, H.-M. Chang, C.-F. Lin, T.-J. Liu, and P.-Y. Wu, "Three Minimum Wet Thickness Regions of Slot Die Coating", *J. Colloid Interface Sci.*, vol. 308, no. 1, pp. 222–230, **2007**.

[147] M. Tolan, *X-ray Scattering from Soft-Matter Thin Films*. Springer Berlin Heidelberg, **1999**.

[148] P. Müller-Buschbaum, "The Active Layer Morphology of Organic Solar Cells probed with Grazing Incidence Scattering Techniques", *Adv. Mater.*, vol. 26, no. 46, pp. 7692–7709, **2014**.

[149] M. D. Foster, "X-ray Scattering Methods for the Study of Polymer Interfaces", *Crit. Rev. Anal. Chem.*, vol. 24, no. 3, pp. 179–241, **1993**.

[150] C. J. Schaffer, C. Wang, A. Hexemer, and P. Müller-Buschbaum, "Grazing Incidence Resonant Soft X-ray Scattering for Analysis of Multi-Component Polymer-Fullerene Blend Thin Films", *Polymer*, vol. 105, no. 22, pp. 357–367, **2016**.

[151] M. Gomez, A. Nogales, M. C. Garcia-Gutierrez, and T. A. Ezquerra, *Applications of Synchrotron Light to Scattering and Diffraction in Materials and Life Sciences*. Springer US New York, **2009**.

[152] Y. Yoneda, "Anomalous Surface Reflection of X-rays", *Phys. Rev.*, vol. 131, no. 5, pp. 2010–2013, **1963**.

[153] P. Müller-Buschbaum, "GISAXS and GISANS as Metrology Technique for Understanding the 3D Morphology of Clock Copolymer Thin Films", *Eur. Polym. J.*, vol. 81, pp. 470–493, **2016**.

[154] A. Hexemer, and P. Müller-Buschbaum, "Advanced Grazing-Incidence Techniques for Modern Soft-Matter Materials Analysis", *IUCrJ*, vol. 2, no. 1, pp. 106–125, **2015**.

[155] P. Müller-Buschbaum, "Grazing Incidence Small-Angle X-ray Scattering: An Advanced Scattering Technique for the Investigation of Nanostructured Polymer Films", *Anal. Bioanal. Chem.*, vol. 376, pp. 3–10, **2003**.

[156] F. Leroy, R. Lazzari, and G. Renaud, "Effects of Near-Neighbor Correlations on the Diffuse Scattering from a One-Dimensional Paracrystal", *Acta Cryst.*, vol. 60, pp. 565–581, **2004**.

[157] G. Pospelov, W. Van Herck, J. Burle, J. M. Carmona Loaiza, C. Durniak, J. M. Fisher, M. Ganeva, D. Yurov, and J. Wuttke, "BornAgain: Software for Simulating and Fitting Grazing-Incidence Small-Angle Scattering", *J. Appl. Cryst.*, vol. 53, pp. 262–276, **2020**.

[158] R. Lazzari, "*IsGISAXS*: A Program for Grazing-Incidence Small-Angle X-ray Scattering Analysis of Supported Islands", *J. Appl. Cryst.*, vol. 35, pp. 406–421, **2001**.

[159] N. Hohn, S. J. Schlosser, L. Bießmann, L. Song, S. Grott, S. Xia, K. Wang, M. Schwartzkopf, S.V. Roth, and P. Müller-Buschbaum, "Impact of Catalytic Additive on Spray Deposited and Nanoporous Titania Thin Films Observed via In Situ X-ray Scattering: Implications for Enhanced Photovoltaics", *ACS Appl. Nano Mater.*, vol. 1, no. 8, pp. 4227–4235, **2018**.

[160] D. Babonneau, "FitGISAXS: Software Package for Modelling and Analysis of GISAXS data using IGOR Pro", *J. Appl. Cryst.*, vol. 43, pp. 929–936, **2010**.

[161] G. Renaud, R. Lazzari, and F. Leroy, "Probing Surface and Interface Morphology with Grazing Incidence Small Angle X-ray Scattering", *Surf. Sci. Rep.*, vol. 64, no. 8, pp. 255–380, **2009**.

[162] R. Hosemann, and S. N. Bagchi, *Direct Analysis of Diffraction by Matter*. Amsterdam: North-Holland Publishing Company, **1962**.

[163] H. Stanjek, and W. Häusler, "Basics of X-ray Diffraction", *Hyperfine Interact.*, vol. 154, pp. 107–119, **2004**.

[164] H. Ibach, and H. Lüth, *Solid-State Physics*. Springer Berlin Heidelberg, **2003**.

[165] P. P. Ewald, "Introduction to the Dynamical Theory of X-ray Diffraction", *Acta Cryst.*, vol. 25, pp. 103–108, **1969**.

[166] G. Strobl, "From the Melt via Mesomorphic and Granular Crystalline Layers to Lamellar Crystallites: A Major Route followed in Polymer Crystallization ", *Eur. Phys. J. E*, vol. 3, pp. 165–183, **2000**.

[167] A. L. Patterson, "The Scherrer Formula for X-ray Particle Size Determination", *Phys. Rev.*, vol. 56, pp. 978–982, **1939**.

[168] D.-M. Smilgies, "Scherrer Grain-Size Analysis adapted to Grazing-Incidence Scattering with Area Detectors", *J. Appl. Cryst.*, vol. 42, p. 1030–1034, **2009**.

[169] J. Franck, and E. G. Dymond, "Elementary Processes of Photochemical Reactions", *Trans. Faraday Soc.*, vol. 21, pp. 536–542, **1926**.

[170] E. U. Condon, "Nuclear Motions Associated with Electron Transitions in Diatomic Molecules", *Phys. Rev.*, vol. 32, p. 858–872, **1928**.

[171] U. Fantz, and D. Wünderlich, "Franck–Condon Factors, Transition Probabilities, and Radiative Lifetimes for Hydrogen Molecules and their Isotopomeres", *At. Data Nucl. Data Tables*, vol. 92, no. 6, p. 853–973, **2006**.

[172] R. Berera, R. van Grondelle, and J. T. M. Kennis, "Ultrafast Transient Absorption Spectroscopy: Principles and Application to Photosynthetic Systems", *Photosyn. Res.*, vol. 101, pp. 105–118, **2009**.

[173] T. G. Mayerhöfer, H. Mutschke, and J. Popp, "Employing Theories Far beyond Their Limits-The Case of the (Boguer-) Beer-Lambert Law", *ChemPhysChem*, vol. 17, no. 13, p. 1948–1955, **2016**.

[174] A. Beer, "Bestimmung der Absorption des rothen Lichts in farbigen Flüssigkeiten", *Ann. Phys.*, vol. 162, no. 5, p. 78–88, **1852**.

[175] J. Gong, and S. Krishnan, in *Dye-Sensitized Solar Cells: Mathematical Modelling, and Materials Design and Optimization*. (Eds.: M. Soroush, and K. S. L. Kenneth), London: Elvesier, **2019**.

[176] H. Fujiwara, *Spectroscopic Ellipsometry: Principles and Applications*. Chichester: Wiley, **2007**.

[177] K. S. Wienhold, V. Körstgens, S. Grott, X. Jiang, M. Schwartzkopf, S.V. Roth, and P. Müller-Buschbaum, "In Situ Printing: Insights into the Morphology Formation and Optical Property Evolution of Slot-Die Coated Active Layers Containing Low Band Gap Polymer Donor and Non-Fullerene Acceptor", *Sol. RRL*, vol. 4, no. 7, p. 2000086, **2020**.

[178] S. T. Hoffmann, H. Bässler, and A. Köhler, "What determines Inhomogeneous Broadening of Electronic Transitions in Conjugated Polymers?", *J. Phys. Chem. B*, vol. 114, no. 51, pp. 17037–17048, **2010**.

[179] G. A. Crosby, and J. N. Demas, "Measurement of Photoluminescence Quantum Yields. Review", *J. Phys. Chem.*, vol. 75, no. 8, p. 991–1024, **1971**.

[180] M. Andersson, and M. Fahlman, in *Organic and Printed Electronics: Fundamentals and Applications*. (Eds.: G. Nisato, D. Lupo, and S. Ganz), Boca Raton: Pan Stanford Publishing, **2016**.

[181] M. Martini, F. Meinardi, A. Paleari, G. Spinolo, and A. Vedda, "SiO_2 : Ge Photoluminescence: Detailed Mapping of the Excitation-Emission UV Pattern", *Phys. Rev. B*, vol. 57, no. 7, p. 3718, **1998**.

[182] F.-J. Kahle, A. Rudnick, H.; Bässler, and A. Köhler, "How to Interpret Absorption and Fluorescence Spectra of Charge Transfer States in an Organic Solar Cell", *Mater. Horiz.*, vol. 5, no. 5, pp. 837–848, **2018**.

[183] R. Koeppe, O. Bossart, G. Calzaferri, and N. Sariciftci, "Advanced Photon-Harvesting Concepts for Low-Energy Gap Organic Solar Cells", *Sol. Energy Mater. Sol. Cells*, vol. 91, no. 11, p. 986–995, **2007**.

[184] A. Jablonski, "Über den Mechanismus der Photolumineszenz von Farbstoffphosphoren", *Z. Physik*, vol. 94, pp. 38–46, **1935**.

[185] M. Mydlak, and D. Volz, in *Organic and Printed Electronics: Fundamentals and Applications*. (Eds.: G. Nisato, D. Lupo, and S. Ganz), Boca Raton: Pan Stanford Publishing, **2016**.

[186] H. L. Malm, and R. R. Haering, "Franck–Condon Effects in the Luminescence of CdS", *Can. J. Phys.*, vol. 49, no. 23, pp. 2970–2988, **1971**.

[187] L. S. Forster, S. A. Greenberg, R. J. Lyon, and M. E. Smith, "Luminescence and Internal Conversion in Biacetyl Solutions", *Spectrochim. Acta*, vol. 16, pp. 335–340, **1960**.

[188] S. Chander, A. Purohit, A. Nehra, S.P. Nehra, and M.S. Dhaka, "A Study on Spectral Response and External Quantum Efficiency of Mono-Crystalline Silicon Solar Cell", *Int. J. Renew. Energy Res.*, vol. 5, no. 1, **2015**.

[189] A. Herguth, B. Raabe, S. Scholz, G. Hahn,H. Haverkamp, R. Nissler, D. Habermann, C. Buchner, and C. Schmid, "Influence of Spectral Mismatch, Cell Reflection Properties and IQE on the Efficiency Measurement", *26th EU PVSEC*, pp. 1555–1557, **2011**.

[190] A. Ingenito, O. Isabella, S. Solntsev, and M. Zeman, "Accurate Opto-Electrical Modeling of Multi-Crystalline Silicon Wafer-Based Solar Cells", *Sol. Energy Mater. Sol. Cells*, vol. 123, p. 17–29, **2014**.

[191] A. J. Moulé, and K. Meerholz, "Minimizing Optical Losses in Bulk Heterojunction Polymer Solar Cells", *Appl. Phys. B*, vol. 86, no. 4, pp. 721–727, **2007**.

[192] K. S. Wienhold, V. Körstgens, S. Grott, X. Jiang, M. Schwartzkopf, S.V. Roth, and P. Müller-Buschbaum, "Effect of Solvent Additives on the Morphology and Device Performance of Printed Nonfullerene Acceptor Based Organic Solar Cells", *ACS Appl. Mater. Interfaces*, vol. 11, no. 45, pp. 42313–42321, **2019**.

[193] V. Shrotriya, G. Li, Y. Yao, T. Moriarty, K. Emery, and Y. Yang, "In-Operando Study of the Effects of Solvent Additives on the Stability of Organic Solar Cells Based on PTB7-Th:PC71BM", *Adv. Funct. Mater.*, vol. 16, no. 15, pp. 2534–2540, **2006**.

[194] D. Chirvase, Z. Chiguvare, M. Knipper, J. Parisi, V. Dyakonov, and J. C. Hummelen, "Temperature dependent Characteristics of Poly(3 hexylthiophene)-Fullerene based Heterojunction Organic Solar Cells", *ACS Appl. Mater. Interfaces*, vol. 93, no. 6, p. 3376, **2003**.

[195] D. R. Myers, K. Emery, and C. Gueymard, "Revising and Validating Spectral Irradiance Reference Standards for Photovoltaic Performance Evaluation", *ACS Appl. Mater. Interfaces*, vol. 126, no. 1, pp. 567–574, **2004**.

[196] C. Hoth, A. Savva, and S. Choulis, in *Organic and Printed Electronics: Fundamentals and Applications*. (Eds.: G. Nisato, D. Lupo, and S. Ganz), Boca Raton: Pan Stanford Publishing, **2016**.

[197] www.pveducation.org, visited on 06.10.2020.

[198] L. J. A. Koster, V. D. Mihailetchi, R. Ramaker, and P. W. M. Blom, "Light Intensity Dependence of Open-Circuit Voltage of Polymer:Fullerene Solar Cells", *Appl. Phys. Lett.*, vol. 86, no. 12, p. 123509, **2005**.

[199] B. Snaith, M.J. Edmondst, and S.D. Probert, "Use of a Profilometer for Surface Mapping", *Precis. Eng.*, vol. 3, no. 2, pp. 87–90, **1981**.

[200] E. C. Teague, F. E. Scire, S. M. Baker, and S. W. Jensen, "Three-Dimensional Stylus Profilometry", *Wear*, vol. 3, no. 2, pp. 1–12, **1982**.

[201] R. H. Webb, "Confocal Optical Mikroscopy", *Rep. Prog. Phys.*, vol. 59, no. 3, pp. 427–471, **1996**.

[202] J. M. Vigoureux, and D. Courjon, "Detection of Nonradiative Fields in Light of the Heisenberg Uncertainty Principle and the Rayleigh Criterion", *Appl. Opt.*, vol. 31, no. 16, pp. 3170–3177, **1992**.

[203] T. J. Collins, "ImageJ for Microscopy", *BioTechniques*, vol. 43, no. 1, pp. 25–30, **2007**.

[204] G. Binnig, C. F. Quate, and Ch. Gerbers, "Atomic Force Microscope", *Phys. Rev. Lett.*, vol. 56, no. 9, pp. 930–934, **1986**.

[205] A. Ikai, "STM and AFM of Bio/Organic Molecules and Structures ", *Surf. Sci. Rep.*, vol. 26, pp. 2613–332, **1996**.

[206] Q. Zhong, D. Inniss, K. Kjoller, and V. B. Elings, "Fractured Polymer/Silica Fiber Surface studied by Tapping Mode Atomic Force Microscopy", *Surf. Sci.*, vol. 290, no. 1-2, pp. L688–L692, **1993**.

[207] F. B. G. Zeng, Y. Duan and M. Dong, in *Atomic Force Microscopy Investigations into Biology: Nanomechanics of Amyloid Materials studied by Atomic Force Microscopy*. (Ed.: C. Frewin), Florida: IntechOpen, **2012**.

[208] N. Yu, and A. A.Polycarpou, "Adhesive Contact based on the Lennard–Jones Potential: A Correction to the Value of the Equilibrium Distance as used in the Potential", *J. Colloid Interface Sci.*, vol. 278, no. 2, pp. 428–435, **2004**.

[209] B. Hartmann, and Z. I. Slawsky , "Vibrational Relaxation with a Lennard-Jones Potential", *J. Chem. Phys.*, vol. 47, no. 7, pp. 2491–2494, **1967**.

[210] H. K. Shin, "Inelastic Molecular Collisions with a Lennard-Jones (12-6) Interaction Energy", *J. Chem. Phys.*, vol. 41, no. 9, pp. 2864–2868, **1964**.

[211] M. Bărbosu, V. Mioc, D. Paşca, and F. Szenkovits, "The Two-Body Problem with Generalized Lennard-Jones Potential", *J. Math. Chem.*, vol. 49, pp. 1961–1975, **2011**.

[212] K. S. Pitzer, "London Force Contributions to Bond Energies", *J. Chem. Phys.*, vol. 23, p. 1735, **1955**.

[213] F. London, "The General Theory of Molecular Forces", *Trans. Faraday Soc.*, pp. 8–26, **1937**.

[214] B. Smit, "Phase Diagrams of Lennard-Jones Fluids ", *J. Chem. Phys.*, vol. 96, no. 11, pp. 8639–8640, **1992**.

[215] J. P. Cleveland, B. Anczykowski, A. E. Schmid, and V. B. Elings, "Energy Dissipation in Tapping-Mode Atomic Force Microscopy", *Appl. Phys. Lett.*, vol. 72, no. 20, pp. 2613–2615, **1998**.

[216] B. Rogers, L. Manning, T. Sulchek, and J. D. Adams, "Improving Tapping Mode Atomic Force Microscopy with Piezoelectric Cantilevers", *Ultramicroscopy*, vol. 100, no. 3-4, pp. 267–276, **2004**.

[217] D. Nečas, and P. Klapetek, "Gwyddion: An Open-Source Software for SPM Data Analysis", *Cent. Eur. J. Phys.*, vol. 10, no. 1, pp. 181–188, **2012**.

[218] A. V. Girão, G. Caputo, and M. C. Ferro, in *Characterization and Analysis of Microplastics*. (Eds.: T. A. P. Rocha-Santos, and A. C. Duarte), London: Elvesier, vol. 75, **2017**.

[219] M. Abd Mutalib, M. A. Rahman, M. H. D. Othman, A. F. Ismail, and J. Jaafar, in *Membrane Characterization*. (Eds.: N. Hilal, A. F. Ismail, T. Matsuura, and D. Oatley-Radcliffe), Amsterdam: Elvesier, **2017**.

[220] L. de Broglie, "Interpretation of Quantum Mechanics by the Double Solution Theory", *Ann. de la Fond. Louis de Broglie*, vol. 12, no. 4, **1987**.

[221] L. de Broglie, "Waves and Quanta", *Nature*, vol. 112, no. 2815, p. 540, **1926**.

[222] D. E. Newbury, D. C. Joy, P. Echlin, C. E. Fiori, and J. I. Goldstein, *Advanced Scanning Electron Microscopy and X-ray Microanalysis*. New York: Springer Science+Business Media, **1986**.

[223] E. MacKinnon, "De Broglie's Thesis: A Critical Retrospective", *Am. J. Phys.*, vol. 44, pp. 1047–1055, **1976**.

[224] H. Bunjes, and J. Kuntsche, in *Analytical Techniques in the Pharmaceutical Sciences.* (Eds.: A. Müllertz, Y. Perrie, and T. Rades), New York: Springer Science+Business Media, **2016**.

[225] M.-J. Park, D. H. Kim, K. Park, D. Y. Jang, and D.-C. Ha, "Design and Fabrication of a Scanning Electron Microscope using a Finite Element Analysis for Electron Optical System", *J. Mech. Sci. Technol.*, vol. 22, pp. 1734–1746, **2008**.

[226] J. Orloff, "Thermal Field Emission for Low Voltage Scanning Electron Microscopy", *J. Microsc.*, vol. 140, no. 3, pp. 303–311, **1985**.

[227] H. Seiler, "Secondary Electron Emission in the Scanning Electron Microscope", *J. Appl. Phys.*, vol. 54, no. 11, pp. R1–R17, **1983**.

[228] B. J. Inkson, in *Materials Characterization using Nondestructive Evaluation (NDE) Methods: Scanning Electron Microscopy (SEM) and Transmission Electron Microscopy (TEM) for Materials Characterization.* (Ed.: G. Hübschen, I. Altpeter, R. Tschuncky, and H.-G. Herrmann), Cambridge: Woodhead Publishing, **2016**.

[229] Z. Jiang, "GIXSGUI : a MATLAB Toolbox for Grazing-Incidence X-ray Scattering Data Visualization and Reduction, and Indexing of Buried Three-Dimensional Periodic Nanostructured Films", *J. Appl. Crystallogr.*, vol. 48, no. 3, pp. 917–926, **2015**.

[230] D. Yang, F. C. Löhrer, V. Körstgens, A. Schreiber, B. Cao, S. Bernstorff, and P. Müller-Buschbaum, "In Operando GISAXS and GIWAXS Stability Study of Organic Solar Cells Based on PffBT4T-2OD:PC71BM with and without Solvent Additive", *Adv. Sci.*, p. 2001117, **2020**.

[231] W. Chen, J. Zhong, J. Li, N. Saxena, L. P. Kreuzer, H. Liu, L. Song, B. Su, D. Yang, K. Wang, J. Schlipf, V. Körstgens, T. He, K. Wang, and P. Müller-Buschbaum, "Structure and Charge Carrier Dynamics in Colloidal PbS Quantum Dot Solids", *J. Phys. Chem. Lett.*, vol. 10, no. 9, pp. 2058–2065, **2019**.

[232] A. Buffet, A. Rothkirch, R. Döhrmann, V. Körstgens, M. M. Abul Kashem, J. Perlich, G. Herzog, M. Schwartzkopf, R. Gehrke, P. Müller-Buschbaum, and S. V. Roth, "P03, the Microfocus and Nanofocus X-ray Scattering (MiNaXS) Beamline of the PETRA III Storage Ring: The Microfocus Endstation", *J. Synchrotron Radiat.*, vol. 19, no. 4, pp. 647–653, **2012**.

[233] H. Fu, Z. Wang, and Y. Sun, "Polymer Donors for High-Performance Non-Fullerene Organic Solar Cells", *Angew. Chem.*, vol. 58, no. 14, pp. 42313–42321, **2018**.

[234] H. Bin, L. Xiao, Y. Liu, P. Shen, and Y. Li, "Effects of Donor Unit and π-Bridge on Photovoltaic Properties of D-A Copolymers based on Benzo[1,2-b:4,5-c']-dithiophene-4,8-dione Acceptor Unit", *J. Polym. Sci. A*, vol. 52, no. 14, pp. 42313–42321, **2014**.

[235] K.-N. Zhang, M.-S. Niu, Z.-N. Jiang, Z.-H. Chen, T. Wang, M.-M. Wei, C.-C. Qin, L. Feng, W. Qin, S.-K. So, and X.-T. Hao, "Multiple Temporal-Scale Photocarrier Dynamics Induced by Synergistic Effects of Fluorination and Chlorination in Highly Efficient Nonfullerene Organic Solar Cells", *Sol. RRL*, vol. 4, no. 4, pp. 42313–42321, **2020**.

[236] Y. Zhang, H. Yao, S. Zhang, Y. Qin, J. Zhang, L. Yang, W. Li, Z. Wei, F. Gao, and J. Hou, "Fluorination vs. Chlorination: A case study on High Performance Organic Photovoltaic Materials", *Sci. China Chem.*, vol. 61, no. 1, pp. 1328–1336, **2018**.

[237] L. Ye, K. Sun, W. Jiang, S. Zhang, W. Zhao, H. Yao, Z. Wang, and J. Hou, "Enhanced Efficiency in Fullerene-Free Polymer Solar Cell by Incorporating Fine-Designed Donor and Acceptor Materials", *ACS Appl. Mater. Interfaces*, vol. 7, no. 17, pp. 9274–9280, **2015**.

[238] S. Rajaram, R. Shivanna, S. K. Kandappa, and K.S. Narayan, "Nonplanar Perylene Diimides as Potential Alternatives to Fullerenes in Organic Solar Cells", *J. Phys. Chem. Lett.*, vol. 3, no. 17, pp. 2405–24080, **2012**.

[239] P. Müller-Buschbaum, "Influence of Surface Cleaning on Dewetting of Thin Polystyrene Films", *Eur. Phys. J. E*, vol. 12, pp. 443–448, **2004**.

[240] D. W. Schubert, and T.Dunkel, "Spin Coating from a Molecular Point of View: Its Concentration Regimes, Influence of Molar Mass and Distribution", *Mater. Res. Innov.*, vol. 7, no. 5, pp. 314–321, **2003**.

[241] S.-H. Liao, H.-J. Jhuo, P.-N. Yeh, Y.-S. Cheng, Y.-L. Li, Y.-H. Lee, S. Sharma, and S.-A. Chen, "Single Junction Inverted Polymer Solar Cell Reaching Power Conversion Efficiency 10.31% by Employing Dual-Doped Zinc Oxide Nano-Film as Cathode Interlayer", *Sci. Rep.*, vol. 4, no. 6813, **2014**.

[242] R. D. Andrés, "Printed Fullerene-Free Organic Thin Films for Photovoltaic Applications", *Master's Thesis*, **2018**.

[243] K. S. Wienhold, C. L. Weindl, S. Yin, T. Tian, M. Schwartzkopf, A. Rothkirch, S.V. Roth, and P. Müller-Buschbaum, "Following In Situ the Evolution of Morphology and Optical Properties during Printing of Thin Films for Application in Non-Fullerene Acceptor Based Organic Solar Cells", *ACS Appl. Mater. Interfaces*, vol. 12, no. 36, pp. 40381–40392, **2020**.

[244] S. Ebbens, R. Hodgkinson, A. J. Parnell, A. Dunbar, S. J. Martin, P. D. Topham, N. Clarke, and J. R. Howse, "In Situ Imaging and Height Reconstruction of Phase

Separation Processes in Polymer Blends during Spin Coating", *ACS Nano*, vol. 5, no. 6, pp. 5124–5131, **2011**.

[245] M. Chang, Y. Wang, Y.-Q.-Q. Yi, X. Ke, X. Wan, C. Li, and Y. Chen, "Fine-Tuning the Side-Chains of Non-Fullerene Small Molecule Acceptors to match with appropriate Polymer Donors", *J. Mater. Chem. A*, vol. 6, no. 18, pp. 8586–8594, **2018**.

[246] B. Kan, H. Feng, H. Yao, M. Chang, X. Wan, C. Li, J. Hou, and Y. Chen, "A Chlorinated Low-Bandgap Small-Molecule Acceptor for Organic Solar Cells with 14.1% Efficiency and Low Energy Loss", *Sci. China Chem.*, vol. 61, no. 10, pp. 1307–1313, **2018**.

[247] A. W. Götz, J. I. Rodríguez, F. L. Castillo-Alvarado, and D. E. Trujillo-González, "Van der Waals Effects on Structure and Optical Properties in Organic Photovoltaics", *Int. J. Quantum Chem.*, vol. 352, p. e25883, **2019**.

[248] Z. Du, X. Bao, Y. Li, D. Liu, J. Wang, C. Yang, R. Wimmer, L. W. Städe, R. Yang, and D. Yu, "Balancing High Open Circuit Voltage over 1.0 V and High Short Circuit Current in Benzodithiophene-Based Polymer Solar Cells with Low Energy Loss: A Synergistic Effect of Fluorination and Alkylthiolation", *Adv. Energy Mater.*, vol. 8, no. 8, p. 1701471, **2018**.

[249] W. W. H. Wong, J. Subbiah, S. R. Puniredd, W. Pisula, D. J. Jones, and A. B. Holmes, "Benzotriazole-based Donor–Acceptor Conjugated Polymers with a Broad Absorption in the Visible Range", *Polym. Chem.*, vol. 5, no. 4, pp. 1258–1263, **2014**.

[250] J. Ma, G. Feng, F. Liu, F. Yang, Y. Guo, Y. Wu, and W. Li, "A Conjugated Polymer based on Alkylthio-Substituted Benzo[1,2-c:4,5-c']dithiophene-4,8-dione Acceptor for Polymer Solar Cells", *Dyes Pigment.*, vol. 165, pp. 335–340, **2019**.

[251] M. Chang, J. Lee, N. Kleinhenz, B. Fu, and E. Reichmanis, "Photoinduced Anisotropic Supramolecular Assembly and Enhanced Charge Transport of Poly(3-hexylthiophene) Thin Films", *Adv. Funct. Mater.*, vol. 24, no. 28, pp. 4457–4465, **2014**.

[252] M. Chang, D. Choi, G. Wang, N. Kleinhenz, N. Persson, B. Park, and E. Reichmanis, "Photoinduced Anisotropic Assembly of Conjugated Polymers in Insulating Polymer Blends", *ACS Appl. Mater. Interfaces*, vol. 7, no. 25, pp. 14095–14103, **2015**.

[253] G. Jo, J. Jung, and M. Chang, "Controlled Self-Assembly of Conjugated Polymers via a Solvent Vapor Pre-Treatment for Use in Organic Field-Effect Transistors", *Polymers*, vol. 11, no. 2, p. 332, **2019**.

[254] P. Müller-Buschbaum, in *Polymer Surfaces and Interfaces: Characterization, Modification and Applications*. (Ed.: M. Stamm), Berlin: Springer, **2008**.

[255] M. A. Ruderer, and P. Müller-Buschbaum, "Morphology of Polymer-based Bulk Heterojunction Films for Organic Photovoltaics", *Soft Matter*, vol. 7, pp. 5482–5493, **2011**.

[256] V. Holy, and T. Baumbach, "Nonspecular X-ray Reflection from Rough Multilayers", *Phys. Rev. B*, vol. 49, no. 15, p. 10668, **1994**.

[257] P. Müller-Buschbaum, and M. Stamm, "Correlated Roughness, Long-Range Correlations, and Dewetting of Thin Polymer Films", *Macromolecules*, vol. 31, no. 11, pp. 3686–3692, **1998**.

[258] J. J. van Franeker, D. Hermida-Merino, C. Gommes, K. Arapov, J. J. Michels, R. A. J. Janssen, and G. Portale, "Sub-Micrometer Structure Formation during Spin Coating Revealed by Time-Resolved In Situ Laser and X-ray Scattering", *Adv. Funct. Mater.*, vol. 27, no. 46, p. 1702516, **2017**.

[259] S. V. Roth, G. Herzog, V. Körstgens, A. Buffet, M. Schwartzkopf, J. Perlich, M. M. A. Kashem, R. Döhrmann, R. Gehrke, A. Rothkirch, K. Stassig, W. Wurth, G. Benecke, C. Li, P. Fratzl, M. Rawolle, and P. Müller-Buschbaum, "In Situ Observation of Cluster Formation during Nanoparticle Solution Casting on a Colloidal Film", *J. Phys. Condens. Matter*, vol. 23, no. 25, p. 091915, **2011**.

[260] S. V. Roth, T. Autenrieth, G. Grübel, C. Riekel, M. Burghammer, R. Hengstler, L. Schulz, and P. Müller-Buschbaum, "In Situ Observation of Nanoparticle Ordering at the Air-Water-Substrate Boundary in Colloidal Solutions using X-ray Nanobeams", *Appl. Phys. Lett.*, vol. 91, no. 9, p. 091915, **2007**.

[261] P. Zhang, G. Santoro, S. Yu, S. K. Vayalil, S. Bommel, and S. V. Roth, "Manipulating the Assembly of Spray-Deposited Nanocolloids: In Situ Study and Monolayer Film Preparation", *Langmuir*, vol. 32, no. 17, pp. 4251–4258, **2016**.

[262] K. S. Wienhold, W. Chen, S. Yin, R. Guo, M. Schwartzkopf, S. V. Roth, and P. Müller-Buschbaum, "Following In Operando the Structure Evolution Induced Degradation in Printed Organic Solar Cells with Nonfullerene Small Molecule Acceptor", *Sol. RRL*, vol. 4, no. 9, p. 2000251, **2020**.

[263] M. Chen, D. Liu, W. Li, R. S. Gurney, D. Li, J. Cai, E. L. K. Spooner, R. C. Kilbride, J. D. McGettrick, T. M. Watson, Z. Li, R. A. L. Jones, D. G. Lidzey, and T. Wang, "Influences of Non-fullerene Acceptor Fluorination on Three-Dimensional Morphology and Photovoltaic Properties of Organic Solar Cells", *ACS Appl. Mater. Interfaces*, vol. 11, no. 29, pp. 26194–26203, **2019**.

[264] J. W. Kim, H. J. Kim, T.-M. Kim, T. G. Kim, J.-H. Lee, J. W. Kim, and J.-J. Kim, "High Performance Organic Planar Heterojunction Solar Cells by Controlling the Molecular Orientation", *Curr. Appl. Phys.*, vol. 13, no. 1, pp. 7–11, **2013**.

[265] X. Guo, N. Zhou, S. J. Lou, J. Smith, D. B. Tice, J. W. Hennek, R. P. Ortiz, J. T. L. Navarrete, S. Li, J. Strzalka, L. X. Chen, R. P. H. Chang, A. Facchetti, and T. J. Marks, "Polymer Solar Cells with Enhanced Fill Factors", *Nat. Photonics*, vol. 7, pp. 825–833, **2013**.

[266] Y. Li, and Y. Zou, "Conjugated Polymer Photovoltaic Materials with Broad Absorption Band and High Charge Carrier Mobility", *Adv. Mater.*, vol. 20, no. 15, pp. 2952–2958, **2008**.

[267] Y. Li, "Molecular Design of Photovoltaic Materials for Polymer Solar Cells: Toward Suitable Electronic Energy Levels and Broad Absorption", *Acc. Chem. Res.*, vol. 45, no. 5, pp. 723–733, **2012**.

[268] M. A. Ruderer, S. Guo, R. Meier, H.-Y. Chiang, V. Körstgens, J. Wiedersich, J. Perlich, S. V. Roth, and P. Müller-Buschbaum, "Solvent-Induced Morphology in Polymer-Based Systems for Organic Photovoltaics", *Adv. Funct. Mater.*, vol. 21, no. 17, pp. 3382–3391, **2011**.

[269] T. M. Clarke, and J. R. Durrant, "Charge Photogeneration in Organic Solar Cells", *Chem. Rev.*, vol. 110, no. 11, pp. 6736–6767, **2010**.

[270] J. R. Tumbleston, B. A. Collins, L. Yang, A. C. Stuart, E. Gann, W. Ma, W. You, and H. Ade, "The Influence of Molecular Orientation on Organic Bulk Heterojunction Solar Cells", *Nat. Photonics*, vol. 8, pp. 385–391, **2014**.

[271] M. S. Menke, and R. J. Holmes, "Exciton Diffusion in Organic Photovoltaic Cells", *Energy Environ. Sci.*, vol. 7, pp. 499–512, **2014**.

[272] D. Veldman, O. Ipek, S. C. J. Meskers, J. Sweelssen, M. M. Koetse, S. C. Veenstra, J. M. Kroon, S. S. van Bavel, J. Loos, and R. Janssen, "Compositional and Electric Field Dependence of the Dissociation of Charge Transfer Excitons in Alternating Polyfluorene Copolymer/Fullerene Blends", *J. Am. Chem. Soc.*, vol. 130, no. 24, pp. 7721–7735, **2008**.

[273] L. J. A. Koster, S. E. Shaheen, and J. C. Hummelen, "Pathways to a new Efficiency Regime for Organic Solar Cells", *Adv. Energy Mater.*, vol. 2, no. 10, pp. 1246–1253, **2012**.

[274] U. Zhokhavets, T. Erb, G. Gobsch, M. Al-Ibrahim, and O. Ambacher, "Relation between Absorption and Crystallinity of Poly(3-hexylthiophene)/Fullerene Films for Plastic Solar Cells", *Chem. Phys. Lett.*, vol. 418, no. 4-6, pp. 347–350, **2006**.

[275] G. Li, Y. Yao, H. Yang, V. Shrotriya, G. Yang, and Y. Yang, ""Solvent Annealing" Effect in Polymer Solar Cells Based on Poly(3-hexylthiophene) and Methanofullerenes", *Adv. Funct. Mater.*, vol. 17, no. 10, pp. 1636–1644, **2007**.

[276] H. B. Yang, Q. L. Song, C. Gong, and C. M. Li, "The Degradation of Indium Tin Oxide/Pentacene/Fullerene/Tris-8-Hydroxy-Quinolinato Aluminum/Alluminum Heterojunction Organic Solar cells: By Oxygen or Moisture?", *Sol. Energy Mater. Sol. Cells*, vol. 94, no. 5, pp. 846–849, **2010**.

[277] P. Schilinsky, C. Waldauf, J. Hauch, and C. J. Brabec, "Simulation of Light Intensity Dependent Current Characteristics of Polymer Solar Cells", *J. Appl. Phys*, vol. 95, no. 5, pp. 2816–2819, **2004**.

[278] B. Ray, and M. A. Alam, "A Compact Physical Model for Morphology Induced Intrinsic Degradation of Organic Bulk Heterojunction Solar Cell", *Appl. Phys. Lett.*, vol. 99, no. 3, p. 033303, **2011**.

[279] X. Du, T. Heumuelle, W. Gruber, O. Almora, A. Classen, J.i Qu, F. He, T. Unruh, N. Li, and C. J. Brabec, "Unraveling the Microstructure Related Device Stability for Polymer Solar Cells Based on Nonfullerene Small Molecular Acceptors", *Adv. Mater.*, vol. 32, no. 16, p. 1908305, **2020**.

[280] H. Yan, S. Swaraj, C. Wang, I. Hwang, N. C. Greenham, C. Groves, H. Ade, and C. R. McNeill, "Influence of Annealing and Interfacial Roughness on the Performance of Bilayer Donor/Acceptor Polymer Photovoltaic Devices", *Adv. Funct. Mater.*, vol. 20, no. 24, pp. 4329–4337, **2010**.

[281] I. A. Howard, R. Mauer, M. Meister, and F. Laquai, "Effect of Morphology on Ultrafast Free Carrier Generation in Polythiophene:Fullerene Organic Solar Cells", *J. Am. Chem. Soc.*, vol. 132, no. 42, pp. 14866–14876, **2010**.

List of Publications

Publications related to the Dissertation

- K. S. Wienhold, V. Körstgens, S. Grott, X. Jiang, M. Schwartzkopf, S. V. Roth, and P. Müller-Buschbaum, "Effect of Solvent Additives on the Morphology and Device Performance of Printed Nonfullerene Acceptor Based Organic Solar Cells", *ACS Appl. Mater. Interfaces*, vol. 11, no. 45, pp. 42313–42321, **2019**.
- K. S. Wienhold, X. Jiang, and P. Müller-Buschbaum, "Organic Solar Cells probed with Advanced Neutron Scattering Techniques", *Appl. Phys. Lett.*, vol. 116, p. 120504, **2020**.
- K. S. Wienhold, V. Körstgens, S. Grott, X. Jiang, M. Schwartzkopf, S. V. Roth, and P. Müller-Buschbaum, "*In Situ* Printing: Insights into the Morphology Formation and Optical Property Evolution of Slot-Die Coated Active Layers Containing Low Bandgap Polymer Donor and Nonfullerene Small Molecule Acceptor", *Sol. RRL*, vol. 4, no. 7, pp. 2000086, **2020**. Associated Front Cover Image: *Sol. RRL*, vol. 7, no. 4, **2020**.
- K. S. Wienhold, W. Chen, S. Yin, R. Guo, M. Schwartzkopf, S. V. Roth, and P. Müller-Buschbaum, "Following *In Operando* the Structure Evolution-Induced Degradation in Printed Organic Solar Cells with Nonfullerene Small Molecule Acceptor", *Sol. RRL*, vol. 4, no. 9, pp. 2000251, **2020**. Associated Front Cover Image: *Sol. RRL*, vol. 4, no. 9, **2020**.
- K. S. Wienhold, C. L. Weindl, S. Yin, T. Tian, M. Schwartzkopf, A. Rothkirch, S. V. Roth, and P. Müller-Buschbaum, "Following *In Situ* the Evolution of Morphology and Optical Properties during Printing of Thin Films for Application in Nonfullerene Acceptor Based Organic Solar Cells", *ACS Appl. Mater. Interfaces*, vol. 12, no. 36, pp. 40381–40392, **2020**.

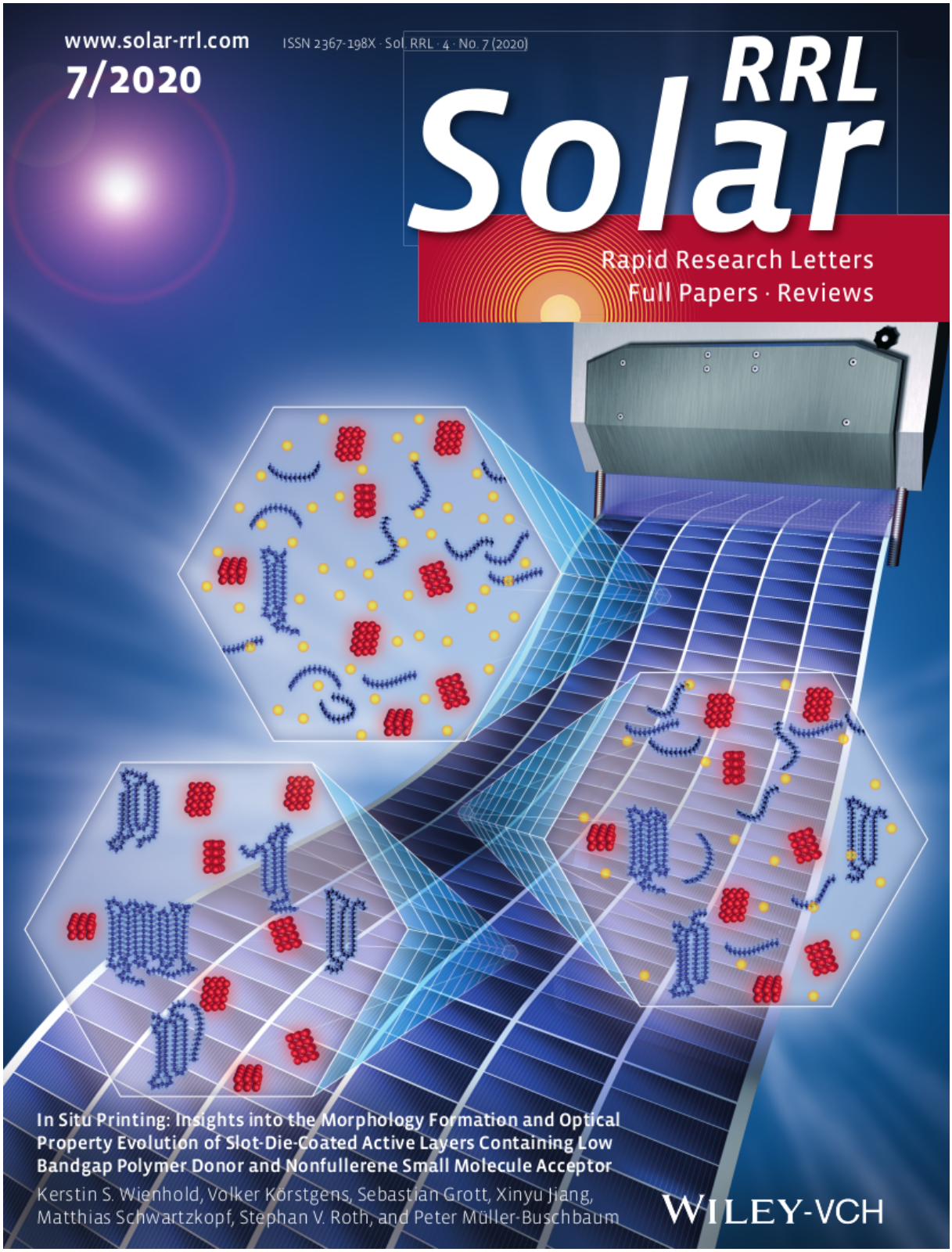

Cover Image featured on *Sol. RRL*, vol. 4, no. 7, **2020**.

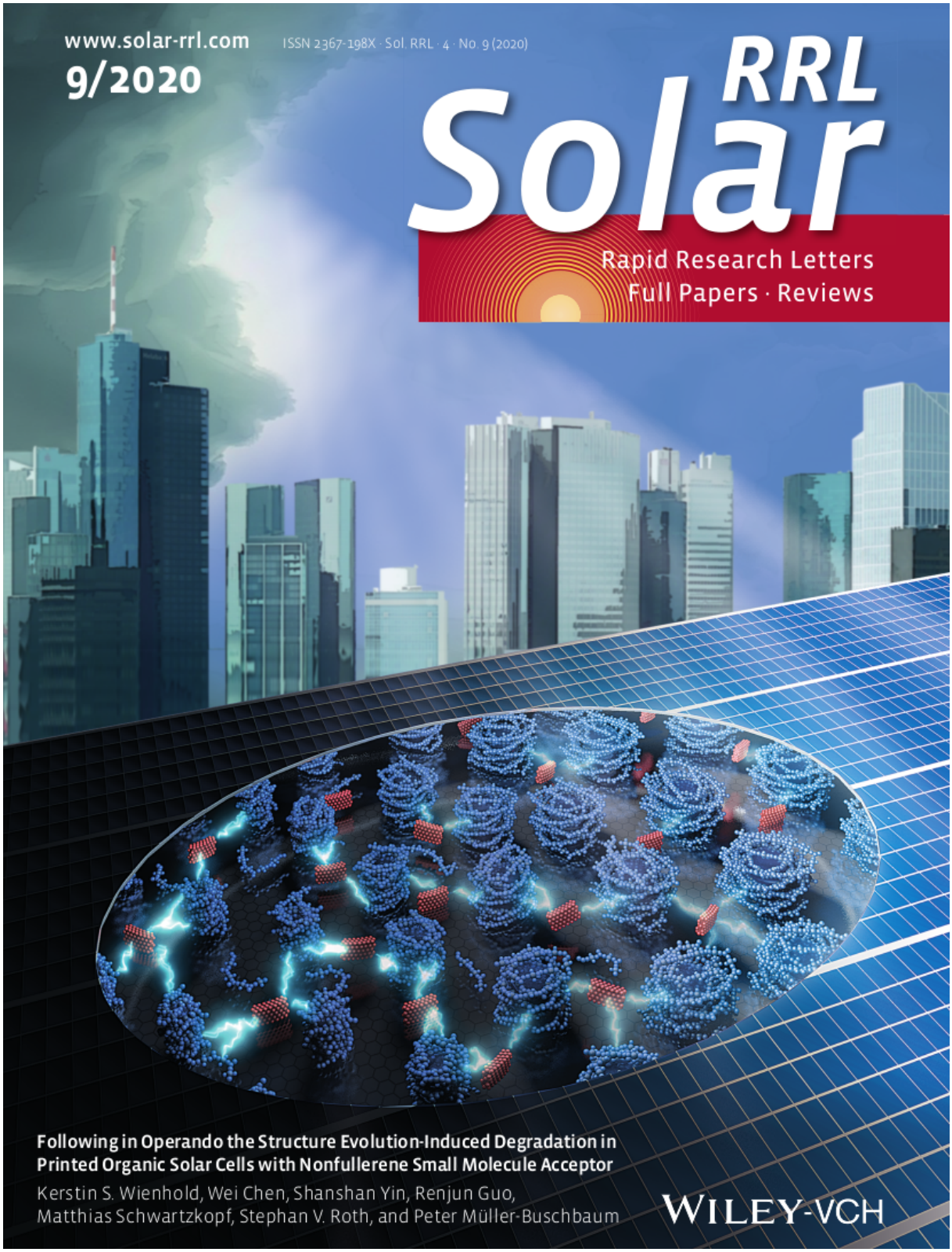

Cover Image featured on *Sol. RRL*, vol. 4, no. 9, **2020**.

Further Publications

- S. Yin, T. Tian, K. S. Wienhold, C. L. Weindl, R. Guo, M. Schwartzkopf, S. V. Roth, and P. Müller-Buschbaum, "Key Factor Study for Amphiphilic Block Copolymer-Templated Mesoporous SnO_2 Thin Film Synthesis: Influence of Solvent and Catalyst", *Adv. Mater. Interfaces*, vol. 7 , no. 18, p. 2001002, **2020**.
- D. Yang, S. Grott, X. Jiang, K. S. Wienhold, M. Schwartzkopf, S. V. Roth, and P. Müller-Buschbaum, "*In Situ* Studies of Solvent Additive Effects on the Morphology Development during Printing of Bulk Heterojunction Films for Organic Solar Cells", *Small Methods*, vol. 4, no. 9, p. 2000418, **2020**.

Scientific Talks

- K. S. Wienhold "Printed Organic Solar Cells based on Nonfullerene Acceptor Molecules", *Seminar Talk*, Chair for Functional Materials, Physics-Department, TU München, Germany, **2018**.
- K. S. Wienhold, N. Saxena, K. Wang, "X-ray Reflectivity and Neutron Reflectivity", *Polymer Physics Summer School*, Obertauern, Austria, **2018**.
- K. S. Wienhold, V. Körstgens, S. Grott, X. Jiang, M. Schwartzkopf, S. V. Roth, and P. Müller-Buschbaum, "*In Situ* Study of Printed Films of PBDB-T-SF:IT-4F for Application in Organic Solar Cell", *DPG-Frühjahrstagung*, Regensburg, Germany, **2019**.
- K. S. Wienhold "Printed Organic Solar Cells based on Nonfullerene Acceptor Molecules", *Seminar Talk*, Chair for Functional Materials, Physics-Department, TU München, Germany, **2019**.
- K. S. Wienhold "Printed Organic Solar Cells based on Nonfullerene Acceptor Molecules", *Seminar Talk*, Chair for Functional Materials, Physics-Department, TU München, Germany, **2020**.
- Kerstin S. Wienhold, V. Körstgens, S. Grott, X. Jiang, S. Yin, C. L. Weindl, T. Tian, M. Schwartzkopf, A. Rothkirch, S. V. Roth, and P. Müller Buschbaum "*In Situ* Printing: Insights into the Evolution of Morphology and Optical Properties of Slot-Die Coated Active Layers for Application in Organic Solar Cells", *9th SolTech Conference*, Online, **2020**.

Scientific Poster Presentations

- K. S. Wienhold, and P. Müller-Buschbaum, "Printed Organic Solar Cells", *DPG-Frühjahrstagung*, Berlin, Germany, **2018**.
- K. S. Wienhold, and P. Müller-Buschbaum, "Printed Films of Conjugated Polymers and Small Acceptor Molecules ", *8th Energy Colloquium of the Munich School of Engineering*, TU München, Germany, **2018**.
- K. S. Wienhold, and P. Müller-Buschbaum, "Printed Films of Conjugated High-Efficiency Polymers and Small Acceptor Molecules ", *4th German SNI Conference*, Garching, Germany, **2018**.
- K. S. Wienhold, V. Körstgens, S. Grott, X. Jiang, M. Schwartzkopf, S. V. Roth, and P. Müller-Buschbaum, "*In Situ* Study of Printed Active Layers of Conjugated Polymers and Small Acceptor Molecules for Application in High-Efficiency Organic Solar Cells", *MLZ User Meeting*, Grainau, Germany, **2019**.
- K. S. Wienhold, V. Körstgens, S. Grott, X. Jiang, M. Schwartzkopf, S. V. Roth, and P. Müller-Buschbaum, "*In Situ* Printing of Active layers of PBDB-T-SF:IT-4F for Application in High-Efficiency Organic Solar Cells", *9th Energy Colloquium of the Munich School of Engineering*, Garching, Germany, **2019**.
- K. S. Wienhold, V. Körstgens, S. Grott, X. Jiang, M. Schwartzkopf, S. V. Roth, and P. Müller-Buschbaum, "*In Situ* Printing of Active Layers of PBDB-T-SF:IT-4F for Application in High Efficiency Organic Solar Cells", *8th SolTech Conference*, Nürnberg, Germany, **2019**.
- K. S. Wienhold, V. Körstgens, S. Grott, X. Jiang, M. Schwartzkopf, S. V. Roth, and P. Müller-Buschbaum, "*In Situ* Printing of PBDB-T-SF:IT-4F for Application in High-Efficiency Organic Solar Cells", *MLZ User Meeting*, Garching, Germany, **2019**.
- K. S. Wienhold, V. Körstgens, S. Grott, X. Jiang, M. Schwartzkopf, S. V. Roth, and P. Müller-Buschbaum, "*In Situ* Study of Printed Active Layers of Conjugated Polymers and Small Acceptor Molecules for Application in High-Efficiency Organic Solar Cells", *10th Energy Colloquium of the Munich School of Engineering*, Garching, Germany, **2020**.
- K. S. Wienhold, V. Körstgens, S. Grott, X. Jiang, M. Schwartzkopf, S. V. Roth, and P. Müller-Buschbaum, "*In Situ* Printing: Insights into the Morphology Formation and Optical Property Evolution of Slot-Die-Coated Active Layers Containing Low Bandgap Polymer Donor and Nonfullerene Small Molecule Acceptor", *MLZ User Meeting*, Online, Germany, **2020**.

Scientific Reports and Proposals

- K. S. Wienhold, and P. Müller-Buschbaum, "PBDB-T-SF for High Efficiency Solar Cells", *Lehrstuhl für Funktionelle Materialien, Annual Report*, **2017**.
- K. S. Wienhold, S. Grott, D. Yang, X. Jiang, and P. Müller-Buschbaum, "Experimental Report: *In Situ* Study of Printed Films for Applications in Organic Solar Cells", *DESY*, **2018**.
- K. S. Wienhold, V. Körstgens, S. Grott, X. Jiang, and P. Müller-Buschbaum, "Experimental Report: *In Situ* Study of Printed Films for Applications in Organic Solar Cells", *DESY*, **2018**.
- K. S. Wienhold, S. Yin, W. Chen, R. Guo, and P. Müller-Buschbaum, "Beamtime Proposal: *In Operando* Study of High Efficiency Organic Solar Cells", *DESY*, **2018**.
- K. S. Wienhold, and P. Müller-Buschbaum, "Printed Organic Solar Cells based on Nonfullerene Acceptor Molecules", *Lehrstuhl für Funktionelle Materialien, Annual Report*, **2018**.
- K. S. Wienhold, S. Yin, W. Chen, R. Guo, and P. Müller-Buschbaum, "Experimental Report: *In Operando* Study of High Efficiency Organic Solar Cells", *DESY*, **2019**.
- K. S. Wienhold, C. Weindl, S. Yin, T. Ting, and P. Müller-Buschbaum, "Experimental Report: *In Situ* Study of Printed Films for Applications in Organic Solar Cells", *DESY*, **2019**.
- K. S. Wienhold, V. Körstgens, S. Grott, X. Jiang, M. Schwartzkopf, S. V. Roth, and P. Müller-Buschbaum, "Effect of Solvent Additives on the Morphology and Device Performance of Organic Solar Cells", *Lehrstuhl für Funktionelle Materialien, Annual Report*, **2019**.
- K. S. Wienhold, W. Chen, S. Yin, R. Guo, M. Schwartzkopf, S. V. Roth, and P. Müller-Buschbaum, "Following *In Operando* the Degradation of Printed Organic Solar Cells", *Lehrstuhl für Funktionelle Materialien, Annual Report*, **2020**.

Scholarships

- Hans-Böckler-Stiftung, Promotionsförderung

Acknowledgments

In my time as PhD student, I did not only learn a lot about science but also, more importantly, made a lot of precious experiences and developed personal skills, which will be valuable for my future life. For that, I want to thank all the people who supported me personally or with scientific advice.

First, I want to thank Prof. Dr. Peter Müller-Buschbaum for the opportunity to join the Chair of Functional Materials at the Physics Department and to work on the interesting topic of organic solar cells. I highly appreciate his continuous effort to strengthen the team spirit and his encouragement to have fun together in order to make the time at his chair as pleasant as possible for all of us. I want to thank Peter for giving me many opportunities to generate good data by sending me to beamtimes at the DESY (Deutsches Elektronen-Synchrotron) in Hamburg as well as by letting me come up with my own ideas, believing in my abilities and by regularly giving me clear and helpful feedback. His drive to send us to beamtimes, conferences and scientific meetings gave me the possibility to become a part of the scientific community and to strengthen my personal skills, such as leading a team, handling responsibility and presenting talks and posters. I am thankful for this great experiences.

Furthermore, I want to thank my mentor Prof. Dr. Christine M. Papadakis for her far-reaching support and our secretaries Carola Kappauf and Marion Waletzki, who always showed sincere interest for the well-being of my son as well as empathy for the challenges of doing a PhD having a child. Moreover, I want to thank Reinhold Funer for helping me as soon as possible whenever I came to his workshop. In addition, I want to thank Reiner Müller for designing two Cover images for Solar RRL to highlight my research.

A big thank you goes to the alumni and current members of the Chair of Functional Materials. You were the best colleagues I could imagine. You made me smile through tough times (such as cloudy Mondays) and laugh through our numerous good times, such as the DPG spring meeting, our summer school, Nockherberg, Wiesn, barbecues, Karaoke

evenings and many coffee breaks, to name a few. Overall, I learned a lot during scientific meetings but also during non-scientific events, as the latter often resulted in fundamental scientific discussions about everything under the sun (and beyond). I want to thank Dr. Volker Körstgens and our alumni Dr. Nitin Saxena, Dr. Johannes Schlipf, Dr. Lorenz Bießmann and Dr. Nuri Hohn for sharing their great humor and their profound knowledge with me and for never being tired of answering all my basic questions about advanced X-ray scattering methods in grazing incidence geometry. Furthermore, I would like to thank Dr. Christoph Schaffer for helping me with data evaluation via phone before we met the first time, which once more proofes how strong our team spirit is. I further want to thank Dr. Volker Körstgens, Sebastian Grott, Dr. Dan Yang, Xinyu Jiang, Dr. Wei Chen, Shanshan Yin, Renjun Guo, Christian Weindl, Ting Tian and Marc Gensch for their vast assistance during DESY beamtimes. Moreover, I thank Franziska C. Löhrer, Christina Geiger, Anna-Lena Oechsle, Julija Reitenbach and Shambhavi Pratap for their scientific and non-scientific support, our collective movie evenings and for contributing to "female power" at our chair. In addition, I thank Julian E. Heger, Simon J. Schaper, Lucas Kreuzer, Manuel Scheel, Tobias Widmann, Lukas Spanier, Roy Schaffrinna, Dominik Schwaiger, Lennart Reb, Dr. Apostolos Vagias, Goran Ivkovic Ivandekic, Lautaro Díaz Piola, Raphael Märkl, Oleg Shindelov, Magdalini Spyranti, Christopher Everett, Kaltrina Shehu, Tommaso Riccitelli and Benjamin Predeschly for their support, nice conversations and the fun we had together. I thank my colleagues from China Dr. Wei Chen, Dr. Dan Yang, Dr. Senlin Xia, Wei Cao and Nian Li for giving me interesting insights into chinese culture. In particular, I appreciate Dr. Wei Chen's efforts to introduce our chair members into chinese culinary art, even though it required courage to try the millennial egg. Moreover, I want to thank the Papadakis-Group, in particular Dr. Bart-Jan Niebuur, Dr. Florian Jung, Chia-Hsin Ko and Jia-Jhen Kang for sharing this precious time period with me. I thank my students Samah Akel, Daniel Steger, Linus Huber, Michael Kopp and Ahmed Krifa for giving me the opportunity to strengthen my team leadership skills.

Furthermore, I want to thank our collaboration partners. I want to thank Prof. Dr. Eva M. Herzig, and her alumni and current group members Dr. Jenny M. Lebert, Mihael Coric and Oliver Filonik for their support and very enjoyable discussions. I want to thank Prof. Dr. Stephan V. Roth, Dr. Matthias Schwartzkopf and Dr. André Rothkirch from the DESY for their assistance during beamtimes. I want to thank Dr. Matthias Schwartzkopf for always being motivated to make the experiments run and for helping us immediately and patiently with all the small, but very urgent problems, occuring at night-time or weekends.

Moreover, I want to thank the Hans-Böckler-Stiftung for the financial support during my Bachelor's studies, Master's studies and finally my PhD project. In particular, I thank my liaison professor Priv. Doz. Dr. Detlef Nattland for his far-reaching assistance.

Lastly, I thank my parents Anna and Matthias Wachinger, all members of my family and my friends for their support. In particular, I want to thank my best friend Angelika Hansen for supporting me in every circumstance of my life and the deep friendship since Kindergarten. The biggest thank you goes to my husband Sebastian for the patience and endorsement and to my son Alexander Elias for changing my view of life and teaching me to focus on the really important things. You are the persons I love and I am happy to have you in my life!